UNIVERSITÀ
DEGLI STUDI
DELL'AQUILA

DSFC
Dipartimento
di Scienze Fisiche
e Chimiche

UNIVERSTY OF L'AQUILA

Department of Physical and Chemical Sciences

PhD in Chemical Sciences - XXXVIII cycle

EXPLORING METAL–ORGANIC FRAMEWORKS AS MULTIFUNCTIONAL MATERIALS

CHEM-02/A Physical Chemistry

PhD Candidate

Nicola Di Nicola

Course Coordinator

Prof. Massimiliano Aschi

Supervisor

Prof. Andrea Lazzarini

A.Y. 2024/2025

The work described in this thesis has been carried out at:

DSFC - Dipartimento di Scienze Fisiche e Chimiche

Università degli Studi dell'Aquila

L'Aquila, Italy

Bernal Institute - Department of Chemical Science

University of Limerick

Limerick, Ireland

Abstract

Metal-Organic Frameworks (MOFs) have attracted increasing attention over the past two decades due to their highly ordered crystalline nature, large specific surface area, possibility of structural modulation, and versatility in host–guest interactions. These unique characteristics make them promising materials not only for traditional applications such as gas storage and catalysis, but also in more advanced fields, including biomedicine and environmental purification. This doctoral thesis is dedicated to the study of MOFs as multifunctional platforms, with particular emphasis on their biomedical potential and complementary applications in the environmental field.

The first part of this work focuses on zeolitic imidazolate framework-8 (ZIF-8), a prototypical MOF that combines structural stability, good biocompatibility and pH-dependent degradation. Thanks to these properties, ZIF-8 has been investigated as a nanocarrier for therapeutic molecules in two different biological contexts. On the one hand, its ability to encapsulate and release anticancer drugs has been explored, highlighting its potential in the development of new, more selective chemotherapy strategies with lower systemic toxicity. On the other hand, ZIF-8 has been evaluated for potential veterinary applications, particularly in the treatment of ruminal acidosis in ruminants, where its ability to load and release bioactive compounds in response to an acidic environment represents a promising approach to counteract this widespread metabolic dysfunction.

The work also considered the porphyrin MOF PCN-224, characterized by a highly ordered structure, large mesoporous channels and excellent photophysical properties. In this case, the material was used as a platform for the delivery of paramagnetic ions, in particular gadolinium and

manganese, in order to explore its use as a multifunctional agent for nuclear magnetic resonance imaging (MRI). The incorporation of these metals has made it possible to obtain systems with modifiable relaxivity profiles, with the aim of overcoming some of the limitations of conventional contrast agents, especially their potential toxicity.

Finally, the environmental aspect of MOFs was addressed through the use of ZIF-8 as an adsorbent for the removal of pesticides from wastewater. Given the growing concern about the persistence of agrochemicals in aquatic ecosystems, the ability of ZIF-8 to adsorb Linuron, a herbicide that persists in the environment after use due to its chemical stability, was systematically evaluated. This study highlights how MOFs can contribute to sustainable water resource management, expanding their role beyond the biomedical field and emphasizing their versatility as materials at the interface between health and ecology.

Overall, this doctoral research offers a comprehensive and integrated overview of the use of MOFs already known for specific applications in various fields. The study demonstrates how materials such as ZIF-8 and PCN-224 can be effectively adapted to biomedical, diagnostic and environmental contexts. The results collected contribute to reinforcing the vision of MOFs as versatile and multifunctional platforms capable of providing concrete solutions to current problems in medicine, diagnostics and environmental sustainability.

Publications

1. Colaiezzi, R.; Saviozzi, C.; di Nicola, N.; Zacchini, S.; Pampaloni, G.; Crucianelli, M.; Marchetti, F.; Di Giuseppe, A.; Biancalana, L. Ruthenium(II) Arene Complexes Bearing Simple Dioxime Ligands: Effective Catalysts for the One-Pot Transfer Hydrogenation/N-Methylation of Nitroarenes with Methanol. *Catal. Sci. Technol.* **2023**, *13*, 2160-2183.

2. di Nicola, N.; Paolucci, V.; Daniele, V.; Taglieri, G.; Crucianelli, M.; Guidoni, L.; Lazzarini, A. ZIF-8 as Potential Vector for Enhanced Target Delivery of Sulfathiazole for the Treatment of Bovine Ruminal Acidosis. *Eur. J. Inorg. Chem.* **2024**, *2024*, e202400504.

3. di Nicola, N.; Di Pelino, M.; Foschi, M.; Passalacqua, R.; Lazzarini, A.; Ruggieri, F. ZIF-8 as Potential Pesticide Adsorbent Medium for Wastewater Treatment: The Case Study of Model Linuron Extraction Conditions Optimization via Design of Experiment. *Molecules* **2025**, *30*, 2480.

4. di Nicola, N.; Giacchi, L.; Vandone, M.; Crucianelli, M.; Guidoni, L.; Colombo, V.; Rucci, N.; Lazzarini, A. Targeted Delivery of Lidocaine in Breast Cancer Cells via Zeolitic Imidazolate Framework-8 Nanoparticles. *ChemPhysChem* **2025**, *26* (16), e202401128.

5. di Nicola, N.; Crucianelli, M. Le nuove frontiere della catalisi ecosostenibile: un viaggio, dai catalizzatori omogenei alla fotocatalisi, ripercorrendo le tappe storiche più rilevanti per il suo sviluppo. *Chimica Nella Scuola* **2025**, *3* (3), 25-34.

Table of Contents

1. Introduction

1.1 The Chemistry of MOFs

Metal-Organic Frameworks (MOFs) represent one of the most promising classes of crystalline materials developed in the field of porous materials chemistry.[1] MOFs are hybrid structures consisting of metal nodes, single ions or polynuclear clusters, connected to each other by multifunctional organic ligands, capable of forming highly ordered and porous three-dimensional lattices (Figure 1).[2] The growing interest in these materials stems from their extreme structural versatility, the possibility of modular synthesis and the unique combination of characteristics that distinguish them: crystallinity, high porosity and chemical functionalizability.[3] MOFs have evolved rapidly over the course of a few decades, from simple coordination compounds to reticular systems designed according to rational and predictive principles, giving rise to a true discipline called "reticular chemistry".[4]

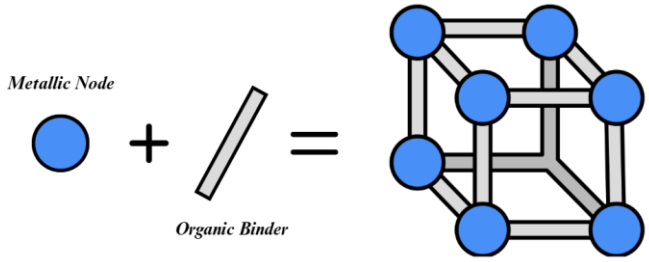

Figure 1: Schematic representation of MOF formation and composition.

The history of MOFs lies between the development of inorganic coordination chemistry, synthetic organic chemistry and materials science.[5] The first real studies date back to the late 1980s, when the term "framework" first appeared.[6]

The breakthrough came in the mid–1990s with the pioneering work of Professor Omar Yaghi and his colleagues, who first realized the possibility of designing crystalline porous architectures through controlled reactions between metal nodes and organic ligands.[7] The publication of MOF-5 in 1999 was a historic moment for materials chemistry,[8] demonstrating for the first time the possibility of obtaining a crystalline material with an extremely high surface area and permanent porosity. Since then, the design of MOFs has taken on an increasingly engineering and modular connotation, based on precise geometric and reticular principles.[9]

The construction of a MOF is based on the concept of self-organization directed by coordination bonds, which allows the formation of extensive and periodic network structures.[10] The metal nodes, which can range from simple cations (Zn^{2+}, Cu^{2+}, Fe^{3+}, etc.) to stable polynuclear clusters (such as Zr_6, Al_8, or Ti_6 units), act as coordination centers for multifunctional organic ligands, often derived from carboxylic, azole, phosphonic or nitrile acids.[11] The ligands, which are generally rigid, act as spatial bridges between metal nodes, determining the extent and final topology of the network.[12] MOFs are typically synthesized under solvothermal conditions by heating precursors in polar solvents at high temperatures,[13] although alternative approaches exist, such as mechanochemical synthesis,[14] microwave-assisted synthesis[15] and solid/liquid interface synthesis.[16] Control of the stoichiometry, solubility of the components and crystallization conditions is essential to obtain pure and well-defined crystalline products.[17]

One of the distinctive features of MOFs is the possibility of predicting and rationalizing their structure starting from their constituent units, through the approach of network chemistry.[18] This method is based on the identification of building blocks, metal nodes and linkers, and their combination according to geometric principles of symmetry and coordination, according to known lattice networks (topologies such as pcu,

dia, fcu, nbo, etc.)(Figure 2).[19] Unlike traditional porous materials, such as zeolites or activated carbons, MOFs can be intentionally designed to adopt a specific structure and geometry.[18]

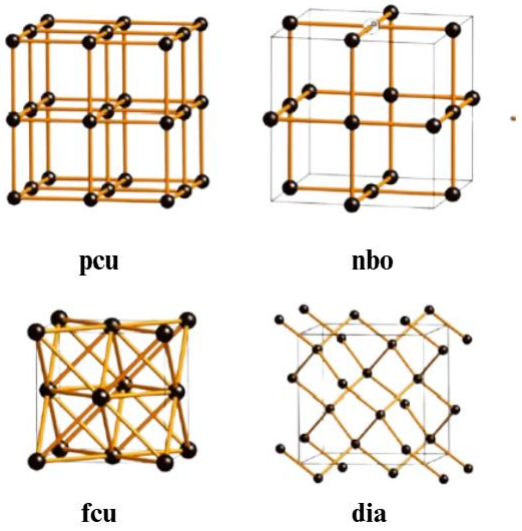

Figure 2. Schematic representation of the main crystal topologies.

From a physical properties standpoint, MOFs are characterized by exceptionally high surface areas, which in some cases exceed 7000 m^2/g.[20] This high porosity is accompanied by fine control of pore size and shape, which can be modulated by the length and rigidity of the organic ligands.[21] MOFs can therefore be considered as "intelligent molecular sponges", capable of recognizing, capturing and releasing molecules according to criteria of chemical affinity and steric selectivity.[22] In addition, many MOFs exhibit dynamic behavior, manifesting phase transitions,[23] reticular expansion[24] or structural changes in response to external stimuli such as pressure,[25] temperature,[26] pH[27] or the presence of specific guests.[28] These dynamic properties, often described as "breathing" or "gate-opening", have

challenged the classic paradigm of crystalline phase rigidity, proposing a new category of dynamic crystalline materials.[29]

An important feature of MOFs is their hybrid composition, which allows the typical properties of organic materials, such as flexibility, lightness and functionalization, to be combined with those of inorganic materials, such as robustness[30] and thermal stability.[31] This hybrid nature paves the way for design strategies that combine synthetic organic chemistry, for the preparation of specific ligands depending on the final purpose, with inorganic chemistry, for the selection of suitable metal nodes.[32] This is complemented by the possibility of post-synthetically modifying MOFs through post-synthetic functionalization techniques that allow reactive or functional groups to be introduced into the already crystallized lattice without compromising its structure.[33]

The extraordinary variety of structures and properties that can be obtained has led MOFs to establish themselves as a true universal language in materials science, a modular system in which knowledge of the constituent units allows the behavior of the final system to be predicted and controlled.[34] Their study continues to stimulate highly topical conceptual, synthetic and theoretical challenges, not only because of their potential applications, but also because of the fundamental contribution they make to our understanding of self-assembly, structural dynamics and reactivity in complex crystalline materials.[35]

1.2 Classification

The extraordinary structural variety of MOFs requires systematic classification to facilitate their study. Classification criteria can be based on various aspects, such as the type of metal node, single ions or polynuclear clusters, the dimensionality and topology of the lattice, porosity and physical-chemical properties, or the chemical and geometric nature of the

organic ligand. Among these, classification based on organic ligands is particularly useful from a structural point of view, as the type, rigidity, functionalization and connectivity of the ligand have a decisive influence on the formation, stability and morphology of MOFs.

1.2.1 MOFs with aromatic carboxylate ligands

Aromatic carboxylic ligands are the most commonly used in MOF synthesis.[36] They allow the formation of strong, directional M–O coordination bonds, promoting the construction of rigid, highly symmetrical and porous lattices.[37] Terephthalate[38] (BDC) and benzene tricarboxylate[39] (BTC) are the prototypes of this category.

MOF-5 ($Zn_4O(BDC)_3$) was the first MOF to be isolated and characterized and is constructed with tetrahedral Zn_4O nodes and linear BDC ligands (Figure 3a).[8] This cubic structure has a specific surface area of over 3000 m^2/g and a pore volume of over 1 cm^3/g. The crystal lattices that make up MOF-5 are called isoreticular metal-organic lattices (IRMOFs), meaning that the BDC linker can be replaced with functionalized analogues (–NH_2, –NO_2, –Br, –OH, etc.) while maintaining the lattice architecture.[40]

Another well-known example of a MOF belonging to this family is HKUST–1 ($Cu_3(BTC)_2$), formed by a tricarboxylic ligand (BTC) that generates a distinct topology, with octahedral cavities and Cu(II) centers exposed in a paddle-wheel configuration (Figure 3b).[41] Although porous and stable up to approximately 300 °C, this material is moderately sensitive to moisture.[42]

MIL (Matériaux de l'Institut Lavoisier) materials, including MIL-53, MIL–100 and MIL–101, represent a family based on trivalent metals (Fe^{3+}, Al^{3+}, Cr^{3+}) and carboxylic ligands (BDC, BTC, etc.).[43] Their salient feature is the presence of reticular flexibility properties, as in the case of MIL-53 (Al), which exhibits "structural breathing" phenomena in response to the adsorption of guest molecules.[44] MIL–101(Cr), on the other hand, is an

exceptionally porous structure (up to 4000 m^2/g) with accessible cavities of nanometric dimensions.[45]

A subfamily of particular relevance is represented by UiO-MOFs (Universitetet i Oslo), whose most representative member is UiO-66(Zr).[46] This framework uses a $Zr_6O_4(OH)_4$ cluster as a node, coordinated with 12 terephthalate ligands (BDC) (Figure 3c).[47] The fcc topology ensures high crystallographic rigidity and, above all, extraordinary chemical and thermal stability.[48] UiO-66 is stable in acidic, basic and aqueous environments even at high temperatures (>200 °C).[49] The use of tetravalent metals such as Zr^{4+} and Hf^{4+} favors the formation of highly connected nodes, which confer tolerance to defects, such as ligand or metal vacancies, making the UiO family extremely modular.[50] Modified versions include UiO-67,[51] where the ligand is biphenyl-4,4'-dicarboxylate (BPDC), and variants functionalized with electron-donating or electron-withdrawing substituents.[52] Furthermore, control of the defect content in UiO materials via synthetic modulation with formic or acetic acid allows the density of coordinatively unsaturated sites to be adjusted, influencing properties such as surface polarity or pore hydrophobicity.[53]

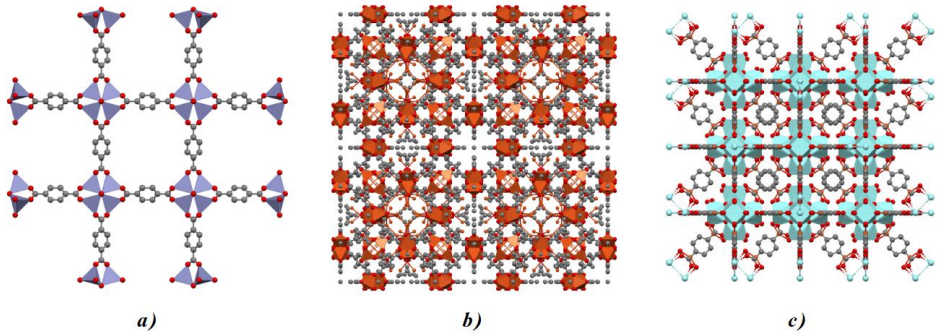

Figure 3: Structural representations of MOF-5 (a), HKUST–1 (b) and UiO-66 (c).

1.2.2 MOFs with azole ligands

Among the most structurally interesting and chemically robust families of MOFs are materials constructed with azole ligands, in particular imidazolates,[54] triazolates[55] and tetrazolates.[56] The ZIF (Zeolitic Imidazolate Frameworks) group is one of the most important subfamilies, not only because of the variety of structures available, but also because of their exceptional chemical, thermal and mechanical stability properties.[57] ZIFs are typically constructed with transition metal cations, mainly Zn^{2+} and Co^{2+}, coordinated by substituted imidazole ligands, such as 2-methylimidazole, 2-nitroimidazole and 2-hydroxymethylimidazole.[58]

The key feature that distinguishes ZIFs from other MOF families is their geometric similarity to zeolites: the M–Im–M bond angle (approximately 145°) is close to the Si–O–Si angle of zeolites (approximately 145°), allowing the formation of crystallographically similar topologies (SOD, LTA, FAU, etc.), and it is precisely this parallelism that inspired the name of the family.[59] The SOD topology of the famous ZIF-8 ($Zn(MeIm)_2$) is among the most studied: the framework has a cubic symmetry, is thermally stable up to 550 °C and has pores of approximately 11.6 Å (Figure 4).[60]

One of the distinctive properties of ZIFs is their exceptional chemical stability.[61] Unlike many carboxylic MOFs, ZIFs are stable in both acidic and basic environments, as well as in protic and aprotic polar solvents.[62] The azole nature of the ligand, with its high basicity and ability to form robust multiple M–N bonds, contributes to this stability.[63] Furthermore, the hydrophobicity of the side groups on many ligands (e.g., methyl, ethyl) promotes water repellency and prevents hydrolysis between the metal and the ligand.[64]

From a crystallographic point of view, ZIFs have unit cells containing a few to tens of nodes and often exhibit framework flexibility phenomena due to

the free rotation of the ligands around the M–N bond. This phenomenon has direct implications on loading and selectivity towards guest molecules.[65]
ZIFs are also known for their ability to be obtained by synthesis at room temperature, in aqueous solvents or even under solvent-free conditions, demonstrating remarkable tolerance to reaction conditions.[66] Some members of the family exhibit reversible crystalline-amorphous behavior under mechanical or thermal stress, indicating intrinsic strength superior to that of conventional crystalline materials.[67]
The extension of the ZIF family to triazole and tetrazole ligands has led to the creation of even denser and more resistant frameworks, in which the greater number of nitrogen heteroatoms allows additional coordination bonds and greater electronic polarizability.[68] This results in reduced porosity compared to classic ZIFs, but a substantial improvement in mechanical robustness, tolerance to aggressive solvents and stability under radiation.[69]

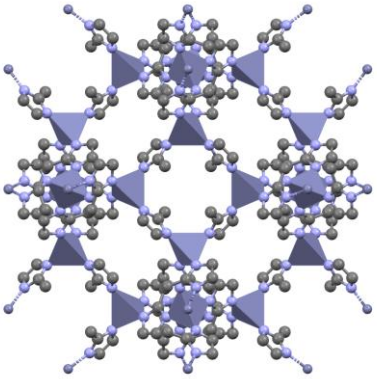

Figure 4: Structure of ZIF-8.

1.2.3 MOF with pyridine ligands

Pyridine ligands, such as 4,4'-bipyridine,[70] 2,2'-bipyridine[71] and terpyridine,[72] represent another important category of organic linkers,

characterized by the presence of nitrogen donor atoms in linear or angulated configurations (Figure 5). These ligands are commonly used with transition metals such as Zn^{2+}, Cu^{2+}, Cd^{2+} and Ru^{2+} to form 1D, 2D and 3D structures, with a remarkable variety of coordination geometries.[73]

Unlike carboxylic ligands, which form relatively strong and directional M–O bonds, the M–N bonds in pyridine systems are generally more labile, giving the materials greater structural flexibility and a tendency to form interpenetrating networks.[74] This can reduce accessible porosity but can enable dynamic behaviors such as topological reconfiguration.[75] Thanks to the weak coordination between the metal and the pyridine nitrogen ion pair, it is possible to easily break and reform coordination bonds, allowing the network to reorganize under thermal, solvent or concentration changes.[76]

The π conjugation present in polypyridine systems contributes to the rigidity of the ligands and the possibility of π–π stacking, conferring optical, electronic and magnetic properties to the lattice.[77] From a structural point of view, however, the crystallinity of these MOFs may be lower than that of previous families and often requires targeted synthetic optimization.[78]

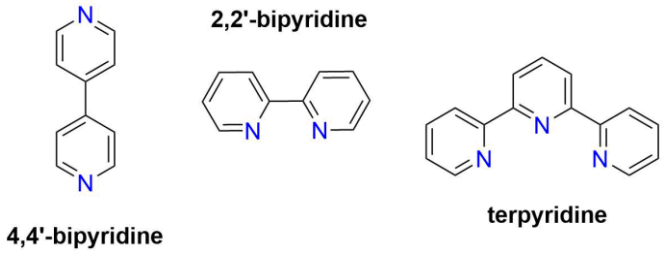

Figure 5: Examples of pyridine linkers used for the synthesis of MOFs.

1.2.4 MOFs with aliphatic ligands

MOFs obtained from aliphatic ligands often exhibit structural behavior that differs from that of their aromatic counterparts.[79] Ligands such as oxalate,[80]

succinate[81] or glutarate[82] allow greater angular flexibility in the M–O bonds, favoring structures with lower symmetries or with a tendency towards lattice distortion. Porosity is often reduced, but structural density is higher, and the possibility of bending allows for conformational adaptation phenomena (Figure 6).[82]

MOFs synthesized from amino acids or natural chiral molecules introduce additional functionalities into the structure, such as the possibility of chiral lattice formation or hydrogen-like interactions between side groups[83]. However, the presence of polar groups or charges can compromise thermal or hydrolytic stability if not adequately protected by multiple coordination or post-synthetic modification.[38]

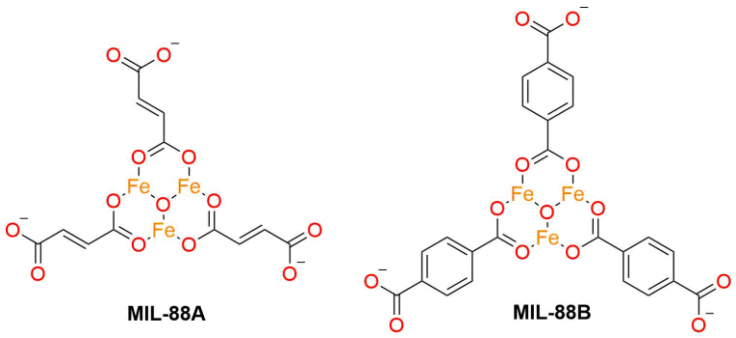

Figure 6: Differences between MIL-88A and MIL-88B secondary building units.

1.2.5 MOFs with extended π-conjugated linkers

MOFs based on extended π-conjugated linkers such as porphyrins, naphthalenes and acenes represent one of the most complex and fascinating classes of MOFs. The planar and rigid ligands allow the formation of very large cavities, often >2 nm, with high symmetries (e.g. cubic, tetragonal) and strong π–π stacking interactions between the layers.[84]

The family of *Porous Coordination Networks* (PCNs) belongs to this category of MOFs, a class of MOFs characterized by the use of extended π-conjugated ligands, often derived from highly planar aromatic molecules such as porphyrins, in combination with highly connected metal nodes.[85] The reticular architecture of PCNs is distinguished by its high crystallographic order, large pore dimensions and extraordinary topological rigidity.[22] These characteristics derive mainly from the use of tetratopic ligands such as *5,10,15,20-tetrakis(4-carboxyphenyl)porphyrin* (TCPP), which, thanks to its planar geometry, allows self-assembly into highly symmetrical three-dimensional lattices.[86]

One of the most representative members of the family is PCN-224 (Figure 7), consisting of $Zr_6O_4(OH)_4$ clusters that act as connecting nodes with 12 coordination bonds, and TCPP porphyrins that occupy the vertices of a highly porous cubic lattice.[87] This lattice has two main types of pores: cubic symmetrical central cavities with a diameter of approximately 2 nm and smaller interconnected channels (approximately 1.5 nm), offering a specific surface area that can exceed 2600 m^2/g.[88] The high symmetry and connectivity of the nodes give the material remarkable thermal stability and chemical resistance, even in moderately acidic or basic aqueous environments.[87]

A distinctive feature of PCN-224 is the presence of porphyrin as an integral part of the reticular structure. This macroaromatic unit allows metal ions to be inserted into its center (such as Fe^{3+}, Mn^{2+}, Cu^{2+}, Gd^{3+}, etc.) without altering the reticular structure, but locally influencing the electronic, magnetic or optical properties of the material. This metallic modularity is possible thanks to the chemical orthogonality between the porphyrin coordination site and the peripheral carboxyl groups used in the formation of the framework.[84]

From a morphological point of view, PCN-224 crystals often show cubic or rhombohedra shapes, with well-defined faces and high crystallinity.[89] The regular distribution of porphyrins in the crystal space confers chemical uniformity and pore accessibility, making PCN-224 one of the few MOFs capable of combining a rigid structure with functional versatility.[90]

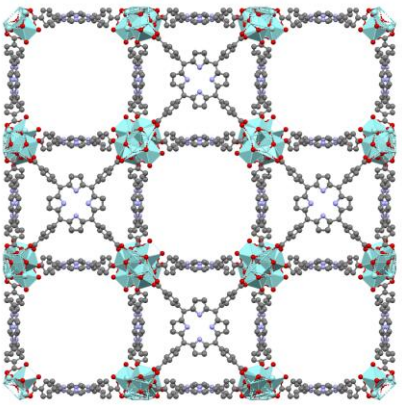

Figure 7: Structure of PCN-224.

1.3 Applications

Over the last twenty years, research into MOFs has expanded rapidly and numerous areas of application have been successfully explored. The most investigated applications can be classified into broad thematic areas: gas capture and storage; molecular separation; catalysis; chemical sensing and biosensing; energy storage and conversion; environmental treatment and water purification; biomedical and pharmaceutical applications. In each of these areas, the unique properties of MOFs enable remarkable performance or new functionalities compared to conventional materials.

1.3.1 Gas capture, storage and separation

One of the most researched areas of application is the selective capture and separation of gases, especially in relation to climate change management and the energy transition.[91] MOFs have an extraordinary ability to adsorb large volumes of gas thanks to their high surface area and the possibility of designing pore sizes and polarities to select specific molecules.[92]

The most significant application in this field is CO_2 capture, both for separation from N_2 in industrial fumes and for separation from H_2 in hydrocarbon reforming (Figure 8).[93] MOFs such as MIL–101(Cr),[94] Mg-MOF-74[95] and UiO-66-NH_2[96] have distinguished themselves for their high CO_2 adsorption capacity and regenerability through temperature or pressure cycles. Binders functionalized with primary or secondary amines improve selective interaction with CO_2 through the formation of carbamates.[97] The design of water-stable MOFs is essential, as the presence of water vapor can compromise the adsorption performance of many porous materials.[98]

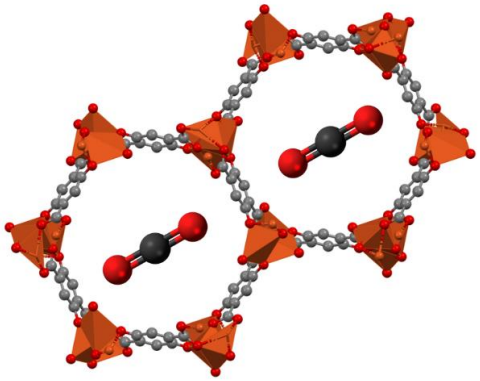

Figure 8: Schematic representation of CO_2 storage inside the pores of a MOF.

In addition to CO_2, MOFs have also been used for reversible hydrogen storage, one of the key challenges in the context of the hydrogen economy.[99] MOFs such as HKUST–1[100] and MOF-5[101] have been investigated for their potential to adsorb H_2 at low temperatures and moderate pressures. The storage capacity depends strongly on the van der Waals interaction between the pore walls and the hydrogen molecule, and research is underway to increase the density of interaction sites through metal doping and structural modifications.[102]

MOFs are also being studied for the separation of industrial gases such as C_2H_2-C_2H_4, as the coordinatively unsaturated sites present in some structures can preferentially bind C_2H_2 over C_2H_4, allowing high-efficiency separations for industrial gas purification.[22]

1.3.2 Catalysis

Catalysis is another key area in the application development of MOFs. Unlike conventional catalysts, MOFs offer a well-defined and uniform distribution of active sites, as well as the possibility of designing chemical microenvironments around the catalytic center.[2] MOFs can act as heterogeneous catalysts, catalytic supports or precursors for nanostructured catalytic materials.[18]

Catalytic MOFs can contain transition metals in the nodes in coordinatively unsaturated positions, which act as activation centers for organic or inorganic substrates.[103] MILs containing Fe(III) or Cr(III), such as MIL-53,[104] MIL-88 and MIL–100 (Scheme 1),[105] have been used for oxidation reactions, such as the degradation of phenols or the transformation of olefins. Cu(II)-based MOFs, such as HKUST–1,[45] effectively catalyze azide-alkyne click reactions and low-temperature oxidations.

An emerging field is photocatalysis, where MOFs act as active materials under UV or visible irradiation to activate redox reactions.[106] Some MOFs

containing π-conjugated ligands or photoredox-active metals (Ti, Zr, Ce) show efficiency in the photodegradation of organic pollutants, in the splitting of water for H_2 production, or in the reduction of CO_2 to value-added products.[107]

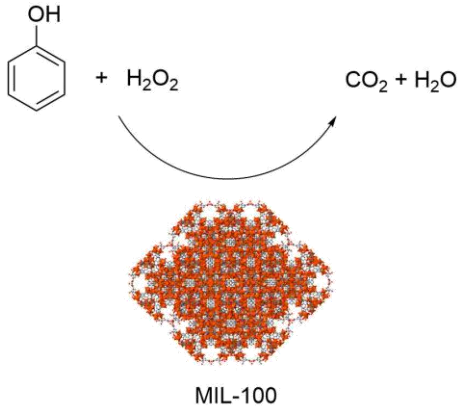

Scheme 1: Oxidation of phenol in the presence of H_2O_2 catalyzed by MIL–100.

1.3.3 Chemical sensing and biosensing

MOFs are particularly suitable as sensing materials due to their porosity, ability to interact selectively with specific analytes, and the possibility of including luminescent or redox-active species.[108] Changes in physical-chemical properties induced by the presence of the analyte are measured as a sensing signal.[109]

Lanthanide-based MOFs exhibit intense light emissions and have been used for the detection of ions, such as Fe^{3+}, Al^{3+} and Ag^{+}, organic solvents, and volatile organic compounds (Figure 9).[110] The sensing mechanism can occur through luminescence quenching, absorption band shifting or changes in the fluorescent lifetime.[109] Other MOFs, such as those containing tetrazole or triazole ligands, are sensitive to small changes in pH or ionic strength,

allowing the detection of altered physiological conditions in the biomedical field.[111]

Biosensing, i.e. the detection of biomolecules, is made possible by the functionalization of MOFs with antibodies, aptamers or enzymes, which confer specificity towards biological analytes. MOFs are thus used for the detection of glucose, DNA, ATP, proteins, pathogenic bacteria and tumor biomarkers.[112]

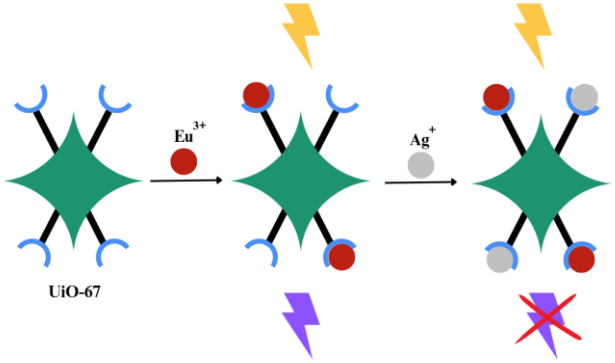

Figure 9: Schematic representation of the luminescence quenching of Eu^{3+} induced by the presence of Ag^{+}.

1.3.4 Energy storage and conversion

The application of MOFs in the energy sector extends to electrochemical storage, such as in batteries and supercapacitors, and to energy conversion, such as in fuel cells and photovoltaic devices.[113]

In lithium batteries, MOFs can act as electrodes, solid electrolytes, or precursors for nanostructured carbonaceous materials (Figure 10).[114] Thanks to their open structure, they promote ion transport and lithium diffusion, increasing specific capacity and cyclic stability.[115] After controlled pyrolysis, some MOFs generate porous structures based on carbon doped with nitrogen or metals, useful as high-performance electrodes.[116] For example, the thermal

treatment of ZIF-8 produces a highly conductive N-doped microporous carbon.[117]

In supercapacitors, MOFs and their derivatives offer high surface area and the possibility of tuning active redox sites. Some conductive MOFs, such as $M_3(HITP)_2$ (M = Ni, Cu), exhibit high electrical conductivity and specific capacitance, offering a promising alternative to conventional carbon-based materials.[118]

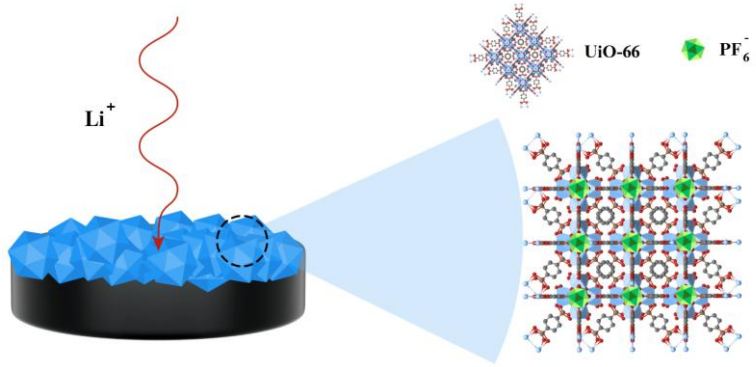

Figure 10: Schematic representation of UiO-66 as electrode front-face on lithium metal anode.

1.3.5 Environmental treatment and water purification

The ability to chemically modify the pores of MOFs makes them effective for environmental applications, including the selective removal of contaminants from water and gas.[119] MOFs are used for the removal of heavy metals (Pb^{2+}, Cd^{2+}, Hg^{2+}),[120] toxic anions (CrO_4^{2-}, AsO_4^{3-}),[121] radionuclides (UO_2^{2+}),[122] organic dyes,[123] pesticides,[124] and residual drugs (Figure 11).[125]

Removal occurs by physical adsorption or through coordination bonding between the contaminant and the functional groups present in the MOF (carboxylates, amines, thiols, phosphonates).[126] Some MOFs, such as UiO-

66[127] and MIL–101,[128] are known for their high stability in water and their ability to sequester a wide range of pollutants. In particular, the presence of structural defects in MOFs can increase the active sites available for adsorption.[129]

MOFs can also act as environmental photocatalysts, capable of degrading organic pollutants under visible light. The combination of photocatalysis and adsorption makes these materials particularly interesting for the treatment of industrial wastewater.[119]

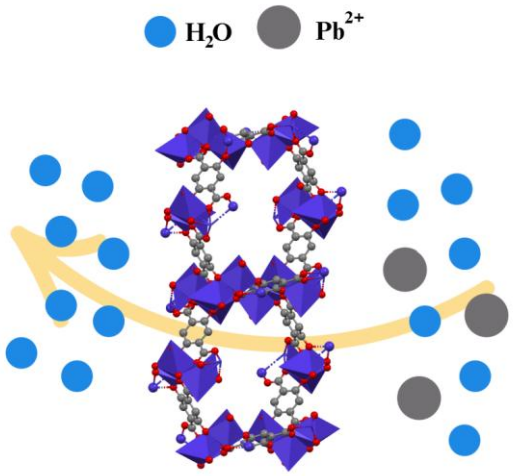

Figure 11: Schematic representation of the use of MOF as a membrane for the removal of Pb^{2+} from wastewater.

1.3.6 Biomedical Applications

MOFs show their most innovative and transformative potential in the biomedical field.[130] The integration of materials chemistry and pharmaceutical sciences has made it possible to explore the use of MOFs as multifunctional platforms capable of revolutionizing traditional therapeutic approaches.[131] However, this transition to biomedical applications requires a few more requirements than other applications, namely greater attention to

biocompatibility, biodegradability, stability in physiological environments, and absence of cytotoxicity.[132]

One of the most promising areas for the use of MOFs in pharmacology is the controlled and targeted delivery of active ingredients.[133] Due to their porosity and the wide variety of possible interactions with the molecules they host, MOFs allow drugs to be encapsulated with high loading efficiency, often superior to traditional materials such as liposomes, micelles, or polymeric nanoparticles.[134] The possibility of designing MOFs with pores suitable for accommodating hydrophilic or hydrophobic drugs broadens their range of applications.[135] In addition, many MOFs have a structure that responds to external stimuli, such as pH,[136] temperature,[137] light,[138] or the presence of specific enzymes.[139] This property allows for targeted and controlled release of the active ingredient. For example, some zinc- or iron-based MOFs selectively decompose in acidic environments such as tumors, releasing the drug only at its destination.[140] This stimulus-responsive approach improves the therapeutic profile of the active ingredient, reduces systemic side effects, and increases treatment efficiency.[141] Among the most studied MOFs for drug delivery are MIL–100(Fe),[136] ZIF-8,[142] and UiO-66,[143] thanks to their stability under physiological conditions and the possibility of being surface-modified to improve their biocompatibility. For example, surface modification with polyethylene glycol (PEG) is often used to improve blood circulation and reduce recognition by the immune system (Figure 12).[144] In addition to functionalization with polymers, specific ligands can be incorporated for active targeting of tumor or infected cells.[145]

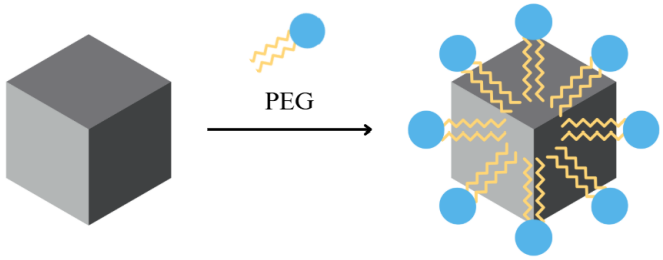

Figure 12: Schematic representation of the surface pegylation of MOF.

MOFs also represent an ideal platform for so-called combination therapy, which consists of integrating multiple therapeutic approaches into a single vehicle.[146] In particular, the ability to simultaneously load chemotherapeutic agents, photosensitizers, and magnetic molecules within the same MOF allows for the synergistic combination of chemotherapy, phototherapy, and magnetic therapy.[147] This approach has proven particularly effective in the treatment of resistant solid tumors. A prime example is MOFs loaded with porphyrins, such as PCN-224, which act both as photosensitizing agents in photodynamic therapy (PDT) and as scaffolds for controlled drug release.[148] In these systems, illumination with light at a specific wavelength generates reactive oxygen species (ROS) in-situ, which damage tumor cells, while the simultaneous release of a chemotherapeutic agent enhances the cytotoxic effect.[149] When combined with magnetic nanoparticles or paramagnetic ions (such as Gd^{3+} or Mn^{2+}), MOFs can also serve as contrast agents for magnetic resonance imaging (MRI), enabling non-invasive treatment monitoring.[150]

The modular nature of MOFs also makes them suitable as advanced diagnostic tools. MOFs containing lanthanides or organic chromophores have optical properties (fluorescence, photoluminescence) that can be exploited for biomarker detection or intracellular tracking.[151] Other MOFs are designed to respond to the presence of specific chemical species (e.g.,

glutathione, ATP, H_2O_2), generating a measurable signal that can be correlated with the pathological state.[152]

The integration of diagnostic and therapeutic functions leads to the concept of "theranostics," in which a single nanomaterial acts as both a diagnostic and therapeutic agent. Theranostic MOFs combine imaging and treatment in a single system, with the potential to optimize dosing, reduce systemic toxicity, and improve therapy monitoring.[153]

In addition to transporting small drugs, MOFs lend themselves to the controlled release of complex biomolecules, including enzymes, peptides, oligonucleotides, and RNA.[154] The confinement of biomolecules in porous environments offers protection from enzymatic degradation and allows for their controlled release in response to specific physiological stimuli.[155] In particular, zinc-based MOFs, such as ZIF-8, have been shown to be effective in transporting DNA and RNA to target cells, thanks to their ability to protect the payload during endocytosis and degrade in the acidic environment of lysosomes.[156]

Enzymes can also be stabilized within the pores of MOFs or bound to the surface, maintaining their catalytic activity under physiological conditions. These hybrid biocatalysts can be used for localized enzyme therapies, where enzyme activity is only required in specific tissue or cell compartments.[157]

One of the main obstacles to the clinical translation of MOFs is the need to ensure safety and tolerability. The biocompatibility of MOFs depends heavily on their chemical composition, morphology, and conditions of administration.[158] MOFs containing non-toxic metals, such as Fe, Zn, and Zr, and toxic ligands at high doses, such as terephthalic acid, are generally well tolerated in vitro and in vivo.[159] However, stability in physiological fluids must be carefully monitored to avoid premature release or persistent accumulation.[160]

Degradability is a critical issue. MOFs that disassemble into metabolizable or physiologically excreted products are considered safer.[161] In this regard, the choice of metal plays a key role: while Zr^{4+}-based MOFs are extremely stable and require structural modifications to increase their biodegradability, those based on Zn^{2+} or Fe^{3+} tend to be more labile in aqueous environments.[162]

The integration of MOFs into commercial pharmaceutical formulations requires overcoming numerous challenges: particle size and distribution control, sterilization, storage stability, synthesis scalability, and regulation.[163] Several studies have focused on the synthesis of MOFs under "green" conditions,[164] using biocompatible solvents such as water or ethanol, moderate temperatures, and scalable methodologies such as spray drying or microfluidics.[165]

Encapsulation in polymer or liposomal matrices is another promising strategy to increase the stability of MOFs and facilitate their integration into conventional pharmaceutical forms.[166] In addition, coating with cell membranes (e.g., erythrocytes, platelets) allows the exploitation of natural targeting and immune evasion mechanisms.[167]

1.4 Drug Delivery

The term *drug delivery* refers to a broad set of technologies, strategies, and devices aimed at the controlled administration of drugs into the human body, with the goal of maximizing therapeutic efficacy and minimizing side effects.[168] Unlike traditional methods of administration, which simply introduce the drug into the body without specific control over how it is transported to the target area, drug delivery systems aim to control the distribution, release kinetics, and selective accumulation of the active ingredient in the target tissues.[169] This increasingly interdisciplinary approach involves chemistry, pharmacology, medicine, materials

engineering, and biotechnology, and is a key element in the transition to more precise, effective, and personalized medicine.[170]

The need for advanced drug delivery strategies arises from well-known limitations of conventional pharmacotherapy. Many active ingredients, despite showing therapeutic potential in vitro, fail in vivo due to problems related to poor bioavailability, rapid metabolic degradation, inefficient absorption, or non-selective systemic distribution.[171] In many cases, drugs reach only a small fraction of the diseased tissue, while the rest of the body is exposed to non-therapeutic but toxic concentrations.[172] This is particularly critical in the treatment of diseases such as cancer, systemic infections, neurological disorders, or chronic inflammatory diseases, where systemic administration can cause serious side effects and collateral damage to healthy tissues.[173]

Furthermore, drug delivery is central to resolving issues related to patient compliance. Innovative modes of administration, such as transdermal patches, smart inhalers, or sustained-release implants, can significantly improve adherence to therapy and reduce the risk of administration errors.[174] This is particularly important in the treatment of chronic or degenerative diseases, where the long-term effectiveness of therapy depends on the consistency and accuracy of treatment.[175]

1.4.1 Types, mechanisms and release

Over the last few decades, numerous platforms for drug delivery have been developed, each with specific advantages and limitations. Among the most relevant are:

- Liposomes:[176] biocompatible lipid vesicles capable of encapsulating hydrophilic or hydrophobic drugs, in some cases already approved for various clinical uses.

- Polymeric nanoparticles:[177] made of biodegradable polymers such as PLGA, they offer high stability, functionalization possibilities and controlled release.
- Dendrimers:[178] branched macromolecules with a modifiable surface, ideal for transporting multiple loads.
- Hydrogels:[179] hydrophilic cross-linked materials that can swell and release drugs in a controlled manner, also suitable as implants.
- Inorganic nanocapsules and nanocarriers:[180] such as metal oxides, mesoporous silica, carbon dots and, more recently, MOFs, which are very promising due to their high porosity and functionalization.

A distinctive feature of drug delivery systems is their ability to control not only where but also when and how a drug is released. The main strategies include:

- Prolonged release:[181] the drug is released slowly over time, reducing the frequency of administration and maintaining stable plasma concentrations.
- Targeted release:[182] the active ingredient is delivered to a specific tissue or cell type, often through binding to surface receptors or the use of carriers with selective affinity.
- Stimulus-responsive release:[183] the system reacts to environmental changes such as pH, temperature, enzyme concentration or the presence of specific molecules to activate drug release.
- Intracellular delivery:[184] some platforms allow penetration into the target cell and release of the drug into specific compartments (e.g. nucleus, mitochondria, lysosomes) (Figure 13).

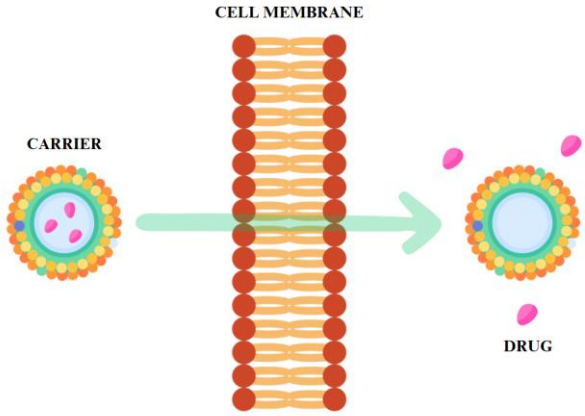

Figure 13: Schematic representation of drug release from the carrier after passing through the cell membrane.

1.5 Magnetic Resonance Imaging

Magnetic resonance imaging (MRI) is one of the most advanced and sophisticated diagnostic techniques available in clinical practice today.[185] Its ability to provide high-resolution images of soft tissues without the use of ionizing radiation makes it an essential tool for the preliminary diagnosis and evaluation of a wide range of conditions, including neurological, musculoskeletal, cardiovascular and oncological disorders.[186] The success of MRI lies in its ability to exploit the magnetic properties of atomic nuclei, particularly those of protons in water molecules, to generate signals that are then converted into three-dimensional images.[187]

The physical principle behind MRI is nuclear magnetic resonance (NMR), a phenomenon observed when nuclei with magnetic moments are subjected to a strong external magnetic field.[188] In the presence of this field, the nuclei align themselves in energetically favorable directions. By applying a radiofrequency wave at a specific frequency, known as the resonance frequency, it is possible to temporarily disrupt this distribution. At the end of the radio pulse, the nuclei release energy and return to their equilibrium

state, a process known as relaxation. The relaxation dynamics can be described by two time constants: T_1 (longitudinal relaxation) and T_2 (transverse relaxation). The differences in the relaxation times of tissues allow images with different contrasts to be obtained from which morphological and functional information can be inferred.[186]

However, in many clinical cases, the tissues have relaxation characteristics that are too similar to be clearly distinguished.[189] This limits the sensitivity and specificity of the technique, especially when detecting small or early-stage lesions. To overcome this limitation, contrast agents are used, substances that can locally modify tissue relaxation times and improve the visibility of certain anatomical structures or pathological processes (Figure 14).[190]

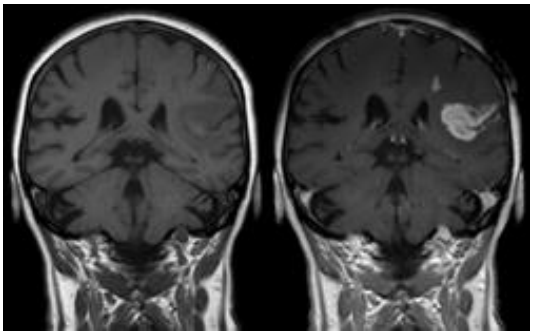

Figure 14: Comparison of MRI images acquired before and after the use of contrast agent.

Contrast agents for MRI are usually composed of paramagnetic agents, capable of interacting with the local magnetic field and accelerating nuclear relaxation processes.[191] The most common of these is Gd^{3+}, a lanthanide with seven unpaired electrons, which makes it highly effective in reducing the T_1 time of nearby protons (Figure 15).[185] To avoid the toxicity of free metal, gadolinium is administered in complex form, i.e. bound to organic chelating molecules, as in the case of Gd-DTPA or Gd-DOTA, which prevent its

dissociation and accumulation in tissues.[192] The diagnostic efficacy of contrast agents is well documented, but their use is not without risks, particularly in patients with renal impairment or a predisposition to adverse reactions.[193] Over the last two decades, the scientific community has focused increasingly on issues related to the safety of these compounds, driving research towards safer and more effective alternatives.[194] The main problem associated with the use of gadolinium-based contrast agents is the possibility that free metal may be released into the body following degradation of the complex. The most well-known and serious risk is the development of nephrogenic systemic fibrosis (NSF), a rare but potentially disabling condition that affects the skin, muscles and internal organs.[195] NSF has been observed mainly in patients with chronic renal failure undergoing gadolinium-based examinations, leading to restrictions on the use of certain linear agents, which are less stable than macrocyclic agents.[196] In addition to NSF, recent studies have highlighted the presence of gadolinium deposits in the brain even in patients with normal kidney function, and further concerns relate to allergic reactions in cancer patients and children, who may undergo numerous follow-up examinations.[197] All these factors have prompted the development of alternative contrast agents, such as contrast media based on Mn^{2+}, Fe^{3+}, or nanoparticles engineered with biocompatible materials.[191]

Current research is strongly focused on creating safer, more effective and selective contrast agents.[198] Among the most promising strategies are functionalization with targeting ligands to increase specificity, and the use of advanced carriers such as nanoparticles,[199] dendrimers,[200] liposomes[201] and MOFs.[202] These systems offer the advantage of greater stability, the possibility of co-incorporating therapeutic agents and fine modulation of magnetic properties.

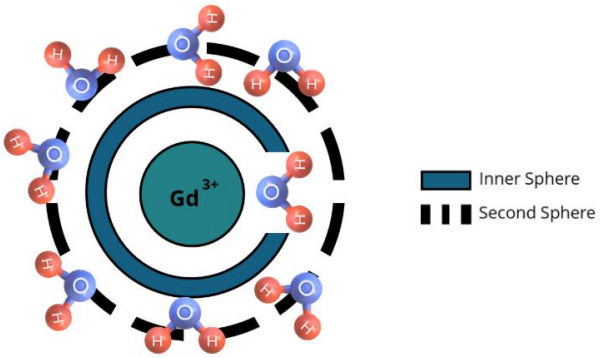

Figure 15: Interaction between water molecules and Gd^{3+}. In the inner sphere, the molecules are directly bound, while in the second sphere the molecules are not bound but very close to the paramagnetic center. Both interactions contribute to the contrast enhancement observed in MRI.

1.6 Bibliography

1. Rowsell, J. L. C.; Yaghi, O. M. Metal–Organic Frameworks: A New Class of Porous Materials. *Microporous Mesoporous Mater.* **2004**, *73* (1–2), 3–14.
2. Furukawa, H.; Cordova, K. E.; O'Keeffe, M.; Yaghi, O. M. The Chemistry and Applications of Metal–Organic Frameworks. *Science* **2013**, *341* (6149), 1230444.
3. Zhou, H.-C.; Long, J. R.; Yaghi, O. M. Introduction to Metal–Organic Frameworks. *Chem. Rev.* **2012**, *112* (2), 673–674.
4. Yaghi, O. M.; O'Keeffe, M.; Ockwig, N. W.; Chae, H. K.; Eddaoudi, M.; Kim, J. Reticular Synthesis and the Design of New Materials. *Nature* **2003**, *423* (6941), 705–714.
5. Férey, G. Hybrid Porous Solids: Past, Present, Future. *Chem. Soc. Rev.* **2008**, *37* (1), 191–214.
6. Hoskins, B. F.; Robson, R. Infinite Polymeric Frameworks Consisting of Three Dimensionally Linked Rod-like Segments. *J. Am. Chem. Soc.* **1989**, *111* (15), 5962–5964.
7. Yaghi, O. M.; Li, G.; Li, H. Selective Binding and Removal of Guests in a Microporous Metal–Organic Framework. *Nature* **1995**, *378* (6558), 703–706.
8. Li, H.; Eddaoudi, M.; O'Keeffe, M.; Yaghi, O. M. Design and Synthesis of an Exceptionally Stable and Highly Porous Metal–Organic Framework. *Nature* **1999**, *402* (6759), 276–279.
9. O'Keeffe, M.; Yaghi, O. M. Deconstructing the Crystal Structures of Metal–Organic Frameworks and Related Materials into Their Underlying Nets. *Chem. Rev.* **2012**, *112* (2), 675–702.
10. Kitagawa, S.; Kitaura, R.; Noro, S.-I. Functional Porous Coordination Polymers. *Angew. Chem. Int. Ed.* **2004**, *43* (18), 2334–2375.

11. Jiao, L.; Seow, J. Y. R.; Skinner, W. S.; Wang, Z. U.; Jiang, H.-L. Metal–Organic Frameworks: Structures and Functional Applications. *Mater. Today* **2019**, *27*, 43–68.
12. Zhao, D.; Timmons, D. J.; Yuan, D.; Zhou, H.-C. Tuning the Topology and Functionality of Metal–Organic Frameworks by Ligand Design. *Acc. Chem. Res.* **2011**, *44* (2), 123–133.
13. Dhakshinamoorthy, A.; Li, Z.; Garcia, H. Catalysis and Photocatalysis by Metal–Organic Frameworks. *Chem. Soc. Rev.* **2018**, *47* (22), 8134–8172.
14. Stock, N.; Biswas, S. Synthesis of Metal–Organic Frameworks (MOFs): Routes to Various MOF Topologies, Morphologies, and Composites. *Chem. Rev.* **2012**, *112* (2), 933–969.
15. Diaz de Grenu, B.; Torres, J.; García-González, J.; Muñoz-Pina, S.; de Los Reyes, R.; Costero, A. M.; Gil, S.; Ros-Lis, J. V. Microwave-Assisted Synthesis of Covalent Organic Frameworks: A Review. *ChemSusChem* **2021**, *14* (1), 208–233.
16. Falcaro, P.; Ricco, R.; Doherty, C. M.; Liang, K.; Hill, A. J.; Styles, M. J. MOF Positioning Technology and Device Fabrication. *Chem. Soc. Rev.* **2014**, *43* (16), 5513–5560.
17. Han, Y.; Yang, H.; Guo, X. Synthesis Methods and Crystallization of MOFs. *Synthesis Methods Crystallization* **2020**, 1–23.
18. Lee, J.; Farha, O. K.; Roberts, J.; Scheidt, K. A.; Nguyen, S. T.; Hupp, J. T. Metal–Organic Framework Materials as Catalysts. *Chem. Soc. Rev.* **2009**, *38* (5), 1450–1459.
19. Ockwig, N. W.; Delgado-Friedrichs, O.; O'Keeffe, M.; Yaghi, O. M. Reticular Chemistry: Occurrence and Taxonomy of Nets and Grammar for the Design of Frameworks. *Acc. Chem. Res.* **2005**, *38* (3), 176–182.
20. Farha, O. K.; Eryazici, I.; Jeong, N. C.; Hauser, B. G.; Wilmer, C. E.; Sarjeant, A. A.; Snurr, R. Q.; Nguyen, S. T.; Yazaydın, A. Ö.; Hupp, J.

T. Metal–Organic Framework Materials with Ultrahigh Surface Areas: Is the Sky the Limit? *J. Am. Chem. Soc.* **2012**, *134* (36), 15016–15021.

21. Kreno, L. E.; Leong, K.; Farha, O. K.; Allendorf, M.; Van Duyne, R. P.; Hupp, J. T. Metal–Organic Framework Materials as Chemical Sensors. *Chem. Rev.* **2012**, *112* (2), 1105–1125.
22. Li, J.-R.; Sculley, J.; Zhou, H.-C. Metal–Organic Frameworks for Separations. *Chem. Rev.* **2012**, *112* (2), 869–932.
23. Schneemann, A.; Bon, V.; Schwedler, I.; Senkovska, I.; Kaskel, S.; Fischer, R. A. Flexible Metal–Organic Frameworks. *Chem. Soc. Rev.* **2014**, *43* (16), 6062–6096.
24. Evans, J. D.; Bocquet, L.; Coudert, F.-X. Origins of Negative Gas Adsorption. *Chem* **2016**, *1* (6), 873–886.
25. Coudert, F.-X.; Fuchs, A. H. Computational Characterization and Prediction of Metal–Organic Framework Properties. *Coord. Chem. Rev.* **2016**, *307*, 211–236.
26. Goodwin, A. L.; Keen, D. A.; Tucker, M. G. Large Negative Linear Compressibility of $Ag_3[Co(CN)_6]$. *Proc. Natl. Acad. Sci. U.S.A.* **2008**, *105* (48), 18708–18713.
27. Hu, Z.; Deibert, B. J.; Li, J. Luminescent Metal–Organic Frameworks for Chemical Sensing and Explosive Detection. *Chem. Soc. Rev.* **2014**, *43* (16), 5815–5840.
28. Horike, S.; Shimomura, S.; Kitagawa, S. Soft Porous Crystals. *Nat. Chem.* **2009**, *1* (9), 695–704.
29. Férey, G.; Serre, C. Large Breathing Effects in Three-Dimensional Porous Hybrid Matter: Facts, Analyses, Rules and Consequences. *Chem. Soc. Rev.* **2009**, *38* (5), 1380–1399.
30. Burtch, N. C.; Jasuja, H.; Walton, K. S. Water Stability and Adsorption in Metal–Organic Frameworks. *Chem. Rev.* **2014**, *114* (20), 10575–10612.

31. Canivet, J.; Fateeva, A.; Guo, Y.; Coasne, B.; Farrusseng, D. Water Adsorption in MOFs: Fundamentals and Applications. *Chem. Soc. Rev.* **2014**, *43* (16), 5594–5617.
32. Kitagawa, S. Metal–Organic Frameworks (MOFs). *Chem. Soc. Rev.* **2014**, *43* (16), 5415–5418.
33. Cohen, S. M. Postsynthetic Methods for the Functionalization of Metal–Organic Frameworks. *Chem. Rev.* **2012**, *112* (2), 970–1000.
34. Han, Z.; Yang, Y.; Rushlow, J.; Huo, J.; Liu, Z.; Hsu, Y.-C.; Yu, J.; Zhou, H.-C. Development of the Design and Synthesis of Metal–Organic Frameworks (MOFs)—From Large Scale Attempts, Functional Oriented Modifications, to Artificial Intelligence (AI) Predictions. *Chem. Soc. Rev.* **2025**, *54* (1), 367–395.
35. Bennett, T. D.; Cheetham, A. K.; Fuchs, A. H.; Coudert, F.-X. Interplay between Defects, Disorder and Flexibility in Metal–Organic Frameworks. *Nat. Chem.* **2017**, *9* (1), 11–16.
36. Tranchemontagne, D. J.; Mendoza-Cortés, J. L.; O'Keeffe, M.; Yaghi, O. M. Secondary Building Units, Nets and Bonding in the Chemistry of Metal–Organic Frameworks. *Chem. Soc. Rev.* **2009**, *38* (5), 1257–1283.
37. Cheetham, A. K.; Rao, C. N. R.; Feller, R. K. Structural Diversity and Chemical Trends in Hybrid Inorganic–Organic Framework Materials. *Chem. Commun.* **2006**, (46), 4780–4795.
38. Cavka, J. H.; Jakobsen, S.; Olsbye, U.; Guillou, N.; Lamberti, C.; Bordiga, S.; Lillerud, K. P. A New Zirconium Inorganic Building Brick Forming Metal–Organic Frameworks with Exceptional Stability. *J. Am. Chem. Soc.* **2008**, *130* (42), 13850–13851.
39. Chui, S. S.-Y.; Lo, S. M.-F.; Charmant, J. P. H.; Orpen, A. G.; Williams, I. D. A Chemically Functionalizable Nanoporous Material $[Cu_3(TMA)_2(H_2O)_3]_n$. *Science* **1999**, *283* (5405), 1148–1150.

40. Eddaoudi, M.; Kim, J.; Rosi, N.; Vodak, D.; Wachter, J.; O'Keeffe, M.; Yaghi, O. M. Systematic Design of Pore Size and Functionality in Isoreticular MOFs and Their Application in Methane Storage. *Science* **2002**, *295* (5554), 469–472.
41. Rosi, N. L.; Eckert, J.; Eddaoudi, M.; Vodak, D. T.; Kim, J.; O'Keeffe, M.; Yaghi, O. M. Hydrogen Storage in Microporous Metal–Organic Frameworks. *Science* **2003**, *300* (5622), 1127–1129.
42. DeCoste, J. B.; Peterson, G. W. Metal–Organic Frameworks for Air Purification of Toxic Chemicals. *Chem. Rev.* **2014**, *114* (11), 5695–5727.
43. Serre, C.; Millange, F.; Thouvenot, C.; Noguès, M.; Marsolier, G.; Louër, D.; Férey, G. Very Large Breathing Effect in the First Nanoporous Chromium(III)-Based Solids: MIL-53 or $CrIII(OH)\cdot\{O_2C–C_6H_4–CO_2\}\cdot\{HO_2C–C_6H_4–CO_2H\}_x\cdot H_2O_\gamma$. *J. Am. Chem. Soc.* **2002**, *124* (45), 13519–13526.
44. Serre, C.; Bourrelly, S.; Vimont, A.; Ramsahye, N. A.; Maurin, G.; Llewellyn, P. L.; Daturi, M.; Filinchuk, Y.; Férey, G. An Explanation for the Very Large Breathing Effect of a Metal–Organic Framework during CO_2 Adsorption. *Adv. Mater.* **2007**, *19* (17), 2246–2251.
45. Wang, Z.; Cohen, S. M. Postsynthetic Modification of Metal–Organic Frameworks. *Chem. Soc. Rev.* **2009**, *38* (5), 1315–1329.
46. Valenzano, L.; Civalleri, B.; Chavan, S.; Bordiga, S.; Nilsen, M. H.; Jakobsen, S.; Lillerud, K. P.; Lamberti, C. Disclosing the Complex Structure of UiO-66 Metal Organic Framework: A Synergic Combination of Experiment and Theory. *Chem. Mater.* **2011**, *23* (7), 1700–1718.
47. Wu, H.; Chua, Y. S.; Krungleviciute, V.; Tyagi, M.; Chen, P.; Yildirim, T.; Zhou, W. Unusual and Highly Tunable Missing-Linker Defects in Zirconium Metal–Organic Framework UiO-66 and Their Important

Effects on Gas Adsorption. *J. Am. Chem. Soc.* **2013**, *135* (28), 10525–10532.

48. Wu, H.; Yildirim, T.; Zhou, W. Exceptional Mechanical Stability of Highly Porous Zirconium Metal–Organic Framework UiO-66 and Its Important Implications. *J. Phys. Chem. Lett.* **2013**, *4* (6), 925–930.
49. Schaate, A.; Roy, P.; Godt, A.; Lippke, J.; Waltz, F.; Wiebcke, M.; Behrens, P. Modulated Synthesis of Zr-Based Metal–Organic Frameworks: From Nano to Single Crystals. *Chem. Eur. J.* **2011**, *17* (24), 6643–6651.
50. Shearer, G. C.; Chavan, S.; Ethiraj, J.; Vitillo, J. G.; Svelle, S.; Olsbye, U.; Lillerud, K. P. Tuned to Perfection: Ironing out the Defects in Metal–Organic Framework UiO-66. *Chem. Mater.* **2014**, *26* (14), 4068–4071.
51. Chavan, S.; Vitillo, J. G.; Gianolio, D.; Zavorotynska, O.; Civalleri, B.; Jakobsen, S.; Bordiga, S. H_2 Storage in Isostructural UiO-67 and UiO-66 MOFs. *Phys. Chem. Chem. Phys.* **2012**, *14* (5), 1614–1626.
52. Trickett, C. A.; Helal, A.; Al-Maythalony, B. A.; Yamani, Z. H.; Cordova, K. E.; Yaghi, O. M. The Chemistry of Metal–Organic Frameworks for CO_2 Capture, Regeneration and Conversion. *Nat. Rev. Mater.* **2017**, *2* (8), 1–16.
53. Liu, N.; Shi, L.; Meng, X. Tuning the Adsorption Properties of UiO-66 via Acetic Acid Modulation. *J. Chem. Sci.* **2019**, *131*, 1–7.
54. Park, K. S.; Ni, Z.; Côté, A. P.; Choi, J. Y.; Huang, R.; Uribe-Romo, F. J.; Yaghi, O. M. Exceptional Chemical and Thermal Stability of Zeolitic Imidazolate Frameworks. *Proc. Natl. Acad. Sci. U.S.A.* **2006**, *103* (27), 10186–10191.
55. Shi, Z.; Tao, Y.; Wu, J.; Zhang, C.; He, H.; Long, L.; Zhang, Y. B. Robust Metal–Triazolate Frameworks for CO_2 Capture from Flue Gas. *J. Am. Chem. Soc.* **2020**, *142* (6), 2750–2754.

56. Zhang, K.; Qiao, Z.; Jiang, J. Molecular Design of Zirconium Tetrazolate Metal–Organic Frameworks for CO_2 Capture. *Cryst. Growth Des.* **2017**, *17* (2), 543–549.
57. Banerjee, R.; Phan, A.; Wang, B.; Knobler, C.; Furukawa, H.; O'Keeffe, M.; Yaghi, O. M. High-Throughput Synthesis of Zeolitic Imidazolate Frameworks and Application to CO_2 Capture. *Science* **2008**, *319* (5865), 939–943.
58. Kouser, S.; Hezam, A.; Khadri, M. N.; Khanum, S. A. A Review on Zeolite Imidazole Frameworks: Synthesis, Properties, and Applications. *J. Porous Mater.* **2022**, *29* (3), 663–681.
59. Nazir, M. A.; Ullah, S.; Shahid, M. U.; Hossain, I.; Najam, T.; Ismail, M. A.; Shah, S. S. A. Zeolitic Imidazolate Frameworks (ZIF-8 & ZIF-67): Synthesis and Application for Wastewater Treatment. *Sep. Purif. Technol.* **2025**, *356*, 129828.
60. Tanaka, S.; Tanaka, Y. A Simple Step toward Enhancing Hydrothermal Stability of ZIF-8. *ACS Omega* **2019**, *4* (22), 19905–19912.
61. Phan, A.; Doonan, C. J.; Uribe-Romo, F. J.; Knobler, C. B.; O'Keeffe, M.; Yaghi, O. M. Synthesis, Structure, and Carbon Dioxide Capture Properties of Zeolitic Imidazolate Frameworks. *Acc. Chem. Res.* **2009**, *43* (1), 58–67.
62. Huang, X. C.; Lin, Y. Y.; Zhang, J. P.; Chen, X. M. Ligand-Directed Strategy for Zeolite-Type Metal–Organic Frameworks: Zinc (II) Imidazolates with Unusual Zeolitic Topologies. *Angew. Chem. Int. Ed.* **2006**, *45* (10), 1557–1559.
63. Caskey, S. R.; Wong-Foy, A. G.; Matzger, A. J. Dramatic Tuning of Carbon Dioxide Uptake via Metal Substitution in a Coordination Polymer with Cylindrical Pores. *J. Am. Chem. Soc.* **2008**, *130* (33), 10870–10871.

64. Xie, L. H.; Xu, M. M.; Liu, X. M.; Zhao, M. J.; Li, J. R. Hydrophobic Metal–Organic Frameworks: Assessment, Construction, and Diverse Applications. *Adv. Sci.* **2020**, *7* (4), 1901758.
65. Coudert, F. X. Responsive Metal–Organic Frameworks and Framework Materials: Under Pressure, Taking the Heat, in the Spotlight, with Friends. *Chem. Mater.* **2015**, *27* (6), 1905–1916.
66. Cravillon, J.; Münzer, S.; Lohmeier, S. J.; Feldhoff, A.; Huber, K.; Wiebcke, M. Rapid Room-Temperature Synthesis and Characterization of Nanocrystals of a Prototypical Zeolitic Imidazolate Framework. *Chem. Mater.* **2009**, *21* (8), 1410–1412.
67. Bennett, T. D.; Cheetham, A. K. Amorphous Metal–Organic Frameworks. *Acc. Chem. Res.* **2014**, *47* (5), 1555–1562.
68. Tan, J. C.; Civalleri, B.; Erba, A.; Albanese, E. Quantum Mechanical Predictions to Elucidate the Anisotropic Elastic Properties of Zeolitic Imidazolate Frameworks: ZIF-4 vs. ZIF-zni. *CrystEngComm* **2015**, *17* (2), 375–382.
69. Mason, J. A.; Veenstra, M.; Long, J. R. Evaluating Metal–Organic Frameworks for Natural Gas Storage. *Chem. Sci.* **2014**, *5* (1), 32–51.
70. Zhang, C.-Y.; Yao, X.-J.; Wang, R.-L.; Xie, C.-Z. Poly[[bis(μ-4,4′-bipyridine-κ²N:N′)copper(I)] Perchlorate 0.24-Hydrate]. *Acta Crystallogr., Sect. E: Struct. Rep. Online* **2012**, *68*(5), m660–m661.
71. Kang, J.; Cha, S.; Ryu, J.; An, B.; Lim, C.; Heo, Y.; Lee, Y.; Kim, J.; Park, J.; Kim, M. Metalations on 2,2′-Bipyridine-Functionalized Metal–Organic Frameworks for Catalytic Platforms. *Bull. Korean Chem. Soc.* **2025**, *46*(3), 231–252.
72. Elahi, S. M.; Raizada, M.; Sahu, P. K.; Konar, S. Terpyridine-Based 3D Metal–Organic Frameworks: A Structure–Property Correlation. *Chem.—Eur. J.* **2021**, *27*(19), 5858–5870.

73. Biradha, K.; Sarkar, M.; Rajput, L. Crystal Engineering of Coordination Polymers Using 4,4′-Bipyridine as a Bond between Transition Metal Atoms. *Chem. Commun.* **2006**, (40), 4169–4179.
74. Ha, H.; Hahm, H.; Jwa, D. G.; Yoo, K.; Park, M. H.; Yoon, M.; Lee, H.; Choi, E.; Kim, M. Flexibility in Metal–Organic Frameworks Derived from Positional and Electronic Effects of Functional Groups. *CrystEngComm* **2017**, *19*(36), 5361–5368.
75. Cao, J.; Ma, W.; Lyu, K.; Zhuang, L.; Cong, H.; Deng, H. Twist and Sliding Dynamics between Interpenetrated Frames in Ti-MOF Revealing High Proton Conductivity. *Chem. Sci.* **2020**, *11*(15), 3978–3985.
76. Xu, M.-M.; Chen, Q.; Xie, L.-H.; Li, J.-R. Exchange Reactions in Metal–Organic Frameworks: New Advances. *Coord. Chem. Rev.* **2020**, *421*, 213421.
77. Laschuk, N. O.; Ebralidze, I. I.; Zenkina, O. V. Polypyridine-Based Architectures for Smart Electrochromic and Energy Storage Materials. *Can. J. Chem.* **2022**, *101*(7), 400–417.
78. Azbell, T. J.; Pitt, T. A.; Jerozal, R. T.; Mandel, R. M.; Milner, P. J. Simplifying the Synthesis of Metal–Organic Frameworks. *Acc. Mater. Res.* **2023**, *4*(10), 867–878.
79. Slyusarchuk, V. D.; Kruger, P. E.; Hawes, C. S. Cyclic Aliphatic Hydrocarbons as Linkers in Metal–Organic Frameworks: New Frontiers for Ligand Design. *ChemPlusChem* **2020**, *85*(5), 845–854.
80. Huskić, I.; Friščić, T. Geomimetic approaches in the design and synthesis of metal-organic frameworks. *Philos. Trans. R. Soc. A* **2019**, *377* (2149), 20180221.
81. Halder, A.; Bhattacharya, B.; Haque, F.; Ghoshal, D. Structural diversity in six mixed ligand Zn(II) metal–organic frameworks

constructed by rigid and flexible dicarboxylates and different N,N′ donor ligands. *Cryst. Growth Des.* **2017**, *17* (12), 6613–6624.

82. Demakov, P. A. Properties of Aliphatic Ligand-Based Metal–Organic Frameworks. *Polymers* **2023**, *15* (13), 2891.
83. Ma, L.; Abney, C.; Lin, W. Enantioselective catalysis with homochiral metal–organic frameworks. *Chem. Soc. Rev.* **2009**, *38* (5), 1248–1256.
84. Allendorf, M. D.; Bauer, C. A.; Bhakta, R. K.; Houk, R. J. T. Luminescent metal–organic frameworks. *Chem. Soc. Rev.* **2009**, *38* (5), 1330–1352.
85. He, Y.; Zhou, W.; Qian, G.; Chen, B. Methane storage in metal–organic frameworks. *Chem. Soc. Rev.* **2014**, *43* (16), 5657–5678.
86. Zhang, X.; Liu, Z.; Shao, B.; Liang, Q.; Wu, T.; Pan, Y.; Huang, J. Porphyrin-Based Metal-Organic Framework Photocatalysts: Structure, Mechanism and Applications. *Small Methods* **2025**, 2402096.
87. Feng, D.; Wang, K.; Wei, Z.; Chen, Y. P.; Simon, C. M.; Arvapally, R. K.; Martin, R. L.; Bosch, M.; Yuan, S.; Zhou, H. C. Kinetically tuned dimensional augmentation as a versatile synthetic route towards robust metal–organic frameworks. *Nat. Commun.* **2014**, *5* (1), 5723.
88. Yuan, S.; Feng, L.; Wang, K.; Pang, J.; Bosch, M.; Lollar, C.; Sun, Y.; Qin, J.; Yang, X.; Zhang, P.; Wang, Q.; Zou, L.; Zhang, Y.; Zhou, H. C. Stable metal–organic frameworks: design, synthesis, and applications. *Adv. Mater.* **2018**, *30* (37), 1704303.
89. Son, H. J.; Jin, S.; Patwardhan, S.; Wezenberg, S. J.; Jeong, N. C.; So, M.; Stoddart, J. F.; Hupp, J. T. Light-harvesting and ultrafast energy migration in porphyrin-based metal–organic frameworks. *J. Am. Chem. Soc.* **2013**, *135* (2), 862–869.
90. Gu, J.; Peng, Y.; Zhou, T.; Ma, J.; Pang, H.; Yamauchi, Y. Porphyrin-based framework materials for energy conversion. *Nano Res. Energy* **2022**, *1*, e9120009.

91. Oschatz, M.; Antonietti, M. A search for selectivity to enable CO2 capture with porous adsorbents. *Energy Environ. Sci.* **2018**, *11* (1), 57–70.
92. Jiang, C.; Wang, X.; Ouyang, Y.; Lu, K.; Jiang, W.; Xu, H.; Sun, D. Recent advances in metal–organic frameworks for gas adsorption/separation. *Nanoscale Adv.* **2022**, *4* (9), 2077–2089.
93. Yu, J.; Xie, L. H.; Li, J. R.; Ma, Y.; Seminario, J. M.; Balbuena, P. B. CO2 capture and separations using MOFs: computational and experimental studies. *Chem. Rev.* **2017**, *117* (14), 9674–9754.
94. Liu, Q.; Ning, L.; Zheng, S.; Tao, M.; Shi, Y.; He, Y. Adsorption of carbon dioxide by MIL-101 (Cr): regeneration conditions and influence of flue gas contaminants. *Sci. Rep.* **2013**, *3* (1), 2916.
95. Yang, D. A.; Cho, H. Y.; Kim, J.; Yang, S. T.; Ahn, W. S. CO2 capture and conversion using Mg-MOF-74 prepared by a sonochemical method. *Energy Environ. Sci.* **2012**, *5* (4), 6465–6473.
96. Kazemi, A.; Moghadaskhou, F.; Pordsari, M. A.; Manteghi, F.; Tadjarodi, A.; Ghaemi, A. Enhanced CO2 capture potential of UiO-66-NH2 synthesized by sonochemical method: experimental findings and performance evaluation. *Sci. Rep.* **2023**, *13* (1), 19891.
97. Hahn, M. W.; Jelic, J.; Berger, E.; Reuter, K.; Jentys, A.; Lercher, J. A. Role of amine functionality for CO2 chemisorption on silica. *J. Phys. Chem. B* **2016**, *120* (8), 1988–1995.
98. Xiao, C.; Tian, J.; Chen, Q.; Hong, M. Water-stable metal–organic frameworks (MOFs): rational construction and carbon dioxide capture. *Chem. Sci.* **2024**, *15* (5), 1570–1610.
99. Suh, M. P.; Park, H. J.; Prasad, T. K.; Lim, D. W. Hydrogen storage in metal–organic frameworks. *Chem. Rev.* **2012**, *112* (2), 782–835.
100. Möller, J.; Möller, A.; Dreisbach, F.; Gläser, R.; Staudt, R. High pressure adsorption of hydrogen, nitrogen, carbon dioxide and

methane on the metal–organic framework HKUST-1. *Microporous Mesoporous Mater.* **2011**, *138* (1-3), 140–148.

101. Zhou, W.; Wu, H.; Hartman, M. R.; Yildirim, T. Hydrogen and methane adsorption in metal–organic frameworks: a high-pressure volumetric study. *J. Phys. Chem. C* **2007**, *111* (44), 16131–16137.
102. Peedikakkal, A. M. P.; Aljundi, I. H. Upgrading the hydrogen storage of MOF-5 by post-synthetic exchange with divalent metal ions. *Appl. Sci.* **2021**, *11* (24), 11687.
103. Kökçam-Demir, Ü.; Goldman, A.; Esrafili, L.; Gharib, M.; Morsali, A.; Weingart, O.; Janiak, C. Coordinatively unsaturated metal sites (open metal sites) in metal–organic frameworks: design and applications. *Chem. Soc. Rev.* **2020**, *49* (9), 2751–2798.
104. Loiseau, T.; Serre, C.; Huguenard, C.; Fink, G.; Taulelle, F.; Henry, M.; Férey, G. A rationale for the large breathing of the porous aluminum terephthalate (MIL-53) upon hydration. *Chem. Eur. J.* **2004**, *10* (6), 1373–1382.
105. Férey, G.; Mellot-Draznieks, C.; Serre, C.; Millange, F.; Dutour, J.; Surblé, S.; Margiolaki, I. A chromium terephthalate-based solid with unusually large pore volumes and surface area. *Science* **2005**, *309* (5743), 2040–2042.
106. Huang, Y. B.; Liang, J.; Wang, X. S.; Cao, R. Multifunctional metal–organic framework catalysts: synergistic catalysis and tandem reactions. *Chem. Soc. Rev.* **2017**, *46* (1), 126–157.
107. Tang, C.; Li, X.; Hu, Y.; Du, X.; Wang, S.; Chen, B.; Wang, S. Porphyrin-based metal-organic framework materials: design, construction, and application in the field of photocatalysis. *Molecules* **2024**, *29* (2), 467.
108. Song, N.; Huai, R.; Zhao, Y.; Yang, L.; Zhang, D.; Zhou, Z. Luminescent metal–organic frameworks as optical sensors for

selective sensing towards Fe3+ and Cu2+. *CrystEngComm* **2024**, *26* (5), 577–593.

109. Hu, M. L.; Razavi, S. A. A.; Piroozzadeh, M.; Morsali, A. Sensing organic analytes by metal–organic frameworks: a new way of considering the topic. *Inorg. Chem. Front.* **2020**, *7* (7), 1598–1632.
110. Su, Y.; Yu, J.; Li, Y.; Phua, S. Z. F.; Liu, G.; Lim, W. Q.; Yang, X.; Yang, S.; Zhang, Y.; Chen, H.; Zhao, Y. Versatile Bimetallic Lanthanide Metal–Organic Frameworks for Tunable Emission and Efficient Fluorescence Sensing. *Commun. Chem.* **2018**, *1*(1), 12.
111. Chi-Durán, I.; Enríquez, J.; Manquian, C.; Wrighton-Araneda, K.; Cañon-Mancisidor, W.; Venegas-Yazigi, D.; Singh, D. P. pH-controlled assembly of 3D and 2D zinc-based metal-organic frameworks with tetrazole ligands. *ACS Omega* **2018**, *3* (1), 801–807.
112. Lv, M.; Zhou, W.; Tavakoli, H.; Bautista, C.; Xia, J.; Wang, Z.; Li, X. Aptamer-functionalized metal-organic frameworks (MOFs) for biosensing. *Biosens. Bioelectron.* **2021**, *176*, 112947.
113. Lu, X. F.; Fang, Y.; Luan, D.; Lou, X. W. D. Metal–organic frameworks derived functional materials for electrochemical energy storage and conversion: a mini review. *Nano Lett.* **2021**, *21* (4), 1555–1565.
114. Liu, Z.; Liu, P.; Tian, L.; Xiao, J.; Cui, R.; Liu, Z. Significantly enhancing the lithium-ion conductivity of solid-state electrolytes via a strategy for fabricating hollow metal–organic frameworks. *Chem. Commun.* **2020**, *56* (93), 14629–14632.
115. Chen, T.; Chen, S.; Chen, Y.; Zhao, M.; Losic, D.; Zhang, S. Metal-organic frameworks containing solid-state electrolytes for lithium metal batteries and beyond. *Mater. Chem. Front.* **2021**, *5* (4), 1771–1794.

116. Xie, X. C.; Huang, K. J.; Wu, X. Metal–organic framework derived hollow materials for electrochemical energy storage. *J. Mater. Chem. A* **2018**, *6* (16), 6754–6771.

117.Tai, Z.; Shi, M.; Chong, S.; Chen, Y.; Shu, C.; Dai, X.; Liu, Y. N-doped ZIF-8-derived carbon (NC-ZIF) as an anodic material for lithium-ion batteries. *J. Alloys Compd.* **2019**, *800*, 1–7.

118. Otun, K. O.; Mukhtar, A.; Nafiu, S. A.; Bello, I. T.; Abdulsalam, J. Incorporation of redox-activity into metal-organic frameworks for enhanced supercapacitors: A review. *J. Energy Storage* **2024**, *84*, 110673.

119. Abonyi, M. N.; Obi, C. C.; Nwabanne, J. T. Degradation of organic pollutants in wastewater using MOF-based catalysts: A review. *Next Mater.* **2025**, *8*, 100696.

120. Ren, Y.; Yang, Y.; Qu, G.; Ning, P.; Ren, N.; Wu, F.; Hu, Y. Study on the mechanism of removing Pb (II) and Cd (II) from industrial wastewater by copper based MOF modified with ethylenediamine. *Fuel Process. Technol.* **2023**, *247*, 107798.

121. Abu Tarboush, B. J.; Chouman, A.; Jonderian, A.; Ahmad, M.; Hmadeh, M.; Al-Ghoul, M. Metal–organic framework-74 for ultratrace arsenic removal from water: experimental and density functional theory studies. *ACS Appl. Nano Mater.* **2018**, *1* (7), 3283–3292.

122. Liu, H.; Fu, T.; Mao, Y. Metal–organic framework-based materials for adsorption and detection of uranium (VI) from aqueous solution. *ACS Omega* **2022**, *7* (17), 14430–14456.

123. Ali, A.; Muslim, M.; Neogi, I.; Afzal, M.; Alarifi, A.; Ahmad, M. Construction of a 3D metal–organic framework and its composite for water remediation via selective adsorption and photocatalytic degradation of hazardous dye. *ACS Omega* **2022**, *7* (28), 24438–24451.

124. Alkhatib, F.; Ibarhiam, S. F.; Alrefaei, A. F.; Alrefaee, S. H.; Pashameah, R.; Habeebullah, T. M.; El-Metwaly, N. M. Efficient Removal of Deltamethrin from Aqueous Solutions Using a Novel Lanthanum Metal–Organic Framework: Adsorption Models and Optimization via Box–Behnken Design. *ACS Omega* **2023**, *8* (35), 32130–32145.

125. Zhang, R.; Wang, Z.; Zhou, Z.; Li, D.; Wang, T.; Su, P.; Yang, Y. Highly effective removal of pharmaceutical compounds from aqueous solution by magnetic Zr-based MOFs composites. *Ind. Eng. Chem. Res.* **2019**, *58* (9), 3876–3884.

126. Yan, C.; Jin, J.; Wang, J.; Zhang, F.; Tian, Y.; Liu, C.; Han, Q. Metal–organic frameworks (MOFs) for the efficient removal of contaminants from water: Underlying mechanisms, recent advances, challenges, and future prospects. *Coord. Chem. Rev.* **2022**, *468*, 214595.

127. Ahmadijokani, F.; Mohammadkhani, R.; Ahmadipouya, S.; Shokrgozar, A.; Rezakazemi, M.; Molavi, H.; Arjmand, M. Superior chemical stability of UiO-66 metal-organic frameworks (MOFs) for selective dye adsorption. *Chem. Eng. J.* **2020**, *399*, 125346.

128. Kuznicki, A.; Lorzing, G. R.; Bloch, E. D. Tuning water adsorption, stability, and phase in Fe-MIL-101 and Fe-MIL-88 analogs with amide functionalization. *Chem. Commun.* **2021**, *57* (67), 8312–8315.

129. Choi, J.; Lin, L. C.; Grossman, J. C. Role of structural defects in the water adsorption properties of MOF-801. *J. Phys. Chem. C* **2018**, *122* (10), 5545–5552.

130. Horcajada, P.; Gref, R.; Baati, T.; Allan, P. K.; Maurin, G.; Couvreur, P.; Férey, G.; Morris, R. E.; Serre, C. Metal–organic frameworks in biomedicine. *Chem. Rev.* **2012**, *112* (2), 1232–1268.

131. Lawson, H. D.; Walton, S. P.; Chan, C. Metal–organic frameworks for drug delivery: a design perspective. *ACS Appl. Mater. Interfaces* **2021**, *13* (6), 7004–7020.

132. Simon-Yarza, T.; Mielcarek, A.; Couvreur, P.; Serre, C. Nanoparticles of metal-organic frameworks: on the road to in vivo efficacy in biomedicine. *Adv. Mater.* **2018**, *30* (37), 1707365.

133. McKinlay, A. C.; Morris, R. E.; Horcajada, P.; Férey, G.; Gref, R.; Couvreur, P.; Serre, C. BioMOFs: metal–organic frameworks for biological and medical applications. *Angew. Chem., Int. Ed.* **2010**, *49* (36), 6260–6266.

134. Horcajada, P.; Serre, C.; Vallet-Regí, M.; Sebban, M.; Taulelle, F.; Férey, G. Metal–organic frameworks as efficient materials for drug delivery. *Angew. Chem., Int. Ed.* **2006**, *45* (36), 5974–5978.

135. Tran, V. A.; Thuan Le, V.; Doan, V. D.; Vo, G. N. Utilization of functionalized metal–organic framework nanoparticle as targeted drug delivery system for cancer therapy. *Pharmaceutics* **2023**, *15* (3), 931.

136. Horcajada, P.; Chalati, T.; Serre, C.; Gillet, B.; Sebrie, C.; Baati, T.; Eubank, J. F.; Heurtaux, D.; Clayette, P.; Kreuz, C.; Chang, J. S.; Hwang, Y. K.; Marsaud, V.; Bories, P. N.; Cynober, L.; Gil, S.; Férey, G.; Couvreur, P.; Gref, R. Porous metal–organic-framework nanoscale carriers as a potential platform for drug delivery and imaging. *Nat. Mater.* **2010**, *9* (2), 172–178.

137. Wang, Y.; Yan, J.; Wen, N.; Xiong, H.; Cai, S.; He, Q.; Qian, Y.; Zhou, J.; Liu, Y. Metal-organic frameworks for stimuli-responsive drug delivery. *Biomaterials* **2020**, *230*, 119619.

138. Dutta, B.; Datta, S.; Mir, M. H. Photoresponsive metal–organic framework materials for advance applications. *Chem. Commun.* **2024**, *60* (69), 9149–9162.

139. Della Rocca, J.; Liu, D.; Lin, W. Nanoscale metal–organic frameworks for biomedical imaging and drug delivery. *Acc. Chem. Res.* **2011**, *44* (10), 957–968.

140. Wang, Q.; Sun, Y.; Li, S.; Zhang, P.; Yao, Q. Synthesis and modification of ZIF-8 and its application in drug delivery and tumor therapy. *RSC Adv.* **2020**, *10* (62), 37600–37620.

141. Liu, J.; Yang, Y.; Zhu, W.; Yi, X.; Dong, Z.; Xu, X.; Liu, Z. Nanoscale metal–organic frameworks for combined photodynamic & radiation therapy in cancer treatment. *Biomaterials* **2016**, *97*, 1–9.

142. Wang, L.; Zheng, M.; Xie, Z. Nanoscale metal–organic frameworks for drug delivery: a conventional platform with new promise. *J. Mater. Chem. B* **2018**, *6* (5), 707–717.

143. Lazaro, I. A.; Haddad, S.; Sacca, S.; Orellana-Tavra, C.; Fairen-Jimenez, D.; Forgan, R. S. Selective surface PEGylation of UiO-66 nanoparticles for enhanced stability, cell uptake, and pH-responsive drug delivery. *Chem* **2017**, *2* (4), 561–578.

144. Suk, J. S.; Xu, Q.; Kim, N.; Hanes, J.; Ensign, L. M. PEGylation as a strategy for improving nanoparticle-based drug and gene delivery. *Adv. Drug Delivery Rev.* **2016**, *99*, 28–51.

145. Tousian, B.; Khosravi, A. R.; Ghasemi, M. H.; Kadkhodaie, M. Biomimetic functionalized metal–organic frameworks as multifunctional agents: paving the way for cancer vaccine advances. *Mater. Today Bio* **2024**, *25*, 101134.

146. Yang, J.; Dai, D.; Zhang, X.; Teng, L.; Ma, L.; Yang, Y. W. Multifunctional metal–organic framework (MOF)-based nanoplatforms for cancer therapy: from single to combination therapy. *Theranostics* **2023**, *13* (1), 295.

147. Chen, Z.; Sun, Y.; Wang, J.; Zhou, X.; Kong, X.; Meng, J.; Zhang, X. Dual-responsive triple-synergistic Fe-MOF for tumor theranostics. *ACS Nano* **2023**, *17* (10), 9003–9013.

148. Wang, Z.; Sun, Q.; Liu, B.; Kuang, Y.; Gulzar, A.; He, F.; Lin, J. Recent advances in porphyrin-based MOFs for cancer therapy and diagnosis therapy. *Coord. Chem. Rev.* **2021**, *439*, 213945.

149. Zhao, Q. G.; Zhou, Y. J.; Cao, D. X.; Tang, A. N.; Kong, D. M. DNA-Functionalized Porphyrinic Metal–Organic Framework-Based Drug Delivery System for Targeted Bimodal Cancer Therapy. *J. Med. Chem.* **2023**, *66* (22), 15370–15379.

150. Mo, G.; Li, X.; Jian, Y.; Xu, W.; Xiao, X.; Chen, A.; Dai, L. Mn (II)-MOF Nanoparticle Conjugated with EOB-PEG as High-Performance Hepatobiliary-Specific MRI Contrast Agent. *Nanoscale* **2025**, *17*, 5743-5754.

151. Wang, X.; Gopalsamy, K.; Clavier, G.; Maurin, G.; Ding, B.; Tissot, A.; Serre, C. Lanthanide MOF-based luminescent sensor arrays for the detection of castration-resistant prostate cancer curing drugs and biomarkers. *Chem. Sci.* **2024**, *15* (17), 6488–6499.

152. Gong, C.; Li, Z.; Liu, G.; Wang, R.; Pu, S. A sensitive fluorescence “turn on” nanosensor for glutathione detection based on Ce-MOF and gold nanoparticles. *Spectrochim. Acta Part A Mol. Biomol. Spectrosc.* **2022**, *265*, 120362.

153. Zhang, H.; Yin, X. B. Mixed-ligand metal–organic frameworks for all-in-one theranostics with controlled drug delivery and enhanced photodynamic therapy. *ACS Appl. Mater. Interfaces* **2022**, *14* (23), 26528–26535.

154. Liu, B.; Jiang, M.; Zhu, D.; Zhang, J.; Wei, G. Metal-organic frameworks functionalized with nucleic acids and amino acids for

structure-and function-specific applications: A tutorial review. *Chem. Eng. J.* **2022**, *428*, 131118.

155. Mishra, N. O.; Quon, A. S.; Nguyen, A.; Papazyan, E. K.; Hao, Y.; Liu, Y. Constructing Physiological Defense Systems against Infectious Disease with Metal–Organic Frameworks: A Review. *ACS Appl. Bio Mater.* **2023**, *6* (8), 3052–3065.
156. Li, Y.; Zhang, K.; Liu, P.; Chen, M.; Zhong, Y.; Ye, Q.; Tang, Z. Encapsulation of plasmid DNA by nanoscale metal–organic frameworks for efficient gene transportation and expression. *Adv. Mater.* **2019**, *31* (29), 1901570.
157. Alvarado-Ramírez, L.; Machorro-García, G.; López-Legarrea, A.; Trejo-Ayala, D.; de Jesús Rostro-Alanis, M.; Sánchez-Sánchez, M.; Parra-Saldívar, R. Metal-organic frameworks for enzyme immobilization and nanozymes: a laccase-focused review. *Biotechnol. Adv.* **2024**, *70*, 108299.
158. Wiśniewska, P.; Haponiuk, J.; Saeb, M. R.; Rabiee, N.; Bencherif, S. A. Mitigating metal-organic framework (MOF) toxicity for biomedical applications. *Chem. Eng. J.* **2023**, *471*, 144400.
159. Li, Z.; He, M.; Wang, Y.; Yang, J.; He, Y.; Chen, X.; Wang, B. Advances in Biocompatible Metal-Organic Frameworks for Biomedical Applications. *Adv. Mater.* **2025**, *37*, 2503946.
160. Taheri, M.; Ashok, D.; Sen, T.; Enge, T. G.; Verma, N. K.; Tricoli, A.; Tsuzuki, T. Stability of ZIF-8 nanopowders in bacterial culture media and its implication for antibacterial properties. *Chem. Eng. J.* **2021**, *413*, 127511.
161. Kumar, P.; Anand, B.; Tsang, Y. F.; Kim, K. H.; Khullar, S.; Wang, B. Regeneration, degradation, and toxicity effect of MOFs: Opportunities and challenges. *Environ. Res.* **2019**, *176*, 108488.

162. Wang, L.; Li, X.; Yang, B.; Xiao, K.; Duan, H.; Zhao, H. The chemical stability of metal-organic frameworks in water treatments: Fundamentals, effect of water matrix and judging methods. *Chem. Eng. J.* **2022**, 450, 138215.

163. Ahmadi, M.; Ayyoubzadeh, S. M.; Ghorbani-Bidkorbeh, F.; Shahhosseini, S.; Dadashzadeh, S.; Asadian, E.; Siavashy, S. An investigation of affecting factors on MOF characteristics for biomedical applications: A systematic review. *Heliyon* **2021**, *7* (4), e06788.

164. Kumar, S.; Jain, S.; Nehra, M.; Dilbaghi, N.; Marrazza, G.; Kim, K. H. Green synthesis of metal–organic frameworks: A state-of-the-art review of potential environmental and medical applications. *Coord. Chem. Rev.* **2020**, *420*, 213407.

165. Chakraborty, D.; Yurdusen, A.; Mouchaham, G.; Nouar, F.; Serre, C. Large-scale production of metal–organic frameworks. *Adv. Funct. Mater.* **2024**, *34* (43), 2309089.

166. Guo, C.; Cheng, F.; Liang, G.; Zhang, S.; Jia, Q.; He, L.; Du, M. Copper-based polymer-metal–organic framework embedded with Ag nanoparticles: Long-acting and intelligent antibacterial activity and accelerated wound healing. *Chem. Eng. J.* **2022**, *435*, 134915.

167. Malankowska, M.; Popkov, A.; DeMartini, M.; Jørgensen, G.; Su, Z.; Pinelo, M. Integrating metal organic frameworks (MOFs) and polyelectrolytes (PEs) in membrane reactors for boosting the activity of immobilized carbonic anhydrase. *Chem. Eng. J.* **2024**, *498*, 155563.

168. Langer, R. Drug delivery and targeting. *Nature* **1998**, *392* (6679), 5–10.

169. Tibbitt, M. W.; Dahlman, J. E.; Langer, R. Emerging frontiers in drug delivery. *J. Am. Chem. Soc.* **2016**, *138* (3), 704–717.

170. Allen, T. M.; Cullis, P. R. Drug Delivery Systems: Entering the Mainstream. *Science* **2004**, *303*(5665), 1818–1822.

171. Torchilin, V. P. Recent Advances with Liposomes as Pharmaceutical Carriers. *Nat. Rev. Drug Discov.* **2005**, *4*(2), 145–160.

172. Peer, D.; Karp, J. M.; Hong, S.; Farokhzad, O. C.; Margalit, R.; Langer, R. Nanocarriers as an Emerging Platform for Cancer Therapy. *Nano-Enabled Medical Applications* **2020**, 61–91.

173. Mitragotri, S.; Lammers, T.; Bae, Y. H.; Schwendeman, S. P.; De Smedt, S. C.; Leroux, J. C.; Park, K. Drug Delivery Research for the Future: Expanding the Nano Horizons and Beyond. *J. Controlled Release* **2017**, *246*, 183–184.

174. Siepmann, J.; Siepmann, F. Mathematical Modeling of Drug Delivery. *Int. J. Pharm.* **2008**, *364*(2), 328–343.

175. Sabaté, E., Ed. *Adherence to Long-Term Therapies: Evidence for Action*; World Health Organization: Geneva, 2003.

176. Akbarzadeh, A.; Rezaei-Sadabady, R.; Davaran, S.; Joo, S. W.; Zarghami, N.; Hanifehpour, Y.; Nejati-Koshki, K. Liposome: Classification, Preparation, and Applications. *Nanoscale Res. Lett.* **2013**, *8*, 102.

177. Makadia, H. K.; Siegel, S. J. Poly Lactic-co-Glycolic Acid (PLGA) as Biodegradable Controlled Drug Delivery Carrier. *Polymers* **2011**, *3*(3), 1377–1397.

178. Gajbhiye, V.; Palanirajan, V. K.; Tekade, R. K.; Jain, N. K. Dendrimers as Therapeutic Agents: A Systematic Review. *J. Pharm. Pharmacol.* **2009**, *61*(8), 989–1003.

179. Caló, E.; Khutoryanskiy, V. V. Biomedical Applications of Hydrogels: A Review of Patents and Commercial Products. *Eur. Polym. J.* **2015**, *65*, 252–267.

180. Slowing, I. I.; Trewyn, B. G.; Giri, S.; Lin, V. Y. Mesoporous Silica Nanoparticles for Drug Delivery and Biosensing Applications. *Adv. Funct. Mater.* **2007**, *17*(8), 1225–1236.

181. Park, K. Controlled Drug Delivery Systems: Past Forward and Future Back. *J. Controlled Release* **2014**, *190*, 3–8.
182. Byrne, J. D.; Betancourt, T.; Brannon-Peppas, L. Active Targeting Schemes for Nanoparticle Systems in Cancer Therapeutics. *Adv. Drug Deliv. Rev.* **2008**, *60*(15), 1615–1626.
183. Mura, S.; Nicolas, J.; Couvreur, P. Stimuli-Responsive Nanocarriers for Drug Delivery. *Nat. Mater.* **2013**, *12*(11), 991–1003.
184. Sahay, G.; Alakhova, D. Y.; Kabanov, A. V. Endocytosis of Nanomedicines. *J. Controlled Release* **2010**, *145*(3), 182–195.
185. Caravan, P.; Ellison, J. J.; McMurry, T. J.; Lauffer, R. B. Gadolinium (III) Chelates as MRI Contrast Agents: Structure, Dynamics, and Applications. *Chem. Rev.* **1999**, *99*(9), 2293–2352.
186. Hussain, S.; Mubeen, I.; Ullah, N.; Shah, S. S. U. D.; Khan, B. A.; Zahoor, M.; Sultan, M. A. Modern Diagnostic Imaging Technique Applications and Risk Factors in the Medical Field: A Review. *BioMed Res. Int.* **2022**, *2022*, 5164970.
187. Brown, R. W.; Cheng, Y. C. N.; Haacke, E. M.; Thompson, M. R.; Venkatesan, R. *Magnetic Resonance Imaging: Physical Principles and Sequence Design*; John Wiley & Sons, 2014.
188. Callaghan, P. T. *Principles of Nuclear Magnetic Resonance Microscopy*; Clarendon Press, 1993.
189. Weissleder, R.; Nahrendorf, M.; Pittet, M. J. Imaging Macrophages with Nanoparticles. *Nat. Mater.* **2014**, *13*(2), 125–138.
190. Caravan, P. Strategies for Increasing the Sensitivity of Gadolinium Based MRI Contrast Agents. *Chem. Soc. Rev.* **2006**, *35*(6), 512–523.
191. Wahsner, J.; Gale, E. M.; Rodríguez-Rodríguez, A.; Caravan, P. Chemistry of MRI Contrast Agents: Current Challenges and New Frontiers. *Chem. Rev.* **2018**, *119*(2), 957–1057.

192. Lauffer, R. B. Paramagnetic Metal Complexes as Water Proton Relaxation Agents for NMR Imaging: Theory and Design. *Chem. Rev.* **1987**, *87*(5), 901–927.

193. Thomsen, H. S.; Marckmann, P.; Logager, V. B. Nephrogenic Systemic Fibrosis (NSF): A Late Adverse Reaction to Some of the Gadolinium Based Contrast Agents. *Cancer Imaging* **2007**, *7*(1), 130.

194. Prince, M. R.; Zhang, H.; Zou, Z.; Staron, R. B.; Brill, P. W. Incidence of Immediate Gadolinium Contrast Media Reactions. *Am. J. Roentgenol.* **2011**, *196*(2), W138–W143.

195. Grobner, T. Gadolinium–A Specific Trigger for the Development of Nephrogenic Fibrosing Dermopathy and Nephrogenic Systemic Fibrosis? *Nephrol. Dial. Transplant.* **2006**, *21*(4), 1104–1108.

196. Kanda, T.; Ishii, K.; Kawaguchi, H.; Kitajima, K.; Takenaka, D. High Signal Intensity in the Dentate Nucleus and Globus Pallidus on Unenhanced T1-Weighted MR Images: Relationship with Increasing Cumulative Dose of a Gadolinium-Based Contrast Material. *Radiology* **2014**, *270*(3), 834–841.

197. McDonald, R. J.; McDonald, J. S.; Kallmes, D. F.; Jentoft, M. E.; Murray, D. L.; Thielen, K. R.; Eckel, L. J. Intracranial Gadolinium Deposition after Contrast-Enhanced MR Imaging. *Radiology* **2015**, *275*(3), 772–782.

198. Lohrke, J.; Berger, M.; Frenzel, T.; Hilger, C. S.; Jost, G.; Panknin, O.; Pietsch, H. Preclinical Profile of Gadoquatrane: A Novel Tetrameric, Macrocyclic High Relaxivity Gadolinium-Based Contrast Agent. *Investig. Radiol.* **2022**, *57*(10), 629–638.

199. Shubayev, V. I.; Pisanic, T. R., II; Jin, S. Magnetic Nanoparticles for Theragnostics. *Adv. Drug Delivery Rev.* **2009**, *61*(6), 467–477.

200. Longmire, M. R.; Ogawa, M.; Choyke, P. L.; Kobayashi, H. Dendrimers as High Relaxivity MR Contrast Agents. *Wiley Interdiscip. Rev. Nanomed. Nanobiotechnol.* **2014**, *6*(2), 155–162.
201. Terreno, E.; Delli Castelli, D.; Cabella, C.; Dastrù, W.; Sanino, A.; Stancanello, J.; Aime, S. Paramagnetic Liposomes as Innovative Contrast Agents for Magnetic Resonance (MR) Molecular Imaging Applications. *Chem. Biodivers.* **2008**, *5*(10), 1901–1912.
202. Liu, Y.; Jiang, T.; Liu, Z. Metal-Organic Frameworks for Bioimaging: Strategies and Challenges. *Nanotheranostics* **2022**, *6*(2), 143.

2. Aim and Outline of the Work

In recent years, Metal-Organic Frameworks (MOFs) have gained an increasingly important role in the field of materials chemistry applied to biomedical sciences, as seen in Chapter 1. Their unique crystalline architecture, characterized by high porosity, an extraordinarily large surface area and remarkable structural versatility, has made these materials the subject of numerous studies aimed at exploring their potential in areas such as controlled drug delivery, diagnostic imaging and targeted delivery of therapeutic agents. These properties, combined with the possibility of targeted molecular engineering, allow MOFs to be adapted to specific physiological contexts, promoting the development of functional platforms for advanced medical applications.

The aim of this work is to study the use of MOFs already widely characterized in the literature as carriers in the biomedical field, with a particular focus on their use for the loading and delivery of drugs not yet explored in association with these materials. The project aims to investigate the dynamics of encapsulation, release and stability, as well as the potential impact of these systems on different cell cultures through in vitro tests. The approach adopted does not focus on structural innovation of the material, but rather on the innovativeness of the therapeutic application, contributing to expanding knowledge on the possible synergies between established MOFs and newly selected bioactive molecules. The following chapters detail the methodologies used for drug loading, material characterization techniques and in vitro tests conducted to evaluate performance in biologically relevant contexts.

In the final part of the work, the focus shifts from drug delivery to a completely different but equally strategic field: wastewater treatment. This

transition aims to highlight the versatility of MOFs, emphasizing their adaptability to environmental as well as biomedical challenges.

Chapter 3: This first chapter, which introduces a series of in-depth studies, is entirely dedicated to ZIF-8, the most studied metal-organic framework in this work. The topics covered form the conceptual basis for understanding the subsequent chapters and represented a starting point for the development of several projects described below. In particular, the optimization of synthesis and loading methods are analyzed, which are fundamental aspects for the use of ZIF-8 as a controlled drug delivery system. Particular attention is paid to the behavior of the material in environments with variable pH: it is precisely its sensitivity to pH that makes ZIF-8 one of the most promising MOFs for drug delivery applications. To this end, sulfathiazole was chosen as the model active ingredient, an antibacterial potentially useful for the treatment of ruminal acidosis, a condition that affects dairy cows, causing metabolic alterations and reduced productivity.

Chapter 4: This second chapter continues the analysis of the potential of ZIF-8 as a drug delivery system, focusing on the field of oncology. In particular, two distinct projects are presented, each characterized by a different loading strategy and a different active ingredient: lidocaine, a local anesthetic sometimes used for cancer pain management and a series of non-steroidal anti-inflammatory drugs (NSAIDs), known for their ability to suppress COX-2 overexpression. The materials obtained were subjected to biological tests on different tumor cell lines, with the aim of evaluating the loading efficiency, stability, controlled release of the active ingredients and their efficacy in vitro. The methods developed in each project differ significantly in terms of approach and operating conditions, confirming the versatility of ZIF-8 and its ability to adapt to molecules of different chemical and physical natures and to heterogeneous therapeutic targets.

Chapter 5: This chapter is dedicated to the study of a structural modification of ZIF-8, aimed at improving its biocompatibility and exploring new application potential in the field of drug delivery. In particular, the partial replacement of Zn^{2+} with Mg^{2+}, a trace element known for its greater biological tolerability, especially in prolonged administration scenarios, was investigated. The replacement with Mg^{2+} not only maintained the crystalline structure of the material but also significantly modified its response in environments with different pH values, making it less susceptible to acid degradation. This unexpected behavior opens up new prospects for the use of ZIF-8 in therapeutic areas where stability in weakly acidic environments is an essential requirement, thus expanding the range of possible applications of this MOF as a drug carrier.

Chapter 6: Moving away from drug delivery but remaining in the biomedical field, this chapter presents a study on PCN-224, a porphyrin-based metal-organic framework used as a platform for the development of new contrast agents for magnetic resonance imaging. The work focused on the possibility of loading the material with paramagnetic Gd^{3+} and Mn^{2+} ions, exploiting the coordinating nature of the porphyrin core and the highly porous structure of the framework. The two metals were incorporated separately, obtaining distinct materials that were then characterized from a chemical-physical point of view and tested in vitro to evaluate their performance in a biological environment. The main objective was to explore the effectiveness of modified PCN-224 as an alternative contrast agent, with potential superiority over commercial compounds not in terms of relaxivity but in terms of stability, thanks to the strong coordination of porphyrin, which in turn is found within a more complex system. The approach adopted aims to combine the high loading capacity of MOF with the biocompatibility and safety of the selected ions, laying the foundations for the development of more efficient and less toxic diagnostic tools for the body.

Chapter 7: The last chapter moves away from the strictly biomedical field to explore the potential of ZIF-8 and PCN-224 in an environmental context, with particular reference to wastewater treatment. The ability of these materials to host molecules or ions within their porous structure has been exploited here for selective adsorption purposes. In the case of ZIF-8, the focus was on the removal of linuron, a widely used but highly persistent and toxic herbicide, with the aim not only of purifying water but also demonstrate the recyclability of the material. These studies demonstrate the functional versatility of the MOFs covered by the thesis, confirming their effectiveness in environmental applications of growing interest. The investigations conducted have made it possible to evaluate the adsorption capacity, selectivity and regenerability of the materials, paving the way for future developments in the field of sustainable industrial water treatment.

3. From Foundations to Frontiers: The Central Role of ZIF-8

This chapter is based on the publication:

di Nicola, N., Paolucci, V., Daniele, V., Taglieri, G., Crucianelli, M., Guidoni, L., & Lazzarini, A. (2024). ZIF-8 as Potential Vector for Enhanced Target Delivery of Sulfathiazole for the Treatment of Bovine Ruminal Acidosis. European Journal of Inorganic Chemistry, 27(36), e202400504.

Among the tens of thousands of MOFs isolated and characterized to date, the most interesting structure and the one best suited for biomedical applications is ZIF-8. There are several characteristics that make ZIF-8 the most investigated in this field, but the most important are undoubtedly its biocompatible chemical composition, its sensitivity to pH and its porosity, which allows it to trap molecules of different sizes. ZIF-8 is made up of Zn^{2+} ions, a metal essential for the human body, and 2-methylimidazole, an organic linker that only becomes toxic at high concentrations. At neutral or basic pH, this MOF is particularly stable, but even a small shift towards more acidic pH is enough to degrade or destroy the framework, due to the re-protonation of 2-methylimidazole and the consequent breakdown of the bond with Zn^{2+}. This sensitivity is the driving force for the controlled release of an active ingredient in the target area of the body, which has a lower pH than the physiological pH.

3.1 Synthesis and loading: overview

ZIF-8 was first synthesized in 2006 and since then numerous synthetic routes have been developed and optimized, both for single crystals and powders.[1] Since the project is biomedical in nature, the focus has been on biocompatible synthesis without the use of toxic and difficult-to-remove solvents such as DMF. The synthesis reaction setup also allows the size of the final crystals to be modulated, which is a fundamental parameter when considering drug delivery. In fact, the size of a hypothetical carrier that must pass through the bloodstream must not be less than 7 nm,[2] to avoid being easily excreted by the kidneys, and greater than 200 nm,[3] to avoid potential problems of intravenous accumulation. ZIF-8 is very versatile in this respect, as the average particle size is between 100 and 150 nm, but synthetic routes have also been reported for obtaining crystals approximately 1 mm[4] and 45 nm[5] in size.

When we talk about loading of an active ingredient, it means the physical trapping of the molecule in question inside the pores of ZIF-8. This is possible thanks to the structural flexibility that brings the pore opening size from 3.4 Å to approximately 4.2 Å, allowing the molecule to be housed in the main cavity, which has a diameter of 11.6 Å.[6] The interactions between the drug, which can be seen as the guest, and ZIF-8, the host, are diverse and depend heavily on the nature of the active ingredient itself.[7] The presence of electron-donating groups, for example, allows coordination interactions with Zn^{2+}, while the presence of aromatic rings leads to π–π stacking interactions with 2-methylimidazole. If lipophilic portions are present in the active ingredient, these interact with the hydrophobic inner walls of the pore and, in general, all active compounds benefit from a favorable entropic/enthalpic factor due to the lower mobility of the confined molecule.[8] The interactions therefore allow the drug to remain stably confined within the ZIF-8, but what allows the latter to efficiently trap the active ingredient is the loading method.

An active ingredient can be loaded into ZIF-8 mainly through two approaches: in-situ encapsulation during material synthesis,[9] or post-synthesis techniques such as adsorption or impregnation.[10] In both cases, the choice of solvent plays a fundamental role, as it significantly influences the loading efficiency.[11]

From a chemical-physical point of view, the solubility of the active ingredient in the selected solvent is a critical parameter: if the drug is insoluble or poorly soluble, the amount actually available to penetrate the pores of ZIF-8 is limited, compromising the efficiency of the process. Conversely, too high solubility can promote interaction of the active ingredient with the solvent rather than with the porous matrix, reducing adsorption capacity and hindering retention within the framework. Furthermore, the solvent must be compatible with the MOF structure, avoiding decomposition or pore opening, phenomena that can occur in the presence of overly polar or acidic media. In general, a balance must be found between the solvent's ability to solubilize the active ingredient and its affinity with the MOF structure: for example, the use of moderately polar organic solvents, such as ethanol or acetonitrile, is often preferred to ensure good diffusion of the drug within the ZIF-8 channels while maintaining its crystalline integrity.

3.2 Subacute Ruminal Acidosis

Subacute ruminal acidosis (SARA) is a metabolic disorder that affects dairy cows and is associated with reduced milk production, diarrhea, milk fat depression, liver abscesses and laminitis.[12] The negative effects of SARA are very costly and can compromise animal health, especially for high producing dairy cows.[13] One of the main causes of this disease is the uncontrolled proliferation of lactic acid producing bacteria, such as Streptoccoccus Bovis and Lactobacillus Ruminis. The physiological pH of the rumen is about 6.4; however, in affected animals, the pH can drop to values close to 5, causing

lesions to the gastrointestinal lining followed by localized or systemic inflammation.[14] This pH range makes ZIF-8 ideal for targeted delivery as the pH drops. The aim of this work is therefore to establish a preliminary methodology for the loading and delivery of sulfathiazole, a broad-spectrum antibacterial drug already used for the treatment of SARA, into ZIF-8 via different loading methods. The procedure for synthesizing ZIF-8 was optimized from a method found in the literature and the resulting material was then thoroughly characterized.[15] Stability tests of the starting material were conducted to check its stability when exposed to different aqueous solutions with different pH. Subsequently, different procedures are available to encapsulate active ingredients within the cavity of a generic MOF.[16] In the case of this first work, four different methods were tested and compared, i.e. one-pot, stirring, drop-by-drop and sonication, in order to identify the most efficient way of preparing the sulphatiazole@ZIF-8 system. The release of the active ingredient was carried out under the same conditions as for the stability tests. Therefore, the sulfathiazole@ZIF-8 system could be an ideal system for time- and pH-controlled release for the treatment of subacute ruminal acidosis, given the pH range in which MOF resists or yields to acid/neutral pH.

3.2.1 Results and Discussion

Before proceeding with an in-depth study of the different methods of loading sulfathiazole into the MOF cavities, a brief optimization of the ZIF-8 synthesis was carried out. This preliminary step was necessary to reduce both the reaction time and the amount of 2-methylimidazole (Hmim) used, but above all to understand whether it was possible to scale up the synthesis to higher quantities while maintaining the quality of the material unchanged.

Although numerous protocols for the synthesis of ZIF-8 in aqueous solvents, even at room temperature, have already been reported in the literature, these methods often require rather long reaction times or a considerable excess of organic ligand to ensure good yield and crystallinity of the final product.[15] Furthermore, reproducibility on a larger scale is not always guaranteed, and optimal conditions can vary significantly depending on the method used. In light of this, it was considered useful to proceed with a systematic evaluation of the synthetic conditions in order to develop a rapid, economical, reproducible and scalable protocol, suitable for use in controlled drug delivery systems. As shown in Table 1, the synthesis of ZIF-8 is generally highly reproducible, even when the synthetic parameters considered vary. A particularly interesting aspect that emerged from this optimization phase concerns the influence of the ratio between zinc and the organic ligand Hmim on the final morphology of the material. In particular, by modifying the Zn:Hmim ratio (Entry 2, Table 1), significant variations in the shape and size of the particles obtained were observed. Using a Zn:Hmim ratio of 1:60, the resulting material consists of spherical and regular particles with an average diameter of approximately 150 nm, as shown in Figure 1. Conversely, by adopting a lower ratio of 1:10, the particles obtained appear significantly larger and with irregular morphologies (Figure 2), which could compromise their applicability in drug delivery, where size and uniformity play a crucial role. Therefore, for subsequent optimizations, it was decided to keep the original Zn:Hmim ratio (1:60) unchanged and to act exclusively on the reaction time variable, in order to reduce the duration of the process without altering the desired morphological characteristics. The data reported in Table 1 (Entries 3 and 4) show that reducing the reaction time does not compromise the crystalline structure of the materials obtained in any way.

Table 1. Optimization of ZIF-8 synthetic parameters.

Entry	$Zn(NO_3)_2$ $6H_2O$ (g)	Hmim (g)	H_2O (mL)	Zn/Hmim/H_2O (mol ratio)	t (h)	Yield (%)
1	0,372	6,15	50	1: 60 :2228	24	97
2	0,372	1,067	50	1: 10 :2228	24	96
3	0,372	6,15	50	1: 60 :2228	12	97
4	0,372	6,15	50	1: 60 :2228	2	94
5	1,488	24,6	200	1: 60 :2228	2	95

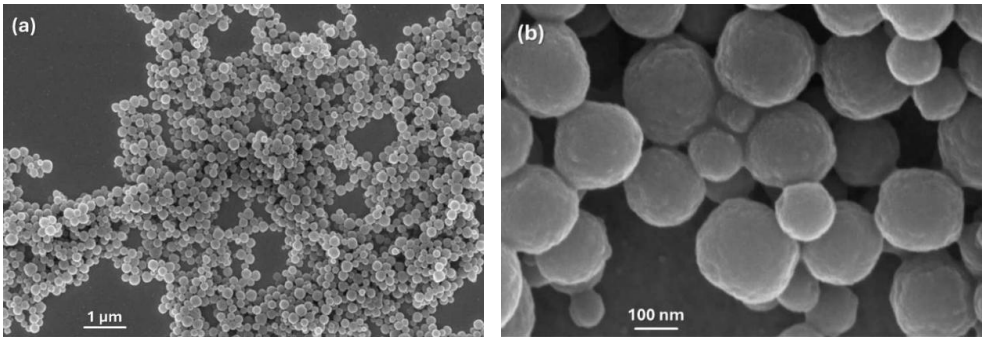

Figure 1. SEM images collected at 10 kX (a) and 100 kX (b) of ZIF-8 sample prepared according to Entry 1 in Table 1.

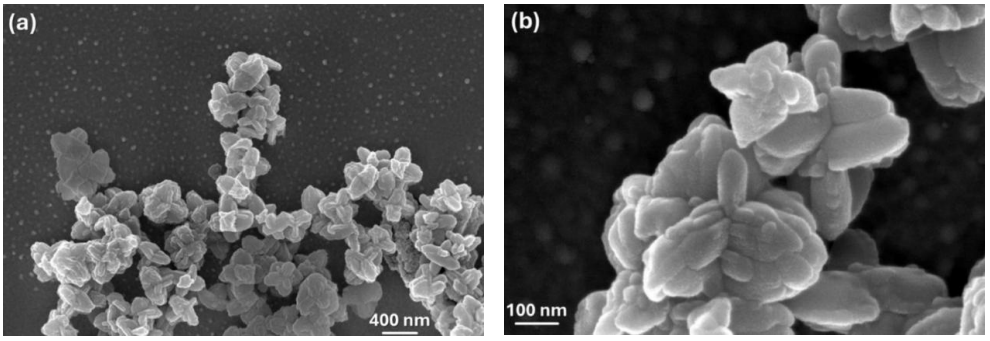

Figure 2. SEM images collected at 20 kX (a) and 100 kX (b) of ZIF-8 sample prepared according to Entry 2 in Table 1.

This observation is confirmed by the perfect overlap of the X-ray diffraction (XRPD) patterns, all of which are superimposable on that characteristic of ZIF-8 (Figure 3).[17] Furthermore, the decrease in reaction time did not produce any changes in either the synthesis yield or the crystal size, thus confirming the remarkable robustness of the synthetic protocol adopted. Subsequently, the optimized synthesis was scaled up to 2 hours with the aim of reducing the number of experimental cycles required for the production of the MOF material (Entry 5, Table 1). The XRPD analyses and SEM images obtained confirm the full reproducibility of the material even on a larger scale, demonstrating that the synthesis protocol is easily adaptable to large-scale production without loss of structural or morphological quality. In order to verify the chemical reproducibility of the synthesized samples (Entries 1–5), attenuated reflection infrared spectroscopy (ATR-MIR) was also performed. The results, shown in Figure 4, show consistent spectra, further confirming the reproducibility of the synthesis. Once the crystalline and chemical reproducibility of the materials had been confirmed, the specific surface area of the sample obtained on a larger scale was determined (Entry 5, Table 1) by nitrogen adsorption measurements at 77 K. The adsorption isotherm is shown in Figure 11 and exhibits behavior typical of microporous materials. The specific surface area measured for the sample is 1610 m^2/g, perfectly in line with those reported in the literature for ZIF-8, confirming the correct formation of the porous structure.[5]

To evaluate the stoichiometric composition of the synthesized material and verify its consistency with the theoretical formula, a thermogravimetric analysis (TGA) was performed, the results of which are shown in Figure 5. The theoretical stoichiometry of ZIF-8 is $Zn^{2+}(mim^-)_2$, with a molecular weight of 227.6 g/mol, which implies that approximately 29% by weight of the material should consist of Zn^{2+} ions.[18] The TGA analysis also confirms the excellent thermal stability of the material: in fact, thermal degradation of the

framework only occurs at temperatures above 350°C. After complete decomposition of the organic ligand (methylimidazolate, mim^-), a weight loss of approximately 64% by weight is observed, leaving a residue of 36% by weight of ZnO. Considering the ratio between the molecular weights of Zn and ZnO, this corresponds to a zinc content of 28.9% by weight, which is in excellent agreement with the expected theoretical stoichiometry. However, the slight discrepancy between the theoretical value (29.0%) and the experimental value (28.9%) could be attributed to the presence of a small amount of "missing cluster" defects, i.e. gaps in the crystal structure where portions of the framework are missing. These defects, although difficult to detect by X-ray diffraction, could justify this minimal deviation.[19] These considerations confirm the high quality of the synthesized material and lay a solid foundation for the subsequent loading of the active ingredient into the MOF.

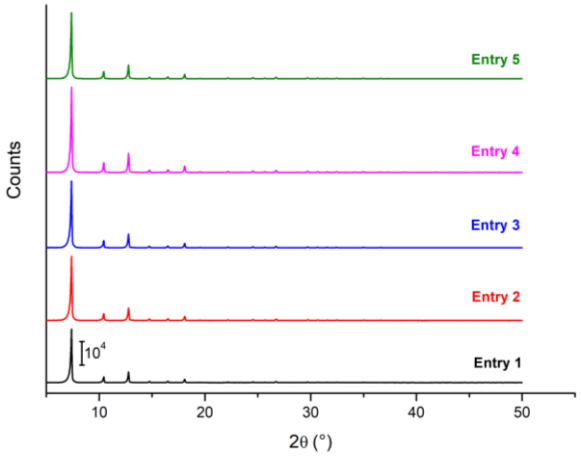

Figure 3. XRPD patterns of the different synthesis of ZIF-8 MOF (Entries 1–5 are referred to Table 1).

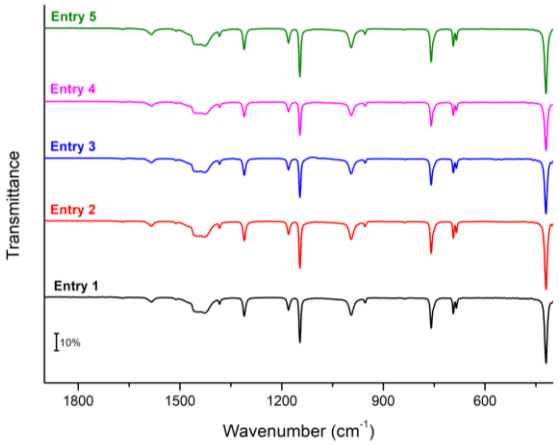

Figure 4. ATR-MIR spectra of the different synthesis of ZIF-8 MOF (Entries 1-5 are referred to Table 1).

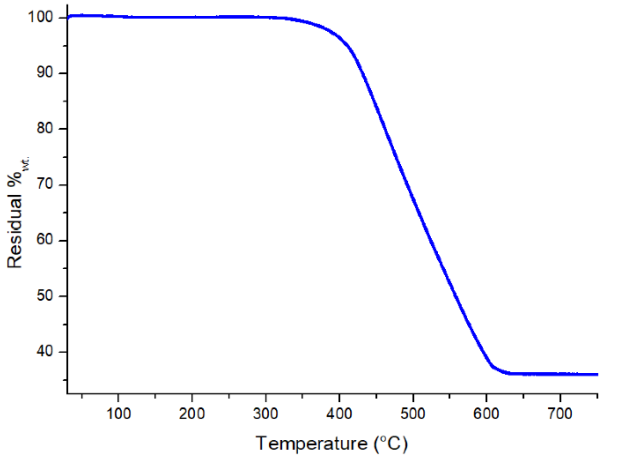

Figure 5. TGA profile of ZIF-8 sample identified as Entry 5 in Table 1.

To identify the most effective procedure for loading the active ingredient into the crystalline framework of ZIF-8, several approaches described in the literature were tested, keeping the weight ratio between the metal-organic framework (MOF) and the drug constant. This allowed the different methods to be compared objectively and under the same experimental conditions. The amount of sulfathiazole actually incorporated into the MOF structure was

determined by UV-Visible spectroscopy, using Lambert-Beer's law. Specifically, the variation in the intensity of the maximum absorption peak of sulfathiazole at 288 nm was measured, comparing the initial solution containing the active ingredient with those obtained after the synthesis and washing phases (Figure 6). This approach allows the fraction of drug not incorporated to be quantified indirectly and, therefore, the effective loading value in the MOF to be obtained by difference.

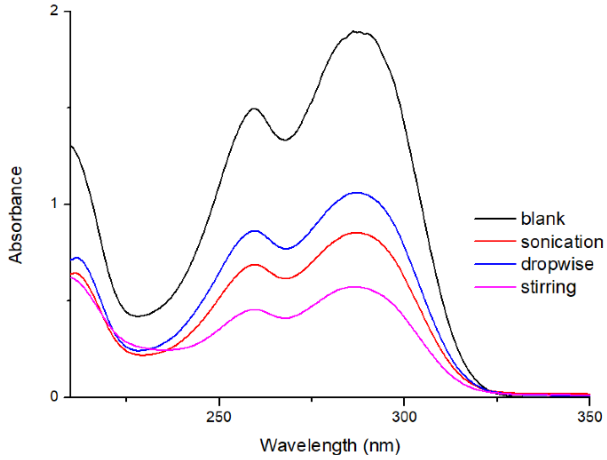

Figure 6. V-Vis spectra of blank sulfathiazole and loading washing solutions.

It is important to note that, among the various loading techniques, the so-called “one-pot” method was also considered, i.e. in-situ growth of the ZIF-8 crystal structure in the direct presence of the drug. In theory, this strategy should allow the simultaneous encapsulation of the active ingredient during the formation of the lattice. However, in our case, this approach did not lead to the formation of the desired crystalline material. On the contrary, the precipitation of a gelatinous, amorphous and unstable substance was observed, probably due to an undesirable interaction between the Zn^{2+} ion and the amino groups present in the sulfathiazole molecule. Since the MOF structure has not yet developed at this early stage, it is plausible that the

metal ion interacts preferentially with the active ingredient, forming complex inorganic salts that prevent the subsequent orderly growth of the ZIF-8 structure. In light of this, the one-pot method was excluded from subsequent comparative analyses as it was not suitable for the system under investigation.

Among the other methods considered, analysis of the UV-Vis data of the post-synthesis residual solutions showed that the mechanical stirring method is the most effective for this type of system, achieving a loading value of 71% in methanol. This result suggests that prolonged exposure of the MOF to the active ingredient under constant stirring conditions promotes more effective interaction between the porosity of the structure and the drug molecules. In comparison, the gradual addition of sulfathiazole in suspension (dropwise) leads to a loading of 46%, while the sonication-based method (use of ultrasound to facilitate drug diffusion into the pores) allows for an intermediate loading of 56%. It is possible that the mechanical forces associated with agitation, in addition to ensuring good dispersion, prevent the formation of aggregates and facilitate the diffusion of the drug into the porous matrix of the MOF.

Once the agitation method (Sulf 1 in Table 2) was identified as the most promising, further optimization was carried out to refine the synthesis conditions. The different samples obtained were characterized by XRPD and ATR-MIR spectroscopy, with the aim of verifying the crystallinity of the material and the presence of the active ingredient in the structure. In a first optimization test, an attempt was made to reduce the amount of drug used to the stoichiometric value with respect to the MOF (Sulf 2 vs Sulf 1). However, the results clearly indicate that, when operating with an excess of sulfathiazole, the final loading of the drug in the MOF is significantly higher. This suggests that encapsulation is partly driven by a dynamic equilibrium between drug diffusion into the matrix and its retention in the pores.

Another important aspect considered is the nature of the solvent used. Although effective, the use of methanol is not always desirable in view of the potential use of the material in the biomedical field. To address this issue, an alternative test was conducted using a 1:1 mixture of MeOH/H_2O, chosen based on the poor solubility of sulfathiazole in pure water. Under these conditions (Sulf 3), a moderate loading of the active ingredient is still observed, although lower than in the preparation in methanol alone (Sulf 1), suggesting that the presence of water may partially limit the availability of the drug or interfere with its diffusion into the pores.

In previous work,[20] the loading process was carried out at temperatures slightly above room temperature (approximately 40 °C) in the hope of facilitating molecular diffusion. Following this recommendation, the stirring method was repeated at 40 °C (Sulf 4), but the loading obtained did not differ significantly from that obtained at room temperature (Sulf 1). However, the different mode of interaction between the drug and the MOF was highlighted by subsequent analyses. The XRPD data (Figure 7) show that the Sulf 4 sample, prepared at 40 °C without a preliminary activation phase, has a diffraction pattern similar to that of pure ZIF-8. In contrast, the Sulf 1 sample shows signals attributable to both the ZIF-8 lattice and the crystalline phase II of sulfathiazole.[21] This indicates that, in the case of Sulf 1, part of the drug is not completely incorporated into the MOF matrix but is probably deposited outside in crystalline form.

Table 2. Optimization of Sulfathiazole loading inside ZIF-8 matrix using the stirring method.

Sample	ZIF-8/Sulfathiazole ratio	T (°C)	Solvent	Loading (%$_{DEE}$)[a]
Sulf 1	2:3	r.t.	MeOH	71
Sulf 2	1:1	r.t.	MeOH	60
Sulf 3	2:3	r.t.	MeOH/H_2O (1:1)	58
Sulf 4	2:3	40	MeOH	72

(a) (%DEE)=percentage of Drug Entrapment Efficiency.

The ATR-MIR spectra of the two samples also confirm these observations (Figure 8). The Sulf 1 sample shows the simultaneous presence of the characteristic bands of MOF and those of sulfathiazole, while Sulf 4 has a spectrum very similar to that of pure ZIF-8, with the exception of a weak doublet associated with the symmetric and antisymmetric vibrations of the O=S=O group of sulfathiazole (dotted box). The almost total absence of drug signals may seem contradictory, but it is known in the literature that the encapsulation of biologically active molecules within nanometric pores causes a significant attenuation of the IR signals of the host species,[22] due to vibrational isolation and reduced rotational and translational freedom.

Further confirmation comes from images obtained by scanning electron microscopy (SEM): in sample Sulf 1 (Figure 9a), ZIF-8 crystals immersed in an amorphous matrix attributable to free sulfathiazole are observed, while in sample Sulf 4 (Figure 9b), no external traces of the drug are visible, suggesting a more effective and complete incorporation. This finding is consistent with the sulfur content mapping performed using EDX spectroscopy (Figure 10), which shows a homogeneous distribution of the active ingredient within the material.

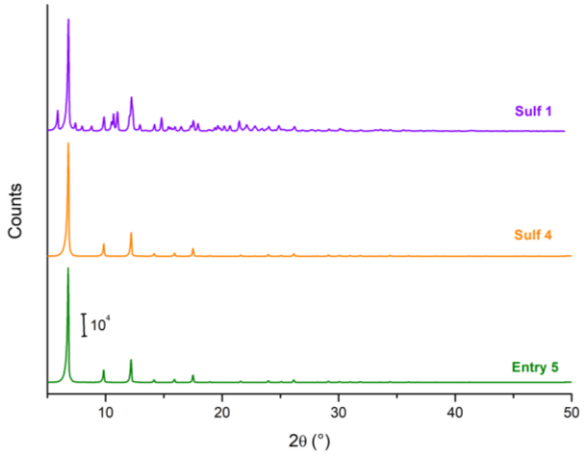

Figure 7. XRPD patterns of pure ZIF-8 MOF (Entry 5), sulfathiazole@ZIF-8 corresponding to Sulf 4 in Table 2, and sulfathiazole@ZIF-8 corresponding to Sulf 1 in Table 2.

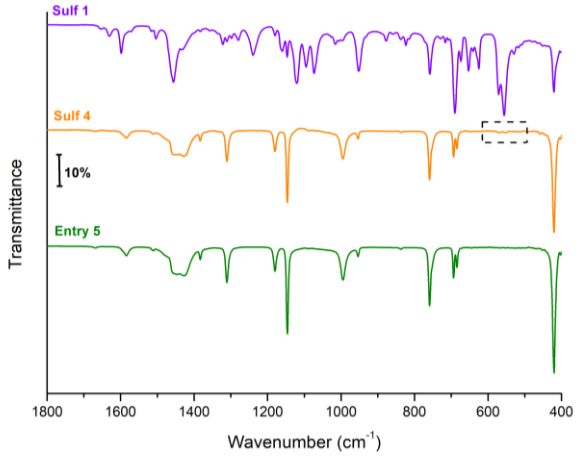

Figure 8. ATR-MIR spectra of pure ZIF-8 MOF (Entry 5), sulfathiazole@ZIF-8 corresponding to Sulf 4 in Table 2, and sulfathiazole@ZIF-8 corresponding to Sulf 1 in Table 2 in the 1800–400 cm^{-1} range. Dotted box for Sulf 4 spectrum highlights the ν_{symm} and $\nu_{antisymm}$ of the O=S=O group of sulfathiazole molecule, much more intense in the Sulf 1 spectrum.

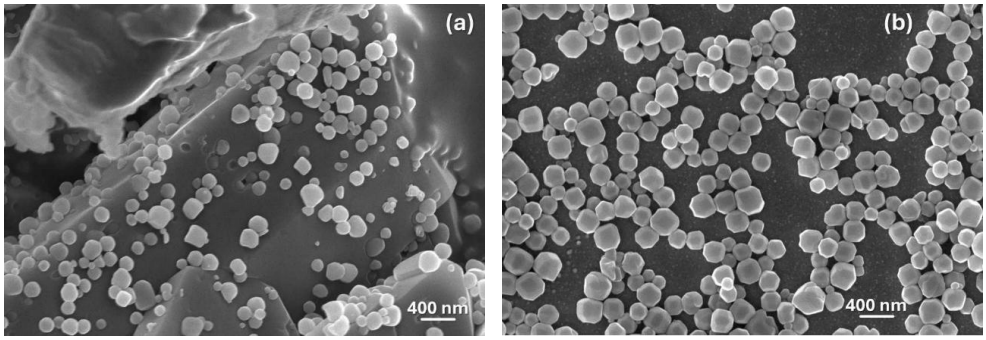

Figure 9. SEM images of sulfathiazole-loaded ZIF-8 samples: (a) 20 kX magnification of Sulf 1 sample in Table 2; (b) 20 kX magnification of Sulf 4 sample in Table 2.

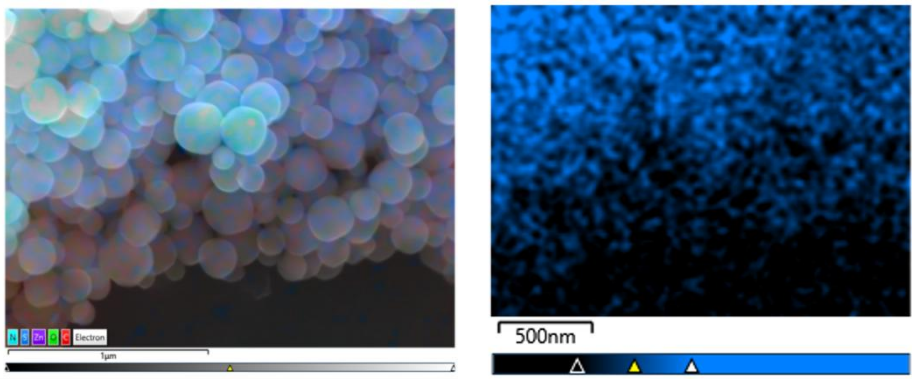

Figure 10. SEM-EDX analyses (left part) of sulfathiazole-loaded ZIF-8 with the stirring method (sample Sulf 4 in Table 2). EDX map (right part) representing sulfur distribution inside sulfathiazole-loaded ZIF-8 (sample Sulf 4 in Table 2)

Finally, to obtain further confirmation of the effective encapsulation of the drug, specific surface area (BET) and pore size distribution (PSD) analyses were performed for the Sulf 4 sample and compared with data from an unloaded sample (Entry 5, Figure 11a–b). A significant reduction in surface area (from 1610 to 1412 m^2/g) was observed, as well as a decrease in total pore volume (from 0.911 to 0.668 cm^3/g), while pore sizes remained virtually unchanged. This behavior clearly indicates that the sulphathiazole molecules have been effectively incorporated into the MOF structure, occupying the available cavities without altering their average size. These results provide

further evidence of the successful encapsulation of the active ingredient and lay the foundations for possible applications in the pharmaceutical and biotechnology fields.

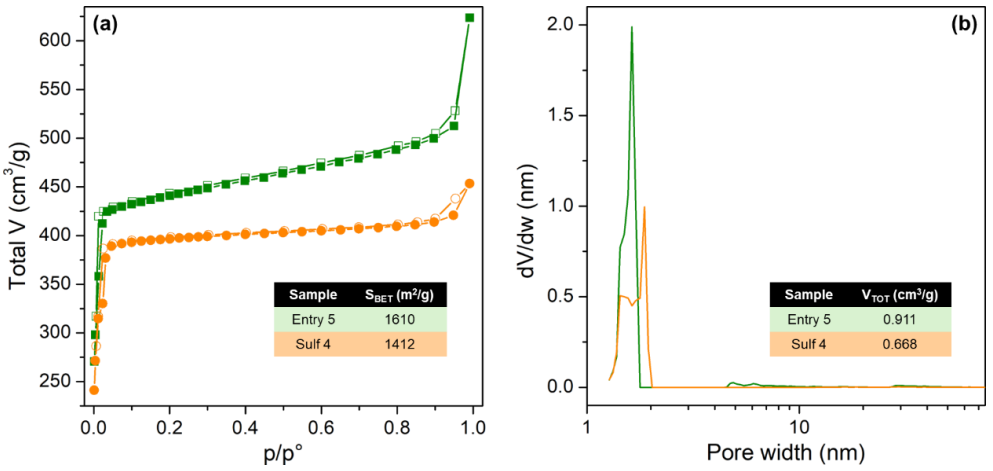

Figure 11. (a): N_2 isotherm adsorption at 77 K profile of samples identified as Entry 5 in Table 1 and Sulf 4 in Table 2). The inset reports surface area values calculated with BET method. (b): Pore Size Distribution measured with N_2 at 77 K for identified as Entry 5 in Table 1 and Sulf 4 in Table 2. The inset reports total pore volume calculated with DTF method.

A rumen affected by SARA (Subacute Ruminal Acidosis), a metabolic condition typical of ruminants fed diets particularly rich in fermentable carbohydrates and low in fiber, can easily reach pH values close to 5. This condition profoundly alters the balance of the ruminal microbiota and can compromise the animal's well-being and productivity. Such an acidic pH therefore represents a particularly challenging environment for any system designed to operate in-situ, as is the case with controlled release systems.

Although the behavior of ZIF-8 in acidic conditions has already been extensively studied, it was nevertheless considered useful to verify its stability in an environment specifically representative of the conditions induced by SARA. For this reason, it was considered appropriate to experimentally verify the stability of ZIF-8 under simulated conditions in

order to understand whether this material can actually be considered suitable for use in biological environments characterized by significant acidity. To this end, before proceeding with drug release tests, a preliminary study was conducted to evaluate the stability of pure ZIF-8 material by exposing it to two different pH conditions: pH 5, which simulates the acidic environment generated by SARA, and pH 7.4, representative of the normal physiological conditions found in many biological tissues and fluids.

The tests were performed by preparing suspensions of the material in two different buffers: acetate buffer for pH 5 and PBS (phosphate-buffered saline) buffer for pH 7.4. The suspensions were kept under constant gentle agitation for a period of several days in order to reproduce dynamic conditions similar to those of a biological environment. Throughout the exposure period, the crystalline state of the material was checked daily by XRPD analysis to assess the possible onset of degradation or structural transformation phenomena.

The analyses clearly showed that ZIF-8 maintains its crystalline structure unchanged over time when stored at physiological pH. This observation is confirmed by XRD analysis, which shows the persistence of the characteristic pattern of the crystalline material (Figure 12a), and by images obtained by scanning electron microscopy, which show an intact and regular surface morphology (Figure 13a). These results further support the evidence in the literature regarding the good stability of ZIF-8 in neutral and biologically compatible environments.

In contrast, at pH 5, a marked degradation of the material is observed after the first 24 hours of exposure. The decomposition process is progressive but rapid, leading to the complete disappearance of the original crystalline structure after approximately 48 hours. This degradation is clearly visible from the analysis of the XRPD patterns (Figure 12b), which show a marked

change: the typical signal of ZIF-8 is completely replaced by a new pattern, attributable to a degraded species. Comparison with reference data allowed this species to be identified as zinc acetate ($Zn(OAc)_2$), a known product of the decomposition of ZIF-8 in an acidic environment. Again, SEM images (Figure 13b) confirm the transformation, showing a different morphology compatible with the formation of zinc salt.

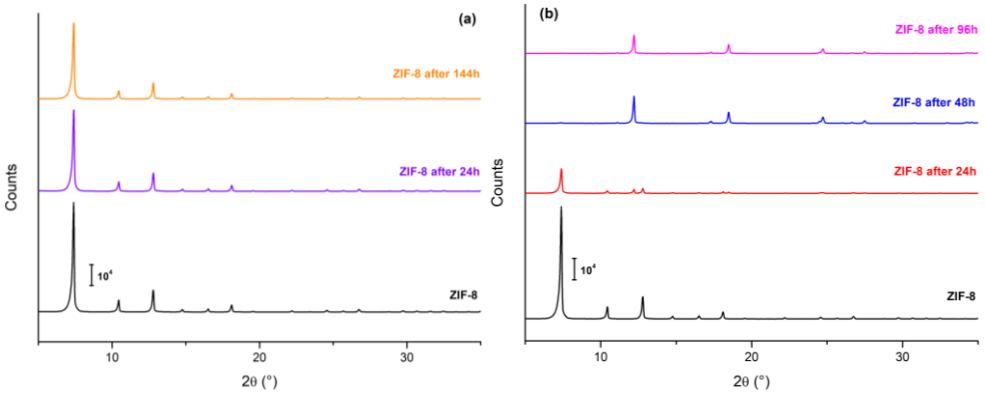

Figure 12. Time-dependent XRD patterns of pure ZIF-8 sample (Entry 5) displaying crystallinity loss/stability when in contact with physiological solution (pH=7.4 – a) or acidic solution (pH=5 - b).

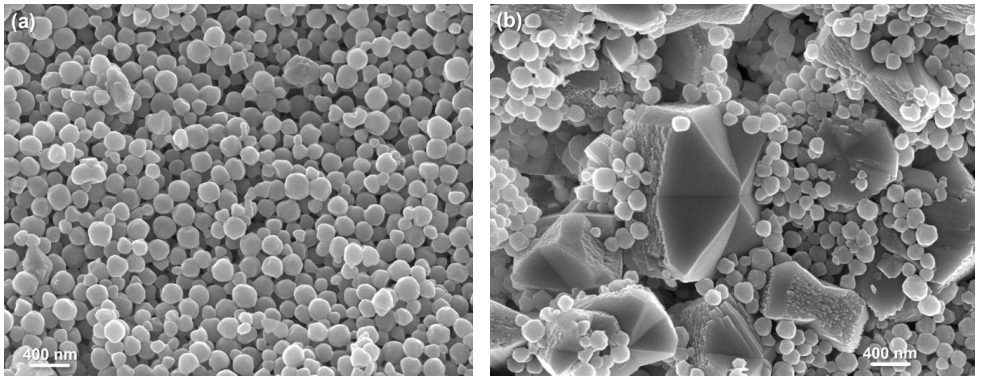

Figure 13. a) SEM images collected at 20 kX of ZIF-8 sample after being suspended in PBS buffer for 6 days (b) SEM images collected at 20 kX of ZIF-8 sample after being suspended in acetate buffer (pH = 5) for 2 days.

Overall, these results highlight the high pH sensitivity of ZIF-8: while it is perfectly stable under physiological conditions, it degrades rapidly in

moderately acidic environments such as those associated with SARA. Although this characteristic represents a limitation in terms of structural stability, it can be advantageously exploited for specific applications, such as the controlled release of drugs in response to acidic stimuli. The possibility of using ZIF-8 as a pH-sensitive carrier fits perfectly into the field of smart drug delivery strategies, where the degradation of the material is used as a mechanism for the selective release of the active ingredient.
Stability tests clearly and effectively demonstrated the pH-sensitive property of ZIF-8, highlighting how this characteristic can be exploited for the targeted release of active ingredients in regions of the body characterized by a specific local pH value.[23] In light of these preliminary results, the next step in this study was to observe the drug release behavior when ZIF-8 contained the active ingredient sulfathiazole. For this purpose, sample Sulf 4 was used, in which the drug had been previously encapsulated within the material. The release was analyzed as a function of pH to verify the effect of the surrounding environment on the behavior of the system.

The graph obtained from the concentration data, obtained by UV-Vis spectroscopy, clearly shows how the release of sulfathiazole varies significantly with pH (Figure 14). In particular, in an acidic environment, a very rapid release of the drug is observed: after just 24 hours, the amount of active ingredient released reaches 88%. In comparison, in the same time interval, in a physiological environment, only 40% of the encapsulated sulfathiazole is released.

Continuing the observation over time, it can be seen that under acidic conditions, the release stabilizes rapidly, reaching a plateau after about 36 hours, at which point 95% of the drug has been released from the material. In contrast, in a neutral environment, it is necessary to wait 7 days to achieve a similar release in terms of percentage.

These results strongly suggest that ZIF-8 can act as a controlled drug release system, whose behavior is regulated by the degree of acidity of the surrounding environment. In particular, in acute conditions of ruminal acidosis, the release of the active ingredient would be significantly faster, allowing for an immediate therapeutic response. However, even in the case of non-acute but early-stage SARA, the system could prove particularly effective: the progressive increase in ruminal acidity would induce an acceleration in the release of the antimicrobial agent, favoring timely and targeted intervention from the early stages of the disease.

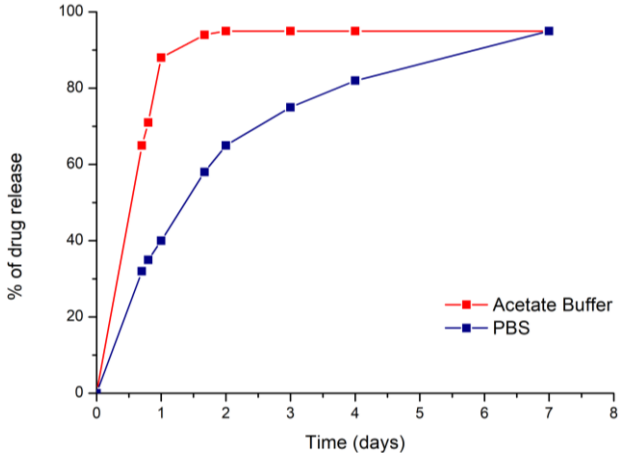

Figure 14. Time-dependent drug release obtained from UV-Vis data of dialysis solution in acetate buffer (pH=5) and PBS buffer (pH=7.4).

3.2.2 Conclusions

This study aimed to investigate the pH sensitivity of the ZIF-8 material and to exploit it for the encapsulation and controlled release of an antibacterial molecule, specifically sulfathiazole, under simulated inflammatory conditions characterized by a locally acidic environment. One of the most significant aspects that emerged from the study concerns the high drug encapsulation efficiency (%DEE), which exceeds 70%, a very high value that makes the system particularly effective. Added to this is the regular

morphology of the particles, which are approximately spherical in shape and have an average size of around 150 nm. These morphological and dimensional characteristics contribute significantly to reducing the amount of MOF needed to achieve the desired therapeutic effect. This also limits the potential risk of adverse effects caused by the material itself or its residual components, which can be released following degradation of the framework structure.

The target pathology for the application of the developed system is SARA, a bacterial infection that causes a drop in pH in the rumen of cattle. This condition can have serious consequences for the health of the animal, with significant economic repercussions for the entire milk production and processing chain.

In light of these premises, and following careful optimization of the synthesis parameters for the preparation of the ZIF-8 material, the high pH sensitivity of this material in an acidic environment was confirmed. At the same time, its remarkable stability in an aqueous environment at neutral pH was also verified. This last observation was by no means obvious, as many MOFs are known to be sensitive to the mere presence of water, regardless of the pH of the solution. The behavior observed therefore represents a further strength of ZIF-8 in the context of biological applications.

However, the degradation that the material undergoes in acidic conditions is not only tolerable but actually proves to be functional to the release mechanism: it allows for faster drug release, potentially accelerating the anti-inflammatory process by reducing the local bacterial load.

Loading the active ingredient was also not a trivial process. Sulfathiazole has several functional groups that could have interfered with the MOF structure during the encapsulation phase, giving rise to undesirable reactions or

structural changes. Despite these difficulties, effective encapsulation was achieved, and, to the best of current knowledge, this is the first work reporting the incorporation of this molecule into a MOF matrix.

3.2.3 Bibliography

1. Park, K. S.; Ni, Z.; Côté, A. P.; Choi, J. Y.; Huang, R.; Uribe-Romo, F. J.; Chae, H. K.; O'Keeffe, M.; Yaghi, O. M. Exceptional Chemical and Thermal Stability of Zeolitic Imidazolate Frameworks. *Proc. Natl. Acad. Sci. U.S.A.* **2006**, *103*(27), 10186–10191.
2. Huang, Y.; Wang, J.; Jiang, K.; Chung, E. J. Improving Kidney Targeting: The Influence of Nanoparticle Physicochemical Properties on Kidney Interactions. *J. Controlled Release* **2021**, *334*, 127–137.
3. Hoshyar, N.; Gray, S.; Han, H.; Bao, G. The Effect of Nanoparticle Size on in Vivo Pharmacokinetics and Cellular Interaction. *Nanomedicine* **2016**, *11*(6), 673–692.
4. Alowasheeir, A.; Torad, N. L.; Asahi, T.; Alshehri, S. M.; Ahamad, T.; Bando, Y.; Hossain, M. S. A.; Kaneti, Y. V.; Yamauchi, Y.; Han, M. Synthesis of Millimeter-Scale ZIF-8 Single Crystals and Their Reversible Crystal Structure Changes. *Sci. Technol. Adv. Mater.* **2024**, *25*(1), 2292485.
5. Cravillon, J.; Münzer, S.; Lohmeier, S. J.; Feldhoff, A.; Huber, K.; Wiebcke, M. Rapid Room-Temperature Synthesis and Characterization of Nanocrystals of a Prototypical Zeolitic Imidazolate Framework. *Chem. Mater.* **2009**, *21*(8), 1410–1412.
6. Fairen-Jimenez, D.; Moggach, S. A.; Wharmby, M. T.; Wright, P. A.; Parsons, S.; Duren, T. Opening the Gate: Framework Flexibility in ZIF-8 Explored by Experiments and Simulations. *J. Am. Chem. Soc.* **2011**, *133*(23), 8900–8902.
7. Haghi, A.; Raissi, H.; Hashemzadeh, H.; Farzad, F. Designing a High-Performance Smart Drug Delivery System for the Synergetic Co-Absorption of DOX and EGCG on ZIF-8. *RSC Adv.* **2020**, *10*(72), 44533–44544.

8. Zhou, H. C.; Long, J. R.; Yaghi, O. M. Introduction to Metal–Organic Frameworks. *Chem. Rev.* **2012**, *112*(2), 673–674.
9. Zhang, Z.; Wang, Y.; Wu, S.; Yuan, H.; Luo, X. In Situ Growth of ZIF-8 on Cellulose Microspheres with High Doxorubicin Loading Capacity and pH-Sensitive for Oral Drug Delivery. *J. Drug Deliv. Sci. Technol.* **2024**, *101*, 106263.
10. Kaur, H.; Mohanta, G. C.; Gupta, V.; Kukkar, D.; Tyagi, S. Synthesis and Characterization of ZIF-8 Nanoparticles for Controlled Release of 6-Mercaptopurine Drug. *J. Drug Deliv. Sci. Technol.* **2017**, *41*, 106–112.
11. Hao, J.; Chen, C.; Pavelic, K.; Ozer, F. ZIF-8 as a pH-Responsive Nanoplatform for 5-Fluorouracil Delivery in the Chemotherapy of Oral Squamous Cell Carcinoma. *Int. J. Mol. Sci.* **2024**, *25*(17), 9292.
12. Plaizier, J. C.; Khafipour, E.; Li, S.; Gozho, G. N.; Krause, D. O. Subacute Ruminal Acidosis (SARA), Endotoxins and Health Consequences. *Anim. Feed Sci. Technol.* **2012**, *172*(1–2), 9–21.
13. Plaizier, J. C.; Krause, D. O.; Gozho, G. N.; McBride, B. W. Subacute Ruminal Acidosis in Dairy Cows: The Physiological Causes, Incidence and Consequences. *Vet. J.* **2008**, *176*(1), 21–31.
14. Kleen, J. L.; Hooijer, G. A.; Rehage, J.; Noordhuizen, J. P. T. M. Subacute Ruminal Acidosis (SARA): A Review. *J. Vet. Med. A* **2003**, *50*(8), 406–414.
15. Kida, K.; Okita, M.; Fujita, K.; Tanaka, S.; Miyake, Y. Formation of High Crystallinity ZIF-8 in an Aqueous Solution. *CrystEngComm* **2013**, *15*(9), 1794–1801.
16. He, S.; Wu, L.; Li, X.; Sun, H.; Xiong, T.; Liu, J.; Wei, Y.; Huang, X.; Zhang, J. Metal–Organic Frameworks for Advanced Drug Delivery. *Acta Pharm. Sin. B* **2021**, *11*(8), 2362–2395.

17. Pan, Y.; Liu, Y.; Zeng, G.; Zhao, L.; Lai, Z. Rapid Synthesis of Zeolitic Imidazolate Framework-8 (ZIF-8) Nanocrystals in an Aqueous System. *Chem. Commun.* **2011**, *47*(7), 2071–2073.
18. Yamamoto, D.; Maki, T.; Watanabe, S.; Tanaka, H.; Miyahara, M. T.; Mae, K. Synthesis and Adsorption Properties of ZIF-8 Nanoparticles Using a Micromixer. *Chem. Eng. J.* **2013**, *227*, 145–150.
19. Zhang, C.; Han, C.; Sholl, D. S.; Schmidt, J. R. Computational Characterization of Defects in Metal–Organic Frameworks: Spontaneous and Water-Induced Point Defects in ZIF-8. *J. Phys. Chem. Lett.* **2016**, *7*(3), 459–464.
20. Sun, C. Y.; Qin, C.; Wang, X. L.; Yang, G. S.; Shao, K. Z.; Lan, Y. Q.; Su, Z. M.; Huang, P.; Wang, C. G.; Wang, E. B. Zeolitic Imidazolate Framework-8 as Efficient pH-Sensitive Drug Delivery Vehicle. *Dalton Trans.* **2012**, *41*(23), 6906–6909.
21. Anwar, J.; Tarling, S. E.; Barnes, P. Polymorphism of Sulfathiazole. *J. Pharm. Sci.* **1989**, *78*(4), 337–342.
22. Abarca, R. L.; Rodríguez, F. J.; Guarda, A.; Galotto, M. J.; Bruna, J. E. Characterization of Beta-Cyclodextrin Inclusion Complexes Containing an Essential Oil Component. *Food Chem.* **2016**, *196*, 968–975.
23. Jung, S.; Chang, S.; Kim, N. E.; Song, Y. J.; Kim, J. ZIF-8 Based Active Wound Dressing for pH Modulation and pH-Responsive Delivery of Curcumin and Zn2+: Effect of Acidity on the Drug Release for Antibacterial and Antioxidant Efficacy. *Macromol. Mater. Eng.* **2023**, *308*(11), 2300141.

4. ZIF-8 for Anticancer Treatment: One Carrier, Many Strategies

---

This chapter is based on the publications:

1. di Nicola, N., Giacchi, L., Vandone, M., Crucianelli, M., Guidoni, L., Colombo, V., Rucci, N. & Lazzarini, A. (2025). Targeted Delivery of Lidocaine in Breast Cancer Cells *via* Zeolitic Imidazolate Framework-8 Nanoparticles. ChemPhysChem, 26(16), e202401128.
2. di Nicola, N., Di Vito Nolfi, M., Vetrano, A., Zazzeroni, F., Guidoni, L., Crucianelli, M., Vecchiotti, D. & Lazzarini, A. (in preparation). pH-responsive targeted delivery of Nonsteroidal Anti-Inflammatory Drugs Using ZIF-8 for anti-cancer application.

The use of smart systems for targeted drug delivery is a promising strategy for improving therapeutic efficacy and reducing side effects in cancer treatment. In this context, ZIF-8 stands out for a combination of chemical and physical properties that make it particularly suitable for interacting with the tumor microenvironment. Its stability under physiological conditions and sensitivity to acidic stimuli make it an ideal candidate for selective drug delivery in the vicinity of malignant tissues, which are characterized by a reduced extracellular pH. Furthermore, its porous structure, easy surface functionalization and overall biocompatibility offer significant potential for adaptation to specific therapeutic needs. These characteristics position ZIF-8 as an extremely interesting platform in the field of nanotechnology applied to oncology.

4.1 Breast Cancer

Breast cancer is the most common malignant neoplasm among women world-wide and is treatable in 70%–80% of patients if recognized at an early-stage, nonmetastatic disease.[1] However, advanced breast cancer with metastasis to distant organs is considered untreatable with the currently available therapies.[2] Treatment strategies vary depending on the molecular subtype of the cancer. Future therapeutic approaches in breast cancer aim at the individualization of treatment, with a focus on de-escalation and escalation of therapy based on tumor biology and early response to treatment.[3] In addition to ongoing therapeutic innovations, ensuring equitable access to these advancements globally remains a critical challenge in the future of breast cancer care. Several retrospective studies have suggested a potential impact of anesthesia on cancer patient survival.[4] In particular, regional anesthesia has been associated with a reduced risk of cancer recurrence, with one proposed explanation being the opioid-sparing effects of regional anesthesia, as opioids have been implicated in promoting cancer progression.[5] Additionally, other studies have shown that perioperative intravenous lidocaine infusion reduces post operative pain and opioid requirements. Lidocaine has also been demonstrated to induce apoptosis and suppress tumor growth in human breast cancer cells, as well as other cancer cell lines in vitro.[6] Furthermore, it has been reported to enhance the sensitivity of breast cancer cells to chemotherapeutic agents.[7] In the recent years, several studies employing lidocaine as such or embedded in either complexes or polymeric media, focusing on cancer and anesthetic therapies, were published.[8] These considerations have led to the present project, which aims to use ZIF-8 as a carrier for lidocaine, exploiting the pH-sensitive properties of this MOF for the targeted and intelligent delivery of the active compound to tumor tissue. Lidocaine has a very short half-life,[9] and its controlled release by ZIF-8 could overcome the limitations associated

with the drug's dosing schedule. The aim of this study is to investigate an efficient and reproducible strategy for loading lidocaine into the pores of ZIF-8,[10] followed by accurate physical-chemical characterization of the empty and loaded material. Once the successful encapsulation of lidocaine within the pores of the MOF structure was established, the focus shifted to in vitro testing to evaluate the efficacy of the promising lidocaine@ZIF-8 system for the treatment of breast cancer.

4.1.1 Results and Discussion

As thoroughly discussed in the previous chapter, ZIF-8 is among the most extensively studied and utilized MOFs in the biomedical field, owing to its structural versatility and the wide range of available synthetic approaches.[11] In this study, ZIF-8 was synthesized and loaded following an optimized procedure previously developed by our group.[10] This method, based on hydrothermal synthesis, is particularly suitable for biomedical applications, as it employs water as the sole solvent, thereby preserving the structural and functional integrity of the resulting material. The synthesized ZIF-8 crystals exhibit a uniform morphology and an average particle size of approximately 150 nm, as shown in Figure 1. The specific surface area, determined by nitrogen adsorption at 77 K (1813 m^2/g), confirms that the morphological features of the material are consistent with those previously reported in the literature (Figure 5).[12]

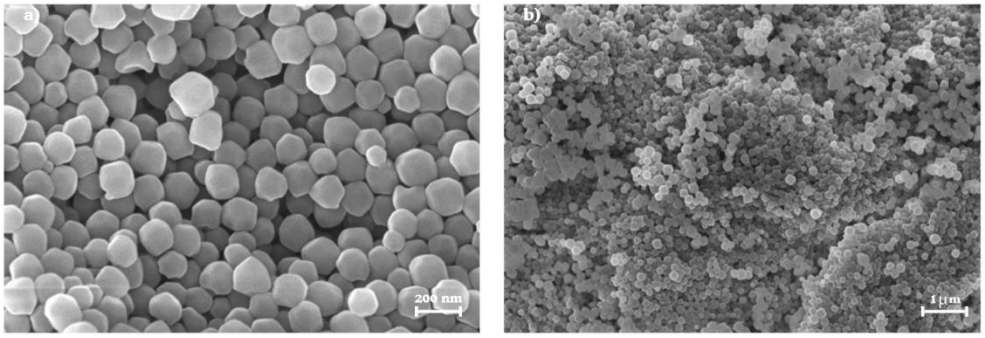

Figure 1. SEM images collected at 50 kX (a) and 10 kX (b) of as-prepared ZIF-8.

Once ZIF-8 was obtained, the next step was optimizing the loading of lidocaine into the crystal cavities. This active principle is in the form of chloride salt and is highly soluble in most organic solvents, making the loading process challenging due to its affinity with the solvent. To overcome this obstacle, the loading procedure was carried out in a thermostatic beaker (at T = 0 °C), in order to reduce lidocaine's solubility. The experiments were conducted using a ZIF-8:lidocaine weight ratio of 2:3, with the mixture stirred for 24 hours. To identify the best solvent for loading, the tests were performed varying the polarity of the medium, without compromising ZIF-8 suspendability: the selected solvents in which the loading procedure was attempted were methanol, acetonitrile, and hexane, respectively. The loading efficiency was determined by calculating the ratio between the initial and final concentrations of lidocaine present in both the synthesis and washing solutions, exploiting the absorption of lidocaine centered at 215 nm by means of UV-Vis spectroscopy. As expected from the UV-Vis spectra (Figure 2),[13] methanol proved to be the least effective solvent for drug loading into ZIF-8, as the lidocaine concentration in the wash solutions remained equal to the initial value. A slight improvement was observed with acetonitrile as the solvent, yielding an efficiency of 6.5%. However, the highest efficiency, approximately 14%, was achieved using hexane, in which lidocaine has the

lowest solubility among the selected solvents, thus facilitating its interaction with the MOF pores.

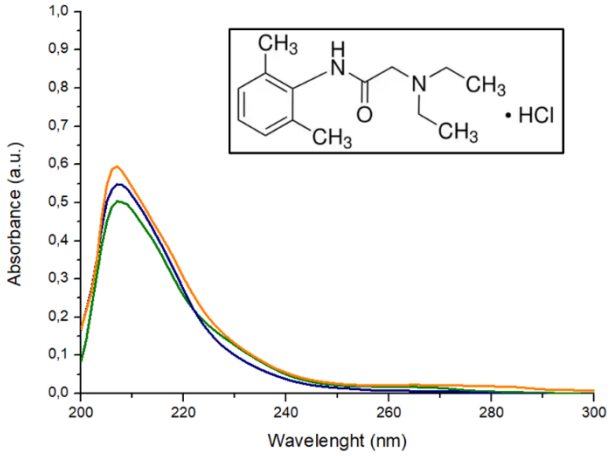

Figure 2. V-Vis spectra of synthesis and washing solutions (i.e. hexane in green, methanol in orange, and acetonitrile in blue) after drug loading for the different solvents employed. Inset reports the scheme of the lidocaine hydrochloride molecule.

After obtaining the lidocaine-loaded ZIF-8 system (lidocaine@ZIF-8), the material was characterized to detect any differences from pure ZIF-8 and determining whether lidocaine was encapsulated within the pores or merely adsorbed onto the crystal surface. Initially, PXRD analysis was performed to assess any possible loss of crystallinity in the MOF. As shown in Figure 3, the crystalline patterns are perfectly overlaid, indicating no degradation of ZIF-8 and excluding the appearance of new peaks associated with lidocaine crystals or eventual additional phases.[14] This result is further confirmed by SEM images (Figure 1a), which show crystals with the same size and morphology as the parent material. Additionally, ATR-MIR spectroscopy was used to confirm the location of the lidocaine. If the drug was adsorbed on the surface, characteristic peaks of its functional groups would be visible (Figure 4). However, the spectra of pure ZIF-8 and lidocaine@ZIF-8 are perfectly overlaid, confirming successful encapsulation of lidocaine within the pores. This because it has been reported that biological active molecules

confined inside small cages of materials provoke a strong decrease of the overall IR intensity of the encapsulated species.[15]

In addition, once the material was obtained, the surface area was measured again by nitrogen physisorption at 77 K to assess any differences in the inner surface area values. Indeed, it can be clearly observed that there is a slight decrease in the surface area value after loading (passing from 1813 to 1482 m^2/g), thus indicating the presence of drug within the pores of the MOF (Figure 5).

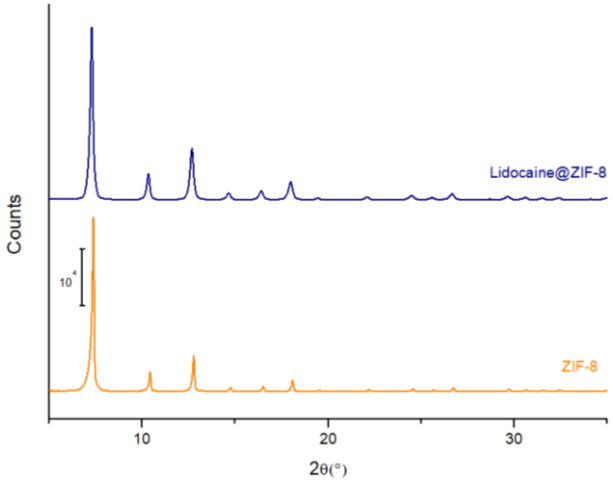

Figure 3. XRD patterns of ZIF-8 (orange) and lidocaine@ZIF-8 (blue).

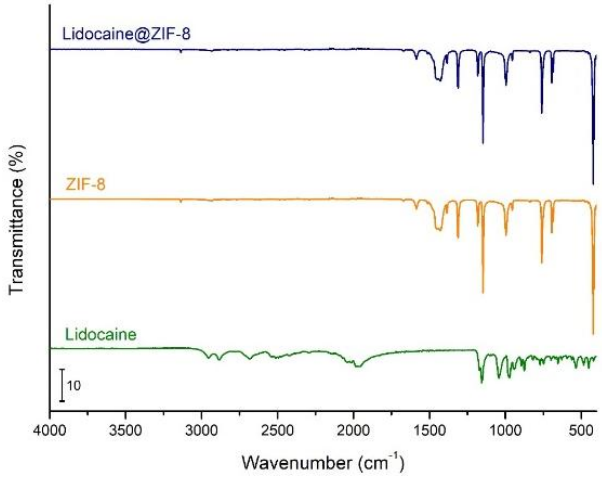

Figure 4. SEM images collected at 50 kX of lidocaine@ZIF-8 (a) and ATR-MIR spectra (b) of pure lidocaine (green), ZIF-8 (orange) and lidocaine@ZIF-8 (blue).

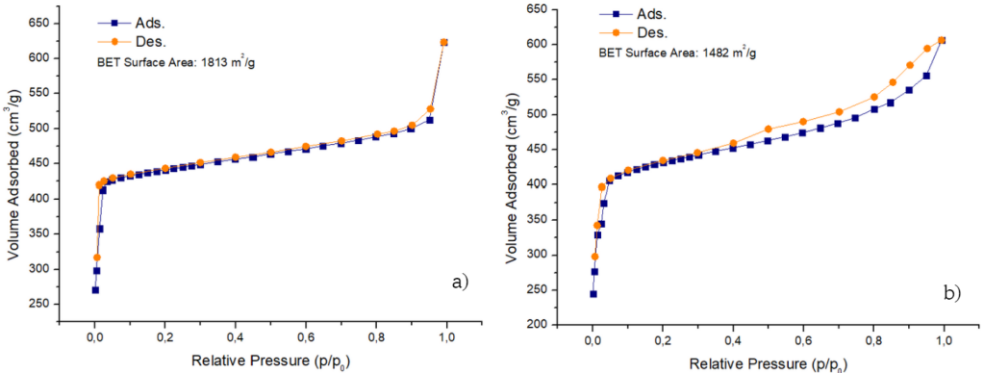

Figure 5. N_2 adsorption-desorption isotherms at 77 K of ZIF-8 (a) and lidocaine@ZIF-8 (b).

Finally, to determine the composition of the lidocaine@ZIF-8 system and to validate the findings obtained from UV-Vis spectroscopy, thermogravimetric analysis (TGA) was performed on both drug-loaded and bare ZIF-8. As shown in Figure 6, unloaded ZIF-8 displays the typical mass loss for such systems (around 350 °C), leaving behind approximately 36%$_{wt.}$ of ZnO coming from MOF degradation, corresponding to the mass remaining for a perfectly stoichiometric ZIF-8 material.[16] The curve of the drug-loaded

material differs from the previous one primarily in the slight initial weight loss around 100 °C, which corresponds to the water adsorbed by lidocaine@ZIF-8 sample (approximately 2%). This is due to better interaction of lidocaine with water from moisture with respect to the bare MOF. A further and more significant weight loss at 150 °C is associated to the presence of lidocaine, accounting for 14%$_{wt.}$ of the newly formed material. The temperature associated to this weight loss is in good agreement with lidocaine boiling temperature,[17] meaning that it has been released from the pores of the material.

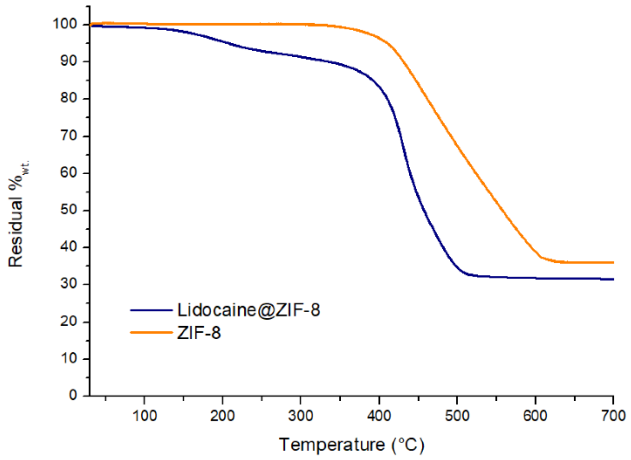

Figure 6. TGA curves of ZIF-8 (orange) and lidocaine@ZIF-8 (blue).

There are several works in the literature demonstrating the stability and pH-sensitive properties of ZIF-8.[18] Therefore, similarly to previous studies,[10] the final aim of this preliminary study is to observe the release behavior of lidocaine@ZIF-8, under different pH conditions. The graphs report the percentage of drug released, based on the absorbance values ratio (obtained through UV-Vis spectroscopy) between the release solution and the one coming from the theoretical amount loaded into the MOF. These data clearly

illustrate the different behaviors of lidocaine release depending on the pH of the working solution (Figure 7). Indeed, in an acidic environment (pH = 5.5), 94% of the drug is released within 24 hours; conversely, in physiological conditions (pH = 7.4), only 67% of the encapsulated lidocaine is released in the same period. Under acidic conditions, the release rapidly reaches a plateau after 36 hours, achieving a total drug delivery of 95,7%. In contrast, to reach the same level of release under neutral pH, a period of 7 days is required. These results suggest a controlled drug release depending on the pH level in the microenvironment. In the case of breast cancer, a more rapid release of lidocaine would occur in the acidic tumoral regions; however, in early-stage treatment, this mechanism could be advantageous by accelerating the release of the active molecule in response to localized acidification in tumor tissues.

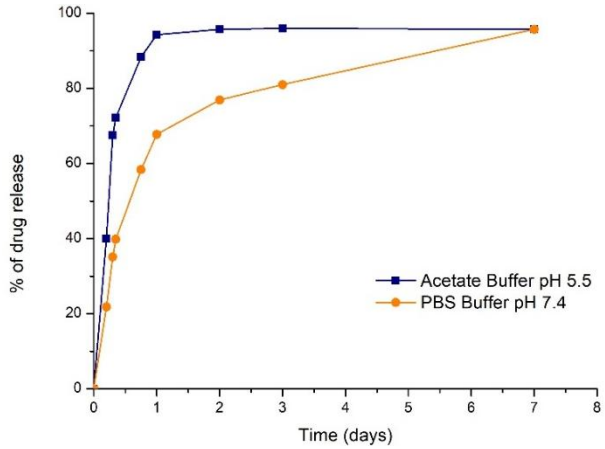

Figure 7. Drug release as a function of time obtained from UV-Vis data of the dialysis solution at pH = 5.5 and pH = 7.4, respectively.

In recent years, it has been observed that lidocaine induces metabolomic changes in breast cancer cells profile,[19] and apoptosis through VDAC1 expression.[20] Moreover has been reported that lidocaine can suppress cancer

cell growth via blocking voltage-gated sodium channels.[21] Although this molecule shows promise in the treatment of breast cancers, to date it is not yet possible to define absolutely what the exact mechanism of action is. Therefore, we finally investigated the effect of lidocaine@ZIF-8 on MDA-MB-231 breast cancer cells viability. After a short period of 24 hours, treatment of breast cancer cells with lidocaine@ZIF-8 0.01 mg/mL did not show any significant differences when compared to lidocaine 0.01 mg/mL, with ZIF-8 0.01 mg/mL, or vehicle, respectively (Figure 8a). Hence, we next treated MDA-MB-231 cells with lidocaine@ZIF-8 0.01 mg/mL for a period of 48 hours. Intriguingly, the treatment showed a *trend* to decrease of cells viability when compared to vehicle (p-value=0.0884) and ZIF-8 0.01 mg/mL (p-value=0.0710), whereas a significant decrease was observed when compared to lidocaine 0.01 mg/mL (Figure 8b). To deeply characterize the time-dependent effect of lidocaine@ZIF-8 on MDA-MB-231 cells, we performed a last treatment of 72 hours. Interestingly, lidocaine@ZIF-8 treatment of breast cancer cells showed a significant reduction of cells viability when compared to lidocaine 0.01 mg/mL, with ZIF-8 0.01 mg/mL, and vehicle, respectively (Figure 8c).

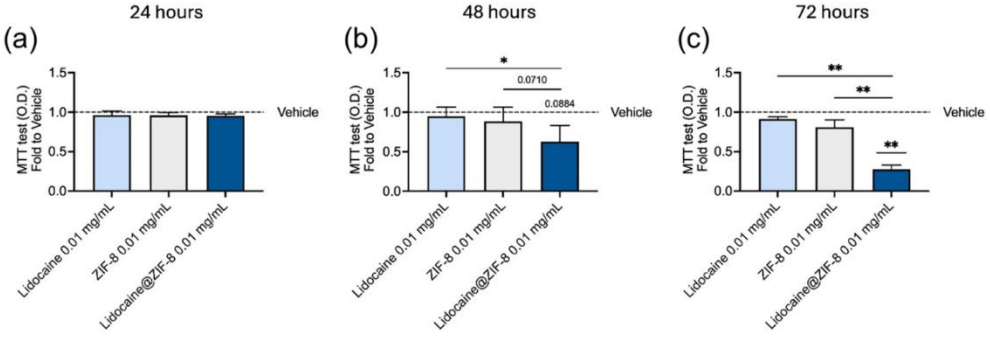

Figure 8. Effect of lidocaine@ZIF-8 on MDA-MB-231 breast cancer cells viability: MDA-MB-231 have been plated at a density of 9000 cells/ cm^2 and, the day after, treated for (a) 24, (b) 48, and (c) 72 hours, with vehicle, lidocaine 0.01 mg/mL, ZIF-8 0.01 mg/mL, and lidocaine@ZIF-8 0.01 mg/mL, respectively. Cells viability was assessed by MTT assay (Number of independent experiment (N) = 3; *p-value (p)<0.05, **p<0.01 versus Lidocaine@ZIF-8 0.01 mg/mL; paired t-test; dot line = vehicle set at 1).

These results may suggest a time-dependent drug release, possibly correlated with the pH level in the tumor microenvironment, corroborating data collected from the release tests previously described. One noticeable fact is the difference in time response between the effect of lidocanine@ZIF-8 observed on cancer cells and the pH-dependent drug release curves reported in Figure 7. Indeed, at pH = 5.5 the total release of lidocaine was observed already at 36 h. Nevertheless, a noticeable effect on the cells inoculated with lidocaine@ZIF-8 started to be visible only after 48 h, reaching its maximum at 72 h. Such delay might be ascribable to differences in pH values of the cell environment with respect to the one of the test release solution: even slight differences in acidity of the medium has been reported to greatly affect ZIF-8 decomposition,[22] thus delaying the drug release. A possible explanation is that we cannot measure pH variation of the working environment, which is strongly influenced by the number of cancer cells present, impacting on the acidity of their surroundings.

However, providing that these are only preliminary results, further studies are required to evaluate the efficacy of the lidocaine@ZIF-8 system and to assess the cytotoxicity of the pure and loaded MOF.

4.1.2 Conclusions

The aim of this study was to investigate the encapsulation of lidocaine within the cavities of ZIF-8, a metal-organic framework highly sensitive to pH variations. This pH-responsive property enables ZIF-8 to release drugs in a controlled manner in the tumor microenvironment. Recent research has shown that, in addition to being a commonly used local anesthetic, lidocaine possesses the ability to inhibit the metastatic potential of breast cancer cells,[20] one of the most widespread cancers overall, preventing them from invading other tissues. After synthesizing ZIF-8 using a well-established

synthetic strategy, an alternative method to conventional stirring was employed to encapsulate lidocaine. This approach involved lowering the working temperature to reduce the solubility of the drug. Once the lidocaine@ZIF-8 system was obtained, it was extensively characterized using various techniques and subsequently tested on cancer cell cultures to evaluate its efficacy. Notably, ZIF-8 facilitated lidocaine release, reducing breast cancer cells viability in a time and pH-dependent manner. Interestingly, despite the low amount of loaded lidocaine (only 14 $\%_{wt.}$) its effect was much higher with respect to the same amount of free drug: indeed, a higher loading, implying multiple cage occupancy by the drug molecules, could have resulted in a slower molecular diffusion or drug release in unnecessary areas, thus potentially reducing the efficacy of the system as a whole. This result is extremely important, since it aims to reduce the dosage of drugs in order to minimize accumulation, excretion and possible side effects. However, to fully understand the mechanism underlying the action of lidocaine for the treatment of breast cancer, more complex *in vitro* studies are needed in the future before moving on to *in vivo* studies.

4.1.3 Bibliography

1. Harbeck, N.; Penault-Llorca, F.; Cortes, J.; Gnant, M.; Houssami, N.; Poortmans, P.; Tsang, J.; Cardoso, F. Breast Cancer. *Nat. Rev. Dis. Primers* **2019**, *5*, 66.
2. Pagani, O.; Senkus, E.; Wood, W.; Colleoni, M.; Cufer, T.; Kyriakides, S.; Cardoso, F. International Guidelines for Management of Metastatic Breast Cancer: Can Metastatic Breast Cancer Be Cured? *J. Natl. Cancer Inst.* **2010**, *102* (7), 456–463.
3. Bailleux, C.; Eberst, L.; Bachelot, T. Treatment Strategies for Breast Cancer Brain Metastases. *Br. J. Cancer* **2021**, *124* (1), 142–155.
4. Kim, R.; Kawai, A.; Wakisaka, M.; Kin, T. Current Status and Prospects of Anesthesia and Breast Cancer: Does Anesthetic Technique Affect Recurrence and Survival Rates in Breast Cancer Surgery? *Front. Oncol.* **2022**, *12*, 795864.
5. Garg, R. Regional Anaesthesia in Breast Cancer: Benefits beyond Pain. *Indian J. Anaesth.* **2017**, *61* (5), 369–372.
6. D'Agostino, G.; Saporito, A.; Cecchinato, V.; Silvestri, Y.; Borgeat, A.; Anselmi, L.; Uguccioni, M. Lidocaine Inhibits Cytoskeletal Remodelling and Human Breast Cancer Cell Migration. *Br. J. Anaesth.* **2018**, *121* (4), 962–968.
7. Chamaraux-Tran, T. N.; Mathelin, C.; Aprahamian, M.; Joshi, G. P.; Tomasetto, C.; Diemunsch, P.; Akladios, C. Antitumor Effects of Lidocaine on Human Breast Cancer Cells: An *In Vitro* and *In Vivo* Experimental Trial. *Anticancer Res.* **2018**, *38* (1), 95–105.
8. Supachawaroj, N.; Limsitthichaikoon, S. Lidocaine HCl-Loaded Polyelectrolyte Complex-Poloxamer Thermoresponsive Hydrogel: *In Vitro–In Vivo* Anesthetic Evaluations for Tooth Socket Wound Delivery. *AAPS PharmSciTech* **2024**, *25* (6), 182.

9. LeLoriér, J.; Grenon, D.; Latour, Y.; Caillé, G.; Dumont, G.; Brosseau, A.; Solignac, A. Pharmacokinetics of Lidocaine after Prolonged Intravenous Infusions in Uncomplicated Myocardial Infarction. *Ann. Intern. Med.* **1977**, *87* (6), 700–702.
10. di Nicola, N.; Paolucci, V.; Daniele, V.; Taglieri, G.; Crucianelli, M.; Guidoni, L.; Lazzarini, A. ZIF-8 as Potential Vector for Enhanced Target Delivery of Sulfathiazole for the Treatment of Bovine Ruminal Acidosis. *Eur. J. Inorg. Chem.* **2024**, *2024* (36), e202400504.
11. Schejn, A.; Balan, L.; Falk, V.; Aranda, L.; Medjahdi, G.; Schneider, R. Controlling ZIF-8 Nano- and Microcrystal Formation and Reactivity through Zinc Salt Variations. *CrystEngComm* **2014**, *16* (21), 4493–4500.
12. Chen, F.; Liu, S.; Huang, H.; Wang, B.; Liu, Z.; Jiang, X.; Xiang, W.; Yang, G.; Liu, G.; Peng, X.; Zhang, Z.; Liu, Z.; Tsubaki, N. Fast synthesis of Cu@zeolitic imidazolate framework-8 (ZIF-8) derived Cu/ZnO catalysts via a facile mechanical grinding method for CO_2 hydrogenation to methanol. *Chem. Sci.* **2025**, *16* (5), 2273–2286.
13. Soni, S.; Pal, A. Spectroscopic Studies on Host–Guest Interactions of α- and β-Cyclodextrin with Lidocaine Hydrochloride and Procaine Hydrochloride. *J. Solution Chem.* **2016**, *45* (5), 665–674.
14. Suksaeree, J.; Waiprib, R.; Pichayakorn, W. Improving the Hydrophilic Properties of Deproteinized Natural Rubber Latex Films for Lidocaine Transdermal Patches by Starch Blending. *J. Polym. Environ.* **2022**, *30* (4), 1574–1586.
15. Abarca, R. L.; Rodríguez, F. J.; Guarda, A.; Galotto, M. J.; Bruna, J. E. Characterization of Beta-Cyclodextrin Inclusion Complexes Containing an Essential Oil Component. *Food Chem.* **2016**, *196*, 968–975.

16. Huang, X. C.; Lin, Y. Y.; Zhang, J. P.; Chen, X. M. Ligand-Directed Strategy for Zeolite-Type Metal–Organic Frameworks: Zinc(II) Imidazolates with Unusual Zeolitic Topologies. *Angew. Chem. Int. Ed.* **2006**, *45* (10), 1557–1559.
17. O'Neil, M. J. *The Merck Index: An Encyclopedia of Chemicals, Drugs, and Biologicals*, 15th ed.; RSC Publishing: Cambridge, U.K., 2013.
18. Spitsyna, A. S.; Poryvaev, A. S.; Sannikova, N. E.; Yazikova, A. A.; Kirilyuk, I. A.; Dobrynin, S. A.; Krumkacheva, O. A. Stability of ZIF-8 Nanoparticles in Most Common Cell Culture Media. *Molecules* **2022**, *27* (10), 3240.
19. Chamaraux-Tran, T. N.; Muller, M.; Pottecher, J.; Diemunsch, P. A.; Tomasetto, C.; Namer, I. J.; Dali-Youcef, N. Metabolomic Impact of Lidocaine on a Triple Negative Breast Cancer Cell Line. *Front. Pharmacol.* **2022**, *13*, 821779.
20. Long, D.; Fang, X.; Yuan, P.; Cheng, L.; Li, H.; Qu, L. Lidocaine Promotes Apoptosis in Breast Cancer Cells by Affecting VDAC1 Expression. *BMC Anesthesiol.* **2022**, *22* (1), 273.
21. Liu, C.; Yu, M.; Li, Y.; Wang, H.; Xu, C.; Zhang, X.; Guo, X. Lidocaine Inhibits the Metastatic Potential of Ovarian Cancer by Blocking NaV1.5-Mediated EMT and FAK/Paxillin Signaling Pathway. *Cancer Med.* **2021**, *10* (1), 337–349.
22. Butonova, S. A.; Ikonnikova, E. V.; Sharsheeva, A.; Chernyshov, I. Y.; Kuchur, O. A.; Mukhin, I. S.; Morozov, M. I. Degradation Kinetic Study of ZIF-8 Microcrystals with and without the Presence of Lactic Acid. *RSC Adv.* **2021**, *11* (62), 39169–39176.

4.2 Prostate cancer

In recent years, the therapeutic approach to prostate cancer treatment has undergone significant evolution, shifting from exclusively cytotoxic strategies to more targeted approaches capable of modulating the tumor microenvironment and associated inflammatory processes.[1] In this context, increasing attention has been paid to the use of non-steroidal anti-inflammatory drugs (NSAIDs), traditionally used to control pain and inflammation, but increasingly recognized for their potential anti-tumor role.[2] Numerous studies have shown that chronic inflammation is a crucial factor in the tumorigenesis and progression of prostate cancer.[3] NSAIDs, particularly cyclooxygenase-2 (COX-2) inhibitors, have been shown to interfere with pro-tumor mechanisms such as cell proliferation, angiogenesis, resistance to apoptosis and neoplastic invasiveness.[4] This evidence has led to a complete re-evaluation of the role of this class of drugs: from mere symptomatic adjuvants to potential chemopreventive or therapeutic agents, to be used in combination with conventional treatments or in specific contexts of indolent or refractory prostate cancer.[5] However, the systemic use of NSAIDs in oncology is often limited by problems of bioavailability, gastrointestinal and cardiovascular side effects, and low selectivity towards tumor tissue.[6] These limitations have prompted the search for alternative delivery systems capable of improving the pharmacokinetic profile and therapeutic efficacy of these compounds.[7] In this perspective, the incorporation of NSAIDs into inorganic nanocarriers such as ZIF-8 offers a promising strategy to maximize their antitumor action while reducing their systemic toxicity, opening up new possibilities for more targeted and safer clinical use. The aim of this work was therefore to study in depth the process of loading different NSAIDs into the pores of ZIF-8, and then to characterize each individual material obtained. In the final phase, the

release kinetics and effect of these new systems on different types of prostate cancer cell cultures were studied and evaluated.

4.2.1 Results and Discussion

As in the previous study, the first step of this work was the synthesis and characterization of ZIF-8, following the procedure previously developed by our research group.[8] This method produces ZIF-8 crystals with an average size of approximately 150 nm and uniform morphology, as illustrated in Figure 1. The surface area, determined by nitrogen adsorption at 77 K, was found to be 1837.14 m^2/g, confirming that the morphological properties of the MOF are consistent with those reported in the literature.

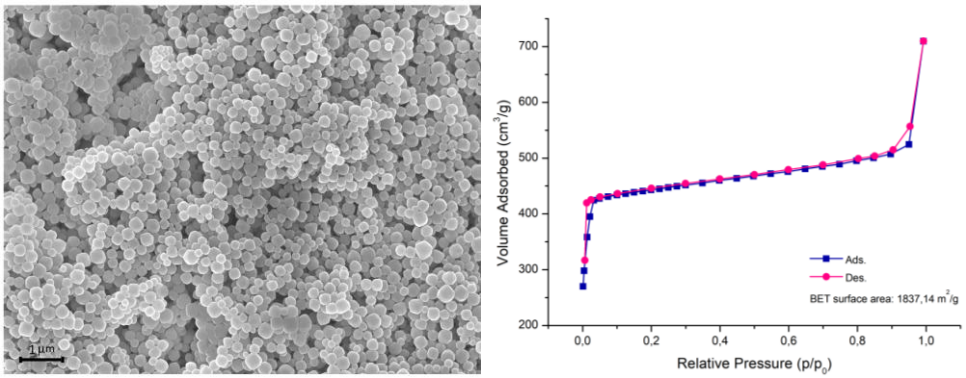

Figure 1. SEM image collected at 10 kX (left) and N_2 adsorption-desorption isotherms at 77 K (right) of ZIF-8.

The next step was to optimize the loading of NSAIDs into the cavities of ZIF-8. Ibuprofen was chosen as the reference compound to optimize loading conditions, as its size represents an average among NSAIDs intended for encapsulation within the MOF. Initially, an attempt was made to load the NSAIDs in their acid form in methanol via the stirring method. However, the presence of the carboxylic acid functional group, characteristic of all these compounds except paracetamol, hindered the loading process. Instead, it led

to the partial decomposition of MOF, which is highly sensitive to pH, a property that is intended to be exploited in this application. The result was a significant decrease in yield, with only about 10% of the initial material recovered; for this reason, we decided to stop loading the active pharmaceutical ingredients in their free acid form and proceed instead with the respective sodium salts. The salification of these compounds is relatively simple due to the presence of carboxylic acid as the only reactive site. The reactions were conducted in the presence of stoichiometric NaOH. The most reactive molecule is acetylsalicylic acid, which also contains an ester group that could undergo hydrolysis under these conditions. To avoid the formation of a mixture of salification and hydrolysis products, the reaction was conducted at low temperatures by adding a dropwise solution of NaOMe. This approach favored the selective reaction with the carboxylic acid over the ester group. Once isolated as dry powders, the products were characterized by ATR-MIR spectroscopy. Although not a quantitative analysis, ATR-MIR is useful in identifying the nature of the products because of the characteristic peaks of the carbonyl and carboxylic groups. As shown in Figure 2, comparison of the spectra of the active ingredient and its corresponding salt clearly shows the disappearance of the characteristic peaks at 1721 cm^{-1}, 1419 cm^{-1} and 948 cm^{-1}, which correspond to C=O stretching and -OH bending, respectively. Furthermore, two new signals appear at 1550 and 1400 cm^{-1}, relative to the symmetrical and antisymmetrical stretching of the carboxylate groups. This confirms the complete consumption of the starting material, which has been quantitatively converted into the salt.

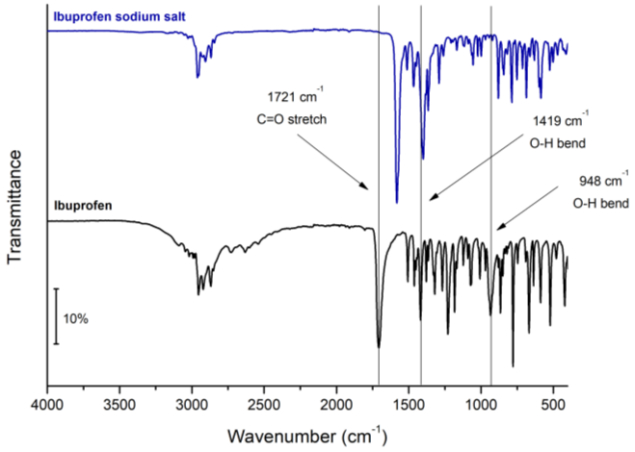

Figure 2. ATR-MIR spectra of ibuprofen and ibuprofen sodium salt.

Once all the drugs were converted into their salt forms, we returned to the primary objective of this study: loading NSAIDs into ZIF-8. However, instead of using the conventional stirring method, we employed a probe sonicator for the loading process. The underlying principle of this approach is to utilize the ultrasonic waves to solubilize the obtained salts in a solvent that is inherently unfavorable for these compounds, thereby making ZIF-8 a more suitable environment for their incorporation. To optimize this process, a solubility screening was conducted in various solvents, including water, methanol, isopropanol, and acetonitrile. Among these, acetonitrile proved to be the most effective, as the selected NSAID salts exhibited poor solubility in this solvent, favoring their entrapment within the ZIF-8 framework (Figure 3).

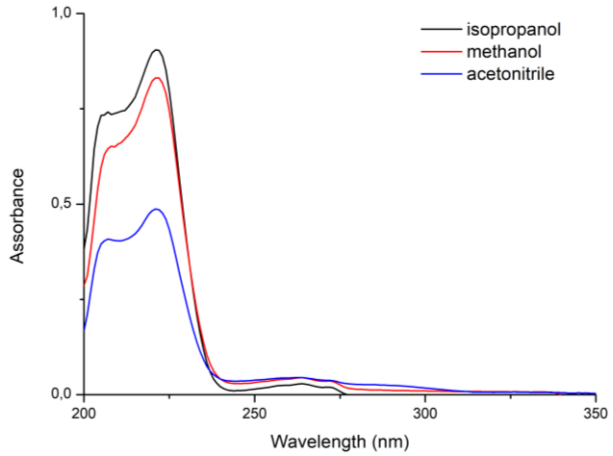

Figure 3. UV-Vis spectra of ibuprofen washing solutions in isopropanol, methanol and acetonitrile.

This approach was applied to all NSAIDs under study, and the resulting materials were thoroughly characterized. XRPD analysis confirmed the structural integrity of the crystal structure (Figure 4), while SEM microscopy (Figure 5) and ATR-MIR spectroscopy (Figure 4) verified the encapsulation of the active pharmaceutical ingredients within ZIF-8 and the superficial structural integrity. In addition, physisorption of nitrogen at 77 K revealed a reduction in surface area, indicative of the incorporation of molecules host (Figure 5).

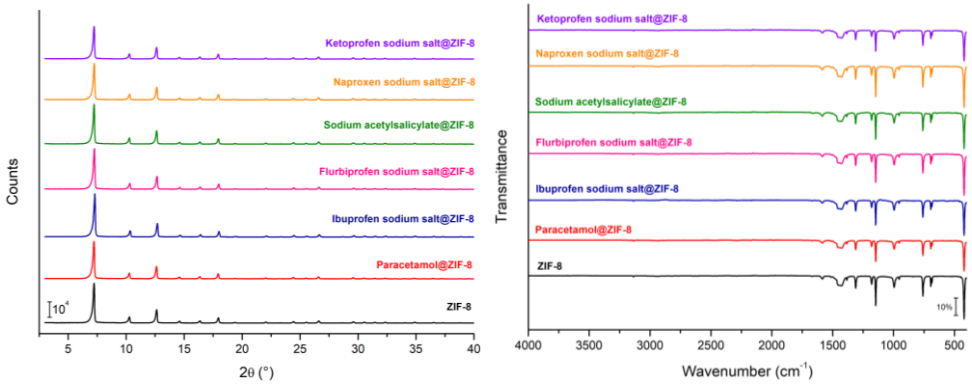

Figure 4. comparison of the experimental XRPD pattern (left) and ATR-MIR spectra (right) of pure ZIF-8 (black), paracetamol@ZIF-8 (red), ibuprofen sodium salt@ZIF-8 (blue), flurbiprofen sodium salt@ZIF-8 (magenta), sodium acetylsalicylate@ZIF-8 (green), naproxen sodium salt@ZIF-8 (orange), ketoprofen sodium salt@ZIF-8 (purple).

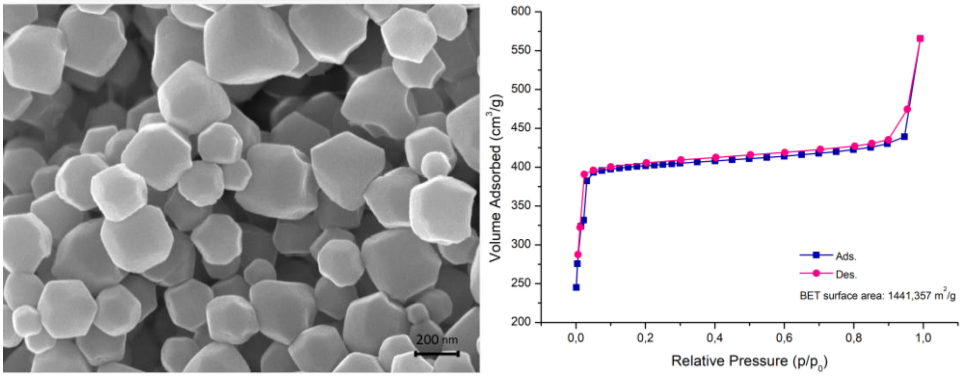

Figure 5. SEM image collected at 50 kX (left) and N_2 adsorption-desorption isotherms at 77 K (right) of the ibuprofen sodium salt@ZIF-8 system (BET surface area: 1441,357 m^2/g).

To quantify the individual active ingredients loaded within the porous structure, measurements were carried out by HPLC. The solutions analyzed were obtained by mixing the acetonitrile solution from the sonicator, after removing the ZIF-8 by centrifugation, and the MeOH washing solution. All solutions are then made up to volume with acetonitrile in a 200 mL volumetric flask. Calibration curves of the individual NSAIDs were constructed using five solutions each of known concentration, prepared to cover a linear range of concentrations representative of the test sample. The peak area values obtained for each standard were plotted against the respective concentration, and the calibration line was determined by linear regression of the data. The concentration of the active principle in the sample was then determined by interpolating the peak area value in the calibration line (Table 1).

Table 1: data from HPLC analysis and DLE% and DL% values.

Sample	DLE%	DL%	area	slope	R^2
Ibuprofen sodium salt	73.2	52.5	854.9559	4801.9	0.999
Sodium acetylsalicylate	93.4	58.5	89.9401	1994.2	0.999
Flurbiprofen sodium salt	66.9	50.3	1398.246	6359.2	0.999
Ketoprofen sodium salt	64.7	49.4	1431.8931	6090.7	0.999
Naproxen sodium salt	58.5	46.9	1224.809	4438.7	0.999
Paracetamol	81.6	55.2	500.7935	8200.9	0.999

The loading and loading efficiency values, shown in Table 1, demonstrate how efficient the use of the pulsed sonicator to load the NSAIDs used is, leading in some cases to a load efficiency of over 80%. The materials obtained show a high percentage of drug, demonstrating the ability of ZIF-8 to trap molecules of different dimensions. The use of ultrasound plays a fundamental role in this process, forcing the drugs under investigation to enter the cavities of the crystal, a more favorable environment than acetonitrile in which they are poorly soluble or insoluble.

The surface area values calculated using the BET equation confirm the loading rates, confirming the presence of the drugs within the pores of ZIF-8. The discrepancy between the surface area value of pure MOF and the different materials obtained results in pore occlusion caused by the presence of the different drugs.

The final step of this work is to observe the release behavior of ZIF-8 with each NSAID encapsulated within it, under different pH conditions. The graph derived from various concentration values obtained through UV-Vis spectroscopy clearly illustrates the different release behaviors of ibuprofen sodium salt depending on pH (Figure 6). In fact, in an acidic environment, 94% of the drug is released within 24 hours, while in a physiological pH, only 62% of the encapsulated active principle is released in the same period. Under acidic conditions, the release rapidly reaches a plateau after 36 hours,

achieving a total drug delivery of 95.7%. In contrast, to reach the same level of release under neutral pH, a period of 7 days is required. These findings indicate a controlled drug release mechanism influenced by the pH levels within the tumor microenvironment. For a generic tumor model, a faster release of ibuprofen is anticipated in the acidic regions of the tumor. This pH-responsive behavior could be particularly beneficial during early-stage treatment by enhancing the release of the anti-inflammatory agent in response to localized acidification, potentially modulating COX-2 activity in the tumor tissues.

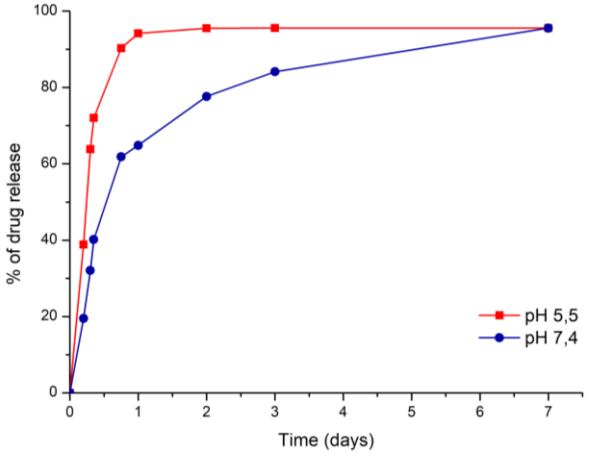

Figure 6. time-dependent release rate trend of ibuprofen at pH 5,5 (red line) and pH 7,4 (blue line).

Inflammation plays a key role in cancer development and progression. NF-κB signaling is a master regulator of inflammation,[9] drives COX-2 transcription,[11] and its upregulation is associated with prostate cancer progression and poor prognosis.[11] Moreover, NF-κB activation correlates with androgen insensitivity thus affecting prostate cancer aggressiveness that increases from androgen sensitive (AS) to androgen insensitive (AI) tumors.[12] Considering the role of inflammation in prostate cancer and

relative expression levels of COX-1 and COX-2 in different prostatic pathologies, we tested our ZIF-8 formulations on BPH, LNCaP, and DU145 cell lines. BPH cell line represents a model of benign prostatic hyperplasia, while LNCaP (AS) and DU145 (AI) are considered models of prostate carcinoma with different grades of aggressiveness. Since NSAIDs show different selectivity in inhibiting COX-1 and COX-2, we chose three ZIF-8 formulations for cell treatment, specifically Sodium Acetylsalicylate@ZIF-8, Ibuprofen sodium salt@ZIF-8, and Naproxen sodium salt@ZIF-8; while Ibuprofen and Naproxen are more selective in inhibiting COX-2, Sodium Acetylsalicylate is more selective for COX-1. To mimic the acidity of tumor microenvironment, prostate cell lines were treated both at physiological pH (7.4) and at acidic pH (6.8) and viability was assessed after 96 h. Although the microenvironment of BPH is not acidic, we treated BPH cells also in acidic pH for clarity. As shown in Figure 7, all formulations have a greater efficacy at acidic pH, confirming that the release of drugs is pH dependent. As expected, viability of BPH cells is not affected by Ibuprofen@ZIF-8 and Naproxen@ZIF-8; notably, most probably due to the expression of COX-1 in BPH,[13] viability decrease only at relatively high doses of Sodium Acetylsalicylate@ZIF-8, suggesting that Sodium Acetylsalicylate could be a good candidate in treatment of BPH disease. On the other hand, the viability of LNCaP is dependent on the concentration of ZIF-8 formulations and although it was observed also an effect at physiological pH, selected formulations showed a better performance at acidic pH, Ibuprofen@ZIF-8 particularly. Best results were obtained in most aggressive prostate cancer cell line DU145; although Sodium Acetylsalicylate@ZIF-8 significantly decrease cell viability, Naproxen@ZIF-8, the most selective towards COX-2 isoform, completely suppress cell viability at pH 6.8 and at low concentration (20 μg/ml). Importantly, viability of prostate cancer cell lines treated with free drugs decreased only at very high concentration (Figure 8) confirming

the efficacy of MOFs as drug delivery systems. Overall, no significative effect was observed in cell treated with vehicle (Methanol) and ZIF-8 alone. In summary, these data show that different NSAIDs have a specific efficacy on different prostatic pathologies and that MOFs-encapsulating formulations can be selective for cancer cells that are characterized by an acidic microenvironment compared to normal tissues.

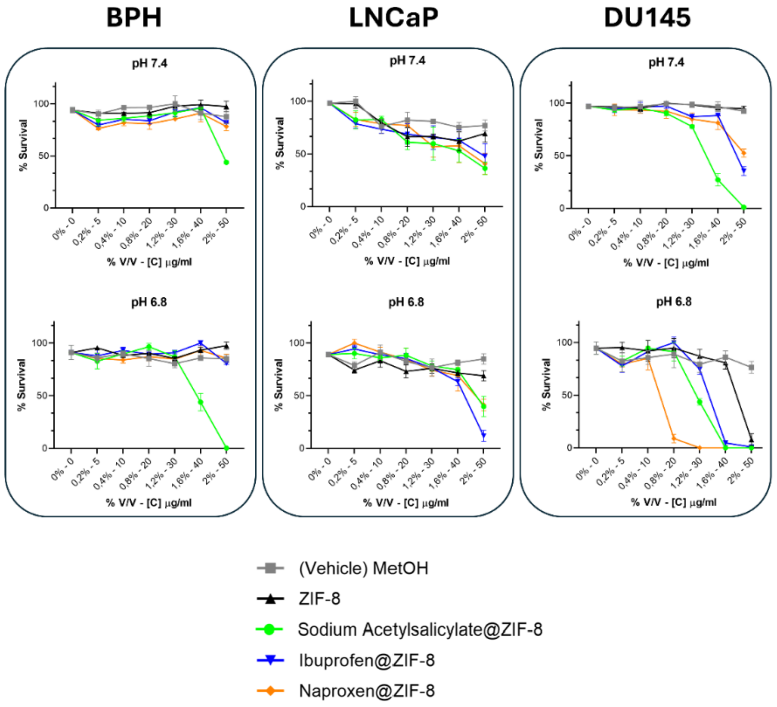

Figure 7. PrestoBlue Viability Assay on prostate cell lines. MOFs formulations were tested at a concentration range varying from 0-50 µg/ml and controls were treated with respective %V/V of Methanol (Vehicle).

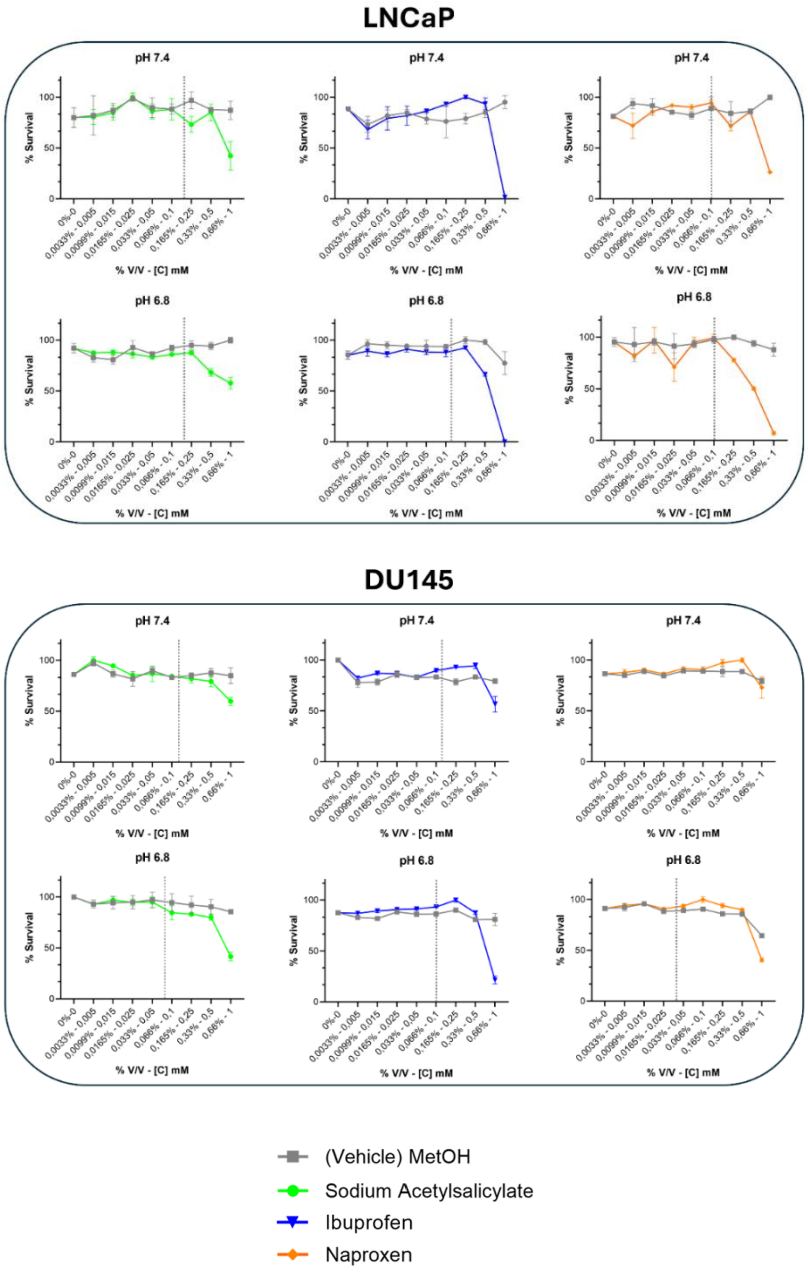

Figure 8. PrestoBlue Viability Assay on LNCaP and DU145 prostate cancer cell lines treated with free drugs. The dotted grey lines indicate the concentrations of MOF-delivered drugs that reduce cell viability to below 50% reported in Figure 7.

4.2.2 Conclusions

This study successfully demonstrated the encapsulation of NSAIDs within the pores of ZIF-8 as a potential platform for drug delivery to tumor tissues. The loading methodology employed proved effective for all NSAID species investigated. In particular, the ultrasound-assisted approach using acetonitrile as the solvent yielded the most promising results, ensuring that the NSAIDs were effectively confined within the ZIF-8 pores rather than merely adsorbed onto the external surface.

Characterization via PXRD, SEM, and ATR-MIR confirmed both the structural integrity of ZIF-8 and the localization of the drugs within the framework. Nitrogen physisorption analysis revealed a reduction in surface area, further supporting successful drug loading. HPLC analysis enabled precise quantification of the encapsulated drugs, underscoring the versatility of ZIF-8 in accommodating diverse NSAIDs.

These findings highlight the potential of ZIF-8 as a robust and adaptable nanocarrier for targeted drug delivery in oncology. The capacity of ZIF-8 to respond to the tumor microenvironment suggests that it could be employed to enhance the therapeutic efficacy of NSAIDs by modulating COX-1 and COX-2 activity in tumor tissues. More specifically, while COX-1 is constitutively expressed in many tissues, COX-2 is an inducible isoform highly expressed in inflammatory conditions such as cancer, predominantly via NF-κB activation.[14] Given the progressive activation of NF-κB during prostate cancer progression and increased tumor aggressiveness, more selective COX-2 inhibitors may prove highly valuable for the treatment of advanced prostate cancer, as demonstrated by the suppression of DU145 cancer cell viability following treatment with Naproxen@ZIF-8.

Interestingly, as observed in Sodium Acetylsalicylate@ZIF-8-treated BPH cells, certain NSAIDs may also have therapeutic potential in other prostatic pathologies. This is most likely attributable to the variable selectivity of NSAIDs towards COX-1 and COX-2, as well as to differences in COX isoform expression across pathological states, which could be exploited to design highly specific targeted therapies.

Future work will focus on the evaluation of additional ZIF-8-based drug formulations, *in vivo* assessment of drug delivery performance, and detailed investigation of release kinetics and biocompatibility.

4.2.3 Bibliography

1. Li, D.; Xu, W.; Chang, Y.; Xiao, Y.; He, Y.; Ren, S. Advances in Landscape and Related Therapeutic Targets of the Prostate Tumor Microenvironment. *Acta Biochim. Biophys. Sin.* **2023**, *55* (6), 956–973.
2. Jafari, S.; Etminan, M.; Afshar, K. Nonsteroidal Anti-Inflammatory Drugs and Prostate Cancer: A Systematic Review of the Literature and Meta-Analysis. *Can. Urol. Assoc. J.* **2009**, *3* (4), 323–330.
3. Sfanos, K. S.; de Marzo, A. M. Prostate Cancer and Inflammation: The Evidence. *Histopathology* **2012**, *60* (1), 199–215.
4. Leahy, K. M.; Ornberg, R. L.; Wang, Y.; Zweifel, B. S.; Koki, A. T.; Masferrer, J. L. Cyclooxygenase-2 Inhibition by Celecoxib Reduces Proliferation and Induces Apoptosis in Angiogenic Endothelial Cells In Vivo. *Cancer Res.* **2002**, *62* (3), 625–631.
5. Maghsoudi, H.; Sheikhnia, F.; Sitarek, P.; Hajmalek, N.; Hassani, S.; Rashidi, V.; Khodagholi, S.; Mir, S. M.; Malekinejad, F.; Kheradmand, F.; Ghorbanpour, M.; Ghasemzadeh, N.; Kowalczyk, T. The Potential Preventive and Therapeutic Roles of NSAIDs in Prostate Cancer. *Cancers* **2023**, *15* (22), 5435.
6. Tucker, G. T. Pharmacokinetic Considerations and Challenges in Oral Anticancer Drug Therapy. *Clin. Pharm.* **2019**, *10*, 1–10.
7. Al-Lawati, H.; Binkhathlan, Z.; Lavasanifar, A. Nanomedicine for the Effective and Safe Delivery of Non-Steroidal Anti-Inflammatory Drugs: A Review of Preclinical Research. *Eur. J. Pharm. Biopharm.* **2019**, *142*, 179–194.
8. di Nicola, N.; Paolucci, V.; Daniele, V.; Taglieri, G.; Crucianelli, M.; Guidoni, L.; Lazzarini, A. ZIF-8 as Potential Vector for Enhanced Target Delivery of Sulfathiazole for the Treatment of Bovine Ruminal Acidosis. *Eur. J. Inorg. Chem.* **2024**, *2024* (36), e202400504.

9. Verzella, D.; Cornice, J.; Arboretto, P.; Vecchiotti, D.; Di Vito Nolfi, M.; Capece, D.; Zazzeroni, F.; Franzoso, G. The NF-κB Pharmacopeia: Novel Strategies to Subdue an Intractable Target. *Biomedicines* **2022**, *10* (9), 2233.
10. Garg, R.; Blando, J. M.; Perez, C. J.; Lal, P.; Feldman, M. D.; Smyth, E. M.; Kazanietz, M. G. COX-2 Mediates Pro-Tumorigenic Effects of PKCε in Prostate Cancer. *Oncogene* **2018**, *37* (34), 4735–4749.
11. Vecchiotti, D.; Verzella, D.; Di Vito Nolfi, M.; D'Andrea, D.; Flati, I.; Di Francesco, B.; Zazzeroni, F.; Franzoso, G. Elevated NF-κB/SHh/GLI1 Signature Denotes a Worse Prognosis and Represents a Novel Potential Therapeutic Target in Advanced Prostate Cancer. *Cells* **2022**, *11* (13), 2118.
12. Jin, R. J.; Lho, Y.; Connelly, L.; Wang, Y.; Yu, X.; Saint Jean, L.; Matusik, R. J. The Nuclear Factor-κB Pathway Controls the Progression of Prostate Cancer to Androgen-Independent Growth. *Cancer Res.* **2008**, *68* (16), 6762–6769.
13. Hudson, C. N.; He, K.; Pascal, L. E.; Liu, T.; Myklebust, L. K.; Dhir, R.; DeFranco, D. B. Increased COX-1 Expression in Benign Prostate Epithelial Cells Is Triggered by Mitochondrial Dysfunction. *Am. J. Clin. Exp. Urol.* **2022**, *10* (4), 234–241.
14. Lim, J. W.; Kim, H.; Kim, K. H. Nuclear Factor-κB Regulates Cyclooxygenase-2 Expression and Cell Proliferation in Human Gastric Cancer Cells. *Lab. Investig.* **2001**, *81* (3), 349–360.

5. Magnesium-Modified ZIF-8: A Step Closer to Biocompatible Drug Delivery

---

This chapter is based on the publication:

di Nicola, N., Spoletti, E., Lazzarini, A. & Lusi, M. (in preparation). Mg alloy affords less toxic and pH tuneable ZIF-8 for drug delivery.

The use of ZIF-8 as a drug delivery system has shown significant advantages in terms of stability and controlled release. However, prolonged use of ZIF-8-based therapies raises concerns about its potential toxicity. In particular, degradation of the structure in acidic physiological environments can release zinc ions in high quantities, with possible cytotoxic and inflammatory effects. Furthermore, the accumulation of residual material in tissues or excretory organs may pose a long-term risk, necessitating thorough toxicological evaluations to ensure safety in chronic treatments.

5.1 Solid Solutions

Solid solutions are an important class of crystalline materials characterized by the isomorphous substitution of one or more lattice constituents without significantly altering the overall crystal structure.[1] This approach allows fine modulation of the chemical, physical and biological properties of materials, making it particularly useful in the field of advanced porous materials, such as metal-organic frameworks.[2] Among these, ZIF-8 (Zeolitic Imidazolate Framework-8), based on Zn^{2+} ions and imidazole ligands, has attracted growing interest for applications in controlled drug delivery due to its high stability, porosity and sensitivity to the acidic environment typical of many

pathological microenvironments.[3] However, one of the main limitations to the prolonged use of ZIF-8 in the biomedical field lies in the potential toxicity associated with the release of zinc ions during the degradation of the framework.[4] High levels of Zn^{2+} can interfere with normal cellular processes, causing oxidative stress, inflammation and, in some cases, cell death, especially in sensitive tissues or in long-term treatments.

To overcome this critical issue, the introduction of solid solutions by partially replacing zinc with less toxic metals, such as magnesium, is a promising option. Magnesium is a biocompatible metal, already widely present in the human body,[5] and its incorporation into the ZIF-8 structure allows its toxicity to be mitigated while maintaining the crystalline structure and essential functional properties of the material. The choice of magnesium is not accidental, as it is the trace element most similar to Zn^{2+} in terms of charge and atomic radius. The inclusion of Mg^{2+} in place of some of the Zn^{2+} ions can significantly reduce the total amount of zinc released into the biological environment, thus improving the tolerability of the material without compromising its ability to encapsulate and release drugs in a controlled manner. Furthermore, this substitution can also influence other crucial parameters, such as degradation kinetics, thermal and chemical stability, and interactions with biomolecules, paving the way for a more rational and safer design of MOFs for advanced therapeutic applications. The aim of this work, carried out in the laboratories of the University of Limerick during a period abroad, was first and foremost to find an effective synthetic strategy for the partial replacement of the Zn^{2+} atoms that form the framework and then to thoroughly characterize the new crystalline material, not only by studying its crystallographic properties but above all by comparing its general aspects with the original ZIF-8.

5.2 Results and Discussion

According to the HSAB theory, the sp^2 nitrogen atoms and the aromaticity of the ring make 2-methylimidazole (MIM) a borderline (soft) base while Zn^{2+} is an intermediate acid, as it is small yet polarizable.[6] In contrast, Mg^{2+} is a hard acid due to its small size and non-polarizable nature. For this reason, less robust coordination with 2-methylimidazole is expected.[7] In fact, zinc-based ZIF-8 can be readily synthesized in water as microcrystalline powder,[8] or in DMF affords larger single crystals.[9] Either method fails to afford the pure Mg or the mixed Zn/Mg phases, yielding instead a mixture of pure Zn-ZIF-8 and other Mg salts. On the other hand, the protonation of 2-methylimidazole in concentrated nitric acid affords a slower nucleation and larger single crystals (around 1 mm^3) (Figure 1 left).[10] Slower kinetic, in the presence of different Zn^{2+}/Mg^{2+} ratios, resulted in equally large single crystals. SEM-EDX analysis confirmed the homogeneous incorporation of both metals within the crystals (Figure 1 right) up to 20% of Mg. However, all crystallization attempts with higher Mg ratio (i.e. > 30%) led to a reduction in the crystallites size and lower incorporation of Mg into the ZIF-8 (5 to 10%).

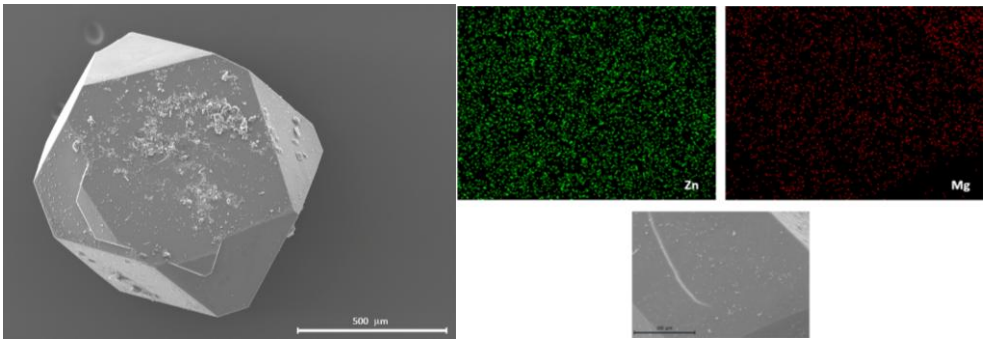

Figure 1. SEM image (left) and EDX map of Zn and Mg distribution (right) of a single crystal of 20%Mg-ZIF-8.

Due to the hydrolysis of DEF to formic acid, single crystals of Mg-formate $[Mg_6(HCOO)_{12}]\cdot DEF$ (CSD Refcode: KAVRIK)[11] appeared when 100% Mg was used (Figure 2 left).[12] From the crystallization batch with 20% Mg, a single crystal was analyzed by X-ray diffraction, confirming the identity of the structure with that of ZIF-8, cubic *I*-43*m* space group. The occupancy refinement of the metal site showed a Zn:Mg ratio of 77:23 while 5 DEF molecules were observed in the pores. XRPD analysis of the ground crystals showed the structural uniformity of the product (Figure 2 right), hence demonstrating the straightforward realization of a solid solution.

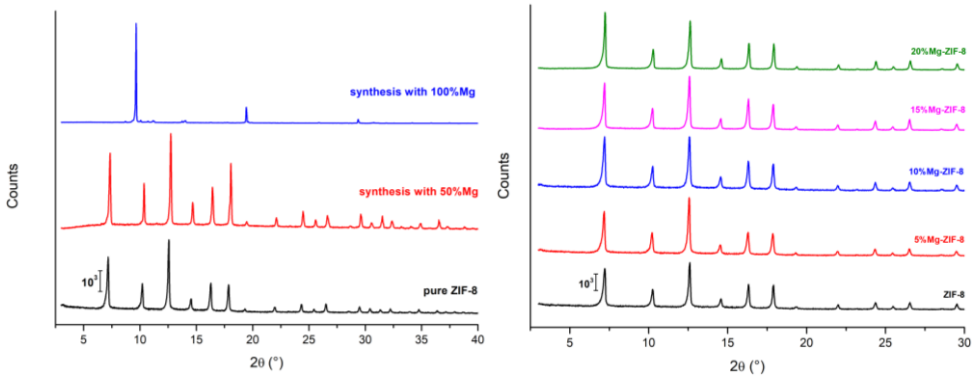

Figure 2. comparison of the experimental XRPD pattern for the synthesis of pure ZIF-8 (black), with the 50% of Mg (red) and the 100% of Mg ($[Mg_6(HCOO)_{12}]\cdot DEF$ complex) (blue) (left) and for the ZIF-8 syntheses performed with different percentages of Mg^{2+}(right).

From each of the four crystallization batches at 5, 10, 15 and 20% Mg/Zn ratio, a few single crystals were isolated and their average composition determined by ICP-MS. Only minor deviations were observed between the stoichiometry of the reacting solutions and that of the products (Table 1). Notably, the Mg/Zn substitution does not affect the surface area of the material, which remains within 5% across all compositions (Table 1) proving the robustness of the synthetic procedure and also the precise control in the stoichiometric range. Microcrystalline Zn/Mg-ZIF-8 of varied compositions

(0%, 10% and 20% Mg) were each suspended in buffer solutions at pH 6.5, in the presence of a known amount of Silicon standard (NIST Silicon powder). At fixed intervals, for up to 24 hours, the slurries were dried and quantitative analysis of the crystalline phases performed by Rietveld method.

Table 1: ICP-MS quantification of Mg^{2+}/Zn^{2+} ratio and BET surface area.

Entry	ppm Mg^{2+}	ppm Zn^{2+}	%[a]	BET surface area (m^2/g)
5% Mg-ZIF-8	84	3885	5.5	1620.189
10% Mg-ZIF-8	161	3655	10.6	1614.149
15% Mg-ZIF-8	221	3507	14.5	1604.541
20% Mg-ZIF-8	350	3135	23.1	1611.495

[a]: experimental molar percentage of Mg^{2+} to total moles of Zn^{2+} and Mg^{2+}.

As expected due to partial hydrolyses, a reduction of the relative amount of ZIF-8 was observed after 2 hours regardless of the metal composition (Figure 7).[13] However, such reduction appeared much more significant for pure Zn-ZIF-8 than for the alloys (40% versus 15%). At pH 6.5 no further decomposition was observed after the initial loss, as if an equilibrium was reached between liquid and solid phases suggesting improved stability for the alloy (Figure 3, 4, 5 left). When the same experiment was repeated at pH 5.5 the stability advantage was much more evident. (Figure 3, 4, 5 right).

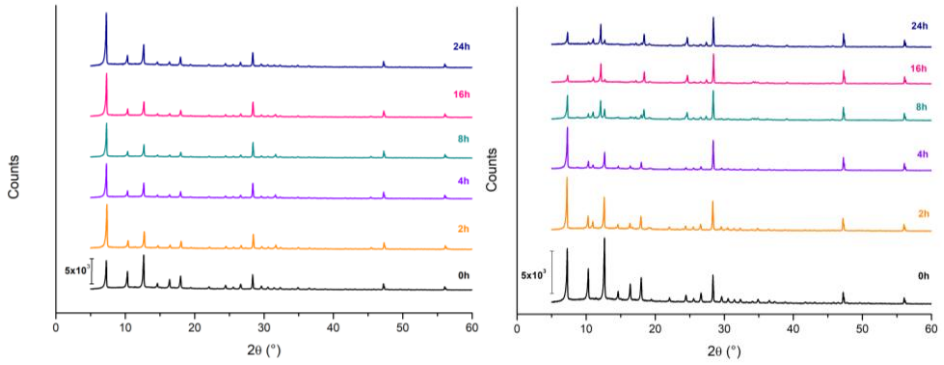

Figure 3. comparison of the experimental XRPD pattern for the suspension of ZIF-8 with Si standard digested for 0 (black), 2 (yellow), 4 (purple), 8 (dark cyan), 16 (magenta) and 24 (blue) hours in buffer solutions at pH 6.5 (left) and pH 5.5 (right).

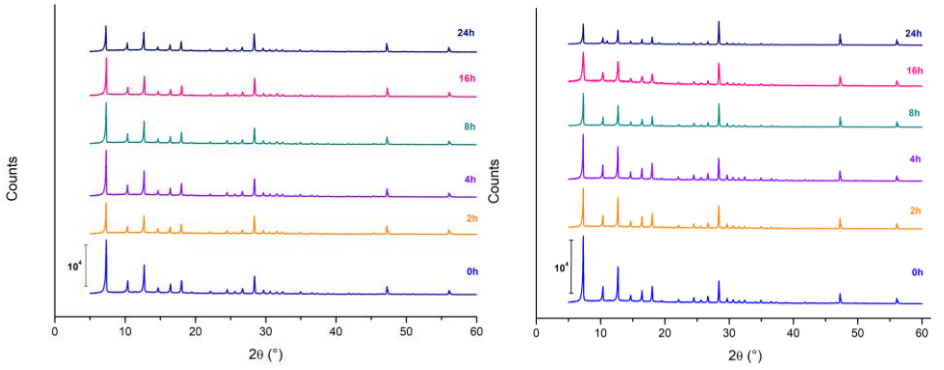

Figure 4. comparison of the experimental XRPD pattern for the suspension of 10%Mg-ZIF-8 with Si standard digested for 0 (blue), 2 (yellow), 4 (purple), 8 (dark cyan), 16 (magenta) and 24 (blue) hours in buffer solutions at pH 6.5 (left) and pH 5.5 (right).

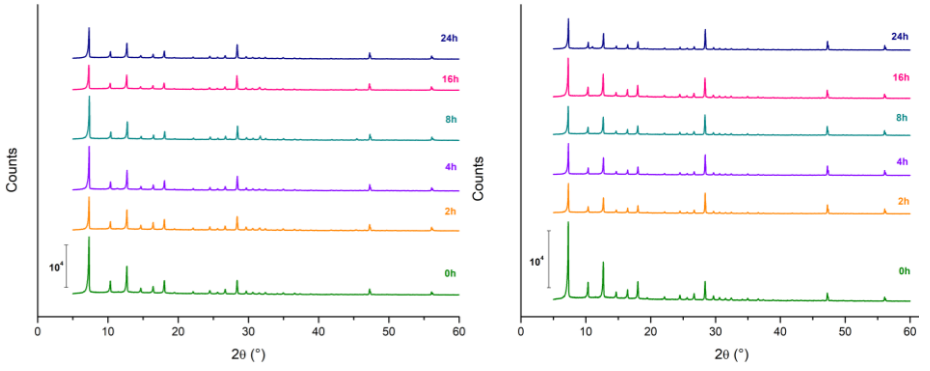

Figure 5. comparison of the experimental XRPD pattern for the suspension of 20%Mg-ZIF-8 with Si standard digested for 0 (green), 2 (yellow), 4 (purple), 8 (dark cyan), 16 (magenta) and 24 (blue) hours in buffer solutions at pH 6.5 (left) and pH 5.5 (right).

In particular, the XRPD analysis of the pure Zn-ZIF-8 showed traces of a different phase (small peak at 11°) after 2 hours digestion, possibly $Zn_5(HMIM)_4(MIM)_6(OH)_4$ hypothesized by H. Zhang et al.[13] As the digestion time increases, additional new peaks appear with increasing intensity (at 12.1°, 18.4° and 24.6°), which could not be indexed by other expected phases (Figure 6) . The idea is that the new phase is a new Zn-MIM complex (as observed in the presence of HCO^{3-} and HPO_4^{2-}).[14]

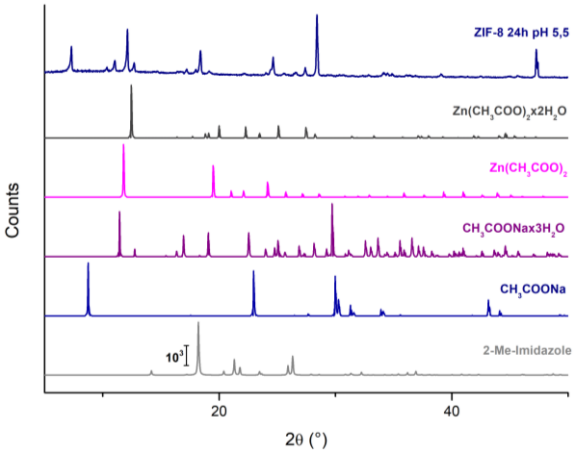

Figure 6. comparison of the experimental XRPD pattern for the suspension of ZIF-8 with Si standard digested for 24 hours in buffer solutions at pH 5.5 and the calculated pattern for HMIM, sodium acetate, sodium acetate trihydrate, zinc acetate and zinc acetate dihydrate.

At the same time Rietveld refinement confirms the exponential decay of the Zn-ZIF-8 phase (Figure 7). In contrast the decomposition of the alloys resulted significantly slower with early trances of the new crystalline product only visible in the XRPD patterns after 24h digestion. Limited decomposition of the Mg/Zn-ZIF-8 was measured in the same lapse of time: around 20-25%, (Figure 7). The stability advantage is not measurable at pH 4.5 as all the

samples fully decompose in less than an hour, leaving only the Si standard as precipitate.

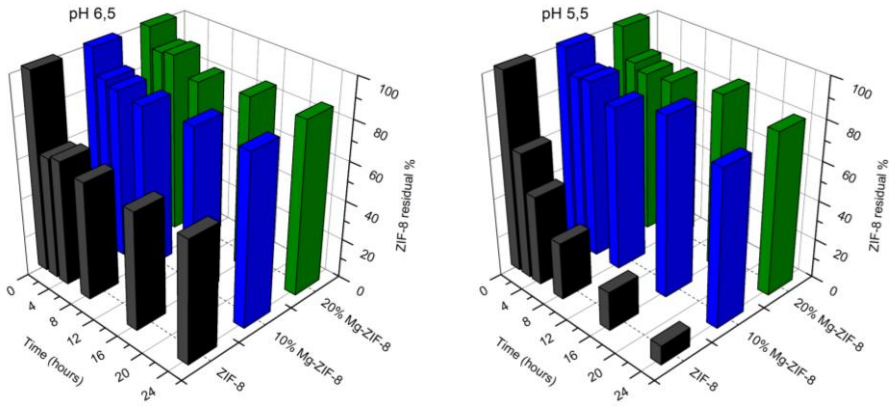

Figure 7. Histograms representing the degradation of ZIF-8, 10%Mg-ZIF-8 and 20%Mg-ZIF-8 at pH 6.5 (left) and 5.5 (right); normalized values obtained from quantitative phase analysis by Rietveld refinement.

The resistance to hydrolysis exhibited by partially substituted Mg/Zn-ZIF-8 is counter intuitive considering that the Zn^{2+}—that pure Mg-ZIF-8 is very unstable.[15] It has been proposed that water solubility (i.e. reactivity in water) increases with both dipole and polarizability. DFT calculation on model substructures confer that MIM-Zn^{2+}-MIM complex has a larger covalent component and smaller dipole than the equivalent MIM-Mg^{2+}-MIM complex (metal valence 2.0 vs 1.7), which justify a higher water stability. However, the higher ionic character translates into lower polarizability (140 vs 131). Additionally, when the simulation is repeated on larger substructures (MIM-Zn^{2+}-MIM-Zn^{2+}-MIM and MIM-Zn^{2+}-MIM-Mg^{2+}-MIM) it appears that the presence Mg increases slightly the valency of the adjacent Zinc (1.974 vs 1.977). Once again this can be explained with the higher acidity of Mg, which delocalizes larger electron density on the MIM and enables a more covalent character in the Zn^{2+}—N coordination (Scheme 1). Then, the stronger Zn^{2+}—N

bonds could compensate for the weaker Mg^{2+}—N ones and translate into a more stable crystal.

The idea is that in the solid solution polarizability and dipole moment or valency have opposite contributions, whose final effect is increased water stability. The effect must reverse, at Mg/Zn ratio larger than 20% (or 1:4), when the probability of having two Mg attached to a single MIM increases.

Equally surprising it is the fixed stability gain measured for the mixed metal ZIF-8 regardless of the composition, with the 10% and 20% alloys behaving almost identically. Perhaps this is due to narrow chemical space investigated in this work that prevents to observe a stoichiometry dependent effect. Shall this be case, it cannot alternative synthetic methods might lead to the incorporation of greater amount of Mg for even greater stability.

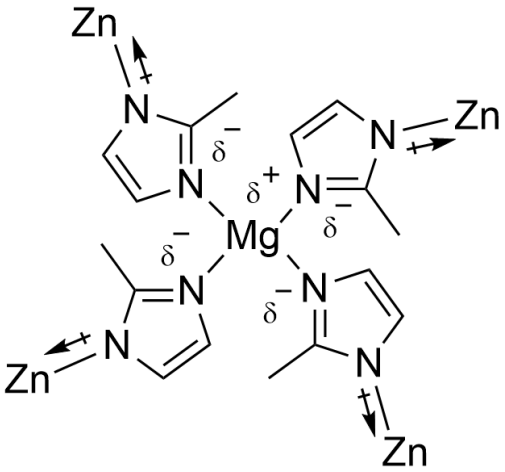

Scheme 1. Mg coordination within the framework and hypothesized electronic distribution.

5.3 Conclusions

The realization of a solid solution of ZIF-8 containing up to 20% of Mg under mild solvothermal condition is demonstrated by single-crystal XRD, ICP-MS, and EDX. XRPD and nitrogen physisorption confirm that incorporation

of the alkaline heart metal does not impact on crystallinity or surface area of the product and degradation studies at pH 6.5 and 5.5 prove that the presence of Mg effectively increases the stability of ZIF-8 in mildly acidic environments. Compared to Zn, which can accumulate over time and potentially lead to toxicity, Mg is an essential trace element that plays a crucial role in various biological processes in the human body and less likely to cause long-term adverse effects. Therefore, its substitution to Zn promises to enhance the biocompatibility of ZIF-8 and reduce its toxicity. At the same time, the improved chemical stability makes the material a good candidate for applications requiring controlled degradation and slow drug release. In this view, alternative synthetic methods may further increase the accessible compositional range and pH stability of ZIF-8. If similar results will be demonstrated for other systems, stability of other PCPs and MOFs could be improved by metal doping, which would address one of the major limitations for their real world applications.

5.4 Bibliography

1. Lusi, M. Engineering Crystal Properties through Solid Solutions. *Cryst. Growth Des.* **2018**, *18* (6), 3704–3712.
2. Liu, S. Y.; Zhou, D. D.; He, C. T.; Liao, P. Q.; Cheng, X. N.; Xu, Y. T.; Chen, X. M. Flexible, Luminescent Metal–Organic Frameworks Showing Synergistic Solid-Solution Effects on Porosity and Sensitivity. *Angew. Chem., Int. Ed.* **2016**, *55* (52), 16021–16025.
3. Gao, W.; Han, X.; Li, L.; Xu, Y.; Xu, M.; Gao, Z.; Wang, C. Functionalized ZIF-8 as a Versatile Platform for Drug Delivery and Cancer Therapy: Strategies, Challenges and Prospects. *J. Mater. Chem. B* **2025**, 13, 3758-3785
4. Plum, L. M.; Rink, L.; Haase, H. The Essential Toxin: Impact of Zinc on Human Health. *Int. J. Environ. Res. Public Health* **2010**, *7* (4), 1342–1365.
5. Martin, R. B. Bioinorganic Chemistry of Magnesium. *Metal Ions Biol. Syst.* **1990**, *26*, 1–13.
6. Dennehy, M.; Delgado, F.; Agotegaray, M.; Campelo, A.; Freire, E.; Baggio, R. Structure and Toxicity of N-Donor Thionate Zn Complexes. *J. Mol. Struct.* **2022**, *1253*, 132241.
7. Schejn, A.; Balan, L.; Falk, V.; Aranda, L.; Medjahdi, G.; Schneider, R. Controlling ZIF-8 Nano- and Microcrystal Formation and Reactivity through Zinc Salt Variations. *CrystEngComm* **2014**, *16* (21), 4493–4500.
8. Pan, Y.; Liu, Y.; Zeng, G.; Zhao, L.; Lai, Z. Rapid Synthesis of Zeolitic Imidazolate Framework-8 (ZIF-8) Nanocrystals in an Aqueous System. *Chem. Commun.* **2011**, *47* (7), 2071–2073.

9. Lee, Y. R.; Jang, M. S.; Cho, H. Y.; Kwon, H. J.; Kim, S.; Ahn, W. S. ZIF-8: A Comparison of Synthesis Methods. *Chem. Eng. J.* **2015**, *271*, 276–280.
10. Deacon, A.; Briquet, L.; Malankowska, M.; Massingberd-Mundy, F.; Rudić, S.; Hyde, T.; Johnson, T. Understanding the ZIF-L to ZIF-8 Transformation from Fundamentals to Fully Costed Kilogram-Scale Production. *Commun. Chem.* **2022**, *5* (1), 18.
11. Kim, H.; Sun, Y.; Kim, Y.; Kajiwara, T.; Yamashita, M.; Kim, K. Metal–Organic Frameworks with Rare Topologies: Lonsdaleite-Type Metal Formates and Their Magnetic Properties. *CrystEngComm* **2011**, *13* (7), 2197–2200.
12. Brown, R. S.; Bennet, A. J.; Slebocka-Tilk, H. Recent Perspectives Concerning the Mechanism of H3O+- and Hydroxide-Promoted Amide Hydrolysis. *Acc. Chem. Res.* **1992**, *25* (11), 481–488.
13. Zhang, H.; Zhao, M.; Yang, Y.; Lin, Y. S. Hydrolysis and Condensation of ZIF-8 in Water. *Microporous Mesoporous Mater.* **2019**, *288*, 109568.
14. Wang, H.; Jian, M.; Qi, Z.; Li, Y.; Liu, R.; Qu, J.; Zhang, X. Specific Anion Effects on the Stability of Zeolitic Imidazolate Framework-8 in Aqueous Solution. *Microporous Mesoporous Mater.* **2018**, *259*, 171–177.
15. Horike, S.; Kadota, K.; Itakura, T.; Inukai, M.; Kitagawa, S. Synthesis of Magnesium ZIF-8 from $Mg(BH_4)_2$. *Dalton Trans.* **2015**, *44* (34), 15107–15110.

6. Beyond Drug Delivery: Exploring PCN-224 for MRI Contrast Enhancement

---

This chapter is based on the publication:

di Nicola, N., Vandone, M., Alonzi, R., Di Vito Nolfi, M., Ferella, F., Guidoni, L., Crucianelli, M., Zazzeroni, F., Colombo, V., Vecchiotti, D., Galante, A. & Lazzarini, A. (in preparation). Gd^{3+}- and Mn^{2+}-Doped Porphyrin-Based Metal Organic Frameworks for MRI Applications.

Magnetic resonance imaging (MRI) is an advanced diagnostic imaging technique widely used in clinical settings due to its ability to provide detailed images of soft tissues without the use of ionizing radiation. The principle behind MRI is based on the alignment of hydrogen nuclei (protons) present in body tissues within an external magnetic field, followed by their excitation by radiofrequency pulses and the subsequent detection of the signal emitted during relaxation. To improve the contrast between different tissues and make lesions or abnormalities more visible, paramagnetic contrast agents are often used, which are capable of altering the relaxation times of protons in the regions where they accumulate. The most common contrast agents are based on gadolinium (Gd^{3+}), a lanthanide metal that is highly effective in reducing the T_1 relaxation time but potentially toxic if not stably complexed. For this reason, the design of new, safer, more effective and possibly multifunctional contrast agents is an area of intense research in biomedical imaging.

6.1 PCN-224 for MRI Applications

Among the different classes of MOFs, the one with porphyrin linkers is one of the most fascinating.[1] PCN-224 is one of the best known of these and is well-known for its ability to chelate various metals.[2] This property enables these materials to be applied in a wide range of fields, including catalysis,[3] wastewater treatment,[4] and biomedical applications.[5] Porphyrin units not only provide photophysical properties suitable for catalytic applications,[6] but they can also potentially serve for biomedical targets such as photodynamic therapy (PDT),[7] or as an ideal scaffold for incorporating metal ions, making PCN-224 an attractive platform for bioimaging, especially Magnetic Resonance Imaging (MRI).[8] MRI is a non-invasive imaging technique widely used in clinical practice due to its ability to provide high-resolution, detailed images of both anatomical structures and physiological function.[9] This technique often involves the use of contrast agents, which affect the relaxation time of water protons in the tissue being imaged by altering the local magnetic field.[10] In clinical practice the most commonly used MRI contrast agents are gadolinium-based (Gd^{3+}) compounds, which are known to increase the longitudinal relaxation rate ($R_1=1/T_1$) and improve signal intensity in T_1-weighted images.[11] However, despite their widespread use, Gd^{3+} contrast media have safety issues related to metal accumulation in living organisms, causing nephrogenic systemic fibrosis (NSF), especially in patients with impaired renal function,[12] as well as accumulating in other. These concerns have pushed research into alternative agents, such as manganese-based ones (Mn^{2+}),[13] which also exhibits excellent paramagnetic properties that enhance T_1-weighted MRI images and may offer a safer toxicity profile.[14] Mn^{2+} is less toxic than Gd^{3+} and allows also tissue-specific imaging.[15] In addition, Mn^{2+} also has larger transverse relaxation rate ($R_2=1/T_2$) than Gd^{3+} (when considered in their ionic form),[16] contributing to contrast enhancement in T_2-weighted images, making it an interesting

candidate for applications requiring both T_1 and T_2 contrast enhancement.[17] In this study, two different PCN-224 functionalized MOFs (with Gd^{3+} and Mn^{2+}, respectively) were developed; noteworthy, instead of binding the Gd^{3+} and Mn^{2+} metals, both at the same time to a single material, the Gd^{3+} and Mn^{2+} ions were loaded separately onto the PCN-224 backbone to create two different materials with different MRI contrast properties. The latter procedure is advantageous in the sense that the paramagnetic properties of each metal could be optimized independently, thus allowing for a comparison of their relaxivity performance. PCN-224, with its high porosity and stable backbone, provides an ideal platform for incorporating these metals, allowing for effective loading and ensuring long-term stability under physiological conditions.[18] By comparing these materials, the potential advantages and limitations of each can be identified, contributing to the ongoing search for safer and more efficient MRI contrast agents. Indeed, the ability of the PCN-224 backbone to chelate these metals in a stable and organized framework may ensure a proper confinement of the metal ions and prevent their leaching. Concerning their applicability, this study focuses solely on *in vitro* testing as a first step toward understanding the potential of these materials in biomedical applications. *In vitro* analyses were performed to test fundamental properties of Gd@PCN-224 and Mn@PCN-224, including structural integrity, metal loading efficiency, and MRI r_1 and r_2 relaxivities measurements at a clinically relevant Larmor frequency. The stability of the materials under physiological conditions was evaluated to test their stability and functionality. Furthermore, their impact on biological systems was evaluated through cell viability assays.[19] Even though they cannot be fully capable of capturing the complexity of a biological system, they can provide the essential data to be used as a foundation for future *in vivo* studies.

The aim of this study was to investigate the synthesis, characterization, and MRI performances of Gd@PCN-224 and Mn@PCN-224. Considering both paramagnetic metals, it is possible to determine which one has the greater potential as a safer and more effective contrast agent. This research may pave the way for the development of a new-generation MRI contrast agent class with interesting imaging and biocompatibility performances.

6.2 Results and Discussion

PCN-224 material was synthetized following the procedure reported by Dawei Feng and coworkers.[20]

The material was characterized using various techniques to confirm its well-established structural and morphological properties (Figures 1 and 2). These analyses verified the integrity and purity of the MOF, prior to the post-synthetic metal loading steps. In particular, Le Bail fitting of the collected PXRD pattern on the pristine PCN-224 MOF confirmed the sample to be highly crystalline and pure,[21] while surface area analysis attested the extremely high inner specific surface possessed by this MOF.[22]

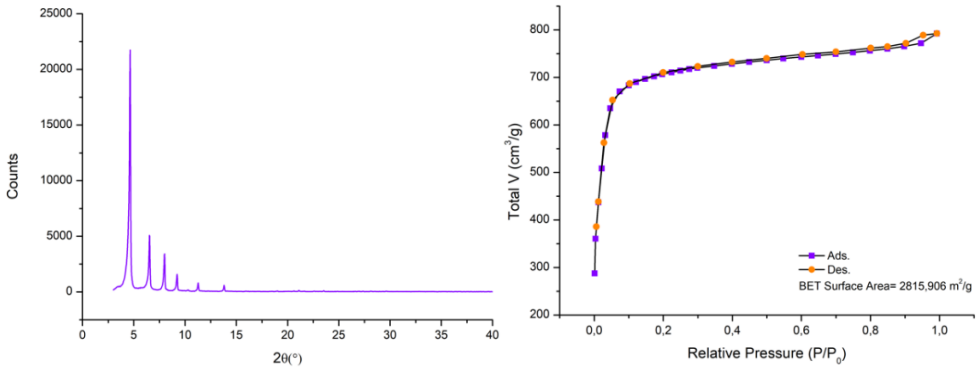

Figure 1. PXRD trace of pristine PCN-224 MOF (left) and N_2 (77 K) isotherm (right) of activated PCN-224 MOF.

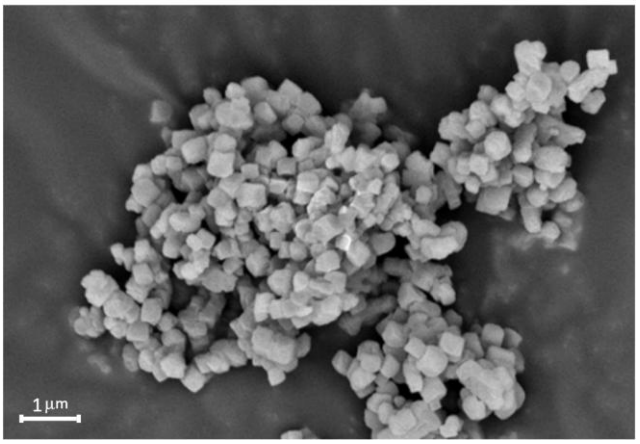

Figure 2. SEM image collected at 10 kX magnification of PCN-224.

A pH-dependent screening was conducted to identify the most effective strategy for metalating the porphyrin moieties within the PCN-224 framework. 80 mg of PCN-224 and 20.1 mg of $GdCl_3 \cdot 6H_2O$ (Gd:PCN-224 molar ratio 3:1 – Entry 1 in Table 1) were suspended in 43.2 mL of water. Such ratio was selected to match the number of porphyritic units per MOF unit cell,[21] thus considering a stoichiometric metalation of the present porphyrins. The solution was then heated at 70 °C for 4h under magnetic stirring. The same procedure was repeated in both acidic and basic environments. In the former case, acetate buffer (pH 5) was used as solvent while, in the case of basic pH, 2.2 mg of NaOH (molar ratio NaOH:Gd^{3+}:PCN-224 3:3:1 – Entry 2 in Table 1) were added into the reaction mixture. Once the reaction was finished, firstly centrifugation and washing with H_2O and then product drying overnight, were accomplished. Centrifuging the acid mixture fails to isolate any product, probably because, under those T and pH conditions, the porphyrin carboxylic acids re-protonate, thus destroying the crystal structure. To be sure to remove all the uncoordinated Gd^{3+} in the porphyrin center, a second purification step is carried out. The dried product is dispersed in 20 ml H_2O, placed in a dialysis membrane, and left under

agitation for 24h in 400 ml H_2O. After this time, the product is recovered by centrifugation and dried in an oven overnight. The amount of coordinated Gd^{3+} was quantified by ICP-MS (Table 1), and the results indicate that the most effective loading strategy involves the use of NaOH. This is likely due to the base-induced deprotonation of the pyrrolic amines in the porphyrin units, which enhances their ability to chelate Gd^{3+} ions (Figure 3).[23] Using a stoichiometric amount of NaOH relative to Gd^{3+}, an initial filling of 15.1 % of the available porphyritic sites in the PCN-224 framework was achieved. To enhance site occupancy, the Gd^{3+} loading conditions were subsequently optimized by varying the amount of base. Two additional experiments were performed: one with a two-fold increase in the NaOH:Gd^{3+} ratio (NaOH:Gd^{3+}:PCN-224 ratio of 6:3:1 – Entry 3 in Table 1), and another with a three-fold increase (NaOH:Gd^{3+}:PCN-224 ratio of 9:3:1 – Entry 4 in Tabel 1) . The latter allowed us to obtain a Gd loading of 8.1 wt.% (obtained with ICP-MS analysis), corresponding to a theoretical occupancy of 82.5% of the available porphyritic sites (Table 1). This massive enhancement in metalation efficiency is likely due to the improved charge stabilization, facilitated by the excess of OH^- anions able to coordinate the Gd^{3+} cations and assisting in balancing the 2+ charge at the deprotonated porphyrin center. Once the Gd loading reaction was optimized, the focus shifted towards loading Mn^{2+}, another paramagnetic metal used in MRI with lower toxicity compared to gadolinium. Using the same molar ratios as those applied for Gd^{3+} loading (NaOH:Mn^{2+}:PCN-224 ratio of 9:3:1), a Mn^{2+} site occupancy of 93.9% was achieved, corresponding to 3.4 wt.% of Mn^{2+} for the Mn@PCN-224 system. This value is significantly lower than that obtained for Gd^{3+}, primarily due to the substantial difference in the molar masses of the two metals.

Table 1: optimization of base stoichiometry for Gd^{3+} and Mn^{2+} loading.

Entry	Eq. NaOH[a]	ppm Gd^{3+}/Mn^{2+}	wt.%[b]	% occupied porphyritic sites
1	/	2108 (Gd)	0.21	1.9
2	1	15973 (Gd)	1.6	15.1
3	2	30060 (Gd)	3	28.8
4	3	81000 (Gd)	8.1	82.5
5	3	34000 (Mn)	3.4	93.9

a: base equivalents vs. M moles (M= Gd^{3+}, Mn^{2+}).
b: M mass vs. M@PCN-224 mass.

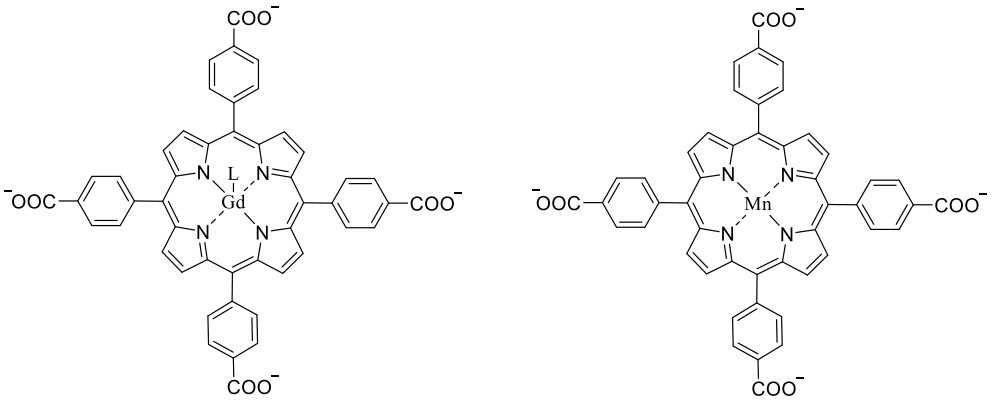

Figure 3. schematics of the coordination of metals within the porphyrin core.

Following the successful loading of both systems, the materials were characterized using a range of techniques. SEM analysis revealed noticeable changes in the crystal morphology, with the loaded samples exhibiting less defined and more heterogeneous structures compared to the pristine PCN-224 (Figure 4).

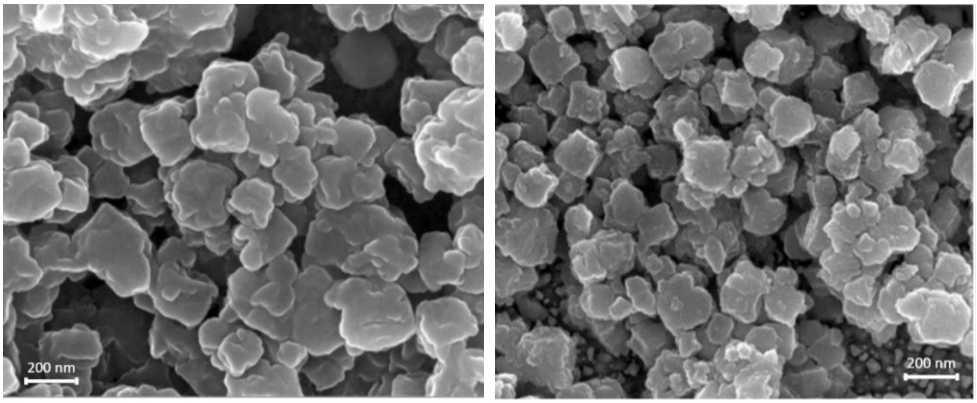

Figure 4. SEM images collected at 20 kX of Entry 4 (left) and Entry 5 (right) (see Table).

The SEM images clearly illustrate the changes in crystal morphology and surface texture; however, EDX analysis shows that these changes did not alter the elemental distribution. This applies not only to the original MOF elements but also to Gd and Mn, demonstrating that the loading within the porphyrin rings is uniform throughout the PCN-224 framework (Figure 5), and averting the formation of Gd/Mn aggregates, such as nanoparticles.

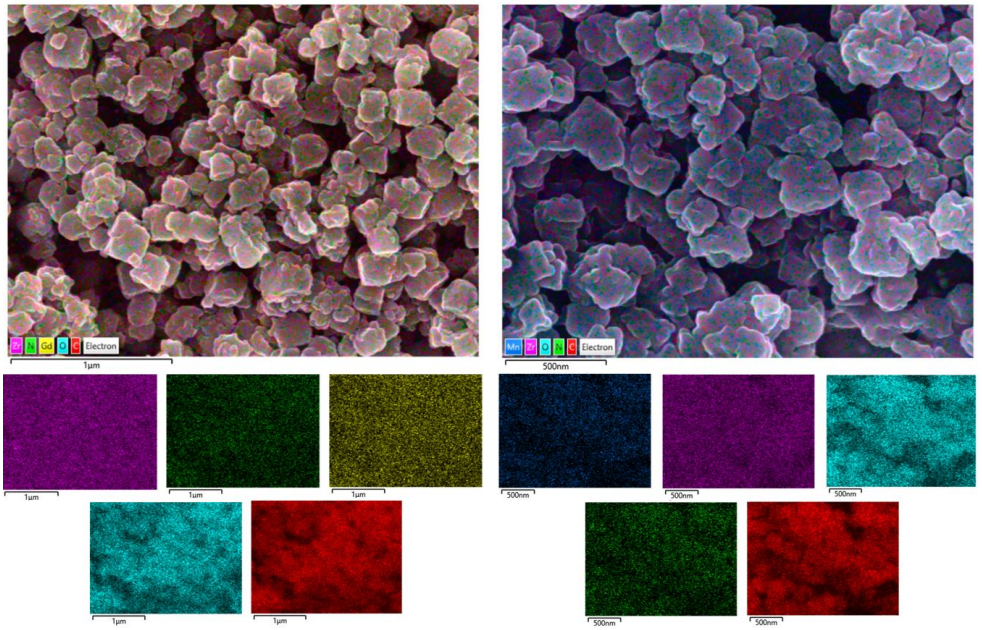

Figure 5. EDX map of the elements distribution for Entry 4 (left) and Entry 5 (right) described in Table . Color reference: purple (Zr), green (N), red (C), cyan (O), yellow (Gd), blue (Mn).

Subsequent measurements of the BET surface area confirmed that this morphological change resulted in a significant decrease in surface area, passing from 2816 m^2/g to 39 and 38 m^2/g for Gd@PCN-224 and Mn@PCN-224, respectively. This result highlights the extent to which the treatment and presence of the metal within the porphyrin core changes the morphology and thus the characteristics of the starting PCN-224 (Figure 6).

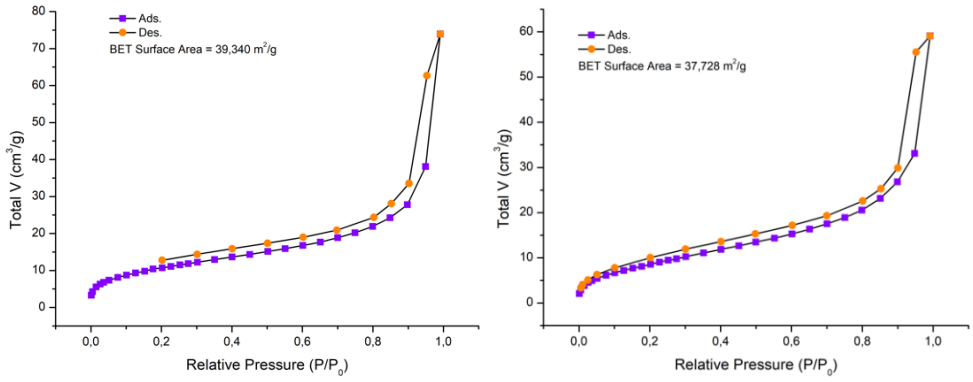

Figure 6. N_2 (77 K) isotherms of Entry 4 (BET surface area: 39.340 m^2/g) (left) and Entry 5 (BET surface area: 37.728 m^2/g) (right) described in Table 1.

The potential collapse in the surface area is also reflected in morphological changes visible in Figure 5. However, to exclude the role of the metal in such modification, a sample soaked in NaOH solution in the same conditions used for entries 4 and 5 was prepared, but without the addition of metalating agent. Figure 7 shows that, despite the retention of the crystals, some smaller though regular MOF particles appear on top of the pristine ones. In addition, rugosity on the surface of some of the MOF crystals starts to occur, potentially due to crystal structure defects appearing as grain boundaries. Both these effects may have a deep impact on the Me@PCN-224 surface area.

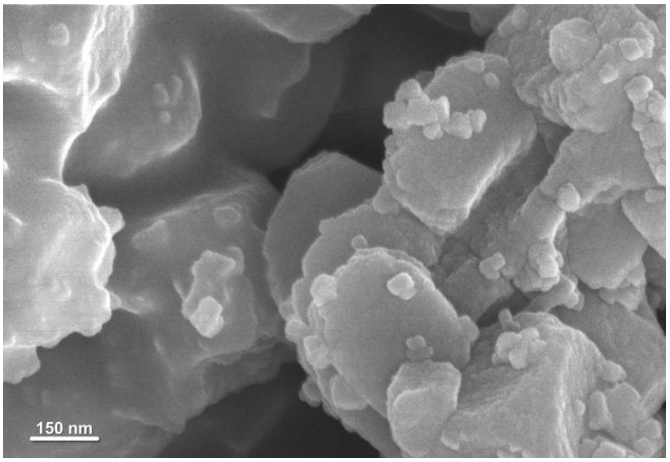

Figure 7. SEM image collected at 75 kX of PCN-224 treated in the metal loading conditions.

To determine whether the observed loss of porosity was due to partial amorphization, pore collapse or decomposition of the pristine PCN-224 sample, the impact of metalation on the materials was examined by collecting High-Resolution Powder X-ray Diffraction (HR-PXRD) data using synchrotron radiation. Figure 8a compares the PXRD patterns of pristine PCN-224 with those of its metalated analogues. Metal doping led to a substantial loss of diffraction intensities and peak broadening. Specifically, the PXRD patterns of the metalated samples were of insufficient quality to allow for the determination of unit cell parameters via Le Bail fitting, thus precluding reliable structural analysis through conventional powder diffraction methods. In contrast, the pristine PCN-224 displayed high crystallinity, as expected. Structureless Le Bail fitting indicate that it crystallizes in the expected cubic crystal system, and its PXRD profile is best described by the *P*m$\bar{3}$m space group, which is consistent with the recently reported disordered model proposed by Koschnick *et al.*, and based on a crystallographic description with a 2x2x2 supercell.[24] Given the loss of crystallinity displayed by the M@PCN-224 samples, and considering the

complementary evidence from gas adsorption isotherms (Figure 6) and SEM images (Figure 7), further investigation was necessary to assess and confirm the preservation of short-range structural order and local connectivity. In this context, Pair Distribution Function (PDF) analysis is emerging as a powerful tool to characterize *non-ideal* MOF materials with compromised ordering and low crystallinity. Accordingly, PDF analysis was employed in this study to probe the retention of local atomic arrangements within the M@PCN-224 samples (Figure 8b).

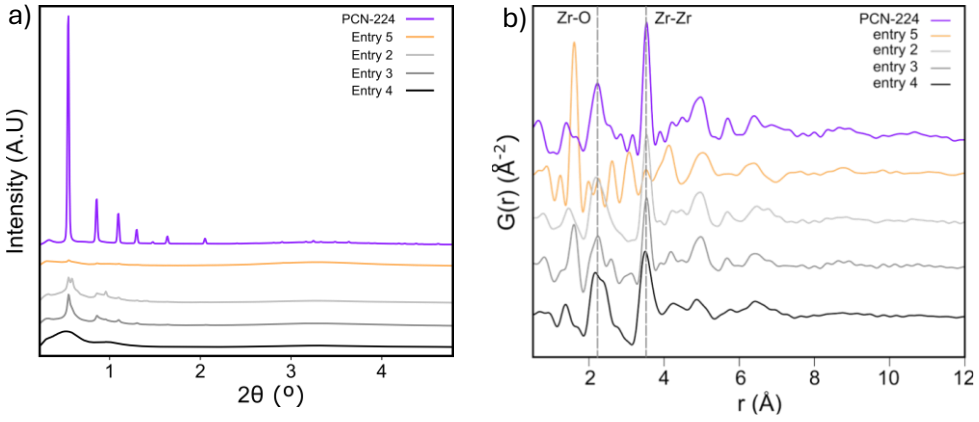

Figure 8. a) Comparison of the HR-PXRD patterns of pristine PCN-224 and M@PCN-224. b) Comparison of the PDF data of the same samples reported in plot. Vertical grey lines indicate the Zr-O and Zr-Zr bond distances.

The strong resemblance between the PDF profiles of the pristine material and the metal-dosed MOFs already suggests that the local structure is largely preserved up to 10 Å. As described above, PCN-224 possess $Zr_6(O)_4(OH)_4$ metal nodes, i.e. a Zr_6-octahedron bridged by μ^3-O and μ^3-OH groups, and with main Zr···O and Zr···Zr distances of 2.2, 3.5, and 5.0 Å, respectively.[25] To aid in the interpretation of the three main oscillations observed in the experimental PDF profiles, simulations of the corresponding partial PDFs were performed. These simulations were based on the 2×2×2 supercell of the disordered structural model in the $Pm\bar{3}m$ space group, as

identified during the structureless Le Bail refinement of the experimental PXRD pattern of the pristine PCN-224 sample used in this study.[24] The simulated profiles successfully reproduced the experimental features, supporting the validity of the structural model for our sample. Figure 9 shows the stacked partial PDFs alongside the experimental PDF of the measured samples. Additionally, simulation of the PDF signal using a Mn-loaded PCN-224 crystallographic structure reported in the CSD (entry 1570585),[26] allowed isolation of the Mn-N partial contribution, clarifying the expected position of the signal related to the Mn-N distance of the metal in the porphyritic core. However, due to the low Mn/Gd-to-Zr ratio in the materials, the corresponding metal-N contribution remains unfortunately weak and could not be clearly resolved in the experimental PDFs.

The simulation of the partial PDF indeed confirmed that these distances are still well represented in our samples, both in the pristine and in the M@PCN-224 ones. This indicates that the framework does not undergo decomposition under the metalation conditions, as substantial changes to Zr–Zr correlations would be expected if only one Zr–O bond were to break. The reduction in intensity and severe broadening of the peaks after 8 Å is indicative of the loss of long range-order of the framework, the observed loss of permanent porosity and the diminished diffraction intensities in the PXRD patterns can thus be attributed to a disruption of the long-range order and amorphization, rather than to framework decomposition.[27]

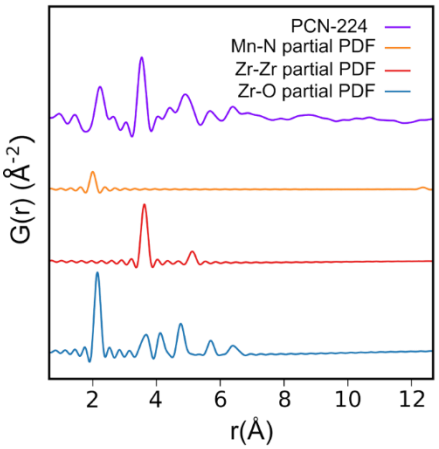

Figure 9. Comparison of the partial PDFs as obtained from the 2x2x2 supercell model,[24] and experimental PDF of the pristine PCN-224 sample. Mn-N Partial PDF signal is obtained from available Mn-dosed model (CCDC 1570585).

Once the short-range order of the metalated MOFs was confirmed, MRI analysis was performed on vials with different concentrations. The concentrations refer directly to the concentration of the paramagnetic agents in the compounds, derived from the relative measured load, except for unloaded MOF, where it refers directly to the carrier. This allows a direct comparison of different data focusing on the efficacy of a given amount of paramagnetic metals shows the longitudinal and transverse relaxation rates as a function of concentration for the different samples, together with the linear fits used to extract the relaxivities (Figure 10). For the r_2 determination we excluded the highest ionic Mn concentration because the sample's T_2 was too short compared to the minimal experimentally achievable echo time (TE), and this would introduce systematic errors in the measurement.

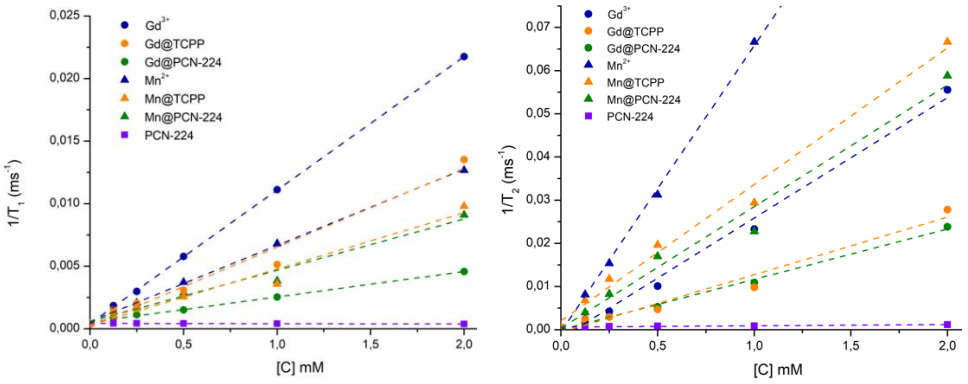

Figure 10. Relaxation rates (R_1, left panel; R_2, right panel) as a function of the concentration for Gd-based (circles) and Mn-based (triangles) complexes and PCN-224 alone (squares). Paramagnetic ions (blue) and their compounds with Tetracarboxyphenyl porphyrin (TCPP) (orange) and PCN-224 (green) are reported. The dashed lines show the regression fit.

In Figure 11, the measured relaxivities reported in Table 2 are shown. As expected, unloaded PCN-224 does not affect the relaxation rate of water protons, with measured relaxivities compatible with zero. All the R^2 values are very close to one, indicating the good water solubility of all considered compounds. Indeed, when the aggregation phenomenon occurs, the typical outcome is the loss of linearity of the relaxation rate with concentration. The paramagnetic atoms display their maximum efficacy in ionic form. When included in the TCPP and PCN-224 structures, the r_1 and r_2 relaxivities decrease by 40%, 80%, and 52%, 57% for Gd^{3+} and Mn^{2+}, respectively. Overall, the relatively large relaxivities indicate that water can easily penetrate the carriers' molecular structures and reach the paramagnetic centers, even in the case of large MOFs. The inclusion within TCPP or PCN-224 reduces the relaxivities due to limited water access to the paramagnetic sites compared to the ionic case. This effect could also be associated with different water dynamics within the porphyrin and MOF molecular structures. When comparing the ionic and MOF cases, the relaxivity reduction is milder for Mn, which maintains values closer to the ionic form.

The r_2/r_1 ratio varies from 2.6 to 5.8 for Gd, ionic and MOF cases respectively, and from 10.9 to 6.8 for Mn. Even if the starting ratios for the two metals are quite different, after inclusion within the MOF structure they seem to converge. This observation suggests that, once confined in the MOF, the relaxivity mechanisms may be dominated by the same physical phenomena. The results obtained for Gd complexes can be compared with a Gd chelate (gadopentetate dimeglumine, Gd-DTPA), widely used in clinical applications for the study of central nervous system pathologies (Magnevist®, Schering, Berlin). In water, at 1.5 T, the experimental relaxivities of the Gd-DTPA complex are $r_1 = 4.79$ and $r_2 = 5.14$, respectively.[28] At 1.0 T, the magnetic field intensities are close enough to the 1.5 T value to allow at least a qualitative comparison of results. Both Gd-DTPA and Gd-MOF relaxivities are smaller than those of ionic Gd, but Gd-MOF displays a smaller r_1 and a larger r_2 than Gd-DTPA. For Mn-DTPA, $r_1 = r_2 \simeq 1.6$ at 0.5 T,[29] with r_1 remaining essentially constant up to 1 T.[30] Contrary to the Gd case, Mn-MOF exhibits both r_1 and r_2 values larger than those of the corresponding Mn-DTPA complex. The experimental relaxivity data indicate that both compounds are promising, although Mn@PCN-224 appears particularly interesting, showing larger relaxivities than Gd@PCN-224, with r_1 and r_2 values close to those of the ionic case (about 30% and 50% reduction, respectively).

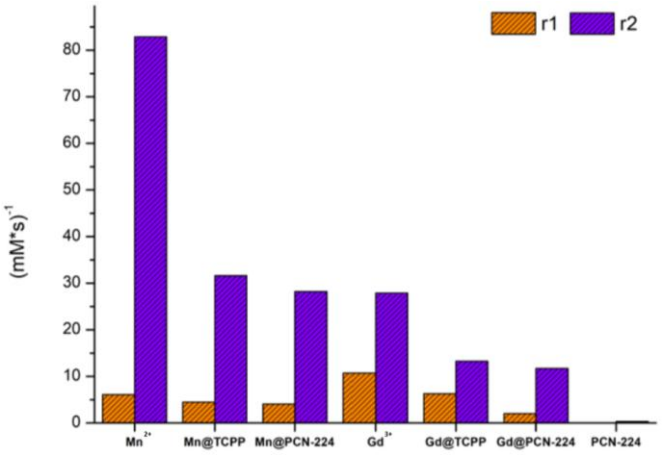

Figure 11. Relaxivities of MOFs and different compounds with Gd and Mn.

After the thorough characterization of the material, tests were performed to evaluate possible metal loss from the functionalized PCN-224. The release study was carried out in acetate buffer at pH 5, representative of the acidic tumor microenvironment relevant for MRI, and at pH 7.4, corresponding to physiological blood pH. Gd@PCN-224 and Mn@PCN-224 were incubated for one week at 37 °C in the respective buffers, confined within dialysis membranes with a molecular weight cut-off of 500 Da.

Table 2: Relaxivity values and the R^2 values of the corresponding fits.

Sample	r_1 [mM*s]$^{-1}$	R^2	r_2 [mM*s]$^{-1}$	R^2
Gd^{3+}	10.7	0.9999	27.9	0.9904
Gd@TCPP	6.3	0.975	13.3	0.9686
Gd@PCN-224	2.0	0.9968	11.7	0.9962
Mn^{2+}	6.1	0.9993	66.3	0.9886
Mn@TCPP	4.5	0.9688	31.6	0.9897
Mn@PCN-224	4.1	0.9792	28.2	0.9802
PCN-224	0	0.9505	0.3	0.9245

At the end of the incubation period, the samples were washed with H_2O and analyzed by ICP-MS to determine the amount of residual Gd^{3+} and Mn^{3+} (Table 3).

Table 3: ICP-MS analysis for the study of metal leaching from porphyrin sites.

Sample	ppm Gd^{3+}/Mn^{2+}	wt.%[a]	% occupied porphyritic sites
Gd@PCN-224 (Entry 4)	80304	8.03	82.1
Mn@PCN-224 (Entry 5)	33178	3.32	91.7

a: M mass vs. M@PCN-224 mass (M= Gd^{3+}, Mn^{2+}).

The results show that the metals inside the porphyrin ring in the Gd@PCN-224 and Mn@PCN-224 samples are stable at both pH values for a prolonged time, meaning that they could also withstand physiological pH for possible *in vivo* testing without any metal leaching.

Finally, the potential toxicity of the metalated MOFs was evaluated on the widely used 3T3 cell line. As reported in Figure 12, Mn@PCN-224 and

Gd@PCN-224 exhibited low toxicity even at high concentrations (20 μg/mL). In contrast, PCN-224 significantly affected cell viability already at very low concentrations, with a marked reduction observed between 1 μg/mL and 2.5 μg/mL. Since the absence of metal leaching from the porphyrin rings had been previously demonstrated, it was hypothesized that the porphyrin core of PCN-224 could be more prone to induce oxidation–reduction reactions, thereby promoting the formation of reactive oxygen species (ROS) and subsequent oxidative stress.[31]

Higher values and variability observed between untreated controls (UNT) and cells treated with 0.5 μg/mL and 1 μg/mL of Gd@PCN-224 may be attributed to increased cell proliferation under stress conditions. It is known that various stress stimuli, including oxidative stress below the lethality threshold, can activate several pathways involved in cell proliferation.

To confirm this hypothesis, 3T3 cells were treated with MOFs at concentrations ranging from 0.5 μg/mL to 2.5 μg/mL, and a CellRox™ assay was performed for ROS detection using a ROS-sensitive green fluorescent probe. As shown in Figure 13, 3T3 cells exposed to PCN-224 displayed higher levels of intracellular ROS compared to those treated with the metalated counterparts. Conversely, Mn@PCN-224 and Gd@PCN-224 induced ROS levels comparable to the untreated control, suggesting that their use for biological applications could be considered safe.

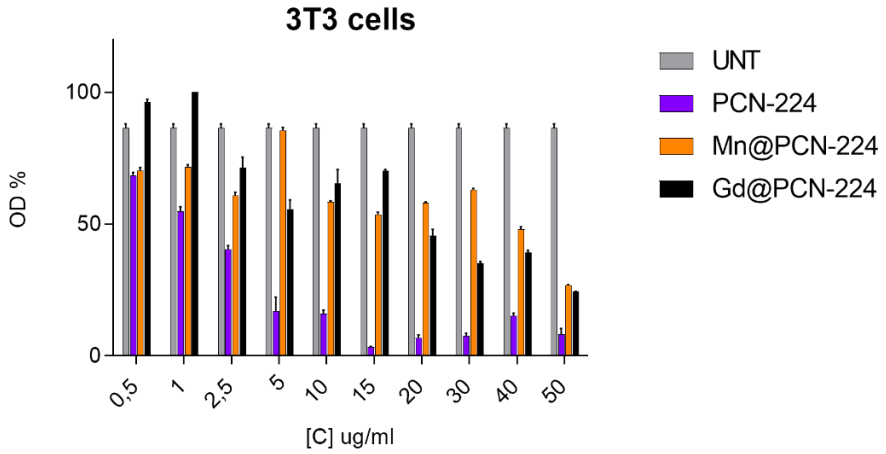

Figure 12. PrestoBlue™ viability assay on 3T3 cell line exposed to the unfunctionalized and metalated MOFs.

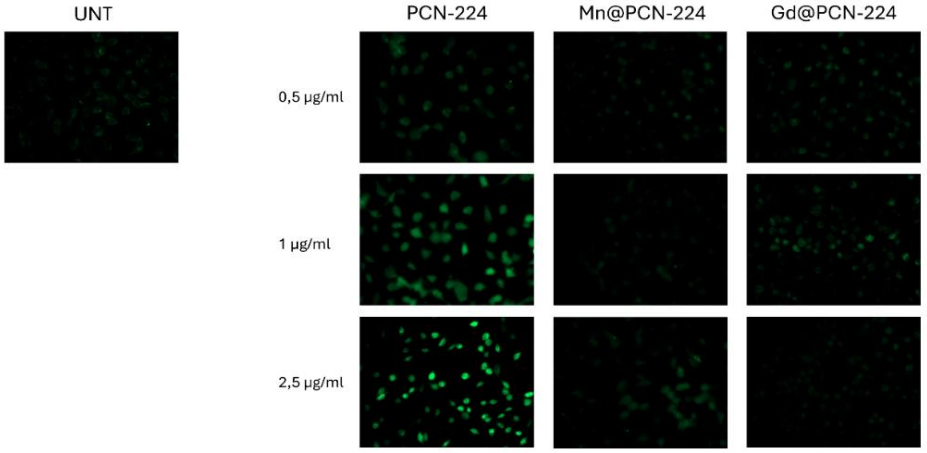

Figure 13. CellRox™ Assay at 72 hours after exposure to the unfunctionalized and metalated MOFs.

6.3 Conclusions

The aim of this work was to establish a reproducible synthetic strategy for encapsulating MRI-active paramagnetic metals, such as Gd^{3+} and Mn^{2+}, within the porphyritic core that acts as the linker of the PCN-224 framework, with the final goal of developing novel MRI contrast agents. The resulting metal-loaded MOFs exhibit biocompatibility due to their stability in physiological environments, while also holding potential for photodynamic therapy in addition to their use as contrast agents. It was observed that increasing the amount of base enhances the loading efficiency, as deprotonation of the pyrrolic amines of the porphyrin facilitates metal chelation. Despite the amorphization of the metalated materials, PDF analysis confirmed the retention of the local structure of the M@PCN-224 MOFs and, consequently, the preservation of the biological activity of the porphyritic core.

MRI measurements revealed that Gd@PCN-224 and Mn@PCN-224 display notably high relaxivities. For both systems, the r_2/r_1 ratio is close to unity, enabling their classification as positive contrast agents, suitable for T_1-weighted MRI sequences where they are expected to enhance tissue signal intensity. An especially relevant result concerns Mn@PCN-224, which exhibits an r_1 value approximately twice that of Gd@PCN-224 and comparable to the clinical standard Gd-DTPA, while offering the advantage of replacing Gd with a less hazardous, though still toxic, alternative.

An essential aspect for clinical translation is particle size, which must allow diffusion beyond the vascular compartment into the extracellular environment. While pristine PCN-224 possesses relatively large dimensions (on the order of 350 nm), the metalated frameworks are typically smaller, a feature favorable for biomedical applications. Toxicological evaluation on 3T3 fibroblasts indicated that Mn@PCN-224 and Gd@PCN-224 are well

tolerated up to 20 μg/mL, whereas PCN-224 exhibited higher toxicity, likely due to its intrinsic ability to induce oxidative stress.

Although further studies are required before assessing the clinical utility of these systems, the present findings provide promising evidence supporting the continued development of Mn@PCN-224 and Gd@PCN-224 for biological, including *in vivo*, applications. Finally, the intrinsic modularity of the PCN-224 framework offers ample opportunities for future functionalization, ranging from the design of multimodal imaging agents to the incorporation of therapeutic payloads,[32] thereby establishing it as a versatile platform for prospective theranostic applications.[7]

6.4 Bibliography

1. Wang, H. S.; Wang, Y. H.; Ding, Y. Development of Biological Metal–Organic Frameworks Designed for Biomedical Applications: From Bio-Sensing/Bio-Imaging to Disease Treatment. *Nanoscale Adv.* **2020**, *2* (9), 3788–3797.
2. Shu, Y.; Liu, X.; Zhang, M.; Liu, B.; Wang, Z. Deactivation of Porphyrin Metal-Organic Framework in Advanced Oxidation Process: Photobleaching and Underlying Mechanism. *Appl. Catal., B* **2024**, *346*, 123746.
3. Ji, J.; Liu, F.; Yang, W.; Tan, M.; Luo, W.; Yin, S. F. Incorporation of Functional Groups in Porphyrinic Metal-Organic Frameworks by Post-Modification for Highly Efficient Oxidation Catalysis. *ChemCatChem* **2020**, *12* (17), 4331–4338.
4. Sajjadinezhad, S. M.; Tanner, K.; Harvey, P. D. Metal-Porphyrinic Framework Nanotechnologies in Modern Agricultural Management. *J. Mater. Chem. B* **2022**, *10* (44), 9054–9080.
5. Chen, L. J.; Zhao, X.; Yan, X. P. Porphyrinic Metal-Organic Frameworks for Biological Applications. *Adv. Sensor Energy Mater.* **2023**, *2* (1), 100045.
6. Zhang, X.; Liu, Z.; Shao, B.; Liang, Q.; Wu, T.; Pan, Y.; Huang, J. Porphyrin-Based Metal-Organic Framework Photocatalysts: Structure, Mechanism and Applications. *Small Methods* **2025**, 2402096.
7. Park, J.; Jiang, Q.; Feng, D.; Mao, L.; Zhou, H. C. Size-Controlled Synthesis of Porphyrinic Metal–Organic Framework and Functionalization for Targeted Photodynamic Therapy. *J. Am. Chem. Soc.* **2016**, *138* (10), 3518–3525.

8. Figueira, F.; Tomé, J. P.; Paz, F. A. A. Porphyrin Nanometal-Organic Frameworks as Cancer Theranostic Agents. *Molecules* **2022**, *27* (10), 3111.
9. Katti, G.; Ara, S. A.; Shireen, A. Magnetic Resonance Imaging (MRI)—A Review. *Int. J. Dent. Clin.* **2011**, *3* (1), 65–70.
10. Xiao, Y. D.; Paudel, R.; Liu, J.; Ma, C.; Zhang, Z. S.; Zhou, S. K. MRI Contrast Agents: Classification and Application. *Int. J. Mol. Med.* **2016**, *38* (5), 1319–1326.
11. Aime, S.; Botta, M.; Terreno, E. Gd(III)-Based Contrast Agents for MRI. *Adv. Inorg. Chem.: Relaxometry of Water-Metal Ion Interactions* **2005**, *57*, 173.
12. Thomsen, H. S.; Morcos, S. K.; Almén, T.; Bellin, M. F.; Bertolotto, M.; Bongartz, G.; Reimer, P.; Webb, J. A. Nephrogenic Systemic Fibrosis and Gadolinium-Based Contrast Media: Updated ESUR Contrast Medium Safety Committee Guidelines. *Eur. Radiol.* **2013**, *23* (2), 307–318.
13. Pan, D.; Schmieder, A. H.; Wickline, S. A.; Lanza, G. M. Manganese-Based MRI Contrast Agents: Past, Present, and Future. *Tetrahedron* **2011**, *67* (44), 8431–8444.
14. Pan, D.; Caruthers, S. D.; Senpan, A.; Schmieder, A. H.; Wickline, S. A.; Lanza, G. M. Revisiting an Old Friend: Manganese-Based MRI Contrast Agents. *Wiley Interdiscip. Rev. Nanomed. Nanobiotechnol.* **2011**, *3* (2), 162–173.
15. Botta, M.; Carniato, F.; Esteban-Gómez, D.; Platas-Iglesias, C.; Tei, L. Mn(II) Compounds as an Alternative to Gd-Based MRI Probes. *Future Med. Chem.* **2019**, *11* (12), 1461–1483.
16. Niu, D.; Luo, X.; Li, Y.; Liu, X.; Wang, X.; Shi, J. Manganese-Loaded Dual-Mesoporous Silica Spheres for Efficient T1- and T2-Weighted

Dual Mode Magnetic Resonance Imaging. *ACS Appl. Mater. Interfaces* **2013**, *5* (20), 9942–9948.

17. Troughton, J. S.; Greenfield, M. T.; Greenwood, J. M.; Dumas, S.; Wiethoff, A. J.; Wang, J.; Caravan, P. Synthesis and Evaluation of a High Relaxivity Manganese(II)-Based MRI Contrast Agent. *Inorg. Chem.* **2004**, *43* (20), 6313–6323.
18. Yu, J.; Li, Q.; Wei, Z.; Fan, G.; Wan, F.; Tian, L. Ultra-Stable MOF@MOF Nanoplatform for Photodynamic Therapy Sensitized by Relieved Hypoxia Due to Mitochondrial Respiration Inhibition. *Acta Biomater.* **2023**, *170*, 330–343.
19. Hao, F.; Yan, Z. Y.; Yan, X. P. Intracellular Fate and Immune Response of Porphyrin-Based Nano-Sized Metal-Organic Frameworks. *Chemosphere* **2022**, *307*, 135680.
20. Feng, D.; Chung, W. C.; Wei, Z.; Gu, Z. Y.; Jiang, H. L.; Chen, Y. P.; Zhou, H. C. Construction of Ultrastable Porphyrin Zr Metal–Organic Frameworks through Linker Elimination. *J. Am. Chem. Soc.* **2013**, *135* (45), 17105–17110.
21. Zee, D. Z.; Harris, T. D. Enhancing Catalytic Alkane Hydroxylation by Tuning the Outer Coordination Sphere in a Heme-Containing Metal–Organic Framework. *Chem. Sci.* **2020**, *11* (21), 5447–5452.
22. Ceballos, M.; Funes-Hernando, S.; Zampini, G.; Cedrún-Morales, M.; Vila-Fungueiriño, J. M.; Pelaz, B.; del Pino, P. Seeded-Growth of PCN-224 onto Plasmonic Nanoparticles: Photoactive Microporous Nanocarriers. *Small Struct.* **2024**, *5* (5), 2300464.
23. Lu, G.; Zhang, X.; Cai, X.; Fang, Y.; Zhu, M.; Zhu, W.; Kadish, K. M. Synthesis, Structural Characterization and Protonation/Deprotonation of Hydroxyl-Substituted Free-Base Tetraphenylporphyrins in Nonaqueous Media. *J. Porphyrins Phthalocyanines* **2013**, *17* (10), 941–953.

24. Koschnick, C.; Stäglich, R.; Scholz, T.; Terban, M. W.; von Mankowski, A.; Savasci, G.; Lotsch, B. V. Understanding Disorder and Linker Deficiency in Porphyrinic Zirconium-Based Metal–Organic Frameworks by Resolving the Zr8O6 Cluster Conundrum in PCN-221. *Nat. Commun.* **2021**, *12* (1), 3099.
25. Koschnick, C.; Terban, M. W.; Canossa, S.; Etter, M.; Dinnebier, R. E.; Lotsch, B. V. Influence of Water Content on Speciation and Phase Formation in Zr–Porphyrin-Based MOFs. *Adv. Mater.* **2024**, *36* (12), 2210613.
26. Gallagher, A. T.; Lee, J. Y.; Kathiresan, V.; Anderson, J. S.; Hoffman, B. M.; Harris, T. D. A Structurally-Characterized Peroxomanganese(IV) Porphyrin from Reversible O2 Binding within a Metal–Organic Framework. *Chem. Sci.* **2018**, *9* (6), 1596–1603.
27. Bennett, T. D.; Todorova, T. K.; Baxter, E. F.; Reid, D. G.; Gervais, C.; Bueken, B.; Van de Voorde, B.; De Vos, D.; Keen, D. A.; Mellot-Draznieks, C. Connecting Defects and Amorphization in UiO-66 and MIL-140 Metal–Organic Frameworks: A Combined Experimental and Computational Study. *Phys. Chem. Chem. Phys.* **2016**, *18*, 2192–2201.
28. Sasaki, M.; Shibata, E.; Kanbara, Y.; Ehara, S. Enhancement Effects and Relaxivities of Gadolinium-DTPA at 1.5 versus 3 Tesla: A Phantom Study. *Magn. Reson. Med. Sci.* **2005**, *4* (3), 145–149.
29. Borodin, O. Y.; Sannikov, M. Y.; Belyanin, M. L.; Filimonov, V. D.; Usov, V. Y.; Rybakov, Y. L.; Shimanovskii, N. L. Relaxivity of Paramagnetic Complexes of Manganese and Gadolinium. *Pharm. Chem. J.* **2019**, *53* (7), 635–637.
30. Jackels, S. C.; Durham, M. M.; Newton, J. E.; Henninger, T. C. Aqueous Proton NMR Relaxation Enhancement by Manganese(II) Macrocyclic Complexes: Structure-Relaxivity Relationships. *Inorg. Chem.* **1992**, *31* (2), 234–239.

31. Maitra, D.; Cunha, B.; Elenbaas, J.; Bonkovsky, H.; Shavit, J.; Omary, B. Porphyrin-Induced Protein Oxidation and Aggregation as a Mechanism of Porphyria-Associated Cell Injury. *Cell. Mol. Gastroenterol. Hepatol.* **2019**, *8* (4), 535–548.
32. Lazzarini, A.; Colaiezzi, R.; Galante, A.; Passacantando, M.; Capista, D.; Ferella, F.; Crucianelli, M. Hybrid Polyphenolic Network/SPIONs Aggregates with Potential Synergistic Effects in MRI Applications. *Results Chem.* **2022**, *4*, 100387.

7. A Different Perspective: MOFs for Wastewater Treatment Applications

---

This chapter is based on the publication:

di Nicola, N., Di Pelino, M., Foschi, M., Passalacqua, R., Lazzarini, A., & Ruggieri, F. (2025). ZIF-8 as Potential Pesticide Adsorbent Medium for Wastewater Treatment: The Case Study of Model Linuron Extraction Conditions Optimization via Design of Experiment. *Molecules*, *30*(12), 2480.

Wastewater treatment is one of the most pressing environmental challenges due to increasing contamination from heavy metals, pharmaceuticals, pesticides and other persistent organic pollutants. In this context, metal-organic frameworks (MOFs) are emerging as highly promising materials due to their high surface area, tunable porosity and possibility of chemical functionalization. These characteristics make MOFs particularly suitable for the selective adsorption of contaminants, the catalysis of degradation reactions and the efficient removal of toxic substances even at low concentrations. Furthermore, the possibility of regenerating and reusing many MOFs makes their use economically and environmentally sustainable. The integration of MOFs into wastewater treatment systems therefore represents a promising frontier for the development of advanced purification technologies, with potential applications in both industrial and municipal settings.

7.1 Herbicide removal from water: the case of Linuron

Linuron is a systemic herbicide belonging to the phenylurea family, widely used in agriculture for the selective control of weeds in various food crops.[1]

Despite its agronomic effectiveness, Linuron is considered a priority environmental contaminant due to its high chemical stability, low water solubility and persistence in soil and water bodies.[2] The molecule tends to resist common biological and photochemical degradation processes, facilitating its accumulation in aquatic ecosystems and its spread through the food chain.[3] The uncontrolled release of Linuron into agricultural and urban wastewater can cause toxic effects on aquatic flora and fauna, endocrine disruption and possible risks to human health, with particular concern for the contamination of drinking water.[4] Faced with the growing need for advanced technologies for the removal of persistent organic contaminants, metal-organic frameworks represent an innovative solution, thanks to their highly porous structure, large surface area and possibility of selective functionalization.[5] In particular, ZIF-8 combines high chemical stability with the ability to adsorb organic compounds through hydrophobic interactions and π–π stacking.[6] The pore size and hydrophobic nature of the internal cavities of ZIF-8 make it particularly suitable for the adsorption of Linuron, allowing effective removal even at low concentrations. Furthermore, the robust structure of ZIF-8 allows for excellent stability in aqueous environments, an essential characteristic for real-world applications in wastewater streams.[7] The use of ZIF-8 for Linuron removal therefore represents a promising strategy not only for addressing an emerging and difficult-to-treat contaminant, but also for contributing to the development of sustainable and regenerative solutions for advanced water treatment. This study explores the effectiveness of ZIF-8 as a potential adsorbent for linuron from both natural and wastewater, focusing on optimizing adsorption conditions to maximize removal efficiency. A Design of Experiments (DoE) methodology was implemented to systematically analyze the effects of various parameters on adsorption performance, allowing the identification of optimal conditions for maximum pesticide removal.[8]

7.2 Results and Discussion

In this study, ZIF-8 was synthesized using an optimized hydrothermal method previously developed by our group,[9] therefore we will just give a brief confirmation on the synthetic outcomes. This approach yields ZIF-8 crystals with a uniform truncated–octahedral morphology and an average size of approximately 150 nm, as illustrated in Figure 1. The specific surface area of 1789 m^2/g,[10] determined via nitrogen adsorption–desorption isotherms at 77 K using the BET method, confirmed that the material's textural properties align with those reported in the literature, further validating the efficiency and reproducibility of the synthesis procedure. Concerning its crystalline structure, from black curve in Figure 2 it is possible to recognize the SOD crystal structure, typical of this class of materials.[11]

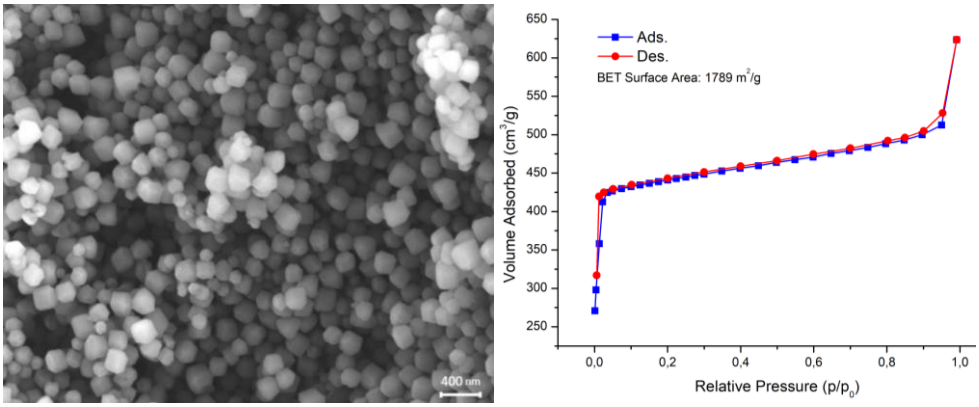

Figure 1. SEM image collected at 20 kX (left) and N2 adsorption-desorption isotherms at 77 K of ZIF-8 (BET surface area: 1789 m^2/g) (right).

The adsorption capacity of ZIF-8 for linuron was assessed under varying conditions using a Central Composite Design experimental design to systematically explore the impact of temperature, linuron concentration, and ionic strength (salt concentration). Table 1 summarizes the percentage of linuron adsorbed under these experimental conditions.

Table 1. Experimental matrix and results of the CCF design for linuron adsorption onto ZIF-8. The table reports the 22 experimental runs with corresponding values for the three independent variables with their coded levels (X_1, X_2, X_3) and the observed response (percentage of linuron removed). Runs marked with an asterisk (*) are replicates.

Run	temperature [°C]	linuron concentration [µg/mL]	ionic strength [mg/mL]	X1	X2	X3	linuron removed (%)
1	40	2	0	+1	-1	-1	91,4
2	40	8	50	+1	+1	-1	97,5
3	40	8	50	+1	+1	+1	93,4
4	40	2	0	+1	-1	+1	92,9
5	40	5	25	+1	0	0	92,1
6	30	5	25	0	0	0	91,5
7*	30	5	25	0	0	0	89,6
8*	30	5	25	0	0	0	89,1
9	30	2	0	0	-1	0	87,7
10	30	8	50	0	1	0	94,6
11	20	8	50	-1	1	-1	86,9
12	20	5	25	-1	0	0	83,2
13	30	5	25	0	0	-1	85,9
14	30	5	25	0	0	1	88,9
15*	30	5	25	0	0	-1	85,9
16*	30	5	25	0	0	1	86,9
17	20	2	0	-1	-1	-1	81,3
18	20	2	0	-1	-1	1	82,7
19*	20	8	50	-1	1	-1	88,7
20	20	8	50	-1	1	1	85,8
21*	20	5	25	-1	0	0	86,6
22*	20	5	25	-1	0	0	86,6

The significance and contribution of each variable and their interactions in the adsorption process were evaluated through regression analysis. Table 2 presents the quadratic model's estimated coefficients, standard deviations, confidence intervals, and p-values. These results provide insight into each factor's relative importance and their second-order and interaction effects on the percentage of linuron removal. Terms with statistically significant p-values ($p < 0.05$) were considered to have a meaningful impact on the model and were used to interpret the effect of experimental parameters.

Table 2. Summary of the regression model and ANOVA results for linuron adsorption onto ZIF-8. The table includes the estimated significant coefficients (with standard deviations) of the quadratic model terms, along with model performance metrics: coefficient of determination (R^2), adjusted R^2, and predictive capability (Q^2). Terms marked with an asterisk (*) are statistically significant ($p < 0.05$).

parameters	value ± SD	R^2	Adj-R^2	Q^2	
intercept	89.5 ± 0.5				
*X_1	4.4 ± 0.4				
*X_2	2.5 ± 0.4	0.909	0.873	0.755	
X_3	0.4 ± 0.4				
*$X_2 \cdot X_3$	−1.1 ± 0.5				
*X_2^2	1.9 ± 0.7				
variation source	sum of squares	degrees of freedom	mean square	F-value	p-value
lack of fit	16.4	8	2.05	0.986	0,5140
pure error	14.5	7	2.1		
model	309.9	6	51.66	25.7	<0,001
residual	30.9	15	2.06		

The adsorption behavior of Linuron onto ZIF-8 was quantitatively assessed using a second-order polynomial regression model developed from a Central Composite Face-centered (CCF) design. The model demonstrated excellent predictive and descriptive performance, with R^2 = 0.909, adjusted R^2 = 0.873, and a leave-one out cross-validated Q^2 = 0.755, indicating strong model reliability and generalizability. The lack-of-fit test was non-significant (p = 0.5140), confirming that the model adequately fit the experimental data without systematic error. Temperature exhibited the strongest positive linear influence on linuron adsorption as shown in Figure 2. This result is consistent with endothermic adsorption processes, in which elevated thermal energy strongly affects activation barriers for diffusion and improves the interactions between analyte and adsorbent. The increased temperature likely promotes higher molecular mobility of linuron in solution and an improved intraparticle diffusion into micro and mesopores of ZIF-8. Another possible effect of temperature is the disruption of weak solvation shells, exposing more active adsorption sites. The absence of a significant quadratic term suggests that the positive effect of temperature is linear in the experimental range (20–40 °C), and that no thermal degradation or desorption occurs under the tested conditions.

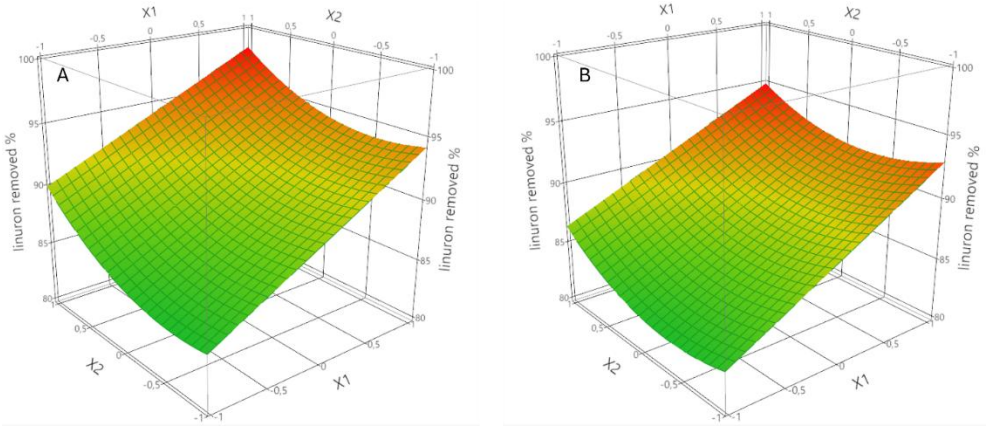

Figure 2. Response surface plots illustrating the interactive effect of temperature (X_1) and linuron concentration (X_2) on the adsorption efficiency of linuron onto ZIF-8, expressed as percentage removed. In figure (A) ionic strength (X_3) is fixed at the center.

Linuron concentration had a positive linear effect, indicating that increasing pollutant concentration enhances the driving force for mass transfer. However, the model shows a non-linear adsorption profile with the occurrence of a significant positive quadratic term. Initially, the increasing of concentration favors interaction and binding with ZIF-8's active sites. Nonetheless, at higher level of concentration site saturation becomes a limiting factor and the removal efficiency declines due to the finite number of adsorption sites as reported in Figure 2. The linear effect of ionic strength was not sufficiently significant, but the quadratic term suggested that the relationship between ionic strength and adsorption efficiency follows a parabolic trend (Figure 3).

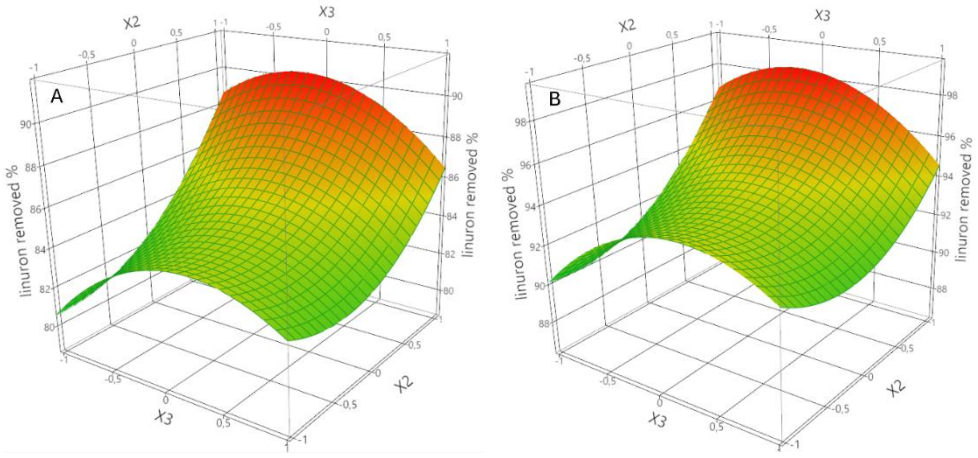

Figure 3. Response surface plots showing the combined effect of Linuron concentration (X_2) and ionic strength (X_3) on Linuron removal efficiency (%), with temperature (X_1) held constant at low level (A) and high level (B), respectively.

At high ionic strengths, competitive adsorption or ion packing may occur, where Na^+ or SO_4^{2-} ions compete with linuron for adsorption sites or modify the hydration shell of the ZIF-8 surface, reducing effective interaction. A medium ionic strength charge reduces repulsion and enhances adsorption by minimizing electrostatic barriers. In the absence of ionic solute, there may be insufficient ionic screening, leading to electrostatic repulsion between Linuron and the ZIF-8 surface. This behavior underscores the dual role of salts in modulating adsorption: acting as both enhancers and inhibitors, depending on concentration. A significant negative interaction between Linuron concentration and ionic strength was observed, suggesting that increasing both simultaneously leads to a decrease in adsorption efficiency; high salt concentrations reduce the solubility of linuron, altering its adsorption behavior. After optimization and study of Linuron adsorption, the ZIF-8 used was characterized again to observe the status of possible degradation. The material was characterized immediately after adsorption, with the pesticide molecule inside the pores, and after desorption of the

pesticide to study the reversibility of the process. XRPD (Figure 4 left), ATR-MIR (Figure 4 right) and SEM (Figure 5) analysis showed no structural or morphological differences between the 3 different materials. The XRPD patterns of the loaded and desorbed ZIF-8 show no new peaks and are the same compared to the pattern of pure ZIF-8, indicating that the entire adsorption-desorption process does not alter the crystallinity of the MOF and that the material can be recovered in its pristine form.

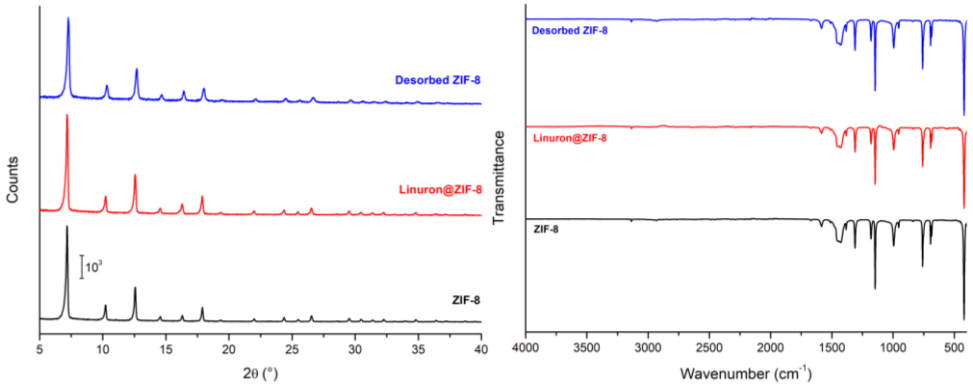

Figure 4. Comparison of the experimental XRPD pattern (left) and ART-MIR spectra (right) for pure ZIF-8, Linuron-loaded ZIF-8 and desorbed ZIF-8.

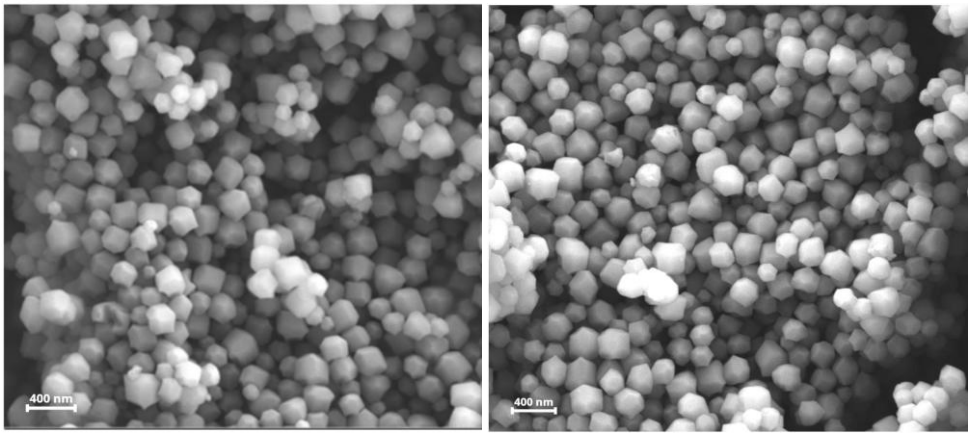

Figure 5. SEM images collected at 20 kX of Linuron@ZIF-8 (left) and desorbed ZIF-8 (right).

7.3 Conclusions

This work presents a comprehensive evaluation of Zeolitic Imidazolate Framework-8 (ZIF-8) as an advanced porous material for the removal of Linuron, a persistent and environmentally relevant herbicide, from aqueous media. The MOF was synthesized via a hydrothermal route and thoroughly characterized, confirming the formation of a nanocrystalline and microporous structure with high surface area and chemical stability—key features enabling its adsorption functionality.

Employing a Central Composite Face-centered (CCF) experimental design and response surface methodology (RSM), the study systematically explored the influence of operational parameters, namely temperature, linuron concentration, and ionic strength, on adsorption performance. The regression analysis revealed that temperature and initial linuron concentration had statistically significant and synergistic effects on removal efficiency, while the influence of ionic strength followed a non-linear trend, with significant quadratic and interaction effects. These findings are consistent with interpretations involving enhanced molecular diffusion, surface accessibility, and competitive interactions modulated by the ionic environment. The resulting second-order polynomial model demonstrated high statistical robustness ($R^2 = 0.909$; $Q^2 = 0.755$; $p < 0.001$) and predictive accuracy across the design space, with the lack-of-fit test confirming model adequacy. Optimal conditions identified through the model enabled removal efficiencies exceeding 95%, underscoring the potential of ZIF-8 for real-world water treatment applications targeting pesticide residues.

This study not only increases the understanding of MOF–pesticide interactions but also highlights the utility of DoE-driven optimization in environmental adsorption science. Future investigations may extend this

approach to multicomponent systems, adsorbent regeneration studies, and the assessment of performance in complex water matrices, thus moving toward scalable and sustainable remediation technologies. ZIF-8 was characterized before and after the adsorption process. To investigate the recyclability of MOF after adsorption, the material was washed with MeOH in order to desorb Linuron within the pores of ZIF-8. XRPD, ATR-MIR and SEM analyses performed on the material at each step of the process show that the structural and morphological integrity of the ZIF-8 nanocrystals is not altered, opening up the possibility of reusing the material several times.

7.4 Bibliography

1. Pant, A. B. *Dictionary of Toxicology*; Springer Nature Singapore: Singapore, 2024.
2. Guzzella, L.; Capri, E.; Di Corcia, A.; Barra Caracciolo, A.; Giuliano, G. Fate of Diuron and Linuron in a Field Lysimeter Experiment. *J. Environ. Qual.* **2006**, *35* (1), 312–323.
3. Swarcewicz, M.; Gregorczyk, A.; Sobczak, J. Comparison of Linuron Degradation in the Presence of Pesticide Mixtures in Soil under Laboratory Conditions. *Environ. Monit. Assess.* **2013**, *185* (10), 8109–8114.
4. Quintaneiro, C.; Patrício, D.; Novais, S. C.; Soares, A. M. V. M.; Monteiro, M. S. Endocrine and Physiological Effects of Linuron and S-Metolachlor in Zebrafish Developing Embryos. *Sci. Total Environ.* **2017**, *586*, 390–400.
5. Wei, J.; Yuan, M.; Wang, S.; Wang, X.; An, N.; Lv, G.; Wu, L. Recent Advances in Metal Organic Frameworks for the Catalytic Degradation of Organic Pollutants. *Collagen Leather* **2023**, *5* (1), 33.
6. Elaouni, A.; El Ouardi, M.; Zbair, M.; BaQais, A.; Saadi, M.; Ait Ahsaine, H. ZIF-8 Metal Organic Framework Materials as a Superb Platform for the Removal and Photocatalytic Degradation of Organic Pollutants: A Review. *RSC Adv.* **2022**, *12* (49), 31801–31817.
7. Ge, D.; Lee, H. K. Water Stability of Zeolite Imidazolate Framework 8 and Application to Porous Membrane-Protected Micro-Solid-Phase Extraction of Polycyclic Aromatic Hydrocarbons from Environmental Water Samples. *J. Chromatogr. A* **2011**, *1218* (47), 8490–8495.
8. Foschi, M.; Capasso, P.; Maggi, M. A.; Ruggieri, F.; Fioravanti, G. Experimental Design and Response Surface Methodology Applied to

Graphene Oxide Reduction for Adsorption of Triazine Herbicides. *ACS Omega* **2021**, *6* (26), 16943–16954.

9. di Nicola, N.; Paolucci, V.; Daniele, V.; Taglieri, G.; Crucianelli, M.; Guidoni, L.; Lazzarini, A. ZIF-8 as Potential Vector for Enhanced Target Delivery of Sulfathiazole for the Treatment of Bovine Ruminal Acidosis. *Eur. J. Inorg. Chem.* **2024**, *27* (36), e202400504.
10. Balliana, E.; Marchand, M.; Di Matteo, V.; Ballarin, B.; Cassani, M. C.; Panzavolta, S.; Zendri, E. Application of Zinc-Based Metal-Organic Framework ZIF-8 on Paper: A Pilot Study on Visual Appearance and Effectiveness. *Polymers* **2025**, *17* (10), 1369.
11. Park, K. S.; Ni, Z.; Côté, A. P.; Choi, J. Y.; Huang, R.; Uribe-Romo, F. J.; Chae, H. K.; O'Keeffe, M.; Yaghi, O. M. Exceptional Chemical and Thermal Stability of Zeolitic Imidazolate Frameworks. *Proc. Natl. Acad. Sci. U.S.A.* **2006**, *103* (27), 10186–10191.

8. General Conclusions

The research presented in this doctoral thesis has thoroughly explored the potential of Metal–Organic Frameworks (MOFs) as multifunctional materials, with particular attention to biomedical applications and, in the final part, to environmental applications. The approach adopted did not focus on the development of new crystalline architectures, but rather on the use of MOFs already known and widely characterized in literature, with the aim of verifying their versatility in application contexts not yet fully explored.

The first part of the work laid the conceptual foundations for the use of ZIF-8 as a drug delivery system. The material's sensitivity to pH, combined with its biocompatibility and ability to host molecules of different chemical and physical natures, was exploited for the loading and controlled release of active ingredients in different fields. On the one hand, attention was focused on the veterinary sector, with the study of sulfathiazole encapsulation for the potential management of ruminal acidosis in dairy cattle. On the other hand, several compounds of oncological interest, such as lidocaine and non-steroidal anti-inflammatory drugs (NSAIDs), have been investigated, demonstrating the ability of ZIF-8 to adapt to heterogeneous therapeutic strategies. The studies conducted have shown that the intrinsic properties of the framework can be effectively exploited to ensure targeted release conditioned by specific biological microenvironments.

The work then considered a structural variant of ZIF-8 obtained by partially replacing zinc with magnesium. This modification, while maintaining the crystalline integrity of the material, showed different behavior in environments with different pH levels, suggesting new application possibilities in therapeutic scenarios that require greater stability in weakly acidic conditions. These results have broadened our understanding of the

link between framework composition and functional behavior, providing useful insights for the future use of established materials in new biomedical areas.

Another area addressed was diagnostic imaging, through the study of PCN-224 doped with paramagnetic Gd^{3+} and Mn^{2+} ions. The materials obtained were analyzed from both a chemical-physical and biological point of view, with the aim of evaluating their potential as contrast agents for magnetic resonance imaging. The results showed that the combination of the high loading capacity of MOFs and the strong coordination offered by the porphyrin ligand can promote the stability of the system and open up prospects for the development of safer and more durable diagnostic tools than conventional agents.

Finally, the work was extended to the field of environmental purification, highlighting the versatility of MOFs beyond the strictly biomedical field. In particular, ZIF-8 was studied as an adsorbent for the removal of linuron, a persistent and toxic herbicide, from wastewater. The tests conducted demonstrated the material's ability to interact selectively with pollutant molecules, confirming its effectiveness even in environmentally relevant contexts.

Taken together, the results of this research demonstrate how established MOFs, such as ZIF-8 and PCN-224, can be effectively used in diverse applications ranging from drug therapy to diagnostic imaging and water treatment. The thesis highlights that, even without introducing new crystalline architectures, innovation lies in identifying new applications for known materials, thus helping to strengthen the role of MOFs as multifunctional platforms capable of addressing current challenges in medicine and environmental sustainability.

Appendix: Experimental Section

This section covers all the experimental parts of the projects described in this thesis.

- The experimental sections are reported following the same order of the thesis.
- This section is fully extracted from the papers published during the PhD.
- This section has to be considered as a tool for a better understanding of the data reported in the main body of the thesis.

Appendix A - Experimental Section

From Foundations to Frontiers: The Central Role of ZIF-8

Extracted from:

di Nicola, N., Paolucci, V., Daniele, V., Taglieri, G., Crucianelli, M., Guidoni, L., & Lazzarini, A. (2024). ZIF-8 as Potential Vector for Enhanced Target Delivery of Sulfathiazole for the Treatment of Bovine Ruminal Acidosis. European Journal of Inorganic Chemistry, 27(36), e202400504.

Materials

Zinc nitrate hexahydrate (98 %), 2-methylimidazole (99%), methanol (99,8 %), acetic acid (99,7 %), phosphate-buffered saline tablets (PBS, 0.0027 M KCl; 0.137 M NaCl; pH=7.4) were purchased from Sigma-Aldrich. Sulfathiazole (>98%) was acquired from TCI. Double deionized water was obtained from a Milli-Q filtration/ purification system (Millipore, Bedford, MA, USA).

Characterization Techniques

X-Ray Powder Diffraction (XRPD)

X-ray powder diffraction patterns were collected with a PW3050/60 X'Pert PRO MPD diffractometer from PANalytical working in the Debye-Scherrer geometry, using as a source a Cu anode filtered by a Ni foil to attenuate the K_β line and focused by a PW3152/63 X-ray mirror (λ=1.5409 Å). The samples were measured as powders deposited onto a zero-background sampleholder.

Attenuated Total Reflectance Mid Infrared Spectroscopy (ATR-MIR)

ATR-MIR measurements were performed with a PerkinElmer Spectrum Two instrument equipped with an atmospheric UATR Two accessory and a DTGS detector. Each spectrum was obtained by averaging 8 scans with a 4 cm^{-1} resolution in the range 4000– 400 cm^{-1}.

Surface Area Analysis

Surface area measurements were performed with the use of a Quantachrome NOVA 2200 instrument. The sample was inserted inside a calibrated-volume sampleholder and treated at 200°C in dynamic vacuum for 2 h directly on the instrument. Surface area was measured with N_2 adsorption-desorption isotherms at 77 K, by using BET method.[1]

Thermogravimetric Analysis (TGA)

Thermogravimetric analysis (TGA) was used to determine the materials stoichiometry and was performed with a Linseis L-81 instrument; the measurements were performed in synthetic air flow (50 ml/min) with a temperature ramp of 10°C/min from r.t. to 750°C.

Scanning Electron Microscopy-Energy Dispersive X-Ray Spectroscopy (SEM-EDX)

The study of the morphology of the samples was carried out by Scanning Electron Microscopy, using a FESEM ZEISS Gemini500 instrument, acquiring images at 10 k, 20 k, and 100 k x with backscattered electrons and operating with an accelerating voltage equal to 20 kV. The samples were deposited on a SEM stab covered with carbon tape and successively metallized with a copper layer film, in order to make it more conductive thus avoiding electrical charging of the samples. The instrument is also equipped

with an Oxford Aztec spectrometer: EDX analysis was performed with the instrument proprietary software.

UV-Vis Spectroscopy

UV-Vis measurements were performed in order to evaluate indirectly the loading of the active molecule, by measuring the residual concentration in the synthesis solvent. This analysis was performed by means of an ONDA UV-30 SCAN spectrophotometer in the 200–350 nm range. The residual concentration of sulfathiazole was evaluated through the intensity of the band centered at 288 nm.

Experimental Section

ZIF-8 Synthesis

In the current state of the art, there are many synthetic methods to obtain ZIF-8, even with small structural differences. For our work, we adapted our synthetic procedure to the method of Koji Kida and coworkers.[2] Thus because it is a hydrothermal synthesis (more congenial for a biomedical application, since water is used as solvent), allowing us to obtain particles with a good surface area. Briefly, 0.372 g of zinc nitrate hexahydrate were dissolved in 10 mL of deionized water and added to a solution consisting of 6.15 g of 2-methylimidazole in 40 mL of Milli-Q water. The mixture, which quickly becomes milky, was stirred at r.t. for a variable time (from 2–24 h). After the reaction time, the suspension obtained was centrifuged at 5000 RPM for 30 min and washed with methanol three times. The products were then dried overnight under reduced pressure at 40°C.

Sulfathiazole Loading

Drug loading inside porous scaffolds for delivery purposes can be achieved in several ways. However, independently from the loading technique (listed below), we evaluated the loading of the active molecule by means of the following equation, describing the percentage of Drug Entrapment Efficiency ($\%_{DEE}$):

$$\%_{DEE} = \frac{\text{moles of drug in MOF}}{\text{moles of drug fed initially}} \times 100$$

The amount of loaded drug was obtained by means of UV-Vis spectroscopy data.

One-Pot Method[3]

The most widely used and certainly the simplest method is the one-pot method. This consists of adding the drug within the solution of zinc nitrate hexahydrate and 2-methylimidazole, so that the MOF can incorporate the drug during its own growth. 0.372 g of Zn was dissolved in 10 mL of deionized water and added to a solution consisting of 6.15 g of Hmim and 0.372 g of sulfathiazole in 40 mL of deionized water. The mixture was stirred at r.t. for 24 h. After the reaction time had elapsed, the resulting suspension was centrifuged at 5000 RPM for 30 min and washed with methanol three times. The product was then dried overnight under reduced pressure at 40°C.

Stirring Method[4]

Another widely used approach is the stirring method. Unlike the previous one, MOF needs to be first synthesized and then added to a solution containing the drug under stirring: in this way, the active principle can

diffuse within the cavity of the crystalline material. 0.136 g of ZIF-8 and 0.206 g of sulfathiazole were dissolved in 34 mL of methanol. The mixture was stirred at r.t. for 2 days. The obtained suspension was washed and centrifuged 2 times at 5000 RPM for 30 min, and after that the product was dried overnight under reduced pressure at 40°C.

Dropwise Method[5]

A similar approach to stirring can be the dropwise method. In this way, the concentration of drug within the suspension containing the ZIF-8 can be more controlled, so that the drug can be gradually and more efficiently loaded. 0.136 g of ZIF-8 and 0.206 g of sulfathiazole were dissolved in 17 mL of methanol respectively. The solution containing the sulfathiazole is added dropwise into the ZIF-8 suspension and left under stirring for 48 h at 40°C. After the reaction time has elapsed, the obtained suspension was washed and centrifuged 2 times at 5000 RPM for 30 min, and after that the product was dried overnight under reduced pressure at 40°C.

Sonication Method[6]

The last method we tested is the sonochemical one, taking advantage of ultrasound to allow the drug to disperse and diffuse homogeneously inside MOF cavity. 0.136 g of ZIF-8 and 0.206 g of sulfathiazole were dissolved in 34 mL of methanol. The mixture was sonicated at 40°C for 8 h by means of an ultrasound bath. After the reaction time had elapsed, the obtained suspension was washed and centrifuged 2 times at 5000 RPM for 30 min, and after that the product was dried overnight under reduced pressure at 40°C.

Stability Tests

In order to check the stability of the materials at physiological pH 5 beakers containing 15 mg of ZIF-8 and 10 mL of PBS solution (pH= 7.4) were prepared. The suspension was kept under stirring for 1, 2, 3, 4, or 6 days at room temperature. The different suspensions were then centrifuged at 5000 RPM for 50 minutes; the recovered powders were then dried overnight under vacuum at 40°C. The tested samples were then measured with XRD technique, in order to control the eventual loss in crystallinity, leading to a degradation of the materials.

The same test was repeated by changing the working pH of the solution, using an acetate buffer solution at pH=5, thus simulating the rumen environment.

Release Tests

Sulfathiazole release tests were performed by dispersing 100 mg of previously synthesized sulfathiazole@ZIF-8 system in a solution consisting of 22.5 ml acetate buffer (pH=5) and 2.5 ml MeOH, due to the material's poor suspensibility in water. The same set up was performed in the case of PBS (pH=7.4). The suspension is left under gentle agitation at 39°C, the average body temperature of a dairy cow, for several days.

In order to evaluate the amount of the active molecule released we employed the following equation, describing the percentage of Drug Release Efficiency ($\%_{DRE}$) as a function of time:

$$\%_{DRE} = \frac{moles\ of\ drug}{moles\ of\ drug\ loaded} \times 100\%$$

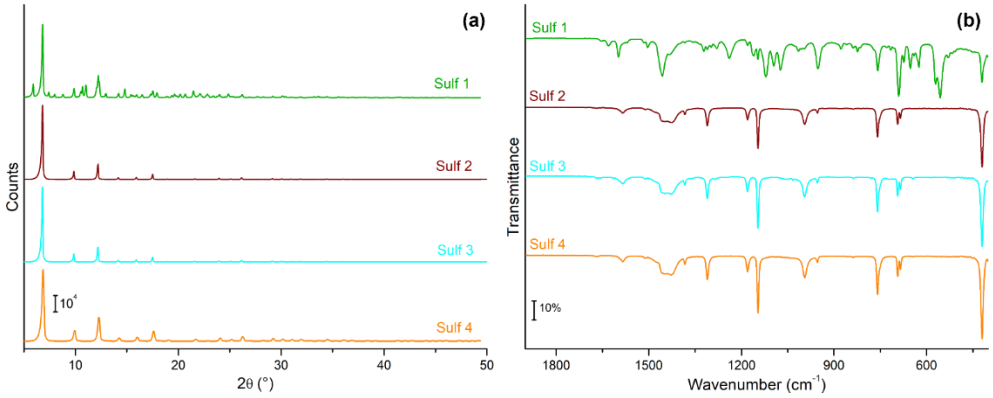

Figure Appendix-A 1. XRD patterns (a) and ATR-MIR spectra (b) of the different sulfathiazole@ZIF-8 samples prepared with the stirring method (Sulf 1-4 are referred to Table 2 of Chapter 3).

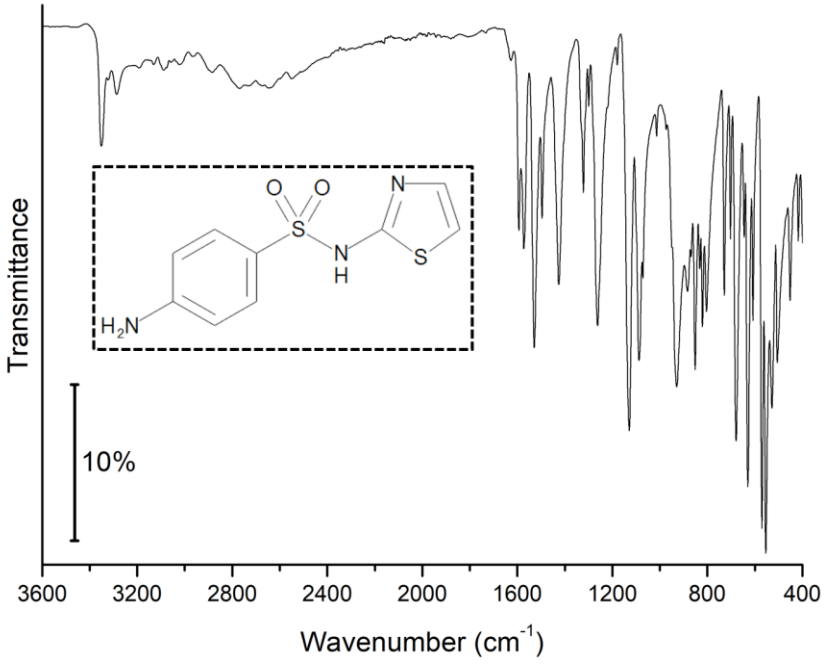

Figure Appendix-A 2. Experimental ATR-MIR spectrum of pure sulfathiazole (molecule displayed in the dotted box).

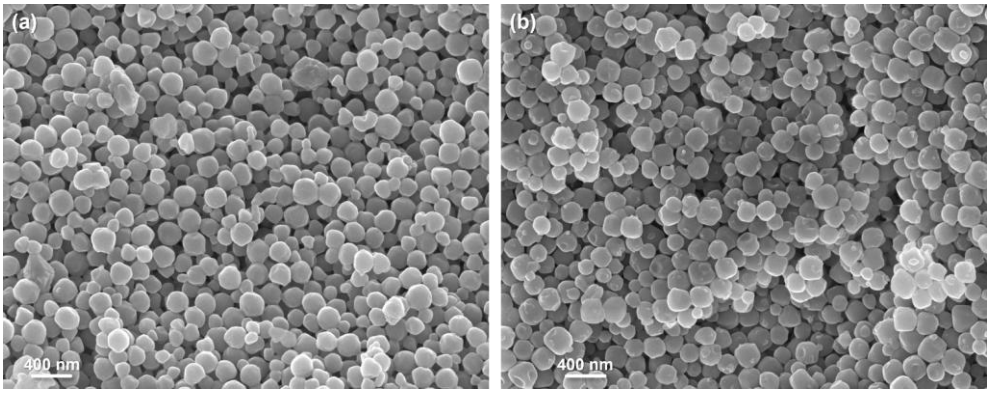

Figure Appendix-A 3. SEM images collected at 20 kX of ZIF-8 sample after being suspended in PBS buffer (pH = 7.4) for 1 day (a) or for 6 days (b).

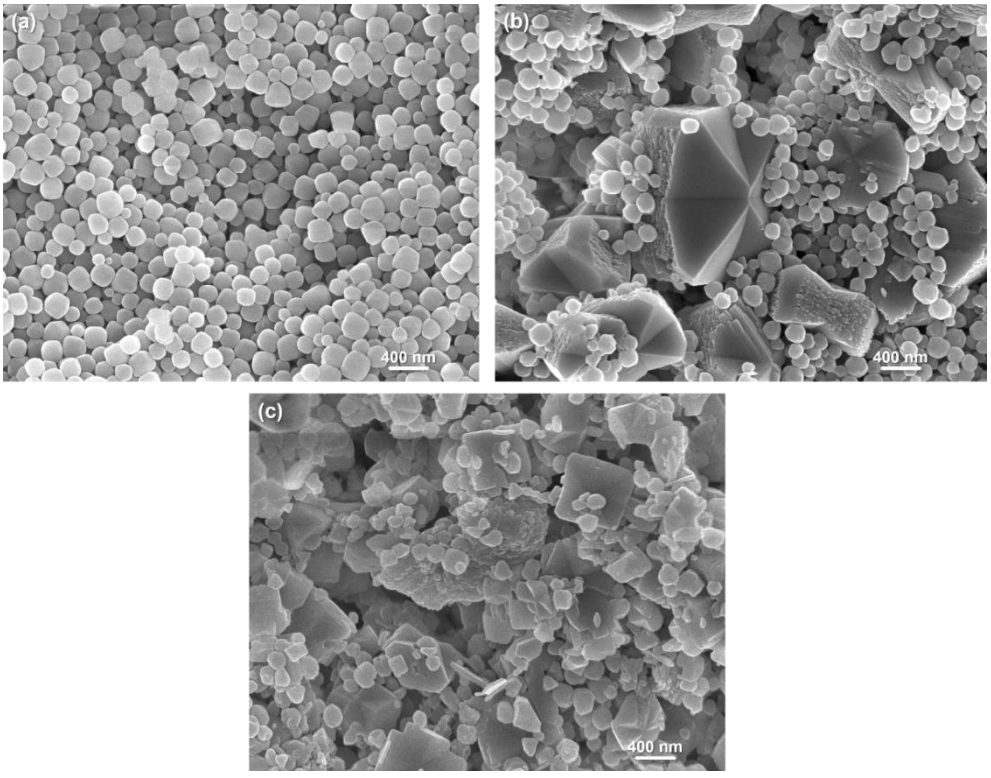

Figure Appendix-A 4. SEM images collected at 20 kX of ZIF-8 sample after being suspended in acetate buffer (pH = 5) for 1 day (a), 2 days (b), or for 4 days (c).

Bibliography

1. Brunauer, S.; Emmett, P. H.; Teller, E. Adsorption of Gases in Multimolecular Layers. *J. Am. Chem. Soc.* **1938**, *60* (2), 309–319.
2. Kida, K.; Okita, M.; Fujita, K.; Tanaka, S.; Miyake, Y. Formation of High Crystalline ZIF-8 in an Aqueous Solution. *CrystEngComm* **2013**, *15* (9), 1794–1801.
3. Amur, S. A.; Soomro, N. A.; Khuhro, Q.; Wei, Y.; Liang, H.; Yuan, Q. Encapsulation of Natural Drug Gentiopicroside into Zinc-Based Zeolitic Imidazolate Frameworks (ZIF-8): In-Vitro Drug Release and Improved Antibacterial Activity. *J. Drug Deliv. Sci. Technol.* **2023**, *84*, 104530.
4. Sun, C. Y.; Qin, C.; Wang, X. L.; Yang, G. S.; Shao, K. Z.; Lan, Y. Q.; Wang, E. B. Zeolitic Imidazolate Framework-8 as Efficient pH-Sensitive Drug Delivery Vehicle. *Dalton Trans.* **2012**, *41* (23), 6906–6909.
5. Zhang, X.; Chen, J. Y.; Pei, X.; Li, Y. H.; Feng, H.; He, Z. H.; Wang, J. One-Pot Facile Encapsulation of Dimethyloxallyl Glycine by Nanoscale Zeolitic Imidazolate Frameworks-8 for Enhancing Vascularized Bone Regeneration. *Adv. Healthcare Mater.* **2023**, *12* (4), 2202317.
6. Ho, P. H.; Salles, F.; Di Renzo, F.; Trens, P. One-Pot Synthesis of 5-FU@ZIF-8 and Ibuprofen@ZIF-8 Nanoparticles. *Inorg. Chim. Acta* **2020**, *500*, 119229.

Appendix B - Experimental Section

ZIF-8 for Anticancer Treatment: One Carrier, Many Strategies

Extracted from:

di Nicola, N., Giacchi, L., Vandone, M., Crucianelli, M., Guidoni, L., Colombo, V., Rucci, N. & Lazzarini, A. (2025). Targeted Delivery of Lidocaine in Breast Cancer Cells *via* Zeolitic Imidazolate Framework-8 Nanoparticles. ChemPhysChem, 26(16), e202401128.

Materials

Zinc nitrate hexahydrate (98%), 2-methylimidazole (99%), methanol (99,8%), acetonitrile (>99,9%), hexane (>99%), acetic acid (99,7%), phosphate-buffered saline tablets (PBS, 0.0027M KCl; 0.137M NaCl; pH = 7.4) were purchased from Sigma-Aldrich. Lidocaine hydrochloride (>95%) was acquired from BLD Pharma. Double deionized water was obtained from a Milli-Q filtration/purification system (Millipore, Bedford, MA, USA). Dulbecco's modified Minimum Essential Medium (DMEM), Fetal Bovine Serum (FBS), penicillin, streptomycin and trypsin were acquired from GIBCO (Uxbridge, UK). Sterile plasticware was bought from Falcon Becton-Dickinson (Cowley, Oxford, UK), Costar (Cambridge, MA, USA) or Euroclone (Milan, Italy). The 3-(4,5-dimethylthiazol-2-yl)-2,5-diphenyltetrazolium (MTT) bromide reduction assay and the dimethyl sulfoxide (DMSO) were purchased by Sigma Aldrich Co. (St. Louis, MO, USA).

Characterization Techniques

X-Ray Powder Diffraction (XRPD)

Gently ground powder of ZIF-8 and lidocaine@ZIF-8 was deposited in the 2 mm deep hollow of a zero background plate (a properly misoriented quartz

monocrystal). The diffraction experiment was performed using Cu-Kα radiation (λ = 1.5418 Å) on a vertical-scan Bruker AXS D8 Advance diffractometer in θ:θ mode, equipped with a Goebel Mirror and a Bruker Lynxeye linear Position Sensitive Detector (PSD), with the following optics: primary and secondary Soller slits, 2.3° and 2.5°, respectively; divergence slit, 0.1°; receiving slit, 2.82°; generator setting: 40 kV, 40 mA. The nominal resolution for the present set-up is 0.08° 2θ (FWHM of the α 1 component) for the LaB_6 peak at about 21.3° (2θ). The accurate diffraction pattern at RT of the sample was acquired in the 3-110° 2θ range, with Δ2θ = 0.02° and exposure time 10 s/step. A Le Bail refinement was carried out in order to check the phase purity within the TOPAS-Academic 6 software.

Attenuated Total Reflectance Mid Infrared Spectroscopy (ATR-MIR)

ATR-MIR measurements were performed with a PerkinElmer Spectrum Two instrument equipped with an atmospheric UATR Two accessory and a DTGS detector. Each spectrum was obtained by averaging 8 scans with a 4 cm^{-1} resolution in the range 4000-400 cm^{-1}.

Surface Area Analysis

Surface area measurements were performed with the use of an Anton Paar Nova 800 instrument. The sample was inserted inside a calibrated-volume sampleholder and treated at 150 °C in dynamic vacuum for 18 h directly on the instrument for activation. N_2 adsorption-desorption isotherms at 77 K where later on measured and Specific Surface Area was calculated applying the BET method.[1]

Thermogravimetric Analysis (TGA)

TGA was carried out on a Perkin-Elmer TGA 7 Thermogravimetric Analyzer. 1.115 mg of sample were placed on an alumina pan and heated under air. The heating ramp used was 10 K/min, from 303 K to 1173 K.

Scanning Electron Microscopy (SEM)

The morphology of the samples was analyzed using Scanning Electron Microscopy (SEM) with a FESEM ZEISS Gemini500 instrument. Images were captured at 10k and 50k magnifications using backscattered electrons, operating at an accelerating voltage of 5 kV. The samples were mounted on SEM stubs covered with carbon tape and subsequently coated with a thin chromium layer to increase conductivity and prevent electrical charging during imaging.

UV-Vis Spectroscopy

UV-Vis measurements were conducted to indirectly assess the loading of the active molecule by determining its residual concentration in the synthesis solvent. This analysis was carried out using an ONDA UV-30 SCAN spectrophotometer in the 200-300 nm range. The residual concentration of lidocaine was quantified based on the intensity of its characteristic absorption band centered at 207 nm.

Experimental Section

ZIF-8 Synthesis

We adapted the synthetic procedure based on the method developed by Koji Kida and coworkers.[2] Briefly, 0.372 g of zinc nitrate hexahydrate were dissolved in 10 mL of deionized water and added to a solution containing 6.15 g of 2-methylimidazole in 40 mL of Milli-Q water. The mixture, which quickly

turns milky, was stirred at room temperature for 2 hours. After the reaction, the resulting suspension was centrifuged at 5000 RPM for 30 minutes and washed three times with methanol. The products were then dried overnight under reduced pressure at 40 °C.

Lidocaine Loading

Lidocaine hydrochloride is a powder that is soluble in both water and most organic solvents. Since drug loading into a porous structure is favored when there is low affinity between solvent and solute, an updated loading method was devised to overcome the challenge of solubility: stirring at low temperature (0 °C). 0.100 g of ZIF-8 and 0.150 g of lidocaine hydrochloride were dissolved in 100 mL of solvent (methanol, acetonitrile, or hexane). The mixture was sonicated for 5 minutes to allow ZIF-8 to homogeneously disperse in the liquid phase, placed in a beaker cooled to 0 °C using a chiller, and finally stirred for 24 hours. After the reaction time had elapsed, the resulting suspension was centrifuged at 5000 RPM for 30 minutes and washed twice with methanol. The product was then dried overnight under reduced pressure at 40 °C.

Release Tests

Lidocaine release tests were conducted by dispersing 100 mg of the previously synthesized Lidocaine@ZIF-8 system in a solution of 9 mL acetate buffer (pH = 5.5) and 1 mL MeOH. The same setup was used with phosphate buffer solution (PBS, pH = 7.4). The suspension was kept under gentle agitation at 37 °C, simulating average body temperature, for several days.

MTT Assay

Metabolic activity of MDA-MB-231 breast cancer cells was assessed by the 3-(4,5-dimethylthiazol-2-yl)-2,5-diphenyltetrazolium (MTT) bromide

reduction assay. Lidocaine, ZIF-8, or lidocaine@ZIF-8, were dissolved in DMEM+1% Pen/Strep and 1% L-Glut (cell culture vehicle). Tumor cells (9000 cells/cm^2) were seeded in 96-well plates and then treated with vehicle, lidocaine 0.01 mg/mL, ZIF-8 0.01 mg/mL, or lidocaine@ZIF-8 0.01 mg/mL, alternatively. MTT was dissolved in DPBS at 5 mg/ml concentration and added at 1:6$_{v/v}$ ratio directly into the cell supernatant. Three hours later, medium was removed and DMSO was added to dissolve the precipitated formazan salts arising from the reaction. Plates were shaken at 320 rpm on an orbital shaker for 10 minutes, then absorbance at 595 nm was recorded and plotted as X-fold to the absorbance of the vehicle.

Extracted from:

di Nicola, N., Di Vito Nolfi, M., Vetrano, A., Zazzeroni, F., Guidoni, L., Crucianelli, M., Vecchiotti, D. & Lazzarini, A. (in preparation). pH-responsive targeted delivery of Nonsteroidal Anti-Inflammatory Drugs Using ZIF-8 for anti-cancer application.

Materials

Zinc nitrate hexahydrate (98%), 2-methylimidazole (99%), Acetylsalicylic acid, Acetaminophen, 4-Isobutyl-alpha-methylphenylacetic acid (>98%), 2'-Fluoro-alpha-methyl-4-biphenylacetic acid, 2-(3-Benzoylphenyl)propionic acid (>98%), 2-(6-Methoxy-2-naphthyl)propanoic acid, Methanol (99.8%), Acetonitrile (>99.9%), sodium hydroxide, acetic acid (99.7%), phosphate-buffered saline tablets (PBS, 0.0027M KCl; 0.137M NaCl; pH = 7.4) were purchased from Sigma-Aldrich. Double deionized water was obtained from a Milli-Q filtration/purification system (Millipore, Bedford, MA, USA).

Characterization Techniques

X-Ray Powder Diffraction (XRPD)

Diffraction patterns were collected using a PANalytical EMPYREAN diffractometer operating in Bragg-Brentano geometry with Cu Kα radiation (λ = 1.5418 Å) over a 2θ range of 3° to 40° (step size: 0.013°; time per step: 30 s; soller slit: 0.04 rad; divergence slit: ⅛; anti-scatter slit: ¼; 45 mA × 40 kV). Measurements at room temperature were conducted using a spinning silicon zero-background sample holder. For the stability tests at varying pH levels, diffraction patterns were recorded with a PANalytical X'Pert MPD Pro diffractometer equipped with an X'Celerator detector, also employing Bragg-Brentano geometry and Cu Kα radiation (λ = 1.5418 Å), within a 2θ range of 5° to 60° (step size: 0.0167113°; time per step: 29.845 s; soller slit: 0.04 rad;

divergence slit: ½; 40 mA × 40 kV). The measurements were performed at room temperature on a spinning silicon zero-background holder.

Attenuated Total Reflectance Mid Infrared Spectroscopy (ATR-MIR)

ATR-MIR measurements were performed with a PerkinElmer Spectrum Two instrument equipped with an atmospheric UATR Two accessory and a DTGS detector. Each spectrum was obtained by averaging 8 scans with a 4 cm^{-1} resolution in the range 4000-400 cm^{-1}.

Surface Area Analysis

Surface area measurements were performed with the use of an Anton Parr Nova 800 instrument. The sample was inserted inside a calibrated-volume sample holder and treated at 150 °C in dynamic vacuum for 18 h directly on the instrument. Surface area was measured with N_2 adsorption-desorption isotherms at 77 K, by using BET method.[1]

Scanning Electron Microscopy (SEM)

The morphology of the samples was analyzed using Scanning Electron Microscopy (SEM) with a FESEM ZEISS Gemini500 instrument. Images were captured at 10k and 50k magnifications using backscattered electrons, operating at an accelerating voltage (HT) of 5 kV. The samples were mounted on SEM stubs covered with carbon tape and subsequently coated with a thin chromium layer to increase conductivity and prevent electrical charging during imaging.

UV-Vis Spectroscopy

UV-Vis measurements were conducted to evaluate the concentration of individual species to assess the release curve by determining individual

concentrations in solution. The analysis was performed with an ONDA UV-30 SCAN spectrophotometer in the 200-350 nm range. The concentrations of the different NSAID salts were quantified on the basis of the intensities of the absorption bands.

High-Performance Liquid Chromatography (HPLC)

Chromatographic analyses of pharmaceutically active compounds were carried out using an Agilent 1100 Series high-performance liquid chromatography (HPLC) system equipped with a diode array detector (DAD). Separation was achieved on a Phenomenex Luna C18 column (250 mm × 4.6 mm i.d., 5 μm particle size), operating under isocratic elution conditions. The mobile phase consisted of water and acetonitrile in an 80:20 (v/v) ratio, delivered at a constant flow rate of 1,0 mL/min. An injection volume of 2 μL was used for all analyses. The detection wavelength was selected individually for each compound based on its specific UV-Vis absorbance profile, allowing optimal sensitivity and selectivity. This setup ensured reproducible retention times and reliable quantification of the target analytes.

Experimental Section

ZIF-8 Synthesis

The synthesis of ZIF-8 has been extensively studied, with various methods reported to achieve slight structural modifications. In this study, we adapted the hydrothermal synthesis procedure developed by Koji Kida and collaborators,[2] particularly suitable for biomedical applications due to the use of water as a solvent, while scaling up the synthesis to produce gram-scale quantities of the material. Specifically, 1.488 g of zinc nitrate hexahydrate were dissolved in 40 mL of deionized water and subsequently

combined with a solution containing 24.6 g of 2-methylimidazole in 160 mL of Milli-Q water. The reaction mixture, which rapidly became turbid, was stirred at room temperature for 2 hours. Following synthesis, the suspension was centrifuged at 5000 rpm for 30 minutes and washed three times with methanol. The final product was dried overnight under reduced pressure at 40 °C.

NSAIDs Salification

All selected NSAIDs, except for paracetamol, were subjected to a salification process to obtain their corresponding sodium salt forms. The reaction was carried out using a stoichiometric amount of NaOH in water (with a concentration of 0.05 M relative to the active compound) for 3 hours at 70 °C. The product was isolated by solvent evaporation, first using a rotary evaporator, and then dried overnight at 70 °C under vacuum. For acetylsalicylic acid and ketoprofen, a different procedure was employed. The active compound and sodium methoxide (NaOMe) were separately dissolved in an 80:20 methanol-to-water solution (both at a concentration of 0.05 M). The solution containing the active compound was cooled in an ice bath while the NaOMe solution was added dropwise. The product was recovered using the previously described isolation procedure.

NSAIDs Loading

The loading process by sonication was performed using a pulsed probe sonicator, with 1 second pulse and 3 seconds of rest (Sonics Materias VCX-500-220). A mixture of 0.88 g of previously synthesized ZIF-8 and 0.133 g of the active compound was dispersed in acetonitrile (with a concentration of 0.005 M relative to the NSAID). The suspension was sonicated for 30 minutes while being thermostated in an ice bath. The product was recovered

by centrifugation at 5000 rpm for 30 minutes, washed once with methanol, and dried overnight at 40 °C under vacuum.

To calculate the percentage of drug loading efficiency ($\%_{DLE}$), we used the following equation:

$$\%_{DLE} = \frac{0{,}133\ \text{g} - \text{mass of the drug in the washing solutions}}{0{,}133\ \text{g}} \times 100$$

To calculate the loading of the drug inside the ZIF-8 ($\%_{DL}$), we used the following equation:

$$\%_{DL} = \frac{0{,}133\ \text{g} - \text{mass of the drug in the washing solutions}}{(0{,}133\ \text{g} - \text{mass of the drug in the washing solutions}) + 0{,}88\ \text{g}} \times 100$$

Release Tests

NSAIDs release tests were conducted by dispersing 100 mg of the previously synthesized NSAID@ZIF-8 system in a solution of 18 mL acetate buffer (pH = 5.5) and 2 mL MeOH, due to the material's poor suspensibility in water. The same setup was used with PBS (pH = 7.4). The suspension was kept under gentle agitation at 37°C, simulating average body temperature, for several days.

In order to evaluate the amount of the active molecule released we employed the following equation, describing the percentage of Drug Release Efficiency ($\%_{DRE}$) as a function of time:

$$\%_{DRE} = \frac{\text{moles of drug}}{\text{moles of drug loaded}} \times 100$$

Cell Cultures and Viability Tests

NSAIDs and different ZIF-8 formulations were tested on benign prostatic hyperplasia (BPH) cells and prostate cancer cell lines LNCaP and DU145. BPH cell line was cultured in RPMI medium supplemented with 20 % Fetal Bovine Serum (FBS) (Immunological Sciences), 1% penicillin/streptomycin (100 U/mL; 100 μg/mL) (Euroclone), and 1% L-glutamin (2 mM) (Euroclone), LNCaP in RPMI medium supplemented with 10% FBS, 1% penicillin/streptomycin, 1% L-glutamin, 1% Na Pyruvate (Lonza) and 1% HEPES (Euroclone), and DU145 in RPMI medium supplemented with 10% FBS, 1% penicillin/streptomycin and 1% L-glutamin. All cell lines were cultured at 37°C with 5% CO_2 and viability was assessed with PrestoBlue™ Cell Viability Reagent (Invitrogen) in accordance with the manufacturer's instructions. Viability values were read with μQuant (BioTek Instruments).

Cell Treatments

Prostate cell lines were cultured in 96-well plates and treated with different concentrations of different compounds. Free drugs and ZIF-8 formulations were dissolved in Methanol at concentration of 150 mM and 2.5 mg/ml respectively and tumor microenvironmental acidity was mimicked adjusting pH of culture media at 6.8 with 1 M sterile filtered HCl.

UV-Vis spectrophotometry was used to evaluate trends in drug release tests (Figure Appendix-B 1). The calibration curves for individual NSAIDs were constructed using five solutions of known concentration, prepared to cover a linear range representative of the sample under consideration. The measured absorbance values for each solution were plotted against the corresponding concentration and the calibration curve was obtained by linear regression analysis (Table Appendix-B 1). The concentration of the pharmaceutical

active substance was then determined by interpolating the measured absorbance value in the resulting calibration curve.

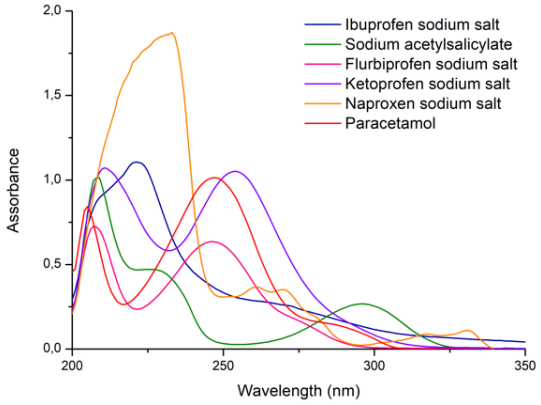

Figure Appendix-B 1. UV-Vis spectra of NSAIDs used.

Table Appendix-B 1: data from HPLC analysis.

Sample	λ_{max} (nm)	ε_λ (m^2/mol)	R^2
Ibuprofen sodium salt	221	$1{,}10 \cdot 10^3$	0,999
Sodium acetylsalicylate	296	$0{,}36 \cdot 10^3$	0,999
Flurbiprofen sodium salt	247	$1{,}87 \cdot 10^3$	0,999
Ketoprofen sodium salt	254	$1{,}39 \cdot 10^3$	0,998
Naproxen sodium salt	261	$0{,}49 \cdot 10^3$	0,999
Paracetamol	247	$1{,}24 \cdot 10^3$	0,998

Sodium Acetylsalicylate

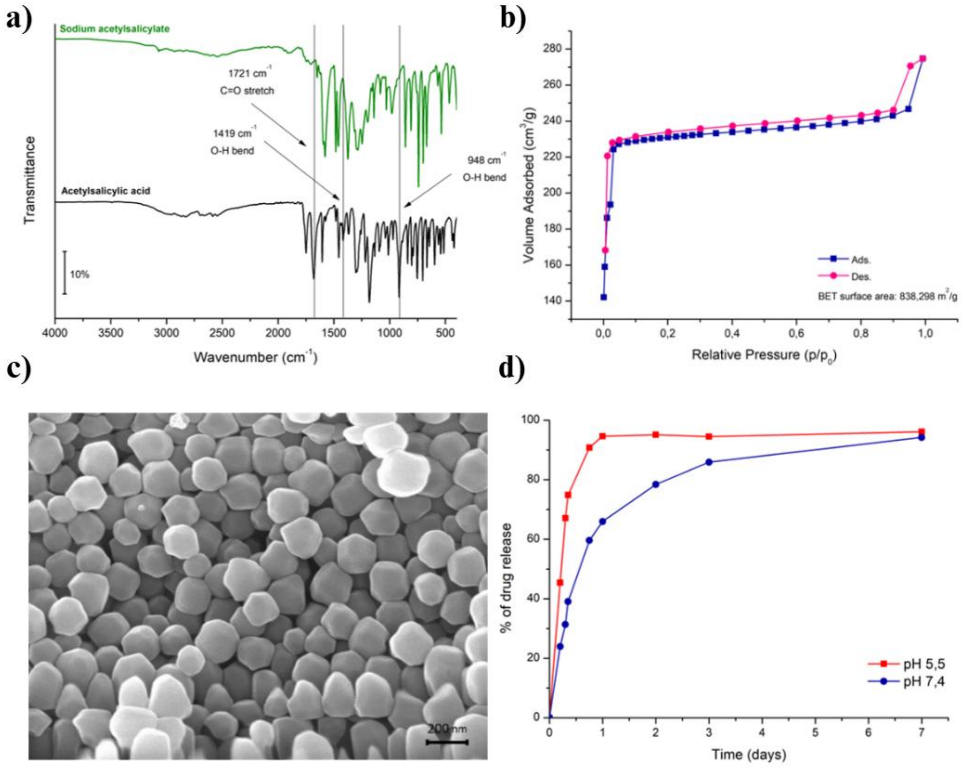

Figure Appendix-B 2. a) ATR-MIR spectra of ketoprofen and ketoprofen sodium salt. b) N_2 adsorption-desorption isotherms at 77 K of ketoprofen sodium salt@ZIF-8. c) SEM image collected at 50 kX of the ketoprofen sodium salt@ZIF-8 system. d) time-dependent release rate trend of ketoprofen sodium salt at pH 5.5 (red line) and pH 7.4 (blue line).

Flurbiprofen Sodium Salt

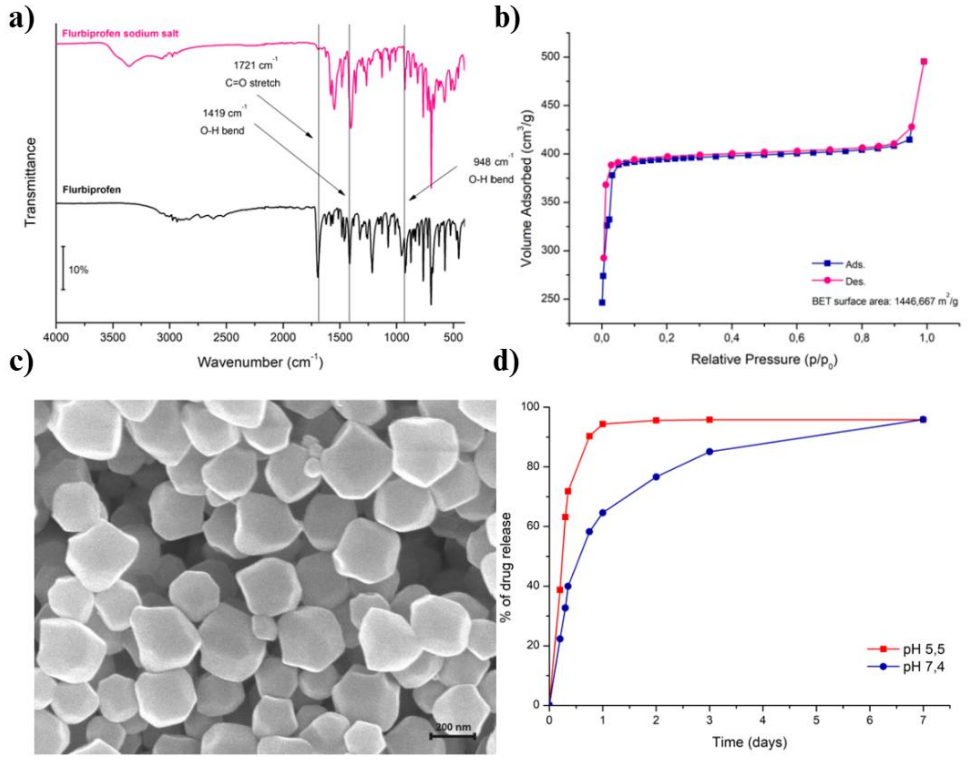

Figure Appendix-B 3. a) ATR-MIR spectra of flurbiprofen and flurbiprofen sodium salt. b) N_2 adsorption-desorption isotherms at 77 K of flurbiprofen sodium salt@ZIF-8. c) SEM image collected at 50 kX of the flurbiprofen sodium salt@ZIF-8 system. d) time-dependent release rate trend of flurbiprofen sodium salt at pH 5.5 (red line) and pH 7.4 (blue line).

Ketoprofen Sodium Salt

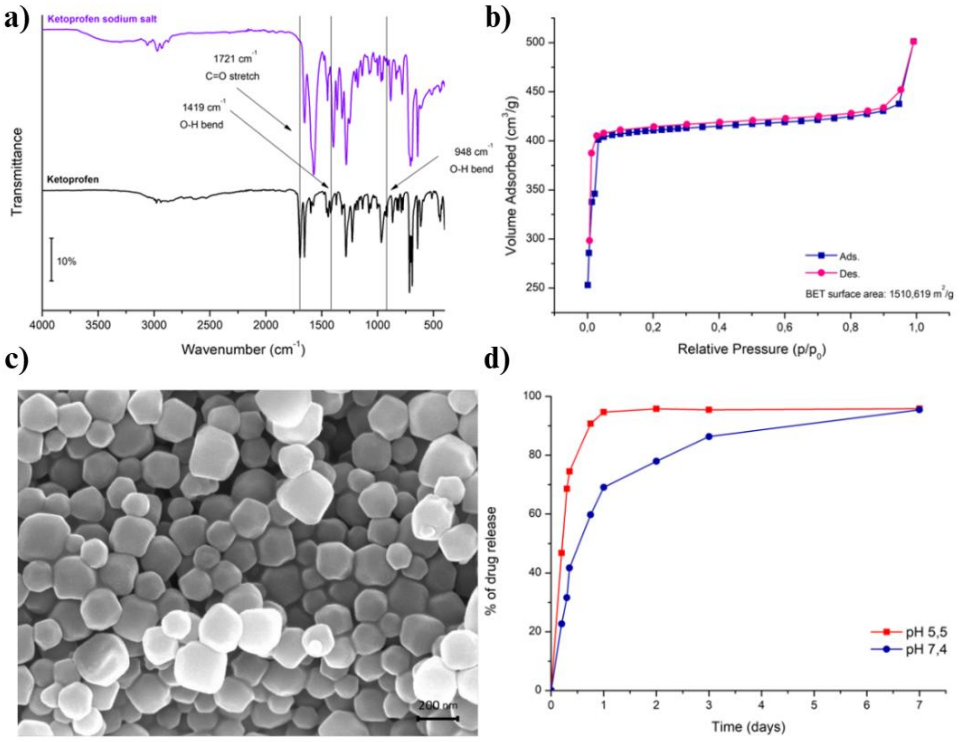

Figure Appendix-B 4. a) ATR-MIR spectra of ketoprofen and ketoprofen sodium salt. b) N_2 adsorption-desorption isotherms at 77 K of ketoprofen sodium salt@ZIF-8. c) SEM image collected at 50 kX of the ketoprofen sodium salt@ZIF-8 system. d) time-dependent release rate trend of ketoprofen sodium salt at pH 5.5 (red line) and pH 7.4 (blue line).

Naproxen Sodium Salt

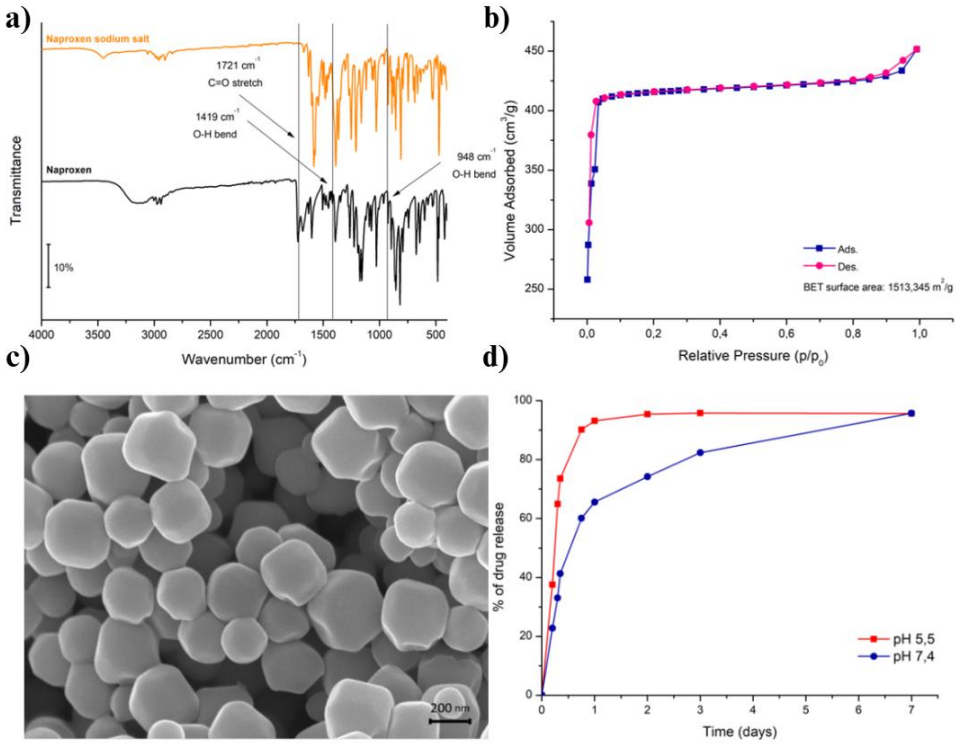

Figure Appendix-B 5. a) ATR-MIR spectra of naproxen and naproxen sodium salt. b) N_2 adsorption-desorption isotherms at 77 K of naproxen sodium salt@ZIF-8. c) SEM image collected at 50 kX of the naproxen sodium salt@ZIF-8 system. d) time-dependent release rate trend of naproxen sodium salt at pH 5.5 (red line) and pH 7.4 (blue line).

Paracetamol

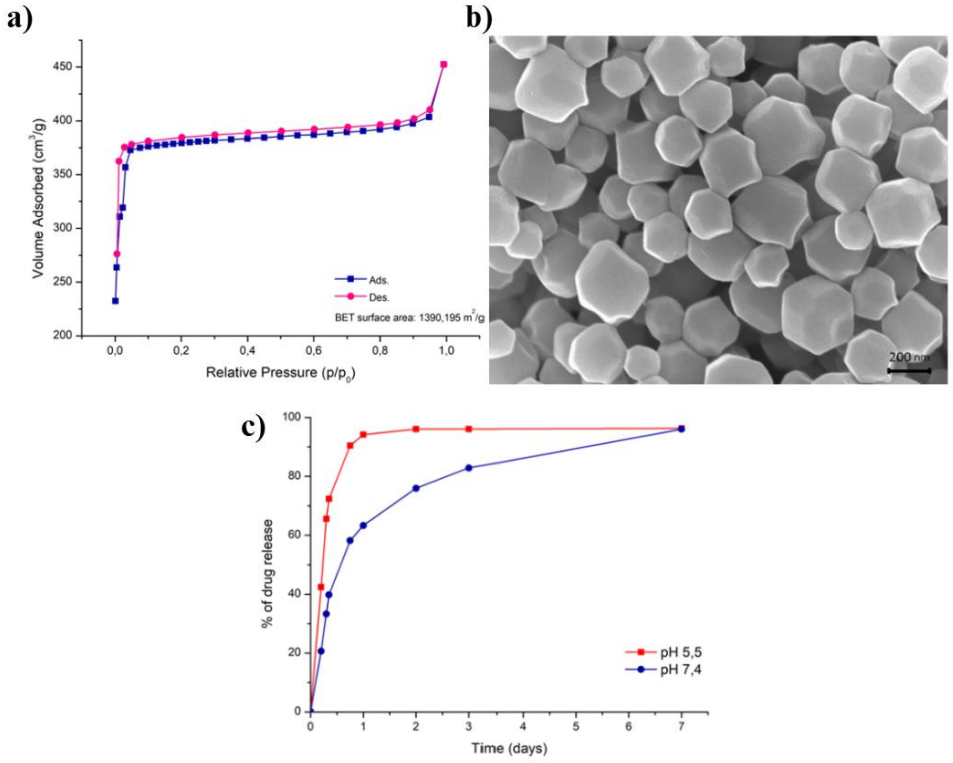

Figure Appendix-B 6. a) N_2 adsorption-desorption isotherms at 77 K of paracetamol@ZIF-8. b) SEM image collected at 50 kX of the paracetamol@ZIF-8 system. c) time-dependent release rate trend of paracetamol at pH 5.5 (red line) and pH 7.4 (blue line).

Bibliography

1. Brunauer, S.; Emmett, P. H.; Teller, E. Adsorption of Gases in Multimolecular Layers. *J. Am. Chem. Soc.* **1938**, *60* (2), 309–319.
2. Kida, K.; Okita, M.; Fujita, K.; Tanaka, S.; Miyake, Y. Formation of High Crystalline ZIF-8 in an Aqueous Solution. *CrystEngComm* **2013**, *15* (9), 1794–1801.

Appendix C - Experimental Section

Magnesium-Modified ZIF-8: A Step Closer to Biocompatible Drug Delivery

---

Extracted from:

di Nicola, N., Spoletti, E., Lazzarini, A. & Lusi, M. (in preparation).
Mg alloy affords less toxic and pH tuneable ZIF-8 for drug delivery.

Materials

Zinc nitrate hexahydrate (98%), Magnesium nitrate hexahydrate (99%), 2-methylimidazole (HMIM, 99%), phosphate-buffered saline tablets (PBS, 0.0027M KCl; 0.137M NaCl; pH = 7.4) were purchased from Sigma-Aldrich. N,N-Diethylformamide (99%), acetic acid (99,7%), nitric acid (70%) were acquired from Thermo Fisher Scientific.

Characterization Techniques

X-Ray Powder Diffraction (XRPD)

Diffraction patterns were recorded on a PANalytical EMPYREAN diffractometer system using Bragg-Brentano geometry and an incident beam of Cu Kα radiation (λ = 1.5418 Å) in the 2θ range between 3° and 40° (step size: 0,013°; time/step: 30 s; soller slit: 0,04 rad; divergence slit: ⅛; anti-scatter slit: ¼; 45 mA X 40 kV). Room temperature scans were performed on a spinning silicon zero-background sample holder. Diffraction patterns for the stability test at different pH values were recorded using a PANalytical X'Pert MPD Pro diffractometer equipped with a X'Celerator detector, in Bragg-Brentano geometry, using an incident beam of Cu Kα radiation (λ = 1.5418 Å) in the 2θ range between 5° and 60° (step size: 0.0167113°;

time/step: 29.845 s; soller slit: 0,04 rad; divergence slit: ½; 40 mA X 40 kV). Room temperature scans were performed on a spinning silicon zero-background sample holder.

Single-Crystal X-Ray Diffraction (SCXRD)

Single crystal X-ray diffraction data were collected on a Bruker D8 Quest diffractometer equipped with Mo Kα (λ = 0.71073 Å) radiation and Photon 100 detector. The data were integrated with Apex 4. Unit cell parameters for all compounds discussed herein are reported in Table Appendix-C 1. The structures were solved by the intrinsic phasing methods and refined by least-squares methods against F^2 using SHELXT[1] and SHELXL[2] through the OLEX2[3] interface. Non-hydrogen atoms were refined anisotropically. Hydrogen atoms were placed in calculated positions. The software Mercury[4] was used for graphic representations.

Table Appendix-C 1: Crystal data and details of measurement for a single crystal of 20%Mg-ZIF-8.

	20%MgZIF-8
Zn:Mg Ratio	80:20
Mg occupancy	0.235(8)
Formula	$C_8\ H_{10}\ Mg_{0.235}\ N_4\ Zn_{0.765}$, $0.417[C_5H_{11}NO]$
Mw, g mol^{-1}	260.12
T / K	273.00
Crystal system	cubic
Space group	*I*-43*m*
a / Å	17.0314(5)
b / Å	17.0314(5)
c / Å	17.0314(5)
α / °	90
β / °	90
γ / °	90

Surface Area Analysis

Surface area measurements were performed with the use of an Anton Parr Nova 800 instrument. The sample was inserted inside a calibrated-volume sample holder and treated at 150 °C in dynamic vacuum for 18 h directly on the instrument. Surface area was measured with N_2 adsorption-desorption isotherms at 77 K, by using BET method.[5]

Scanning Electron Microscopy-Energy Dispersive X-Ray Spectroscopy (SEM-EDX)

The morphology of the crystals was characterized using a HITACHI SU-70 scanning electron microscope (SEM) instrument. A small amount of the crystals was placed onto an adhesive carbon tape previously attached to a cylindrical aluminium 15 mm SEM stub. The samples were coated with gold using an Emitech K550 sputter coater at 20 mA for 45 s. The particles were imaged at a voltage of 20 kV. The instrument was also equipped with an Oxford X-Max 50 spectrometer. The EDX analysis was performed with the instrument proprietary software.

Thermogravimetric Analysis (TGA)

Thermogravimetric measurements were performed on TA TGA Q-50 under air stream (40 mL/min for furnace and 60 mL/min for balance) using 4 to 6 mg of ground powder, between room temperature and 600 °C, at 10 °C/min heating rate.

Inductively Coupled Plasma Mass Spectrometry

ICP-MS analysis was conducted using an Agilent 7850 mass spectrometer equipped with a collision cell. Measurements were performed in semi-quantitative mode, employing a calibration solution containing Li, Y, Co, Ce,

and Tl at a concentration of 10^{-9} g/g. Ultrapure water (18.2 MΩ), produced by a Milli-Q system (Millipore, USA), and ultrapure-grade nitric acid, obtained through a sub-boiling system, were used for sample solubilization.

Experimental Section

ZIF-8 Synthesis

The single-crystal synthesis of ZIF-8 was adapted from the procedure of A. Alowasheeir et al.[6] In this method, 0.175 g of $Zn(NO_3)_2$ and 0.1 g of 2-methylimidazole were dissolved in 7 mL of N,N-diethylformamide (DEF). Subsequently, 30 µL of 70% HNO_3 was added, and the mixture was sonicated until a clear solution was obtained. The solution was then placed in a sand bath inside an oven at 120°C for 72 hours. After the reaction time, the solution was gradually cooled inside the oven to facilitate crystal growth along the edges of the vial. The resulting crystals were collected and washed with acetone. To remove residual DEF, the crystals were dried under vacuum at 250 °C overnight.

Mg-ZIF-8 Synthesis (20%)

The single-crystal synthesis of Mg-substituted ZIF-8 was performed following the procedure previously published by A. Alowasheeir et al.[6] with the following modification. 0.149 g of $Zn(NO_3)_2$, 0.033 g of $Mg(NO_3)_2$, and 0.1 g of 2-methylimidazole (MIM) were dissolved in 7 mL of N,N-diethylformamide (DEF). Subsequently, 30 µL of 70% HNO_3 was added, and the mixture was sonicated until a clear solution was obtained. The solution was then placed in a sand bath inside an oven at 120 °C for 72 hours. After the reaction time, the solution was gradually cooled inside the oven using latent heat to facilitate crystal growth along the edges of the vial. The

resulting crystals were collected and washed with acetone. To remove residual DEF, the crystals were dried under vacuum at 250 °C overnight.

Stability Tests

To test the stability of the materials at different pH values, several batches were prepared containing 20 mg of ground ZIF-8 or Mg-ZIF-8, 5 mg of standard (NIST Silicon powder) and 5 mL of selected buffer solution (PBS pH 6.5 acetate pH 5.5 and pH 4.5). The different suspensions were kept under stirring for several times at room temperature. Once the test time had elapsed, the powder was recovered by centrifugation at 3500 RPM for 15 minutes, washed with water once and then dried in an oven. The tested samples were then measured by XRD technique to check for any loss of crystallinity leading to material degradation and quantitative phase analysis by Rietveld refinement performed to measure the amount of ZIF-8 still presents.

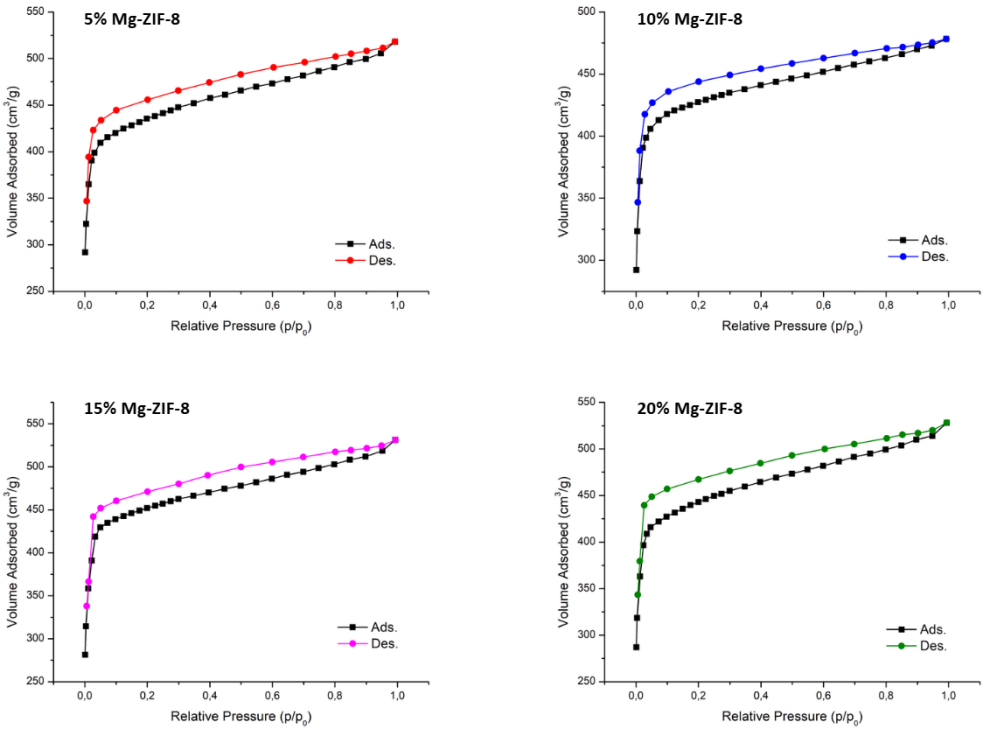

Figure Appendix-C 1. N_2 adsorption-desorption isotherms for 5%Mg-ZIF-8, 10%Mg-ZIF-8, 15%Mg-ZIF-8 and 20%Mg-ZIF-8 at 77K.

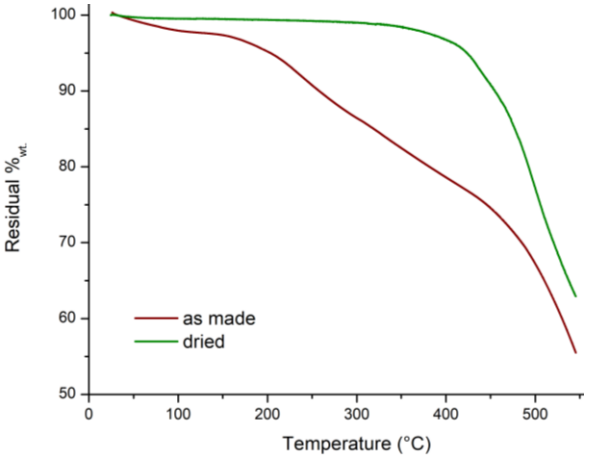

Figure Appendix-C 2. TGA of 20%Mg-ZIF-8 before and after activation.

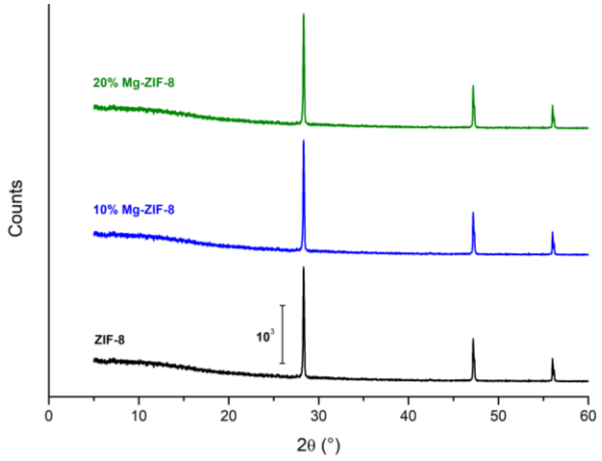

Figure Appendix-C 3. comparison of the experimental XRPD pattern for the suspension of ZIF-8, 10%Mg-ZIF-8 and 20%Mg-ZIF-8 with Si standard digested for 1h in buffer solutions at pH 4.5.

Table Appendix-C 2: Summary of the Rietveld refinement for the experimental XRPD pattern of the suspension of ZIF-8 with Si standard digested for 0, 2, 4, 8, 16 and 24 hours in buffer solutions at pH 6.5 and pH 5.5.

Time (hours)	ZIF-8 (%)		Silicon (%)		R weighted	
	pH 6.5	pH 5.5	pH 6.5	pH 5.5	pH 6.5	pH 5.5
0	75.5	75.5	24.5	24.5	17.7	17.7
2	46.3	48.1	53.7	51.9	12	15
4	47.6	34.2	52.4	65.8	11.8	14.2
8	44.8	21.8	55.2	78.2	12.5	22.2
16	44.7	14.8	55.3	85.2	11.5	22.6
24	46.3	7.3	53.7	92.7	12	22.3

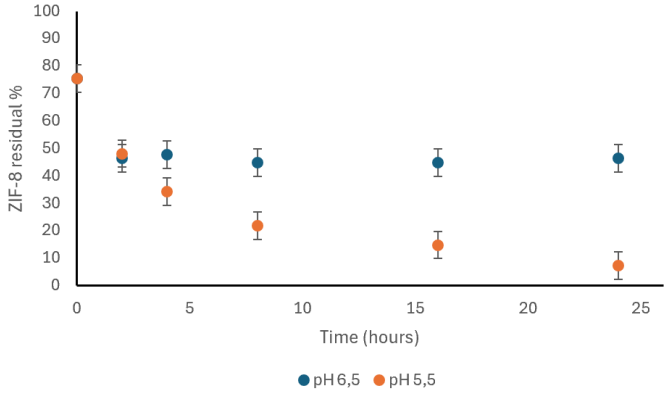

Figure Appendix-C 4. degradation trend of ZIF-8 at pH 5.5 and pH 6.5.

Table Appendix-C 3: Summary of the Rietveld refinement for the experimental XRPD pattern of the suspension of 10%Mg-ZIF-8 with Si standard digested for 0, 2, 4, 8, 16 and 24 hours in buffer solutions at pH 6.5 and pH 5.5.

Time (hours)	10%Mg-ZIF-8 (%)		Silicon (%)		R weighted	
	pH 6.5	pH 5.5	pH 6.5	pH 5.5	pH 6.5	pH 5.5
0	75.1	75.1	24.9	0	75.1	75.1
2	65.4	66	34.6	2	65.4	66
4	63.6	66.7	36.4	4	63.6	66.7
8	62.1	61.6	37.9	8	62.1	61.6
16	63.6	67.3	36.4	16	63.6	67.3
24	64.2	58.9	35.8	24	64.2	58.9

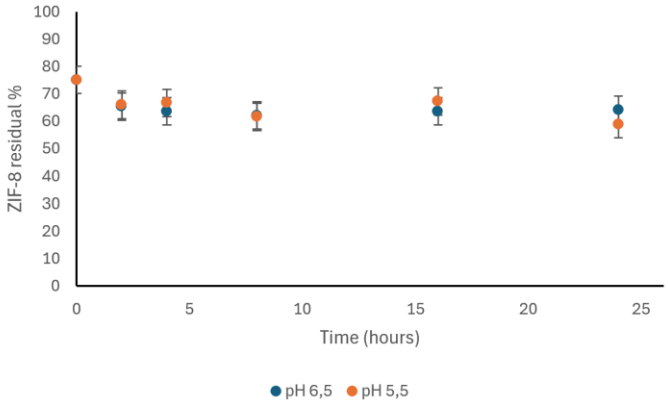

Figure Appendix-C 5. degradation trend of 10%Mg-ZIF-8 at pH 5.5 and pH 6.5.

Table Appendix-C 4: Summary of the Rietveld refinement for the experimental XRPD pattern of the suspension of 20%Mg-ZIF-8 with Si standard digested for 0, 2, 4, 8, 16 and 24 hours in buffer solutions at pH 6.5 and pH 5.5.

Time (hours)	20%Mg-ZIF-8 (%)		Silicon (%)		R weighted	
	pH 6.5	pH 5.5	pH 6.5	pH 5.5	pH 6.5	pH 5.5
0	72.8	72.8	27.2	0	72.8	72.8
2	65.3	61.6	34.7	2	65.3	61.6
4	66.2	59.4	33.8	4	66.2	59.4
8	60.3	60.2	39.7	8	60.3	60.2
16	62.9	63.6	37.1	16	62.9	63.6
24	63.4	59.3	36.6	24	63.4	59.3

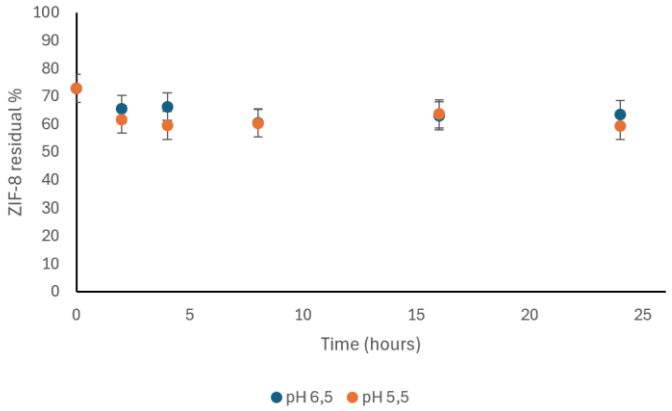

Figure Appendix-C 6. degradation trend of 10%Mg-ZIF-8 at pH 5.5 and pH 6.5.

Bibliography

1. Sheldrick, G. M. SHELXT—Integrated Space-Group and Crystal-Structure Determination. *Found. Crystallogr.* **2015**, *71* (1), 3–8.
2. Sheldrick, G. M. Crystal Structure Refinement with SHELXL. *Cryst. Struct. Commun.* **2015**, *71* (1), 3–8.
3. Dolomanov, O. V.; Bourhis, L. J.; Gildea, R. J.; Howard, J. A. K.; Puschmann, H. OLEX2: A Complete Structure Solution, Refinement and Analysis Program. *J. Appl. Crystallogr.* **2009**, *42* (2), 339–341.
4. Macrae, C. F.; Sovago, I.; Cottrell, S. J.; Galek, P. T. A.; McCabe, P.; Pidcock, E.; Platings, M.; Shields, G. P.; Stevens, J. S.; Towler, M.; Wood, P. A. Mercury 4.0: From Visualization to Analysis, Design and Prediction. *J. Appl. Crystallogr.* **2020**, *53* (1), 226–235.
5. Brunauer, S.; Emmett, P. H.; Teller, E. Adsorption of Gases in Multimolecular Layers. *J. Am. Chem. Soc.* **1938**, *60* (2), 309–319.
6. Alowasheeir, A.; Torad, N. L.; Asahi, T.; Alshehri, S. M.; Ahamad, T.; Bando, Y.; Han, M. Synthesis of Millimeter-Scale ZIF-8 Single Crystals and Their Reversible Crystal Structure Changes. *Sci. Technol. Adv. Mater.* **2024**, *25* (1), 2292485.

Appendix D - Experimental Section

Exploring PCN-224 for MRI Contrast Enhancement

Extracted from:

di Nicola, N., Vandone, M., Alonzi, R., Di Vito Nolfi, M., Ferella, F., Guidoni, L., Crucianelli, M., Zazzeroni, F., Colombo, V., Vecchiotti, D., Galante, A. & Lazzarini, A. (in preparation). Gd^{3+}- and Mn^{2+}-Doped Porphyrin-Based Metal Organic Frameworks for MRI Applications.

Materials

Zirconyl chloride octahydrate (98%). benzoic acid (99.5%). Gadolinium(III) chloride hexahydrate (99%). Manganese(II) chloride tetrahydrate (98%). sodium hydroxide (98%). N.N-Dimethylformamide (99.8%). acetone (99.5%). acetic acid (99.7%) and phosphate-buffered saline tablets (PBS. 0.0027M KCl; 0.137M NaCl; pH = 7.4) were purchased from Sigma-Aldrich. Tetrakis(4-carboxyphenyl)porphyrin (TCPP) (97%) was acquired from TCI chemicals. Double deionized water was obtained from a Milli-Q filtration/purification system (Millipore. Bedford. MA. USA).

Characterization Techniques

X-ray Powder Diffraction (XRPD) and Pair Distribution Function (PDF)

LABORATORY XRPD

X-ray Powder Diffraction patterns were collected using Cu-Kα radiation (λ=1.5418 Å) on a vertical-scan Bruker AXS D8 Advance diffractometer in θ:θ mode. equipped with a Goebel Mirror and a Bruker Lynxeye Linear Position Sensitive detector. with the following optics: primary and secondary Soller

slits. 2.3° and 2.5° respectively; divergence slit. 0.1°; receiving slit. 2.82°. The generator operated at 40 kV with a 40 mA current. The nominal resolution for the present set-up is 0.08° 2θ (FWHM of the α_1 component for the LaB6 peak at about 21.3° 2θ). The sample was gently ground over an agate mortar and then deposited in the 2 mm deep hollow of a zero-background plate (a properly misoriented quartz monocrystal). Each scan was acquired. unless otherwise specified. in the 4–60° 2θ range with an exposure time of 1 s/step. Le Bail fittings[1] of each collected pattern were performed using TOPAS-Academic 6 software.[2] The instrumental contribution to the peak shape was described using the fundamental parameters approach.[3] The background was modeled by a Chebyshev polynomial function.

HIGH RESOLUTION XRPD

High-resolution XRPD measurements suitable for PDF data extraction were performed at the BM31 beamline at ESRF synchrotron with a wavelength of 0.24486 Å using a Pilatus CdTe 2 M detector from DECTRIS. The diffraction setup was calibrated by measuring a Si standard. Each scan had an exposure time of 60 seconds with 10 repetitions that were later averaged together. The sample-detector distance was set to 90 mm with an angle of 15° to the incoming beam. This configuration allows for the collection of high-angle data. which can be used to generate Pair Distribution Function (PDF) signals. In a typical procedure the ground powder of each sample was gently packed into a 0.5 mm quartz capillary and measured at room temperature as explained before. For the background subtraction an empty quartz capillary of 0.5 mm was also measured with the same experimental parameters.

PAIR DISTRIBUTION FUNCTION (PDF) DATA EXTRACTION AND SIMULATION OF THEORETICAL PDF SIGNALS

For the scattering data analysis each set of ten unmasked images was averaged into a single image using the Python fast azimuthal integration (pyFAI) software.[4] The calibration was done for a crystalline Si standard. A static mask was created by masking beamstop; beamstop arm; the dead pixels. and the over-exposed pixels. The obtained masked image was then integrated using the Dioptas software.[5] giving a classical XRPD pattern as a function of theta. The PDFgetX3 algorithm was employed to perform background subtraction and normalization. yielding the total scattering structure function. *S(Q)*. Subsequent reductions were carried out to derive the reduced total scattering structure function. *F(Q)*. followed by inverse Fourier transformation to achieve the reduced atomic pair distribution function. *G(r)*. The final Q ranges (Q_{min} and Q_{max}) used to obtain the *G(r)* function were then chosen by inspecting *F(Q)* and *G(r)* functions. trying to reduce the noise in the *G(r)* oscillations as much as possible. but also keeping the wider *Q* range possible. Table Appendix-D 1 shows the values used for each parameter for the PDF data conversion for each sample. The r_{poly} value was kept under the 1.1 threshold for the entire dataset. This value. smaller than any feasible bond distance (excluding any hydrogen bond) present in the MOFs. ensured a good profile for the processed data. As a result. any oscillations in the *G(r)* plot at $r < 1.1$ - 1.2 should be disregarded.

PDF signals were simulated for published structures using the DiffpyCMI software package through Jupyter Notebooks.[6] Due to the large number of models reported in the databases for this MOF careful selection of the .cif file used for PDF simulations was conducted to maximize the accuracy of the simulated PDFs. The selected .cif files (see below) were downloaded from the CCDC database (CCDC n° 1570585).[7] the Crystallographic Open Database (COD) and from the paper by Koschnick et al.[8] The crystal structures were loaded in DiffPyCMI through the *loadStructure* method. The PDF signals were generated using the following parameters: Q_{min} = 0 Å^{-1}. Q_{max} = 20 Å^{-1}.

r_{min} = 0 Å. r_{max} = 30 Å. q_{iso}= 0.01. Individual bond contributions to the simulated PDF signals were generated using a type - mask through the *setTypeMask* method. In this way. the single contributions for the Zr-Zr. Zr-O. C-O. and Mn-N bonds were generated for the literature reported structures.

Table Appendix-D 1: List of pdfgetX3 parameters used for the conversion of PXRD patterns in PDF signals.

	PCN-224	**Entry 2**	**Entry 3**	**Entry 4**	**Entry 5**
Q_{min}. Å	0.2	0.19	0.2	0.2	0.2
Q_{max}. Å	21.2	21.2	21.2	21.2	21.2
$Q_{maxinst}$. Å	22.58	22.58	22.58	22.58	22.58
R_{poly}.	0.9	1.1	1.1	1.1	1

CHRYSTALLOGRAPHIC ANALYSIS

The structureless Le Bail fitting of the experimental PXRD pattern for the pristine material verified the adoption of the $Pm\bar{3}m$ unit cell. As documented in the literature for this MOF.[8] the presence of broad. low-intensity peaks at 2θ values around 5° and 7°. as opposed to narrow. intense reflections. is a significant characteristic that differentiates the $Pm\bar{3}m$ space group from the $Im\bar{3}m$ group. This distinction pertains to the presence and level of ordering in missing linker defects within the MOF structure. Specifically. ordered defects result in additional intense Bragg peaks in the PXRD pattern. corresponding to the $Im\bar{3}m$ cell. In contrast. a disordered configuration. as observed in our study. leads to the attenuation or complete absence of these peaks.

To construct a more accurate structural model for our samples that accounts for structural disorder and is suitable for simulating PDF signals of the MOF framework. which is essential for correlating experimental PDF fluctuations with key interatomic bond lengths. a 2×2×2 supercell model with $P1$

symmetry was considered. as described by Koschnick et al.[8] Selecting the right model for simulating PDF signals is especially important when dealing with materials that have defects. If the model fails to properly incorporate disorder non-physical oscillations may appear in the simulated profiles. Thus. to determine the applicability of the reported *P*1 unit cell to the experimental data. a Le Bail fitting was executed using the same cell. This fitting provided better visual agreement together with a reduced R_{wp} value (Figure Appendix-D 1) compared to the $Pm\bar{3}m$ model (a = 19.365 Å). Ultimately these results suggest that the initial PCN-224 structure inherently exhibits a certain level of structural disorder. which likely continues in the metal-doped versions.

Although we did not perform structural refinement on our samples the *P*1 unit cell's Le Bail fitting provided a satisfactory correlation with the experimental data. Additionally. it uncovered extra reflections related to broad peaks not accounted for by the $Pm\bar{3}m$ model. suggesting that the defective model is a suitable representation of our systems. Consequently. based on the outcomes of the Le Bail analysis. the 2×2×2 *P*1 model was chosen for subsequent PDF analysis.

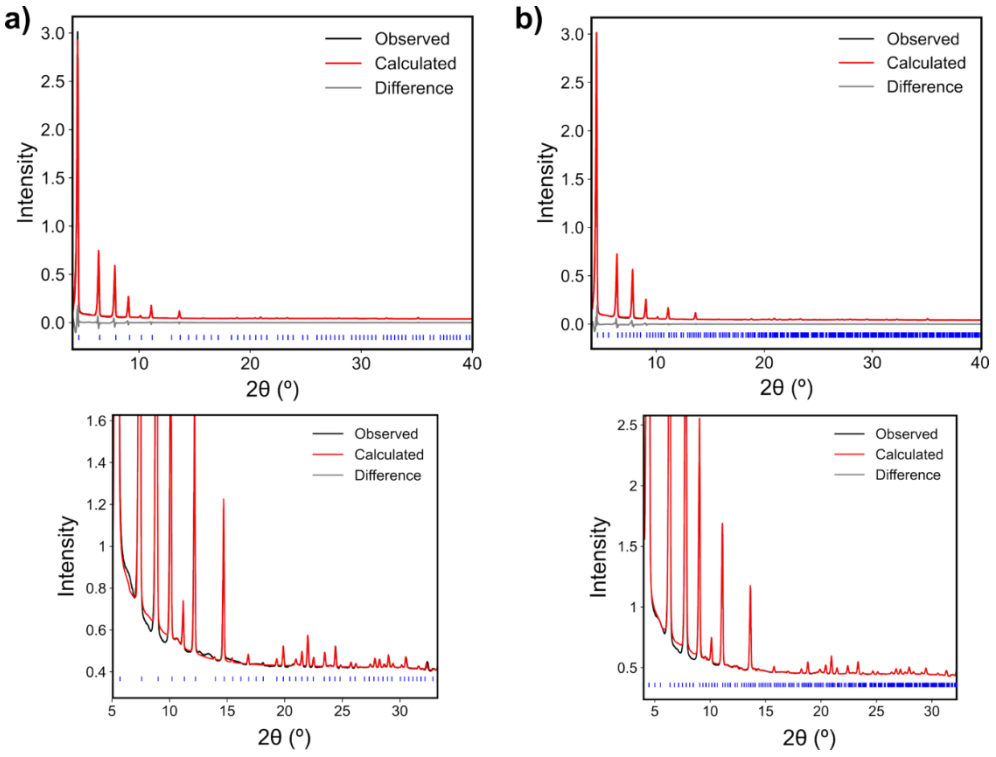

Figure Appendix-D 1. a) Le Bail fitting of PCN-224 using literature reported unit cell. R_{wp}: 9.897; space group: $Pm\bar{3}m$; a. b. c: 19.363(7) Å. Volume: 7260.572(2) Å^3. b) Le Bail fitting of PCN-224 using literature 2x2x2 supercell. R_{wp}:7.989; space group: P1; a.b.c: 38.749(8) Å. α.β.γ: 90°. Volume: 58184.645(9) Å^3. λ: Cu Kα1.

Attenuated Total Reflectance Mid Infrared Spectroscopy (ATR-MIR)

ATR-MIR measurements were performed with a PerkinElmer Spectrum Two instrument equipped with an atmospheric UATR Two accessory and a DTGS detector. Each spectrum was obtained by averaging 8 scans with a 4 cm^{-1} resolution in the range 4000-400 cm^{-1}.

Surface Area Analysis

Surface area measurements were performed with the use of an Anton Parr Nova 800 instrument. The sample was inserted inside a calibrated-volume

sample holder and treated at 200 °C in dynamic vacuum for 18 h directly on the instrument. Surface area was measured with N_2 adsorption-desorption isotherms at 77 K. by using BET method.[9]

Scanning Electron Microscopy-Energy Dispersive X-Ray Spectroscopy (SEM-EDX)

The morphology of the samples was analyzed using Scanning Electron Microscopy (SEM) with a FESEM ZEISS Gemini500 instrument. Images were captured at 10k and 50k magnifications using backscattered electrons. operating at an accelerating voltage (HT) of 5 kV. The samples were mounted on SEM stubs covered with carbon tape and subsequently coated with a thin chromium layer to increase conductivity and prevent electrical charging during imaging. The instrument is also equipped with an Oxford Aztec spectrometer: EDX analysis was performed with thevendor's proprietary software.

Inductively Coupled Plasma-Mass Spectrometry (ICP-MS)

ICP-MS characterization was performed by mass spectrometer Agilent 7850 with collision cell. Measurements were carried out in semi-quantitative mode using calibration solution with Li. Y. Co. Ce. Tl at 10^{-9} g/g. Ultrapure water (18.2 MΩ) produced by milliQ system from Millipore (USA). nitric acid ultrapure grade obtained by sub-boiling system was used to solubilize samples.

Magnetic Resonance Imaging (MRI)

MRI scans were performed with a preclinical M2™ compact high-performance MRI system (Aspect Imaging. Shoham. Israel) with 1.05 T magnetic field (proton frequency of 45 MHz) equipped with a cylindrical solenoid radiofrequency coil. 8 cm long and 3.5 cm of inner diameter.

Relaxivity Analyses

For extracting both T_1 and T_2 relaxivities we relied on spin-echo sequences. For the T_1 relaxivity (r_1). we acquired axial images with three 2 ml vials at the same time. for a total of six different concentrations for each compound. The T_1-weighted images were acquired without averaging (NEX=1). with the minimum available echo time (TE = 4.1 ms). different repetition times (TR = 21; 40; 80; 100; 150; 200; 300; 500; 750; 1000; 2000; 5000; 9000 ms). 32 mm x 32 mm Field Of View. 32 x 32 frequency and phase encoding steps (1 mm x 1 mm voxel size). and slice thickness of 3mm. T_1 maps were calculated by the exponential signal recovery within each image voxel. and the T_1 value of each sample by the average of the corresponding voxels' values.

For the T_2 relaxivity (r_2). we used a fast spin-echo sequence (NEX = 1) with echo train length equal to 128 and disabled gradients. allowing a whole-sample CPMG (Car-Purcell-Meiboom-Gill) acquisition of each single vial. Multiple echoes from a single vial (TE = 4.4 ms) were acquired. extracting T_2 from the echoes' amplitude exponential decay. Voxel intensities and CPMG echoes amplitude fit were performed with in-house developed Matlab scripts (The MathWorks. Inc. Natick. MA. USA) using a 3 parameters mono-exponential fitting based on the Levenberg–Marquardt nonlinear least-squares algorithm. All MRI measurements were done at 22 ± 1 °C.

Finally. the molar relaxivities were calculated from the slope of the linear regression of $1/T_1$ and $1/T_2$ as a function of CA concentrations (mM).

Cell Culture. Toxicity and Oxidative Stress Analysis

3T3 murine fibroblasts cells were cultured in High-Glucose Dulbecco's Modified Eagle Medium (Euroclone. Milan. Italy) supplemented with 10% Fetal Bovine Serum (FBS) (Gibco. Thermo Fisher Scientific. Wilmington. NC. USA). 1% penicillin/streptomycin (100 U/mL; 100 μg/mL) (Euroclone. Milan. Italy). and 1% L-glutamine (2 mM) (Euroclone. Milan. Italy) at 37 °C

with 5% CO_2. PCN-224. Mn@PCN-224. and Gd@PCN-224 were resuspended in Milli-Q sterile water at a concentration of 5 mg/ml. and cytotoxicity tests were performed by culturing 3T3 cells in 96-well plates and treating with different compounds at a concentration of between 0.5 µg/ml and 50 µg/ml. After 72 hours Prestoblue viability assay was performed in accordance with the manufacturer's instructions. CellRox™ oxidative detection assay was carried out by culturing 3T3 cells for 72 hours in SlideFlask™ (Nunc. Thermo Fisher Scientific. Wilmington. NC. USA). treating cells with MOFs at a concentration of between 0.5 µg/ml and 2.5 µg/ml. and adding CellRox™ green reagent to culture medium before microscopic analysis.

Experimental Section

Synthesis of PCN-224 (PRISTINE)

PCN-244 was synthesized from the procedure of Dawei Feng and coworkers.[10] 313 mg of $ZrOCl_2$. 77 mg of TCPP. and 3 g of benzoic acid were added to 15 mL of DMF in a 22 mL vial and sonicated for 5 minutes. The solution was heated at 120°C in an oven for 24 h. The suspension obtained was centrifuged and washed with DMF 3 times and acetone 3 times. The products were then dried overnight under reduced pressure at 70°C.

Synthesis of Gd@PCN-224

80 mg of previously synthesized PCN-224. 20.1 mg of $GdCl_3x6H_2O$ and 6.7 mg of NaOH (PCN-224/Gd^{3+}/NaOH molar ratio 1:3:9) were dissolved in 43.2 mL of water. The solution was heated to 70°C for 4 h under stirring. The suspension obtained was centrifuged and washed with H_2O once and acetone once. The products were then dried overnight under reduced pressure at 40°C. The dried sample is suspended in 20 mL of H_2O and inserted into a dialysis membrane (cut-off 14k Da). The membrane is left under stirring at

RT for 24 h in 400 mL of H_2O. The sample is then recovered. centrifuged. and washed with acetone once. The products were then dried overnight under reduced pressure at 40°C.

Synthesis of Mn@PCN-224

80 mg of previously synthesized PCN-224. 10.7 mg of $MnCl_2x4H_2O$ and 6.7 mg of NaOH (PCN-224/Mn^{2+}/NaOH molar ratio 1:3:9) were dissolved in 43.2 mL of water. The solution was heated to 70°C for 4 h under stirring. The suspension obtained was centrifuged and washed with H_2O once and acetone once. The products were then dried overnight under reduced pressure at 40°C. The dried sample is suspended in 20 mL of H_2O and inserted into a dialysis membrane (cut-off 14k Da). The membrane is left under stirring at RT for 24 h in 400 mL of H_2O. The sample is then recovered. centrifuged. and washed with acetone once. The products were then dried overnight under reduced pressure at 40°C.

Synthesis of Gd@TCPP

200 mg of TCPP and 94 mg of $GdCl_3x6H_2O$ (Gd^{3+}/TCPP molar ratio 1:1) were dissolved in 202.4 mL of water. The solution was heated at 70°C for 4h under stirring. The solution obtained was dried by rotavapor. and the dried sample was suspended in 10 mL of H_2O and inserted into a dialysis membrane (cut-off 500 Da). The membrane is left under stirring at RT for 24h in 400 mL of H_2O. The sample is then recovered and decanted. The products were then dried overnight under reduced pressure at 40°C.

Synthesis of Mn@TCPP

200 mg of TCPP and 50.1 mg of $MnCl_2x4H_2O$ (Mn^{2+}/TCPP molar ratio 1:1) were dissolved in 202.4 mL of water. The solution was heated at 70°C for 4h under stirring. The solution obtained was dried by rotavapor. and the dried

sample was suspended in 10 mL of H_2O and inserted into a dialysis membrane (cut-off 500 Da). The membrane is left under stirring at RT for 24h in 400 mL of H_2O. The sample is then recovered and decanted. The products were then dried overnight under reduced pressure at 40°C.

Stability Tests

Gd^{3+} and Mn^{2+} release assays were conducted by dispersing 5 mg of previously synthesized Gd@PCN-224 and Mn@PCN-224 in 3 mL acetate buffer (pH 5). respectively. The resulting suspensions were individually loaded into a dialysis membrane (cut-off 500 Da) and then immersed in 17 mL of acetate buffer. The same setup was used with PBS (pH 7.4). The suspensions were kept under gentle agitation at 37°C. the average body temperature of a human being. for several days. After one week the sample is recovered and dried to measure the amount of Gd^{3+} and Mn^{2+} possibly lost from PCN-224 by ICP-MS.

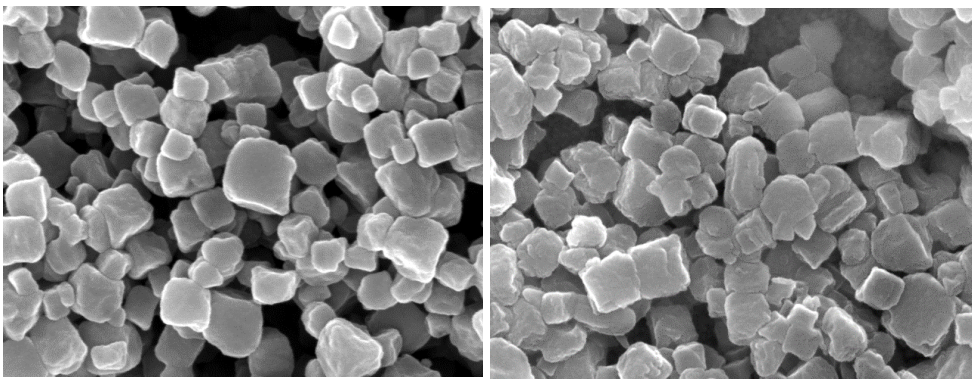

Figure Appendix-D 2. 50 kx SEM image of Entry 2 (left) and Entry 3 (right).

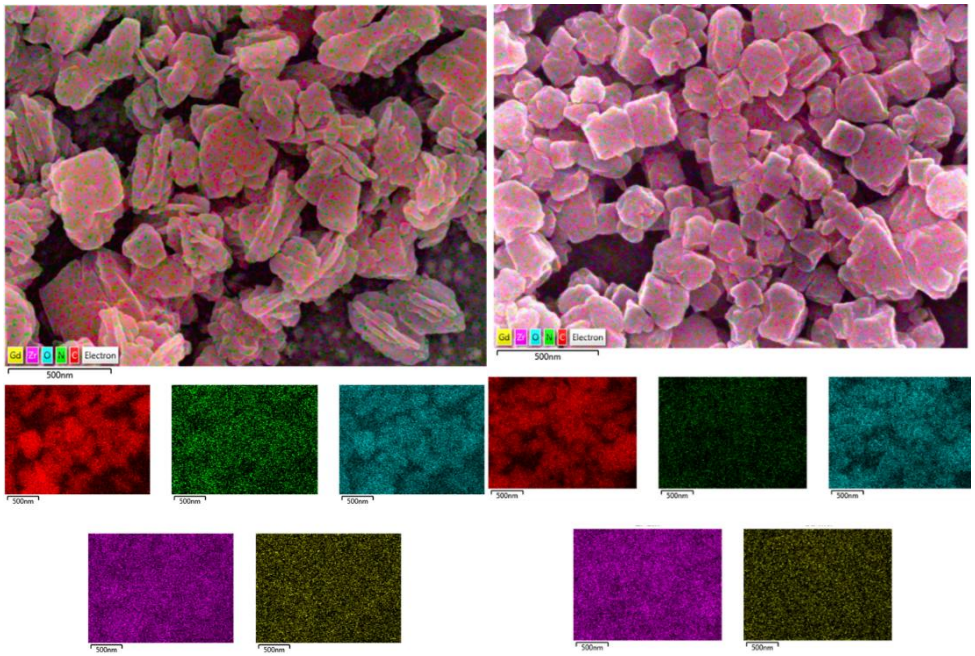

Figure Appendix-D 3. EDX map of the distribution of elements (carbon in red, nitrogen in green, oxygen in aqua green, zirconium in purple and gadolinium in yellow)of Entry 2 (left) and Entry 3 (right).

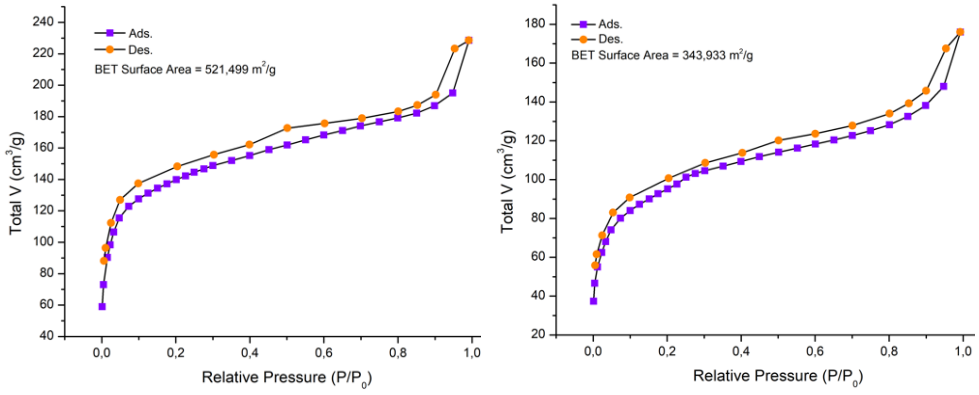

Figure Appendix-D 4. 77K adsorption-desorption isotherms of Entry 2 (BET surface area: 521.499 m^2/g) (left) and Entry 3 (BET surface area: 343.933 m^2/g) (right).

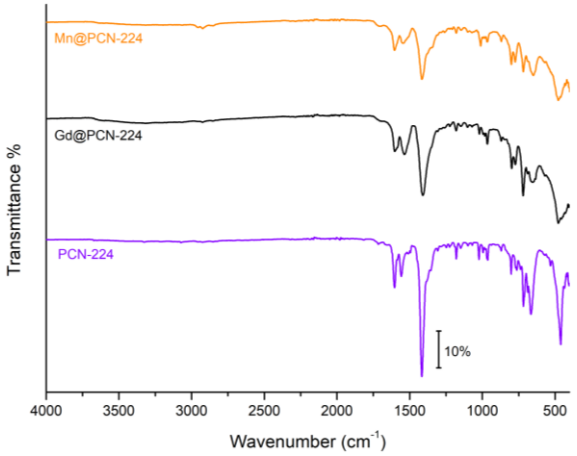

Figure Appendix-D 5. Comparison between ATR-MIR of PCN-224. Gd@PCN-224 and Mn@PCN-224.

Bibliography

1. Le Bail, A.; Duroy, H.; Fourquet, J. L. Ab-Initio Structure Determination of LiSbWO6 by X-Ray Powder Diffraction. *Mater. Res. Bull.* **1988**, *23*, 447–452.
2. Coelho, A. A. TOPAS and TOPAS-Academic: An Optimization Program Integrating Computer Algebra and Crystallographic Objects Written in C++. *J. Appl. Crystallogr.* **2018**, *51* (1), 210–218.
3. Cheary, R. W.; Coelho, A. A. A Fundamental Parameters Approach to X-ray Line-Profile Fitting. *J. Appl. Crystallogr.* **1992**, *25* (2), 109–121.
4. Ashiotis, G.; Deschildre, A.; Nawaz, Z.; Wright, J. P.; Karkoulis, D.; Picca, F. E.; Kieffer, J. The Fast Azimuthal Integration Python Library: pyFAI. *J. Appl. Crystallogr.* **2015**, *48* (2), 510–519.
5. Prescher, C.; Prakapenka, V. B. DIOPTAS: A Program for Reduction of Two-Dimensional X-Ray Diffraction Data and Data Exploration. *High Press. Res.* **2015**, *35* (3), 223–230.
6. Juhás, P.; Farrow, C. L.; Yang, X.; Knox, K.; Billinge, S. J. L. Complex Modeling: A Strategy and Software Program for Combining Multiple Information Sources to Solve Ill-Posed Structure and Nanostructure Inverse Problems. *Found. Crystallogr.* **2015**, *71* (6), 562–568.
7. Cambridge Crystallographic Data Centre (CCDC). *https://www.ccdc.cam.ac.uk/structures/* (accessed Jun 20, 2025).
8. Koschnick, C.; Stäglich, R.; Scholz, T.; Terban, M. W.; von Mankowski, A.; Savasci, G.; Lotsch, B. V. Understanding Disorder and Linker Deficiency in Porphyrinic Zirconium-Based Metal–Organic Frameworks by Resolving the Zr8O6 Cluster Conundrum in PCN-221. *Nat. Commun.* **2021**, *12* (1), 3099.
9. Brunauer, S.; Emmett, P. H.; Teller, E. Adsorption of Gases in Multimolecular Layers. *J. Am. Chem. Soc.* **1938**, *60* (2), 309–319.

10. Feng, D.; Chung, W. C.; Wei, Z.; Gu, Z. Y.; Jiang, H. L.; Chen, Y. P.; Zhou, H. C. Construction of Ultrastable Porphyrin Zr Metal–Organic Frameworks through Linker Elimination. *J. Am. Chem. Soc.* **2013**, *135* (45), 17105–17110.

Appendix E - Experimental Section

A Different Perspective: MOFs for Wastewater Treatment Applications

---

Extracted from:

di Nicola, N., Di Pelino, M., Foschi, M., Passalacqua, R., Lazzarini, A. & Ruggieri, F. (2025). ZIF-8 as Potential Pesticide Adsorbent Medium for Wastewater Treatment: The Case Study of Model Linuron Extraction Conditions Optimization *via* Design of Experiment. *Molecules*. *30*(12). 2480.

Materials

Zinc nitrate hexahydrate (98%). 2-methylimidazole (99%). Na_2SO_4 and Methanol (99.8%) were purchased from Sigma-Aldrich (Saint Louis. MO. USA). Linuron standard (purity 99.9%) was obtained from Labor Dr Ehrenstorfer-Schäfers (Augsburg. Germany) and was used without further purification. A stock solution (1.00 g/L) of linuron was prepared by dissolving accurately-weighed 10 mg of pesticide in 10 mL of acetonitrile (HPLC grade. Carlo Erba Reagenti. Milano. Italy) and stored at 4 °C. Deionized water obtained by a water filtration/purification system (Millipore. Bedford. MA. USA) was used.

Characterization Techniques

X-Ray Powder Diffraction (XRPD)

The XRD patterns of the investigated samples were acquired by a Bruker D2 Phaser benchtop X-ray diffractometer (Bruker AXS GmbH. Karlsruhe. Germany) using Cu Ka radiation operating with the conventional Bragg–

Brentano geometry. in the 2θ = 5–40° range. Patterns were acquired with a resolution of 0.05°. acquiring each point for 20 s.

Attenuated Total Reflectance Mid Infrared Spectroscopy (ATR-MIR)

ATR-MIR measurements were carried out using a PerkinElmer (Waltham. MA. USA) Spectrum Two spectrometer equipped with an atmospheric UATR Two accessory and a DTGS detector. Spectra were recorded by averaging 8 scans at a resolution of 4 cm^{-1}. covering the spectral range from 4000 to 400 cm^{-1}.

Surface Area Analysis

Surface area measurements were performed with the use of an Anton Parr Nova 800 instrument. The sample was inserted inside a calibrated-volume sample holder and treated at 150 °C in dynamic vacuum for 18 h directly on the instrument. Surface area was measured with N_2 adsorption-desorption isotherms at 77 K. by using BET method.[1]

Scanning Electron Microscopy (SEM)

The morphology of the samples was examined via Scanning Electron Microscopy (SEM) using a FESEM ZEISS (Oberkochen. Germany) Gemini500 instrument. Images were acquired at magnifications of 20k. employing backscattered electrons and operating at an accelerating voltage of 5 kV. The samples were mounted on SEM stubs covered with carbon tape and coated with a thin layer of chromium to enhance conductivity and minimize electrical charging during imaging.

High-Performance Liquid Chromatography (HPLC)

High-performance liquid chromatography (HPLC) was employed to quantify the residual concentration of Linuron in solution Analyses were performed using a C18 reverse-phase column (250 mm × 4.6 mm. 5 µm particle size) with a mobile phase composed of acetonitrile and water (70:30 v/v). The flow rate was set to 1.0 mL/min and the injection volume was 20 µL. Detection was carried out using a UV-Vis detector at a wavelength of 248 nm. Each sample was analyzed in triplicate. and calibration curves were constructed from standard solutions of known Linuron concentrations to ensure accurate quantification.

Experimental Section

ZIF-8 Synthesis

Numerous synthetic methods are currently available to produce ZIF-8. even with slight structural variations. For this work we adapted the synthetic procedure based on the method developed by Koji Kida and coworkers.[2] This method utilizes hydrothermal synthesis. which is particularly well suited for green applications due to the use of water as the solvent. facilitating the production of particles with a high surface area. In brief. 1.488 g of zinc nitrate hexahydrate were dissolved in 40 mL of deionized water and mixed with a solution containing 24.6 g of 2-methylimidazole in 160 mL of deionized water. The mixture. which rapidly became milky. was stirred at room temperature for 2 h. After the reaction. the resulting suspension was centrifuged at 5000 rpm for 30 min and washed three times with methanol. Finally. the products were dried overnight under reduced pressure at 40 °C.

Preliminary Experimental Procedure

For the adsorption experiments. preliminary tests involved mixing 5 mL of an aqueous pesticide solution (5 µg/mL) with 10 mg of ZIF-8 in a vial. followed by agitation for 1 hour. After mixing the suspensions were transferred to Falcon tubes and centrifuged at 4000 rpm for 5 minutes. The supernatants were analyzed using High-Performance Liquid Chromatography (HPLC) to determine the residual pesticide concentration. Subsequently the aqueous phase was removed. and the remaining ZIF-8 solid was washed with acetonitrile to desorb and recover the pesticide. providing an estimate of the amount trapped within the framework. A kinetic study was conducted at three time intervals: 30. 60. and 90 minutes. In this phase. 10 mg of ZIF-8 was introduced into vials containing 7 mL of a 5 µg/mL Linuron solution. The vials were shaken and then transferred into 10–15 mL Falcon tubes and centrifuged for 5 minutes at 4000 rpm. The upper supernatant was collected for analysis. and the residual liquid was removed. The precipitate was then treated with 7 mL of acetonitrile. agitated. and the resulting supernatant was transferred for final analysis.

Results from these tests indicated that the adsorption efficiency remained relatively constant (10– 12%) regardless of contact time. and 30 minutes was selected as the standard duration for subsequent experiments. The effect of ionic strength was assessed by preparing a 100 µg/mL calcium chloride solution in phosphate buffer (pH = 6.0) and using it to dilute the Linuron solution. A 10% decrease in pesticide peak area post-adsorption confirmed modest binding under these conditions. Comparable adsorption values (~10%) were observed at pH 7.0 with phosphate buffer.

To enhance removal. the ZIF-8 dose was increased to 50 mg. resulting in an adsorption efficiency of ~90%. confirmed through methanol extraction. Using 25 mg of ZIF-8 slightly reduced adsorption. a trend consistent with the

desorption analysis. To evaluate phosphate competition. adsorption was repeated in deionized water. yielding an efficiency of 70.2%.

Calibration Curve

A calibration curve for the quantification of linuron was established in the concentration range of 0.2– 10 μg·mL⁻¹. Each concentration level was analyzed in triplicate under identical experimental conditions. A strong linear relationship was observed between analyte concentration and detector response. The resulting regression equation was:

$$y = 92233x + 6574$$

where y represents the chromatographic area and x the concentration of linuron (μg·mL⁻¹). The correlation coefficient was $R^2 = 0.9996$. indicating excellent linearity across the examined range. The standard error of the estimate (SEE) was 4985. confirming the minimal dispersion of the data around the regression line.

The standard error of the slope was 311. and the standard error of the intercept was 1745. supporting the reliability of the regression parameters. Residuals analysis showed no systematic deviation. and precision at each calibration level was satisfactory. In particular. the relative standard deviation for the 0.2 μg·mL⁻¹ triplicates was below 1%. highlighting excellent repeatability at low concentration levels. Sensitivity parameters were calculated following international guidelines. The limit of detection (LOD) was found to be 0.175 μg·mL⁻¹. and the limit of quantification (LOQ) was 0.529 μg·mL⁻¹. using the formulas:

$$LOD = \frac{3.3\,\sigma}{S} \quad ; \quad LOQ = \frac{10\,\sigma}{S}$$

where σ is the standard deviation of the residuals and S is the slope of the calibration curve.

These results confirm that the method is highly sensitive. precise. and well-suited for the quantitative determination of linuron in aqueous samples at trace levels.

Experimental Design

A Design of Experiments (DoE) approach was employed to optimize the adsorption conditions and identify the most influential factors affecting pesticide removal. The Central Composite Design (CCD). employed with response surface methodology (RSM). was selected due to its ability to evaluate both main effects. interaction effects of the variables and curvatures in multivariate systems. The investigated factors were the temperature (X1). linuron concentration (X2) and ionic strength (X3). Each variable was tested at three levels: low (−1). medium (0). and high (+1) corresponding at the following 20. 30 and 40 °C for X1; 2. 5 and 8 µg/mL for X2 and 0. 25. 50 mg/mL Na_2SO_4 for X3. A total of 22 experiments were performed. including replicates at the center point to estimate experimental error. The response variable was the percentage of linuron removed. calculated based on HPLC measurements. Model fitting. and statistical analysis were conducted using Matlab R2020a statistical software.

The influence of the three selected factors was modeled by a second-degree polynomial Equation.

$$Y = a_1 + a_2 \cdot X1 + a_3 \cdot X2 + a_4 \cdot X3 + a_5 \cdot X1 \cdot X2 + a_6 \cdot X1 \cdot X3 + a_7 \cdot X2 \cdot X3 + a_8 \cdot X1^2 + a_9 \cdot X2^2 + a_{10} \cdot X3^2$$

where Y represents the percentage of linuron removed and a_1–a_{10} represent the model coefficients that were determined by ordinary least squares regression. In addition the leave-one-out cross-validation method was used to assess the generalization of the model. The significance of the model and lack-of-fit was estimated by analysis of variance. ANOVA.

Bibliography

1. Brunauer, S.; Emmett, P. H.; Teller, E. Adsorption of Gases in Multimolecular Layers. *J. Am. Chem. Soc.* **1938**, *60* (2), 309–319.
2. Kida, K.; Okita, M.; Fujita, K.; Tanaka, S.; Miyake, Y. Formation of High Crystalline ZIF-8 in an Aqueous Solution. *CrystEngComm* **2013**, *15* (9), 1794–1801.

Finanziato dall'Unione europea-*NextGeneration EU*
Missione 4, Componente 1 – CUP E13C22001060006